Álvaro Muelas Expósito

Experimental characterization and modeling of liquid fuel combustion. From pure compounds to real fuels.

Director/es

Ballester Castañer, Javier Manuel

Universidad Zaragoza
1542

<div style="border:1px solid">

Tesis Doctoral

</div>

EXPERIMENTAL CHARACTERIZATION AND MODELING OF LIQUID FUEL COMBUSTION. FROM PURE COMPOUNDS TO REAL FUELS.

Autor

Álvaro Muelas Expósito

Director/es

Ballester Castañer, Javier Manuel

UNIVERSIDAD DE ZARAGOZA
Escuela de Doctorado

2021

Universidad Zaragoza

1542

PhD Dissertation

Experimental characterization and modeling of liquid fuel combustion. From pure compounds to real fuels.

Author

Álvaro Muelas Expósito

Thesis supervisor

Javier Ballester Castañer

Escuela de Ingeniería y Arquitectura

2020

Agradecimientos

En primer lugar, mi más sincero agradecimiento a Javier Ballester por darme la oportunidad de realizar esta tesis, así como por todo su apoyo, ayuda y consejo durante estos años.

Asimismo, me gustaría agradecer a los profesores A. Sánchez y F. Williams por su fantástica acogida en los meses que pasé en San Diego, así como por darme la oportunidad de trabajar y aprender con ellos. Gracias también a Jaime y a Cándido, por toda su ayuda y buenos momentos durante mi estancia, así como al resto del equipo de UCSD: Wil, Ana, José, Adam, Praba, Jenna y Raquel.

Agradecer también a R. Murillo y M.S. Callén por su colaboración en proyectos conjuntos que, seguro, continuarán en el futuro.

Y cómo olvidarme de los compañeros del Liftec, del AMF y del departamento, donde he tenido la suerte de conocer a tanta gente que me ha prestado una inestimable ayuda a lo largo de todos estos años. Comenzando por Mario, cuyo gran trabajo en el diseño y construcción de la instalación fue fundamental para arrancar la línea de trabajo en la que he podido realizar la tesis. Agradecer también a Antonio Lozano su ayuda con las medidas PIV, y a Álvaro Sobrino por su inestimable apoyo en todo lo relacionado con Matlab y electrónica. Gracias también a Yago por estar siempre dispuesto a resolverme cualquier duda, y, muy especialmente, gracias a Luis Ojeda y Alberto Campos por estar siempre ahí, ayudándome a preparar montajes o a arreglar cualquier problema en el laboratorio (que los hubo...). Gracias a su inestimable trabajo la parte experimental ha salido siempre adelante.

Agradecimiento especial también a Pilar R. y Diego A., con quienes más horas he pasado en la instalación, peleándonos con mil tipos de combustibles y con otros tantos imprevistos. Gracias también a Mohamad A. y a Francisco L. por su trabajo y apoyo, así como a Antonio Pina por su inestimable ayuda en los ensayos en la caldereta.

Por su paciencia y ayuda en la preparación de todos los papeles relacionados con contratos, becas, compras, envíos, desplazamientos, matrículas... mil gracias a Olga, Macarena, Marisol, Isabel D., Lola, Isabel R. e Irene. Gracias también a todos los compañeros del AMF que me han acompañado y ayudado en mis horas de colaboración en prácticas de MIF y Mecánica de Fluidos: Radu, Javier M., Pilar B., Jorge B., Mario M., Esteban C., Luis Manuel C., José

Ignacio G., Jesús M. y Pilar G. Agradecer también a Norberto F. por su ayuda en todo lo relacionado con el programa de doctorado.

Acordarme también de todos aquellos con los que quizá he colaborado menos en el transcurso de la tesis, pero que han contribuido a crear un extraordinario ambiente de trabajo durante todos estos años: Ennio L., Eduardo T., Ángel. S., Picazo, Cinthia A., Laura A., David S., Jaime N., Adrián M., Javier M., Jorge, Raúl, Said, Fernando, Cristina, Jesús O., Manuel C., Manuel M., Ángel G., Sergio, Xavi...

Por último, quiero agradecer a mis amigos por su apoyo y ánimo durante todos estos años. Y, finalmente, a mi familia, especialmente a mis padres, a mi hermana y a Bea, por su apoyo incondicional, ahora y siempre.

Resumen

A pesar de su indudable importancia como fuente de energía, es bien conocido que los procesos de combustión pueden llevar aparejados serios inconvenientes, como la emisión de contaminantes o el agotamiento de recursos. Con el objetivo de reducir al máximo su impacto en el medio ambiente y en la salud humana, la industria de la combustión se halla inmersa en un proceso de evolución continua, donde una serie de desarrollos y medidas complementarias se están llevando a cabo. Claros ejemplos de ello son la reducción gradual de los niveles de emisión de contaminantes mediante la optimización de los procesos de combustión, o el reemplazo de los tradicionales combustibles fósiles por combustibles más respetuosos con el medio ambiente. Es indudable que ambos enfoques requieren de un profundo conocimiento de los procesos de combustión. Por tanto, para implementar este tipo de estrategias con éxito, se hace necesaria una precisa caracterización de los complejos comportamientos que típicamente se encuentran en las aplicaciones de combustión.

Una revisión bibliográfica reveló claros retrasos en el desarrollo de este tipo de estrategias para combustibles líquidos destinados a la generación de calor y energía en comparación con el carbón, gas natural o incluso combustibles líquidos destinados al transporte. Este diagnóstico fue la principal motivación para comenzar esta tesis, cuyo principal objetivo es el desarrollo de metodologías experimentales y de modelaje que permitan caracterizar el comportamiento de combustibles líquidos bajo condiciones representativas de su uso real. Aunque estas metodologías podrían en principio aplicarse a cualquier combustible líquido, en esta tesis se ha hecho especial hincapié en los combustibles líquidos destinados a la generación de calor y energía.

Para este objetivo, se ha elegido como idónea la configuración de gota aislada. Una de sus principales ventajas es su simplicidad, que permite un buen control de todos los parámetros relevantes para el proceso, de forma que los resultados obtenidos pueden ser intrínsecamente atribuidos al combustible ensayado. Una instalación de combustión de gotas denominada DCF (*Droplet Combustion Facility*) fue desarrollada con el objetivo de caracterizar experimentalmente diferentes combustibles líquidos de interés. Las condiciones experimentales utilizadas en la DCF (tamaños de gota, composición del gas, temperatura, etc.) se diseñaron para ser similares al rango de condiciones que habitualmente se pueden encontrar en llamas reales, tratando además de minimizar la convección, tanto natural como forzada. Esto permitió conseguir una configuración cercana a 1-D en los alrededores de la gota, facilitando significativamente la comparación entre los experimentos y los modelos teóricos.

En cuanto a los combustibles líquidos caracterizados, distintas revisiones bibliográficas revelaron claras oportunidades de estudio, como la glicerina cruda (subproducto de la producción de biodiesel) o distintos aceites de pirólisis, entre otros. La valorización energética de la glicerina cruda se considera una solución viable para abordar el importante problema ambiental causado por el gran exceso de este subproducto. Sin embargo, es bien conocido que sus propiedades causan dificultades a la hora de valorizarla en calderas y quemadores. Una caracterización detallada de las propiedades de combustión de este combustible en la instalación DCF revelaron bajas tasas de evaporación, así como la aparición de microexplosiones, tanto para la glicerina cruda original (GC), como para la muestra sometida a un proceso de desalinización (GD). Es interesante señalar que la tipología de estas microexplosiones difirió entre GC y GD, reforzando la hipótesis de que el contenido en sales puede jugar un papel relevante en el mecanismo de aparición de este fenómeno.

También se ha abordado la caracterización de distintos aceites de pirólisis producidos a partir de residuos tales como neumáticos usados, poliestireno y biomasa. Los graves problemas ambientales causados por algunos de estos desechos hacen de la pirólisis una alternativa atractiva y realista para eliminarlos, convirtiéndolos en productos con valor añadido. De entre estos productos, la fracción líquida es de especial interés para su combustión en calderas y quemadores destinados a la generación de calor y energía. Por consiguiente, una serie de aceites de pirólisis producidos a partir de diferentes materias primas y mediante varios catalizadores se caracterizó experimentalmente en la instalación DCF, generando información acerca de los comportamientos de combustión de estos aceites. Análogamente, otros combustibles y mezclas de combustibles, como biodiesel, gasóleo de calefacción o bio-butanol fueron ensayados, generando una base de datos con las características de combustión de una amplia variedad de combustibles de interés.

Además de combustibles reales, varios líquidos puros de distintas familias químicas fueron caracterizados experimentalmente en la DCF. Los datos obtenidos en estos ensayos sirvieron para validar el modelo de evaporación de gotas desarrollado, basado en la teoría clásica. Este modelo fue capaz de conseguir un buen acuerdo con los experimentos para los compuestos de la familia de los alcoholes pero, inesperadamente, sobreestimaba las tasas de evaporación de todos los alcanos evaluados. Estas divergencias fueron atribuidas a la descomposición endotérmica de vapores de combustible cerca de la superficie de la gota, ya que las altas temperaturas presentes en los experimentos pueden favorecer la pirólisis del los vapores de hidrocarburos, especialmente de aquellos con largas cadenas de carbono. La aparición de partículas de hollín en los alrededores de la gota parece respaldar esta hipótesis. Como resultado de estas observaciones, se desarrolló un nuevo modelo analítico que introduce estas reacciones de

pirólisis en fase gas al problema de una gota aislada evaporando en un ambiente infinito. Este modelo se basó en un estudio asintótico, y se considera de clara relevancia para el campo de la combustión, ya que aborda un fenómeno poco estudiado que, sin embargo, es de claro interés para aplicaciones reales.

Finalmente, un trabajo que combina los métodos experimental y de modelaje anteriormente descritos se desarrolló con el objetivo de formular y validar distintos *surrogates* diseñados para emular las características evaporativas y de producción de hollín de un combustible químicamente complejo, como es el gasóleo de calefacción. Este estudio puede considerarse como un trabajo exploratorio que pretende proponer nuevas metodologías que introduzcan la configuración de gota aislada al proceso de diseño de *surrogates*. Los resultados obtenidos respaldan el interés de esta línea de trabajo, que podría ser especialmente beneficiosa para el caso de combustibles líquidos que, en su aplicación real, presenten una combustión en fase gas sustentada por la evaporación de gotas dentro de la cámara de combustión. Es decir, para aplicaciones en las que el combustible líquido no se pre-evapora, como puede ser el diesel en MACI o el fuel-oil en calderas. Para este tipo de combustibles y aplicaciones, el uso de una configuración simplificada y, al mismo tiempo, realista como la configuración de gota aislada puede contribuir al diseño de *surrogates* que reproduzcan fielmente los comportamientos deseados, siendo este un paso fundamental para el diseño de estrategias de optimización que precisen de una completa descripción de la composición y propiedades del combustible, como habitualmente ocurre en la mayoría de métodos computacionales.

Abstract

In spite of its undeniable importance as energy source, it is well known that combustion can entail significant drawbacks, such as pollutant emission or resource depletion. To mitigate its impact on both environment and human health, the combustion industry is immersed in a continuous evolution process, where a series of complementary measures and developments are being adopted and implemented. Examples of these are the gradual reduction of pollutant emission levels through the optimization of combustion processes or the replacement of conventional fossil fuels with novel, more environmentally-friendly fuels. Both approaches require a comprehensive knowledge of the combustion process, and therefore a key step towards their successful implementation is a precise characterization of the complex behaviors typically found in combustion applications.

A literature review revealed a clear gap in the development of this kind of strategies for liquid fuels aimed to heat and stationary energy production in comparison with coal, natural gas or even liquid fuels for transportation. This diagnosis was the main motivation for starting this thesis, whose main objective is to develop experimental and modeling methodologies that allow the characterization of the complex behaviors of liquid fuels when burning under representative conditions. Although these methodologies might in principle be applied to any liquid fuel, a particular focus has been placed on liquid fuels for heat and stationary energy production.

To this end, the isolated droplet configuration was chosen as a suitable canonical setup. Its simplicity allows for a good control of all the parameters relevant to the process, and therefore the obtained results can be attributable to the tested fuel under the well-known experimental conditions. A free-falling droplet apparatus, named droplet combustion facility (DCF) was developed in order to experimentally characterize different liquid fuels of interest. The experimental conditions applied at the DCF (droplet sizes, gas composition, temperature, etc.) were designed to be close to the range of conditions found in real flames, while also minimizing forced and natural convection. This enabled a configuration close to 1-D in the droplet vicinity, significantly easing the comparison with theoretical models.

As for the liquid fuels tested, different literature reviews highlighted clear opportunities of study, such as that of crude glycerol, a by-product of biodiesel production, or pyrolysis oils, among others. The energetic valorization of crude glycerol could arise as a viable solution to tackle the environmental problem caused by its large surplus. However, its properties cause well-known difficulties in boilers and furnaces when using it as a fuel. A detailed

characterization of its combustion behaviors through DCF tests revealed low burning rates and the consistent occurrence of microexplosions for crude glycerol droplets, both as received (CG) and after a desalination process (DG). Interestingly, the microexplosion typology was found to differ between CG and DG, strengthening the hypothesis that alkali salts might play a significant role in these bursting events.

This study has also addressed the characterization of pyrolysis oils produced from residues such as waste tires, polystyrene and biomass. The environmental concerns associated with the disposal of some of these wastes promote the pyrolysis process as a feasible and interesting alternative, since it transforms these residues into products with added value. Among these products, the liquid fraction is of particular interest for heat and stationary energy generation in boilers and furnaces. Thus, a series of pyrolysis liquids obtained from different feedstocks and with different catalysts were experimentally tested at the DCF, gaining insight into the combustion behaviors of these novel fuels. Similarly, other fuels and mixtures such as UCO biodiesel, heating oil or bio-butanol, were extensively tested, as to generate a complete database with the droplet combustion characteristics of a wide variety of fuels of interest to the field.

Besides real fuels, a test matrix with pure compounds of different chemical families was also experimentally characterized at the DCF. The obtained data served to validate the developed droplet vaporization model, which was based on the classical theory. Unexpectedly, the model was able to achieve a good agreement with the experiments for pure alcohols, whereas it overestimated the evaporation rates of all the alkanes tested. This fact was ascribed to the endothermic decomposition of hydrocarbon vapors near the droplet surface, as the high temperatures present at the DCF tests favored the pyrolysis of the vaporized fuel. The onset of soot particles in the droplet vicinity supported this hypothesis. In the wake of these observations, a new analytical model was developed, aiming to introduce the gas-phase pyrolysis reactions to the well-known problem of an isolated evaporating droplet. This model was based on activation-energy asymptotics, and it is thought to be of clear relevance to the field, since it addresses a quite unstudied phenomenon that, however, is of clear interest for real application conditions.

Finally, a work combining the aforementioned experimental and modeling methodologies was developed in order to formulate and validate different surrogates designed to emulate the vaporization and the sooting tendency of a chemically complex fuel such as heating oil. This study can be considered as an exploratory step aiming to propose new methodologies that introduce the isolated droplet configuration to the surrogate design environment. The obtained results seem to support the interest of this line of work, which could be particularly beneficial

for the case of liquid fuels whose gas-phase combustion in real applications is sustained by droplet evaporation inside the combustion chamber (i.e., non-prevaporized cases, such as diesel in compression-ignition engines, or fuel-oil in furnaces). For these fuels and applications, the use of a simplified yet realistic configuration such as the isolated droplet could contribute to the design of accurate surrogates, a fundamental step towards the design of optimization strategies that require a complete description of the fuel composition and properties, as it typically occurs in most computational tools.

Prologue

This dissertation is presented as a compendium of six previously published papers, in accordance with the pertinent form approved by the thesis supervisor and the coordinator of the doctoral program. The work was carried out at LIFTEC / Fluid Mechanics Group of the University of Zaragoza, with Prof. J. Ballester as thesis supervisor, and it is submitted in partial fulfillment of the requirements for the degree of Ph.D. at the University of Zaragoza.

The complete references of the six papers which constitute the body of the dissertation are presented below. All these papers have been accepted in different journals on fuel and combustion science, and complete copies will be provided in a later chapter.

I. Muelas, Á., Remacha, P., Ballester, J. (2019). Droplet Combustion and Sooting Characteristics of UCO Biodiesel, Heating Oil and their Mixtures under Realistic Conditions. *Combustion and Flame*, 203, 190-203. DOI:10.1016/j.combustflame.2019.02.014.

II. Muelas, Á., Callén, M. S., Murillo, R., Ballester, J. (2019). Production and Droplet Combustion Characteristics of Waste Tire Pyrolysis Oil. *Fuel Processing Technology*, 196, 106149. DOI:10.1016/j.fuproc.2019.106149.

III. Muelas, Á., Aranda, D., Callén, M. S., Murillo, R., Veses, A., Asrardel, M., Ballester, J. (2020). Properties and Combustion Characteristics of Bio-oils from Catalytic Co-pyrolysis of Grape Seeds, Polystyrene and Waste Tires. *Energy & Fuels*, 34(11), 14190-14203. DOI:10.1021/acs.energyfuels.0c02257.

IV. Muelas, Á., Remacha, P., Pina, A., Barroso, J., Sobrino, Á., Aranda, D., Bayarri, N., Estévez, C., Ballester, J. (2020). Combustion of Crude Glycerol and its Blends with Acetals. *Experimental Thermal and Fluid Science*, 114, 110076. DOI:10.1016/j.expthermflusci.2020.110076.

V. Muelas, Á., Carpio J., Ballester, J., Sánchez A.L., Williams, F.A. (2020). Pyrolysis Effects during High-Temperature Vaporization of Alkane Droplets. *Combustion and Flame*, 217, 38-47. DOI:10.1016/j.combustflame.2020.03.033.

VI. Muelas, Á., Aranda, D., Ballester, J. (2019). Alternative Method for the Formulation of Surrogate Liquid Fuels Based on Evaporative and Sooting Behaviors. *Energy & Fuels*, 33(6), 5719-5731. DOI:10.1021/acs.energyfuels.9b00737.

Besides these works, other publications and communications have been developed within the thesis framework, and therefore it seems appropriate to mention them here as well. A brief description and, where applicable, DOI references are included below. All of them correspond to communications to peer-reviewed international conferences.

i. Muelas, Á., Remacha, P., Pina, A., Barroso, J., Sobrino, Á., Aranda, D., Bayarri, N., Estévez, C., Ballester, J., Combustion of Crude Glycerol and its Blends with Acetals, presented as an oral communication by P. Remacha at the *11th Mediterranean Combustion Symposium* (Tenerife, June 16, 2019 - June 20, 2019). This communication was the base for publication number IV.

ii. Muelas, Á., Callén, M. S., Murillo, R., Ballester, J., Production and Droplet Combustion Characteristics of Waste Tire Pyrolysis Oil, presented as an oral communication by Á. Muelas at the *3rd SEE SDEWES Conference* (Novi Sad, June 30, 2018 - July 4, 2018). This communication was the base for publication number II.

iii. Muelas, Á., Remacha, P., Ballester, J., Combustion Characteristics of Isolated Free-Falling Droplets of Jet A Blended With Ethanol and Butanol, presented as an oral communication by J. Ballester at the *ASME Turbo Expo 2018 Conference* (Oslo, June 11, 2018 - June 15, 2018). DOI:10.1115/GT2018-76841.

iv. Muelas, Á., Remacha, P., Ballester, J., Evaluation of the Combustion Characteristics of Isolated Droplets of Jet A Blended with Ethanol and Butanol, presented as an oral communication by Á. Muelas at the *28th Conference on Liquid Atomization and Spray Systems* (Valencia, September 6, 2017 - September 8, 2017). DOI:10.4995/ILASS2017.2017.4990.

v. Muelas, Á., Remacha, P., Martínez, A., Ballester, J., Combustion Behavior of Jet A Droplets and its Blends With Butanol, presented as an oral communication by J. Ballester at the *ASME Turbo Expo 2017 Conference* (Charlotte, June 26, 2017 - June 30, 2017). DOI:10.1115/GT2017-64181.

vi. Muelas, Á., Remacha, P., Martínez, A., Sobrino, Á., Ballester, J., Droplet Combustion and Sooting Characteristics of Biodiesel, Heating Oil and their Mixtures, presented as a poster by Á. Muelas at the *8th European Combustion Meeting* (Dubrovnik, April 18, 2017 - April 21, 2017).

Table of contents

Nomenclature

Abbreviations

CG	Crude Glycerol	*PG*	Pure Glycerol
DCF	Droplet Combustion Facility	*PIV*	Particle Image Velocimetry
DG	Desalted Glycerol	*PS*	Polystyrene
FAGE	Fatty Acid formal Glycerol Ester	*SD*	Standard Deviation
FO	Fuel Oil	*TPL*	Tire Pyrolysis Liquid
FSR	Flame Standoff Ratio	*SEM*	Scanning Electron Microscope
GF*	Acetal mixture	*UCO*	Used Cooking Oil
GS	Grape Seeds	*WT*	Waste Tires
IDSY	Isolated Droplet Soot Yield	*YSI*	Yield Soot Index
MNP	Methylnaphthalene		

Variables

a	Droplet radius	$\dot{q}_d$	Sensible heat
B	Pre-exponential factor	q	Enthalpy of reaction
c	Heat capacity	r	Radial coordinate
c_p	Heat capacity at constant pressure	R_0	Universal gas constant
d	Droplet diameter	Re	Reynolds number
D	Mass diffusion coefficient	Sc	Schmidt number
E_a	Activation energy	Sh	Sherwood number
k	Thermal conductivity	t	Time
K	Vaporization rate	T	Temperature
L	Length after the injection plane	v	Velocity
Le	Lewis number	X	Mole fraction
L_v	Latent heat of vaporization	Y	Mass fraction
m	Mass	α	Thermal diffusivity
MW	Molecular mass	λ	Dimensionless vaporization rate
Nu	Nusselt number	μ	Dynamic viscosity
P	Pressure	ρ	Density
Pe	Péclet number	ω	Reaction rate
Pr	Prandtl number	Δ	Damköhler number

Subscripts and superscripts

0	Initial conditions		*l*	Liquid phase
∞	Bulk gas conditions		*p*	At the pyrolysis reaction layer
~	Dimensionless		*ref*	Reference state
*	Modified		*qs*	Quasi-steady
b	Boiling		*s*	Conditions at the surface
eff	Effective		*v*	Vapor phase
exp	Experimental		˙	Time-derivative
f	Fuel		-	In the chemically frozen region
i	i^{th} specie		+	In the chemical equilibrium region

General introduction

<u>Motivation</u>

It is widely accepted that the combustion of fossil fuels entails significant drawbacks, such as resource depletion, emission of pollutants harmful to the human health and to the environment, as well as the release of greenhouse gases responsible for climate change. However, the importance of combustion as a technology able to meet the growing energy demands of humankind is undeniable. According to the International Energy Agency, more than 90% of the global primary energy supply in 2017 was based on either coal, oil, natural gas or biofuels (IEA (2019)). Therefore, even if other renewable technologies such as wind or solar are expected to grow their share, combustion is expected to remain the predominant energy source in the foreseeable future (Kijewska and Bluszcz (2016)).

In this context, a fundamental goal of the combustion industry is to mitigate its impact on both environment and human health. For that purpose, different complementary approaches are being adopted. The first of these consists in the reduction of pollutant emission levels by optimizing combustion processes, whereas a second approach aims to gradually replace conventional fossil fuels with new, alternative fuels which display more environmentally friendly characteristics. A large fraction of these alternative fuels derives from biomass, and therefore their carbon footprint is substantially reduced in comparison to their equivalent fossil fuels.

Both the optimization of combustion-related applications and the introduction of novel biofuels require a comprehensive knowledge of the process, being therefore the development of experimental and modeling strategies aiming to characterize the complex behaviors typically found in these applications a key step towards their successful implementation. It is clear that these strategies have achieved a significant reduction of the negative effects of combustion in both human health and the environment during the last decades. Without pretending to be exhaustive, the increasingly restrictive emission regulations applied to internal combustion engines for transportation or the fact that in 2018 biofuels already accounted for 7.1% of all the energy used in transport in the European Union (Flach *et al.* (2019)) are proofs of the gradual improvements achieved during the last years. However, most of these developments have been applied to the transportation sector or, in the case of the stationary energy generation industry, to solid and gaseous fuels. There is currently a clear gap in the development of such strategies and improvements when it comes to liquid fuels for stationary energy production in boilers, furnaces or even gas turbines. Admittedly, this is partly due to the lower relevance of these

liquid fuels for energy production in comparison with natural gas or coal, although it is also a consequence of the lack of systematic methods for the generation of knowledge in the field. The deficiencies in the understanding of the complex and interconnected phenomena occurring in these systems significantly hamper the design of new technologies and combustion equipment adapted to novel fuels or new conditions.

This diagnosis has been the main motivation for the research work wherein this thesis is framed. Therefore, the aim of the thesis is to develop experimental and modeling methodologies for characterizing the combustion behavior of liquid fuels when burning under representative conditions. Although the aforementioned methodologies could in principle be applied to a wide variety of liquid fuels, a particular focus will be placed on liquid fuels for heat and stationary energy generation, as it will be specified further on.

Thematic unit outline

When aiming to characterize the combustion behavior of a liquid fuel, different approaches can be followed. Probably the most extended one is to test the fuel at its final application, e.g., at boilers, furnaces or engines. For that purpose, a wide spectrum of facilities might be used, ranging from small experimental rigs to large industrial facilities. For the case of liquid fuels for stationary energy production, small-scale or semi-industrial facilities reproducing the main features of real applications have been used in a number of studies. Examples of such works are (Ballester and Dopazo (1994), Ballester *et al.* (1996)) for heavy oil and its emulsions with water at a semi-industrial furnace, or (Bohon *et al.* (2011)) for crude glycerol at a laboratory-scaled furnace. This approach has the advantage of providing information of clear interest and applicability for real combustion equipment, although it also entails the drawback that the obtained results depend not only on the fuel tested, but also on the experimental facility used. The geometrical complexity of real combustion rigs such as furnaces or boilers gives rise to a vast number of interrelated phenomena, many of them being non completely controllable during the experiment. This greatly hampers the interpretation of results, since a global effect observed in one of the measured parameters (e.g., a change in the flame stability) could be a result of a variety of causal factors, such as fuel properties, atomization quality, burner aerodynamics, etc. This dependence on the experimental facility limits the validity of the results, and it is not uncommon in the literature that different studies aiming to characterize the same effect yield dissimilar (and sometimes even contradictory) results. An example of this is the study of the NOx emission in residential boilers when adding biodiesel to conventional heating oil. Whereas some works display a decrease in NOx emission levels when using biodiesel (e.g., (Tashtoush *et*

al. (2003)), (Batey (2003)) or (Ghorbani *et al.* (2011))), others report an increase (e.g., (Kermes and Bělohradský (2013)) or (Ng and Gan (2010))). The differences in combustion equipment or in the test conditions used in those works can explain the dissimilar results, and significantly restrict the generalization of the results when aiming to explore new fuels or conditions.

A completely different approach to characterize the combustion of liquid fuels is through the study of simplified configurations such as the isolated droplet setup, where a single fuel droplet evaporates and burns under fixed and well controlled conditions. The simplicity of this configuration allows for a precise knowledge of all the parameters affecting the process (gas temperature, composition, etc.) and therefore, the combustion characteristics obtained are solely attributable to the tested fuel under the well-known experimental conditions. The dependency of the results on the particular facility is eliminated, and this allows for comparative studies where the differences in the observed behaviors can be related to the particular experimental conditions or, if kept constant for different fuels, can be intrinsically attributable to the tested substances. Furthermore, if the droplet combustion rig is designed to reproduce the range of conditions found in real flames (in terms of droplet size, gas composition, temperature, etc.), the obtained results can also be comparable to those occurring in real applications. In this respect, the literature displays a wide variety of single droplet combustion setups, ranging from 1 mm sized droplets suspended in filaments and burning in air (Yang and Wu (2017)) to small droplets in the order of 60 μm free-falling within an inert hot gaseous coflow (Garcia-Perez *et al.* (2006)). Most of the studies are performed under normal gravity, although some of them aim to eliminate buoyancy effects by running tests under microgravity conditions achieved through free-falling apparatus (Xu and Avedisian (2015)), parabolic flights (Chauveau *et al.* (2011)) or even by performing the experiments at the International Space Station (Dietrich *et al.* (2014)).

This wide variety in experimental setups and conditions provides complementary descriptions, although sometimes can also lead to some discrepancies. For that reason, as it will be detailed in the overview of Paper I, special care was taken when designing the experimental conditions of our single droplet tests, as to approximate them as much as possible to those existing in real flames while also minimizing other undesired effects such as forced convection. For that purpose, droplets of small size (approximately 150 μm in diameter) were chosen, free-falling within the combustion products of a flat-flame burner with temperature and compositions which aim to emulate typical flame conditions. The very small Reynolds numbers and the practically negligible natural convection effects occurring under that small-sized scale assured a configuration close to 1-D in the droplet vicinity, even though tests were performed at normal

gravity. As it will be detailed below, this represents an important advantage when comparing with models.

After acknowledging that spray combustion is far too complex to be used for a detailed characterization of liquid fuel combustion, the isolated droplet has been used by many authors as a canonical configuration for that purpose. Its simplicity greatly facilitates the interpretation of results and the comparison with models, and the fact that the isolated droplet configuration is nothing else but the fine-grid structure of sprays (Avedisian (2014)), favors the extrapolation of results to the conditions in the final application, where a complex spray comprising a large number of droplets is burned. This simplified configuration has been applied for a detailed characterization of both conventional and alternative liquid fuels, although a literature review reveals that a majority of these works target the experimental characterization of liquid fuels of interest for transportation (i.e., diesel, gasoline, biodiesel, kerosene, bio-alcohols, etc.), being the studies addressing fuels for heating and energy generation comparatively less common.

Without aiming to be exhaustive, some of the works found in the literature addressing the experimental characterization of conventional and alternative fuels are summarized in this paragraph. Both Pan *et al.* (2009) and Li *et al.* (2011) studied the distinct characteristics of diesel and biodiesel when burning under well controlled conditions. Whereas the former employed 500 μm droplets suspended on very thin (7 μm) filaments and under microgravity conditions, the latter used free-falling droplets of around 250 μm and almost negligible forced convection conditions (Re<1). Both studies highlighted the higher burning rate of biodiesel and its lower propensity to generate soot when compared to conventional diesel. Another fuel type of clear interest for transportation engines is gasoline and its prospective blending with bio-alcohols. Xu and Avedisian (2015) studied the single droplet combustion behaviors of gasoline and butanol under strictly controlled microgravity conditions, using droplets of 520-630 μm in diameter suspended on thin (14 μm) filaments. The results point to very similar burning rates between both fuels, but with substantial differences in the rest of the studied characteristics (soot formation, relative position of the droplet and the flame, etc.). Similar works using this same droplet combustion rig can be found for the study of an aviation kerosene such as Jet-A and two biofuels considered as a potential replacement for conventional jet fuels (Liu *et al.* (2013a)). In this case, in spite of the clear differences in compositional characteristics, with both biofuels showing a much richer composition in paraffins, practically all the studied behaviors were very similar, with the only exception of Jet-A forming significantly thicker soot clouds. These results supported the use of the mentioned biofuels as a partial replacement for conventional kerosene in aviation, as confirmed by actual turbine and flight tests where blends

of these biofuels were noted to yield essentially indistinguishable performance when compared to neat Jet-A (Rahmes *et al.* (2009)).

When it comes to fuels for stationary energy generation, there are both alternative and conventional fuels which could undoubtedly benefit from these characterization methodologies, which until now have been rather focused on liquid fuels for transportation. The reference fossil fuel in this regard can be considered to be fuel-oil (FO), in its different grades: from FO #2 or heating oil for use in rather small-scale burners for domestic heating, to the high-viscosity FO #6 or heavy fuel oil for use in power generation and big-scale industrial heating. These applications offer the advantage of allowing a much greater variety of blending or even total replacement with novel alternative fuels, as furnace and boilers are typically less demanding than internal combustion engines or aircraft turbines when it comes to fuel properties. This broader flexibility is a great advantage for addressing challenging issues with great environmental impact, where the generation of waste-based fuels is sometimes the best option to tackle the problem.

A clear example of this backdrop is the case of crude glycerol (CG), a major by-product of the biodiesel production whose large surplus, difficult management as waste, little economic value and lack of higher added value alternatives, point to its energetic valorization in boilers as a feasible solution to address this serious environmental problem (Bohon *et al.* (2011), Quispe *et al.* (2013), Thompson and He (2006)). CG displays major differences between its physicochemical properties and those of conventional fossil fuels (e.g., high viscosity, low calorific value, high water and mineral content, etc.), resulting in well-known difficulties when used as a fuel. A few studies such as Bohon *et al.* (2011), Queirós *et al.* (2013), and Steinmetz *et al.* (2013), have addressed the combustion of CG, either neat or blended with premium fuels at laboratory-scale furnaces, providing valuable information regarding the possibilities and limitations of this fuel when burning in a final application. However, as discussed above, this kind of studies is significantly restricted by the experimental setup used when it comes to extrapolating the results to other facilities or conditions, and therefore it would be most desirable to complement them with other approaches and methodologies which are able to extract general characteristics intrinsically linked to the fuel. For that purpose, the isolated droplet configuration can act as a useful benchmark, as it has proved for the case of liquid fuels for transportation.

Besides crude glycerol, a wide variety of potential fuels for stationary energy production could benefit from this characterization methodology. Another clear opportunity of study comprises the different kinds of pyrolysis oils, whose development has drawn considerable scientific

attention during the last years (Brassard *et al.* (2017)). Pyrolysis is a thermochemical process where an organic feedstock is heated at temperatures between 350 °C and 700 °C under an inert environment, converting the raw material into gas, liquid and a carbonaceous solid or char. Normally, the feedstock is biomass-based, and therefore the obtained liquid (pyrolysis oil) can be considered a bio-oil. The conversion of the solid biomass to a liquid fuel significantly eases its transportation, increases its volumetric calorific content and also enables it to be conveniently used in existing equipment such as boilers or furnaces (Dhyani and Bhaskar (2018)). Furthermore, the biomass used as raw material for the pyrolysis process is often of residual nature (e.g., agricultural or forestry wastes), and thus the obtained bio-oils would be considered as second generation biofuels. This fact points out their clear advantages in terms of environmental impact, as the European Union recently approved the Directive (EU)2015/1513 to transition from conventional crop or food-based biofuels to these second generation, or advanced biofuels (Woltjer *et al.* (2017)). These benefits have motivated the spread of multiple initiatives in Europe, with some of them reaching the commercial scale. An example of this is the Empyro plant in the Netherlands, commissioned in 2015, which converts 5000 kg/h of wood residues into pyrolysis oil and process steam through the fast pyrolysis technology (BTG-BTL (2020)).

Nevertheless, bio-oil obtained from pyrolysis processes also displays some serious drawbacks when it comes to its use in combustion applications, most of them related with its oxygenated nature. This causes storage and transportation issues due to corrosion and aging reactions, poor miscibility with conventional hydrocarbons, high water content and low calorific value (Alvarez *et al.* (2019), Uzoejinwa *et al.* (2018)). An intense research is being carried out in order to improve the bio-oil characteristics through different technologies: hydrogenation, hydrodeoxygenation, catalytic cracking, catalytic pyrolysis or steam reforming, among others (Uzoejinwa *et al.* (2018)). Another strategy to obtain a high-grade liquid is to pyrolyze a blend of the biomass with another carbon-rich polymeric residue, such as plastics or waste tires. This co-pyrolysis technique benefits from the synergistic effects occurring during the joint pyrolyzation of these feedstocks, yielding a stable and deoxygenized oil with significantly improved properties (Abnisa and Daud (2014)). Furthermore, the co-pyrolysis technology allows for the valorization of residues like plastics and waste tires which pose serious environmental problems. Especially beneficial is the valorization of scrap tires, whose huge volume (estimated in around 1 billion units/year worldwide, Martínez *et al.* (2013)), challenging recovery or recycling (Sienkiewicz *et al.* (2017)), and the ban of their disposal in landfills due to the high risk of dangerous and extremely pollutant fires (Council Directive EU 1999/31/EC (1999)), points to their pyrolysis as a promising alternative to cope with this problem, while also

allowing for the production of a high-grade fuel (Martínez *et al.* (2013)). A number of recent studies aim to develop and improve this process, both by using only scrap tires as feedstock (Aylón *et al.* (2010)) or blended with biomass in a co-pyrolysis process (Sanahuja-Parejo *et al.* (2019)). These state-of-the-art experimental studies generate a variety of different pyrolysis liquids, whose combustion characteristics are a key aspect when evaluating the suitability of a certain process, since the final liquid is intended for a combustion application.

As it was the case for crude glycerol, the use of the isolated droplet configuration appears to be a most appropriate technique for assessing these combustion characteristics, since it allows for the extraction of intrinsic behaviors for the tested fuel. This was the motivation for Papers II, III and IV, which (as it will be detailed further on) aimed to study the single droplet combustion characteristics of different pyrolysis oils and of crude glycerol, respectively. These two opportunities of study were considered to be of special pertinence and relevance to the field, although they are not the only ones which would benefit from a detailed experimental characterization by means of this simplified configuration. Another example is the case of heating oil and its blends with biodiesel. Although of a lower magnitude than diesel-biodiesel mixtures, several companies have recently started to supply heating oil-biodiesel blends, primarily intended for domestic use and with biodiesel additions typically up to 20% by volume. In addition to the aforementioned detailed characterization of the single droplet combustion experiments, this subject was complementarily addressed in Paper I, as it will be explained below. Similarly, the main droplet combustion features of a conventional kerosene such as Jet-A and its blends with different alcohols (ethanol and butanol) was found to be of interest for contributing to the lack of these data in the literature, which however has pointed to the potential of such blends in stationary engines for power generation (Mendez *et al.* (2012, 2014)). The main findings of these studies were presented to various international conferences, as detailed in the Prologue.

Due to the simplicity of the isolated droplet configuration and to its many applications in several fields of study (not limited to, but primarily in combustion science), the theoretical modeling of evaporating and burning droplets has been extensively studied since the 1950s with the pioneer works of Spalding (1950) and Godsave (1949). Starting with these early analytical developments, the field of the single droplet modeling has shown an intense activity over the last decades, investigating different aspects such as the enhancement of the droplet evaporation rates due to convection effects, the treatment of heat and mass transport within the liquid phase or the impact of thermal radiation on the liquid temperature evolution. These considerations have been addressed through different approaches, from analytical models such as those of

Spalding and Godsave to numerical simulations such as (Farouk and Dryer (2011)) or (Reutzsch *et al.* (2020)). Recent developments in modeling the heating and evaporation processes of fuel droplets were comprehensively reviewed by Sazhin (2006, 2017). In these review works, a myriad of models and submodels are examined, each of them addressing different phenomena that might occur in the evaporation or combustion process of a single droplet, and placing a special emphasis on the identification of unsolved problems.

Before developing a model, it is useful to be aware of the range of conditions that are going to be applied in the simulations, since they significantly affect the phenomena that ought to be considered. In this sense, the model should be regarded as a complementary tool to the single droplet experiments described above. The combined use of experiments and theoretical models appears as a particularly suitable approach to progress towards the main objective of the thesis, which is the development of novel methodologies to characterize the combustion behavior of liquid fuels. As previously stated, the experimental conditions were carefully selected and characterized in Paper I for the droplet combustion tests, and therefore the theoretical model should be able to take into account all the phenomena that might occur under such conditions. In particular, the small droplet sizes and low relative velocities between the droplet and the coflow minimize both forced and natural convection effects, assuring therefore a configuration close to 1-D and greatly simplifying the model and the results interpretation. The use of droplets in the range of 150 μm also implies a negligible effect of thermal radiation on the evaporation behavior, both when the droplet is evaporating in a hot atmosphere (Long *et al.* (2015)) and for the case of a droplet burning at room temperature (Liu *et al.* (2016)). These considerations, as well as others which will be detailed further on, were used as the basis for designing a suitable droplet evaporation model.

The droplet evaporation model finally implemented was based on that of Abramzon and Sirignano (1989), and thus on the standard theory of droplet vaporization with some additional features such as the possibility of simulating multicomponent fuels by following the discrete component approach presented by Maqua *et al.* (2008), Sazhin *et al.* (2010) and Sirignano (2010). Therefore, the model allowed for the simulation of blends by taking into account the so-called Effective Thermal Conductivity and Effective Diffusivity for addressing respectively the heat and mass diffusion processes in the liquid phase. The validation of this model with the data obtained in the experimental tests yielded some unexpected results, as the model was able to achieve a good agreement with the experiments for different pure alcohols (ethanol, butanol, glycerol), whereas it consistently overestimated the evaporation rate of all the alkanes tested (n-heptane, n-dodecane, n-hexadecane). A literature review revealed a lack of experimental

validation data for the evaporation of these compounds under similar conditions, which hindered the problem identification. Also, it should be noted that the high temperature conditions explored here are representative of those prevailing in real applications and, hence, it was rather surprising that they had not been covered by previous experimental studies. The appearance of soot particles in our alkane droplet vaporization tests suggested that the hydrocarbon vapors were undergoing endothermic thermal decomposition reactions which ultimately led to soot formation. This behavior is perfectly consistent with the known pyrolysis chemistry, as a hydrocarbon vapor exposed to a high temperature and inert environment favors thermal decomposition reactions. The fact that discrepancies between model and experiments increased with the molecular weight of the alkanes (in accordance with a higher soot yield for heavier paraffins) also supported this hypothesis.

A collaboration with the University of California San Diego (framed in a predoctoral research visit) was focused on studying this issue which, to the best of our knowledge, has not been addressed so far in the extensive droplet evaporation literature. As a result, a new analytical model was developed, aiming to introduce these endothermic pyrolysis reactions to the problem of a single vaporizing droplet. This model was based on activation-energy asymptotics, and its description is included in the next Chapter as Paper V. By combining the experimental data and the analytical model, it was possible to extract kinetic parameters of these decomposition reactions, such as a characteristic pyrolysis temperature for each fuel. Due to the particularities of obtaining gas-phase kinetic data from the single droplet configuration, this pyrolysis temperature was identified in Paper V to be a useful replacement at leading order for the more common Arrhenius parameters. This work is thought to be of relevance to the field, since it addresses a rather unstudied phenomenon which is of clear interest for real applications condition. As detailed in (Sánchez *et al.* (2015)), in spray combustion an important fraction of liquid droplets burn in a group-combustion regime where the droplets do not feature individual diffusion flames, but are vaporizing within a low-oxygen and high-temperature atmosphere. Thus, the study of this gas-phase reactions and their impact on the vaporizing characteristics of different hydrocarbons is thought to contribute to the scarce data available for these phenomena (both from the experimental and theoretical modeling sides), presenting therefore a clear interest for many liquid fuel combustion applications.

Finally, it is well known that most real fuels are chemically complex mixtures comprising hundreds or even thousands of different compounds. This is not only the case of conventional petroleum-derived fuels such as fuel oil or diesel, but also of alternative fuels such as tire pyrolysis liquids or jet biofuels. Even if it would be possible to perfectly identify all individual

compounds, the combustion modeling of such complex mixtures would be impractical and even unfeasible due to the lack of detailed information for all the constituents and huge computation costs (Kim and Violi (2018), Pitz and Mueller (2011)). This fact further complicates the development of the aforementioned strategies aiming to characterize the complex behaviors of liquid fuels. A well-known approach to tackle this problem is through the use of surrogates, i.e., mixtures comprising a small number of pure compounds whose characteristics emulate selected behaviors of a target fuel. After a proper formulation process followed by validation tests, a simple mixture of compounds of well-characterized properties (named surrogate) is proven to display certain behaviors close to those of the complex target fuel, allowing thus for its substitution by the surrogate in computational studies. The use of surrogates not only significantly eases the modeling of complex fuels (Farrell *et al.* (2007)), but also offers experimental advantages such as the creation of standardized fuels with fixed compositions. This enhances experimental reproducibility, as it is well known that the variability typically found in real fuels is a factor that complicates comparisons between experiments (Pitz and Mueller (2011)). An example of this effort to obtain standardized fuels is the recent development by the US Department of Energy of various sets of gasoline fuels, named *Fuels for Advanced Combustion Engines* (FACE), with clearly defined compositions and properties (e.g., see (Elwardany *et al.* (2016))).

Most of the surrogate developments in combustion science have been so far related to the gas phase characteristics and, more specifically, to the emulation of gas phase kinetic phenomena such as the autoignition behavior or the laminar flame velocity (e.g., see (Dooley *et al.* (2012)) or (Naik *et al.* (2011))). The configurations typically used in this kind of works consist in a single-phase layout, where the liquid fuel is completely vaporized prior to its study (e.g., shock tubes, rapid compression machines, counterflow burners, etc.). In spite of the relevance of these gas-phase kinetic aspects, several authors have also noted the importance of physical behaviors such as the evaporation for applications where the liquid fuel is not completely vaporized before ignition, and therefore the combustion reactions are sustained by the phase change (Avedisian (2014), Chen *et al.* (2016), Liu *et al.* (2013b), Su and Chen (2015)). In addition to this, given the multicomponent nature of most real fuels, the liquid and vapor compositions are not fixed (as it happens for the case of a prevaporized fuel), but they would change along the liquid residence time in the combustion chamber, with a preferential vaporization of the light-end compounds near the spray injection. This has a significant impact on the combustion characteristics of the fuel that, however, cannot be predicted through the use of surrogates which only take into account chemical aspects (Su and Chen (2015)). Therefore, for designing surrogates that can adequately emulate real behaviors of fuels in applications where the liquid is not prevaporized

(such as in burners, furnaces, compression-ignition engines, etc.), the introduction of the volatility characteristic as a design property to match is highly desirable.

In order to take into account this liquid-vapor phase change, it seems important to use a configuration that can provide conditions close to those existing in the final application. To this effect, the single droplet approach displays some advantages when compared to other setups commonly used to extract the vaporization behavior of multicomponent mixtures, such as the distillation curve. The very high vaporization rates typically found in combustion applications imply that the evaporation process of a droplet inside a real flame is far from the distillation scenario, where very low evaporation rates favors the diffusion of all the components within the liquid (ideally to the point where its composition is always kept spatially uniform). However, under real combustion conditions, the droplets are exposed to a huge heat input which causes a strong vaporization rate at the surface, quickly depleting the more volatile compounds in that zone. Typically, the slow liquid mass diffusion mechanism is not capable of supplying the different species at the required rate, and relevant compositional gradients appear near the surface (Makino and Law (1988)). Thus, if the surrogate should match the vaporization characteristics of a multicomponent fuel, using an application-oriented configuration such as the single droplet setup featuring realistic conditions would appear to be a good alternative.

In fact, several works have recently used this approach for either designing or validating surrogates, with a special focus on targeting fuels for transportation such as diesel or gasoline. For instance, Liu et al. experimentally examined the droplet combustion characteristics of different surrogates which were previously designed to replicate certain gas phase combustion characteristics of commercial Jet A (Liu *et al.* (2013b)) and gasoline (Liu and Avedisian (2012), Liu *et al.* (2012)). For that purpose, they used an isolated droplet apparatus which promoted spherical symmetry, allowing for a completely one-dimensional configuration which greatly facilitated evaluating the surrogate fuel performance (Avedisian (2014)). Other works relied on multicomponent droplet evaporation models, such as those of Elwardany *et al.* (2013, 2016), which validated the ability of different surrogates in matching the evaporation characteristics of gasoline. The joint use of droplet evaporation experiments and models is thought to provide a powerful approach to the surrogate field, as it is shown by Chen *et al.* (2016), where the evaporation behavior estimated through a droplet evaporation model for a 4-component surrogate was compared with experimental results for a real kerosene. In this work, the surrogate aimed to emulate both chemical and physical aspects, being the evaporation characteristic included in the formulation process through an inverse distillation method.

As previously detailed, this thesis has focused on developing novel ways to characterize the main combustion behaviors of liquid fuels through the use of the single droplet environment. This resulted in six publications, being papers I to IV devoted to the experimental approach, whereas paper V focused on the modeling front. The last one, paper VI, combined both approaches to formulate and subsequently validate different surrogates aiming to match the evaporative and sooting characteristics of a conventional Spanish heating oil, which has been used as a reference fuel over the course of the thesis (its experimental characterization was extensively detailed in paper I). To this end, the multicomponent droplet evaporation model was used as a predictive tool which allowed estimating the behavior of a broad range of potential surrogate mixtures. The comparison of the predicted vaporization curves with that of heating oil (experimentally obtained), was the base for a surrogate design methodology designed to match this characteristic. A second behavior of interest for a fuel such as heating oil was the soot yield under the reducing and high-temperature environments typically found in boilers. The design property used to emulate this behavior was the *Yield Soot Index* or YSI, a well-known parameter based on the soot concentration measured in a doped flame. The literature offers a quite complete database for this index (Das *et al.* (2018), Das *et al.* (2017)), and therefore it was possible to estimate the sooting behaviors of both heating oil and the range of studied mixtures through this parameter. Two different surrogate blends based on these design methods were formulated, whereas a third one was created by following a more standard methodology (i.e., matching a number of relatively simple physicochemical properties related to the final complex behaviors). After this design process, the three surrogates were validated by means of single droplet tests, assessing the closeness of each surrogate to the experimental behaviors of the target heating oil. For this purpose, the vaporization curves and the amount of soot collected with a sampling probe were used for determining the behavior of each fuel under conditions which are thought to be representative of those occurring in real combustion applications.

The work summarized in paper VI has been a first step towards introducing the single droplet configuration to the surrogate design and validation environment. If it is experimentally verified that the resulting mixtures of simple compounds display close behaviors to those of the target fuel, these blends could be used in methodologies that require a complete description of the fuel composition and properties, as it typically occurs with most computational tools. Thus, the chemically complex fuels that are so common in combustion applications could benefit from these modeling and computational tools as a way to devise optimization strategies that reduce their impact on human health and on the environment (either through an optimization of the combustion processes or by means of their replacement with novel and less harmful fuels). Given the complexity of most combustion applications, this is undoubtedly a challenging

objective for which the isolated droplet configuration can contribute, as it provides a simplified and, at the same time, realistic environment for studying the combustion of liquid fuels.

Copy of the papers

Droplet combustion and sooting characteristics of UCO biodiesel, heating oil and their mixtures under realistic conditions

Álvaro Muelas[a], Pilar Remacha[a], Javier Ballester[b],*

[a] *Laboratory of Research on Fluid Dynamics and Combustion Technologies (LIFTEC), CSIC – University of Zaragoza, Spain*
[b] *Fluid Mechanics Group / LIFTEC, School of Engineering and Architecture, CSIC-University of Zaragoza, María de Luna, 3, 50018 Zaragoza, Spain*

ARTICLE INFO

ABSTRACT

The droplet combustion characteristics of conventional heating oil, UCO biodiesel and their mixtures (10 and 20% biodiesel by volume) were examined in a free-falling droplet combustion facility designed to approach the typical temperature and oxygen conditions around individual droplets in real boiler flames. Moreover, and given the importance of avoiding effects due to gravity or convection in this type of experiments, the quite spherical soot shells recorded (infrequent event in free-falling droplet combustion studies) reveal a configuration close to 1-D, even though tests were performed at normal gravity. The droplet combustion characteristics were evaluated at four different oxygen levels (0,3,5 and 10% O_2), and comprise droplet size evolution, burning rates and sizing of the occurring soot shells and envelope flames. Results show indistinguishable behaviors between heating oil and their mixtures, whereas biodiesel displays longer initial heating transients and higher quasi-steady burning rates. Even though the UCO biodiesel studied is highly unsaturated, no signs of polymerization were observed for any of the tests. In addition to these combustion characteristics, an aspirating soot probe was used to quantitatively evaluate the propensity to soot of each fuel at different oxygen levels. The amount of collected soot was found to significantly decrease with biodiesel addition, even though similar results were obtained for both mixtures. The practically identical droplet combustion characteristics between heating oil and its mixtures with biodiesel, in addition to the lower propensity to soot of the latter, support the feasibility of using such blends as drop-in replacement for conventional heating oil. The experimental results obtained are thought to constitute a valuable database for the development and validation of modeling tools for the prediction of droplet evaporation and combustion of practical fuels in realistic conditions.

© 2019 The Combustion Institute. Published by Elsevier Inc. All rights reserved.

1. Introduction

Biodiesel can be produced from a wide variety of bio-feedstocks, including vegetable oils (mainly sunflower, soy, palm and rapeseed), used cooking oils or animal fats. Transesterification with methanol yields a mixture of methyl esters, and therefore biodiesel is also known as FAME (Fatty Acid Methyl Esters). Biodiesel addition to petroleum-based diesel has proven to be a successful way to reduce greenhouse gas emissions and to facilitate energy sustainability and security. In light of its increasing use, regulations have been created regarding some selected properties; in Europe biodiesel is required to meet the EN 14,214 standard for transportation and the EN 14,213 standard for heating applications. These standards reflect the two main current usages of biodiesel.

The blending of biodiesel with petro-diesel for transportation is by far its most common use, and therefore the behavior of biodiesel in internal combustion engines has been very well documented in the literature (e.g., see reviews [1–3]).

Even though its use for heat generation is less relevant, blends of heating oil and biodiesel are currently being commercially supplied both in America and Europe. These blends are intended both for domestic and industrial use, with biodiesel additions typically up to 20% by volume (B20). Recent studies in residential and industrial boilers show the following results when blending heating oil with biodiesel [4–9]:

- Boiler efficiency does not change significantly.
- Similar gaseous emissions, except for SO_2, which clearly decreases due to the lower sulfur content of biodiesel. Some studies show a slight increase in NO_x and CO emissions, others a reduction.
- Particulate matter emissions decrease significantly with biodiesel addition.

- Specific consumption increases slightly due to the lower heating value of biodiesel.
- The use of mixtures up to B20 does not require any modification in conventional burners.

These experimental results support the feasibility and environmental benefits of biodiesel addition to conventional heating oil for domestic and industrial boilers. It should be noted, however, that testing in pilot or industrial boilers can introduce some dependency on the experimental facility used due to the complexity of the configuration and the impossibility to strictly control and characterize all the involved variables (e.g., mixing, spray patterns, temperature profiles, etc.). Unfortunately, there is a lack of standardized, or at least, broadly accepted testing methods to obtain generalizable data on the combustion characteristics of liquid fuels, as it would be required to rationally address new applications, but also to characterize in a systematic way the combustion behavior of different substances.

It can be said that most of the knowledge on liquid fuel combustion has been generated in simplified configurations and, more specifically, in different setups designed to study the combustion of isolated droplets. They offer the advantage of a good control and knowledge of the relevant parameters, so that the combustion characteristics observed can be related to the particular experimental conditions or, if kept constant for different fuels, can be intrinsically attributable to the tested substances. Different versions of single droplet apparatus exist, each with its advantages and limitations, and there is also a wide diversity of the conditions used in the tests. This provides interesting complementary descriptions but also introduces heterogeneity and, in some cases, may even lead to discrepant conclusions. The causes can be the differences in setups (e.g., free-falling vs. filament-suspended droplets or gravity-related effects) but also in the test conditions (temperature or oxygen content in the surrounding gas, droplet size). In spite of the importance of all these issues, in our opinion and apart from a few studies on some specific aspects (e.g., effect of filaments in [10,11]), there has been little discussion on the effect of the particular setup or, simply, of the conditions selected for the tests. Given the importance of all these issues, and although it is not the objective here to analyze the various approaches, we believe that it is essential to explicitly comment on the method used and the conditions selected for the tests.

As it will be described later, the experiments were performed on a train of free-falling monosized droplets, in normal gravity. A potential drawback of this configuration is the eventual loss of spherical symmetry due to slip and buoyancy effects; however, the selected experimental conditions made possible to minimize these issues, with the visible elements (soot shell, chemiluminescent envelope flame) actually revealing a nearly spherical configuration. An order-of-magnitude analysis of the potential impact of convection effects on the spherical symmetry for the experimental setup used in this work is presented in the Appendix A of the Supplementary materials.

Initial droplet size is one of the most critical test parameters. On the one hand, it should be similar to the one in real applications; i.e., several tens of microns to reproduce the mean spray drop size or in the order of a hundred microns if the interest is focused on the largest fraction (with longest combustion times and, hence, usually related to unburnt fuel) [12,13]. On the other hand, it should be large enough to ensure a correct spatial resolution for imaging techniques and to adequately resolve its temporal evolution. In this case, 150 mm was the size used. This leads to fully satisfactory results regarding experimental requirements and, at the same time, it is not very far away from target sizes in real systems.

Finally, the conditions of the gas surrounding the droplet can also affect the results, not only quantitatively but even in a qual-itative way. The criteria applied here was to approach the range of conditions representative of those seen by the droplets during their evolution inside real flames. Although burners normally inject fresh and even cold air, the main part of the evolution of droplets occurs once the liquid is mixed with flame gases and, hence, under high temperature and, in many cases, low oxygen conditions. Moreover, a large fraction of the fuel can evaporate inside the flame core, with practically no oxygen around. In order to cover the range of most relevant conditions, the tests were performed by injecting the droplets coaxially with a coflow of hot combustion products with different oxygen concentrations; namely, at 0, 3, 5 and 10%. In particular, the 0% O_2 case can be taken as representative of the situation in the reducing inner flame core and, at the same time, can serve as suitable reference data for models of droplet evaporation in high temperature environments.

Further details will be explained later, but these aspects describe the essential characteristics of the tests and results presented here. There is some coincidence, at least partial, with the conditions used in some previous works, but also important differences with others. For example, the oxygen concentration differs from most previous studies, normally using 21% O_2. Being aware that the different options may have both some advantages and drawbacks, we believe that further analysis, and even some debate, in this respect would be most enriching and could help to better define the range of applicability and the eventual limitations of the various approaches. In this context, an objective of this work is to report and analyze the results obtained with the apparatus and method applied here for the characterization of single droplet evaporation and combustion.

Another objective, and the primary motivation of the study, is to provide detailed results on biodiesel, heating oil and their blends. Previous works have examined the droplet combustion characteristics of different biodiesels and their blends with vehicle petro-diesel [14–19], but to the authors' knowledge none has addressed droplet combustion of biodiesel-heating oil mixtures.Given the increasing interest of such blends, this work is aimed at providing new, detailed experimental data on the droplet combustion and sooting characteristics of a Used Cooking Oil (UCO) biodiesel, both pure and as an additive to conventional Spanish heating oil. The studied combustion characteristics comprise droplet size evolution, burning rates, images of the occurring soot shells and envelope flames (with their respective measurements) and sooting propensity, determined through an aspirating soot probe.

2. Experimental methodology

2.1. Fuels investigated

Commercial Spanish heating oil (fuel-oil No. 2) and a distilled UCO biodiesel provided by Biodiesel Aragón S.L were used for the tests. Additionally, two mixtures of heating oil and biodiesel were prepared with 10 and 20% biodiesel by volume (B10 and B20 respectively). Neat n-hexadecane (99% purity) was also studied in order to provide a baseline for comparison with a pure and well-known compound used in previous works on biodiesel droplet combustion (e.g., [14,17,19]). Its inclusion in the current work would therefore allow a comparison with the cited studies, which use droplet vaporization and combustion rigs with quite different features.

The heating oil and biodiesel samples were analyzed at the Instituto de Carboquímica (ICB-CSIC) to determine their composition and most significant properties (Table 1). Regarding the distribution of chemical families, a GC-MS analysis was performed on both the UCO biodiesel and the heating oil, with results summarized in the Appendix C of the Supplementary materials.

Table 1
Selected properties of the fuels investigated.

Fuel	Molecular formula	MW (g/mol)	C (%mass)	H (% mass)	O (% mass)	Boiling point (°C)	LHV (MJ/kg)	Density at 20 °C (kg/m^3)	Viscosity at 40 °C (cP)
UCO Biodiesel	$C_{17.32}H_{32.41}O_{1.96}$	271.7	76.5	11.9	11.6	340–353[b]	36.95	881	3.80
Heating Oil (FO No.2)	$C_{13.21}H_{24.63}$	184.5	86.5	13.5	0.0	271–352[b]	41.92	861	3.43
Hexadecane [a]	$C_{16}H_{34}$	226.4	84.9	15.1	0.0	286	44.20	773	2.26

[a] Properties extracted from ref. [20].
[b] Distillation curve (20–80% mass distilled).
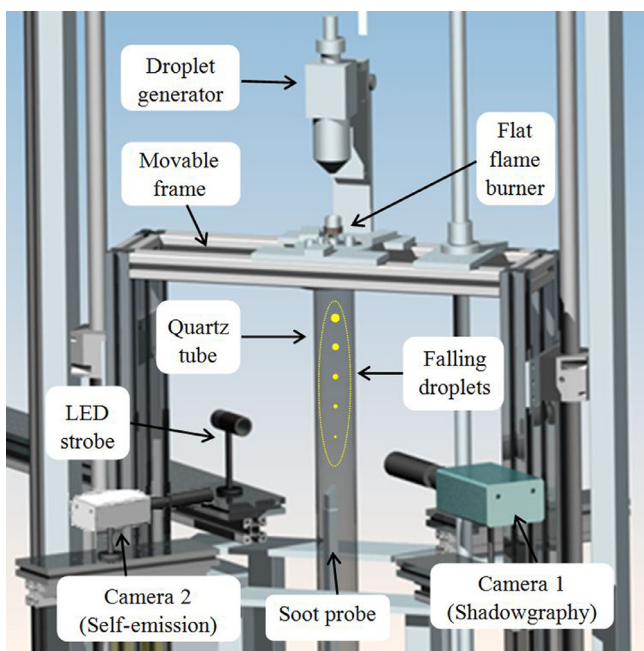
Fig. 1. General view of the DCF.

2.2. Droplet combustion facility

The combustion process of the free-falling isolated droplets was characterized using the Droplet Combustion Facility (DCF) developed at LIFTEC. A general view showing the main elements of the rig is presented in Fig. 1. Further details can be found elsewhere [21,22].

Fuel droplets were injected from a piezoelectric generator with initial diameters (D_0) of 150 mm (150.3 ± 0.5 µm). A generation rate of 25 Hz provided an interdroplet spacing large enough (>110 droplet diameters) to effectively prevent any interaction, as pointed out in other free-falling droplet combustions works such as [14,15]. In fact, from the axial profiles of gas and particle velocity along the centreline (as measured with PIV and direct imaging, respectively), it could be verified that slip velocity was small enough to prevent a given droplet from reaching any gaseous product released by the preceding one (injected 40 ms before). A critical issue for the validity of results is droplet generation stability, as any drift in D_0 would affect the subsequent measurement points. In order to confirm the steadiness of the generation process, the initial droplet diameter was repeatedly checked at the first optically accessible point (3 mm below the injection plane). The rms deviation in D_0 calculated from these verifications was found to be 0.48 µm, indicating negligible changes in D_0 during the running of the experiments. Only one experimental run was performed for each studied fuel and condition, but for heating oil at the vaporization atmosphere (without oxygen), which was replicated in order to check the repeatability of the experimental procedure.

Relative differences in droplet consumption times between both runs (performed 4 months apart) were found to be 0.5%, whereas differences in time-averaged evaporation rates were 0.7%.

Once formed, the free-falling droplets were coaxially injected into the exhaust gases produced by a McKenna flat-flame burner fed with a mixture of methane, air and oxygen. The relative velocity between the free-falling droplets and the hot coflow was very low (Reynolds number based on slip velocity <0.4 for the whole droplet history and <0.1 along the quasi-steady evaporation stage), and therefore forced convection effects are expected to be minimal. This, in combination with the small droplet sizes used allows achieving reasonably good spherical symmetries (see Appendix A in the Supplementary materials) and, hence, facilitates the extrapolation and generalization of the experimental results.

The four coflow conditions studied (0, 3, 5 and 10% O$_2$) were achieved by adjusting the McKenna burner feed flow rates to the values which provided such oxygen fractions in the burner exhaust gases. The oxygen volumetric fraction in the coflow was monitored with an online oxygen analyzer (paramagnetic). The axial temperature profiles along the tube centreline were measured by means of a 50 µm thermocouple (type S) for all the listed oxygen conditions (information included in Appendix C of the Supplementary materials).

The droplet combustion process was characterized from images acquired with different techniques. A CCD camera (QImaging Retiga SRV, 12-bit Mono) was used to determine the size and velocity evolution of the droplets. The optical system, consisting of a long distance microscope and a LED strobe, was programmed to acquire two sequential shots with a delay of 500 µs between them. A high sensitivity CMOS camera (Hamamatsu C11440-36U, 12-bit) captured the light spontaneously emitted from the flames and soot particles. This second camera was faintly backlighted to highlight the droplet shadow, and therefore these pictures display the free-falling droplet along with its self-illuminated envelope flame. In cases of low intensity flames, this backlight had to be switched off so that the dim flame became distinguishable. The acquired pictures were post-processed to extract relevant droplet combustion characteristics, as it will be discussed further below.

Finally, the amount of soot yielded by the different fuels and mixtures was quantitatively measured through a soot sampling technique. For these tests the initial droplet size was increased to 180 ± 0.9 µm in order to increase the soot yield. The main constituents of the soot sampling probe and images illustrating its operation are displayed in Fig. 2. As it can be observed in Fig. 2(c), the visible trace due to black-body emission from soot particles is suctioned through the lateral probe inlet. The intake flow, consisting of a mixture of hot gases and small soot particles, is quenched by a cold N$_2$ flow (Fig. 2(a)), preventing therefore the oxidation of the soot particles collected on a quartz microfiber filter. Due to the broad differences between the inertia of big free-falling droplets and of the small soot particles, the intake flow can be adjusted so as to completely aspirate the soot cloud, while not affecting the trajectory of the much heavier liquid droplets (Fig. 2(b)). The soot collected throughout a certain period of time is dried in a furnace at 150 °C for 24 h and subsequently weighed on an analytical scale
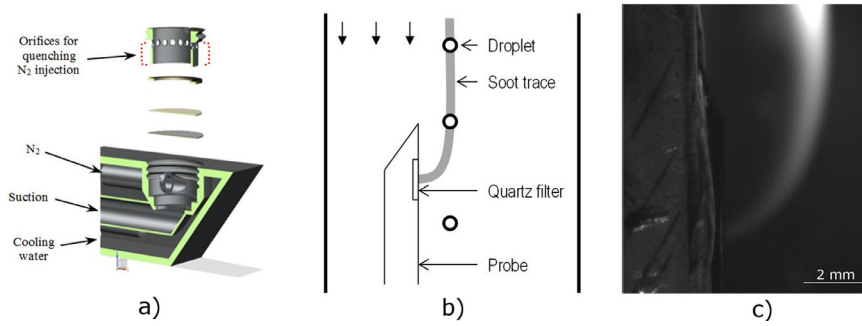
Fig. 2. Soot sampling probe: (a) Main components of the soot probe; (b) Schematic drawing of probe in operation; (c) Self-emission, long-exposure picture of the incandescent soot cloud aspirated by the probe.
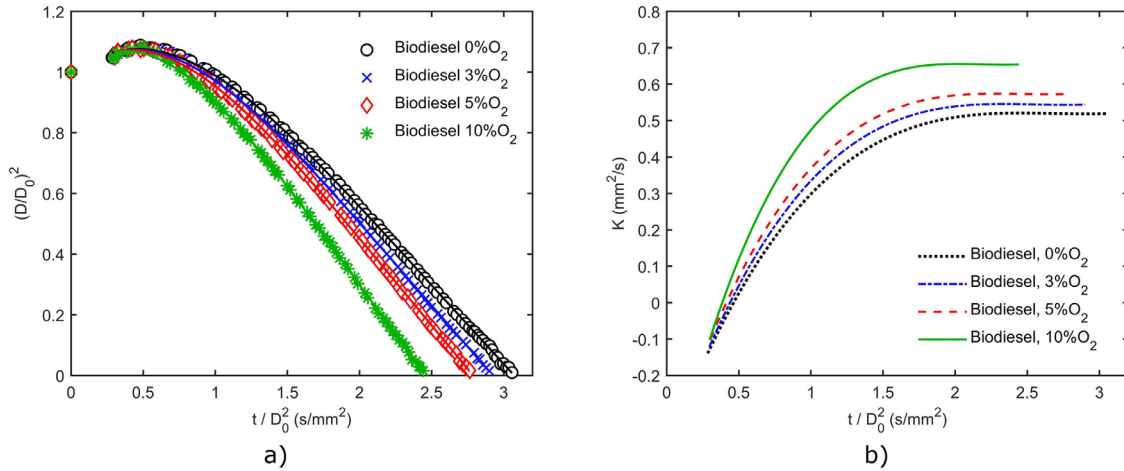

Fig. 3. Normalized droplet size (a) and burning rate (b) evolution for biodiesel at the four oxygen conditions. The experimental points in (a) are fitted to 4th order polynomials constrained at the final region ($R^2 > 0.99$ in all cases), also shown.

(Sartorius CP225D, repeatability $\pm$ 20 µg). A soot index, calculated as weight of soot per unit of injected fuel mass, can be therefore obtained for each probe position.

3. Results and Discussion

3.1. Droplet size and burning rate evolution

The evolution of biodiesel droplet sizes are shown in Fig. 3a for the four oxygen levels evaluated. The results are displayed in accordance with the quasi-steady theory of droplet burning: normalized diameter squared versus normalized time, using the droplet diameter at injection (D_0) as the reference for normalization. Due to practical constraints, the first 3 mm after injection are not optically accessible, and therefore the displayed curves lack a few points in this initial region. Droplet diameter, D, is measured at different distances from injection, which are converted into droplet residence times, t, by numerically integrating the droplet velocity curves along the axial coordinate (measured at the same locations by the double-shot technique mentioned above). Curves displayed in Fig. 3(a) display clear unsteady effects, with a noticeable heat-up period which involves volumetric expansion. Only at the end of the droplet lifespan do the observed slopes (i.e., the burning rates K) of the curves appear to reach a constant value.

In order to analyze in more detail the evolution of K with time, the burning rates of biodiesel were quantified as the time derivatives of the curves presented in Fig. 3a: $K = -d(D^2/dt)$. As in [23–25], the already displayed D^2-t curves were fitted with a 4th order polynomial, whose derivative directly yields the burning rate evolution with time. However, this approach has been reported to artificially generate non-physical behaviors at the limits, especially

towards the end of droplet burning [25]. To avoid this, the steady final region where K reaches a constant value was identified, and its value K_{steady} obtained by means of linear fitting. Then, a 4th order polynomial fit was performed to the whole droplet size evolution data, with an added constrain on the time-derivative in the final region, so that the fitting needs to match both the values and the slope of the experimental curve. This was an effective procedure to correctly reproduce the burning rate depicted by the experimental data, without the numerical artifacts stemming from the utilization of a high-order polynomial. The obtained curves are displayed in Fig. 3b, where the evolution of K with respect to the normalized time is shown. The burning rates start at negative values due to the initial volumetric expansion of biodiesel, and progressively increase as the droplet heats up. It is noteworthy that this gradual increase in K spans for more than half of the droplet lifetime. These progressive changes in K could, to some extent, be attributed to a temperature increase in the hot coflow which surrounds the droplets within the first millimetres (see axial profiles of temperature in the Supplementary materials). However, besides this experimental effect, most of the observed gradual increase in burning rate is ascribed to the heating transient experienced by the liquid phase, which was already found to last for a considerable fraction of the droplets lifespan in previous studies under quite different experimental conditions (e.g., [23,24]). After this prolonged initial transient period, stemmed mainly from the liquid phase unsteadiness intrinsic of the process, the burning rates reach a practically constant value in the final stages of droplet combustion, which would agree with the quasi-steady theory. However, as it will be shown later, other results like the evolution of flame standoff location cannot be explained by this simplified theory.

The effect of oxygen availability in the combustion process of biodiesel is clearly ascertained from Fig. 3, with a distinct enhancement of the burning rate as oxygen concentration increases. Since evaporation is largely driven by the heat transferred to the droplet from the surrounding gas, the cause for this difference should be sought in the changes in the temperature field around the droplet. For 0% O_2, no flame is generated, and the heat transfer is determined by the temperature of the gas coflow. On the contrary, if the coflow contains oxygen, a shell flame will be formed, modifying the temperature of the gas surrounding the droplet. In a first approximation, the evaporation rate can be related to the well-known Spalding transfer number, B, proportional to (T_∞-$T_{droplet}$), where T_∞ is the temperature of the coflow for 0% O_2, or the temperature of the envelop diffusion flame otherwise. This flame temperature can be estimated as that reached by an adiabatic flame for the stoichiometric mixture of fuel and coflow. Reference gas temperatures calculated for a representative alkane such as n-hexadecane burning in the gaseous coflows used in this work yield 1437, 1570, 1714 and 2059 °C for 0, 3, 5 and 10%, respectively. These differences in the gas temperature 'seen' by the droplet (free stream temperature for evaporation, shell flame temperature for oxygen-containing coflow) are perfectly consistent with the gradual rise in K as oxygen concentration increases between 0 and 10%. The relative position of the flame for each condition will be discussed (and quantified) in Section 3.4.

Once the effect of oxygen availability for a single fuel is ascertained, Fig. 4 displays a comparison between all the studied fuels subjected to the four proposed oxygen conditions (0, 3, 5 and 10%). For certain fuels at high oxygen levels, the occurrence of thick soot shells surrounding the droplets hindered in some cases droplet identification and sizing. For this reason the FO, B10 and B20 curves at 5 and 10% O_2 lack several points in the regions where it was not possible to measure droplet sizes with sufficient accuracy. This effect was particularly pronounced for the 10% O_2 condition, where droplet measurements had to be performed manually, and the few available points measured for FO and B10 did not allow extracting reliable burning rate curves.

The behaviors observed in Fig. 4 for FO No.2 and its two blends B10 and B20 are practically identical throughout all the combustion process, both in terms of droplet size and burning rate evolution. This coincident behavior is noted for evaporation (0% O_2) as well as for combustion (3, 5 and 10% O_2).

Pure biodiesel displays a clearly distinct behavior, with a longer heat-up period involving some volumetric expansion. This can be noted in the negative initial burning rates recorded for biodiesel, which are closer to zero in the case of FO and its mixtures. These results are consistent with the higher boiling point of the main constituents of biodiesel compared to hexadecane and to the lighter fractions of FO No.2, as displayed in Table 1. In spite of this longer heat-up period, biodiesel droplets reach very similar consumption times to those of heating oil. This is a consequence of its higher quasi-steady burning rate for all the evaluated oxygen conditions. The higher burning rate of biodiesel was ascribed in a previous work to its thermal decomposition into smaller molecules when exposed to high temperatures [14]. The apparition of smaller molecules such as Free Fatty Acids (FFA) in the droplet surface layer could be indeed responsible for the vaporization process acceleration, as FFA display lower boiling points and enthalpies of vaporization. Another possible chemical reaction which might undergo biodiesel when exposed to high temperatures is polymerization of the unsaturated methyl esters in the liquid phase [14,19]. The studied UCO biodiesel contains a high amount of unsaturated fatty acid methyl esters (70.63%, Table C1 in the Supplementary materials), and therefore it would display a higher propensity to undergo polymerization reactions than other more-saturated biodiesel. None of the tests performed for biodiesel

showed any indication of such polymerization, reported in previous works as an abrupt decay in the burning rate in the last stages of the droplet lifespan. As suggested in [19], this is ascribed to the competition between the evaporation and the polymerization reaction rates. As the experimental conditions used in this work involve small droplet diameters and high ambient temperatures, the droplet lifetime is considerably shorter than the time required by the reaction to form polymers, and therefore none residue was found. These qualitative results are in accordance with [19] where, even for highly unsaturated methyl esters, it was found that increasing the ambience temperature minimized (or even inhibited) the polymeric residue formation.

Hexadecane displays the shortest droplet lifetime for all the evaluated oxygen conditions. This is a result of both a shorter heat-up period and a slightly higher quasi-steady burning rate when compared with FO and biodiesel. Hexadecane and biodiesel display some common features for all the oxygen conditions. Namely, their droplet sizes curves run almost parallel, with a quite constant offset in the $(D/D_0)^2$ axis. This offset is caused by the already mentioned initial heating transient, slower for biodiesel. This can also be noted in the burning rate curves, which show significant differences between both fuels at the initial stages. After that, biodiesel and hexadecane burning rates slowly converge, their final quasi-steady values being very similar (as suggested by their droplet sizes curves being parallel). Although the experimental conditions are quite different, these results are found to be consistent with previous studies on hexadecane and biodiesel droplet vaporization [19] and combustion [14,17], with quite similar relative behaviors between both fuels. As hexadecane is a well know compound, it is possible to simulate its behavior by means of theoretical models. Appendix B in the Supplementary materials shows a brief comparison of the experimental data obtained for hexadecane at the 0% O_2 condition and its simulation through a vaporization model. The good agreement between model and experimental results points to the well-controlled conditions used in the tests, and can be considered as further evidence that the experimental results are comparable to those that would occur in a totally convection-free, one-dimensional configuration.

In addition to the temporal burning rate evolutions presented in Fig. 4, the final quasi-steady values for K (K_{steady}) are displayed in Fig. 5 for all the studied fuels and oxygen conditions. Heating oil and B10 at 10% O_2 were not included because of the lack of enough reliable measurements in the final region due to the large quantity of soot agglomerates in the droplet's vicinity, as mentioned earlier.

It is noteworthy that the displayed K_{steady} are only representative of the last fraction of the droplets lifespan, being most of the evaporation/burning process intrinsically unsteady, as illustrated in Fig. 4. The extracted K_{steady} values show clear tendencies, with a monotonic increase with oxygen availability for a given fuel and also reflect the trends already discussed above when comparing fuels for a fixed oxygen level.

3.2. Visual appearance of the flame traces

The combustion of the free-falling droplet stream generates a characteristic flame trace which can provide qualitative information regarding fuel behavior (e.g., microexplosion occurrence, soot or chemiluminescent emission, length of droplet consumption, etc.). Thus, a color camera (Teledyne DALSA Genie Nano C4060) was used to record these flame traces for all the studied cases. The flame streaks captured for the 10% O_2 condition are displayed in Fig. 6, with clearly observable differences among fuels. Heating oil and its mixtures display strong sooty flame traces, whereas hexadecane presents a much fainter bluish flame streak ascribed to chemiluminescent emission. Biodiesel, on the other hand, shows a mixed behavior, with an initial blue region followed by a stronger
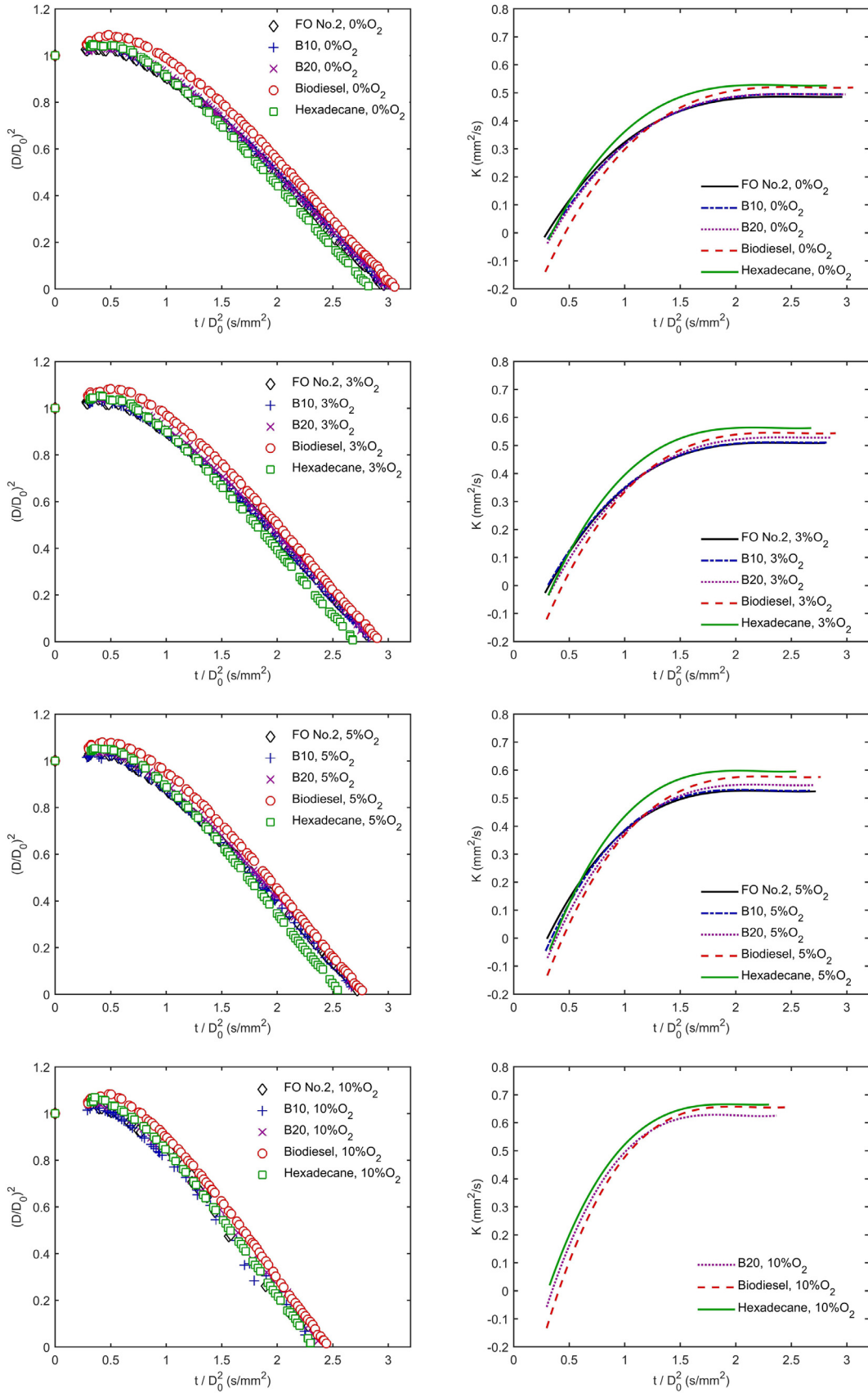
Fig. 4. Evolution of normalized droplet sizes and burning rates for FO No.2, B10, B20, biodiesel and hexadecane at the four oxygen conditions.
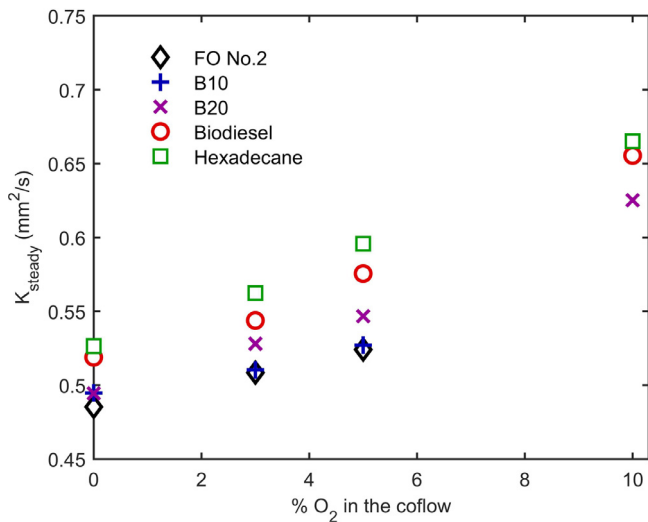
Fig. 5. Final quasi-steady burning rates attained by all the studied fuels at different oxygen availabilities.

Fig. 7. Droplet and soot shell evolution for all fuels at the 5% O_2 condition. Pictures are arranged according to their normalized time after injection, t/D_0^2 (s/mm^2).

Fig. 8. Droplet and soot shell evolution for all fuels at the 10% O_2 condition. Pictures are arranged according to their normalized time after injection, t/D_0^2 (s/mm^2).

black-body yellowish emission thereafter. It is also noteworthy that FO, B10 and B20 traces feature a thin, orangish streak after the droplet extinction length ($L = 40$ mm approximately). This streak is entirely ascribed to the thermal emission of soot agglomerates formed in the fuel-side of the envelope flame, whose consumption rates are much slower than the droplets themselves. Further insight into these soot agglomerates will be provided in the following sections.

3.3. Droplet and soot shell evolution

The already presented results regarding droplet size and burning rate evolutions are extracted from the double-shoot back-lighted images taken by Camera 1 (Fig. 1). Descriptive selections of such images are presented in Fig. 7 (5% O_2) and Fig. 8 (10% O_2) in order to give insight into the observed differences among fuels and oxygen conditions.

It can be noted that, for both oxygen conditions, the FO, B10 and B20 droplets appear surrounded by quite spherical soot shells during most of their combustion lifespan. Similar soot shells usually occur in totally convection-free environments obtained
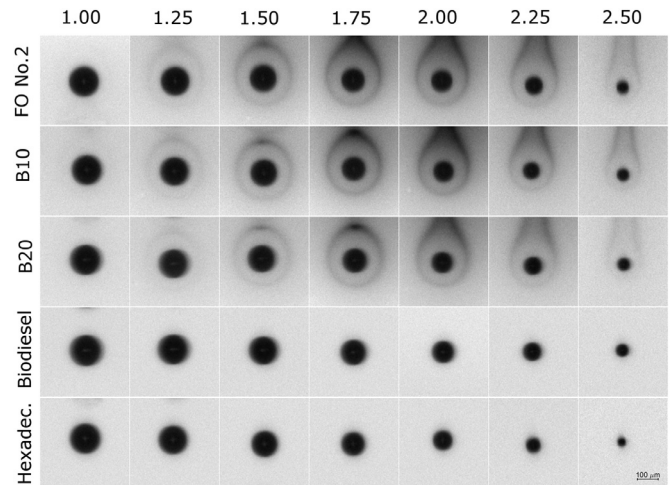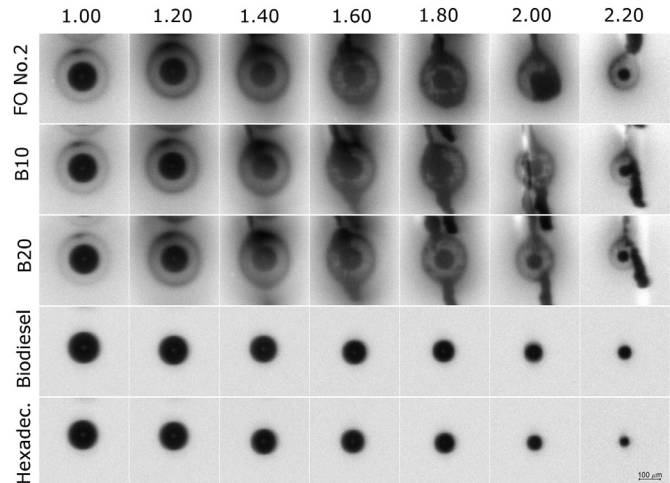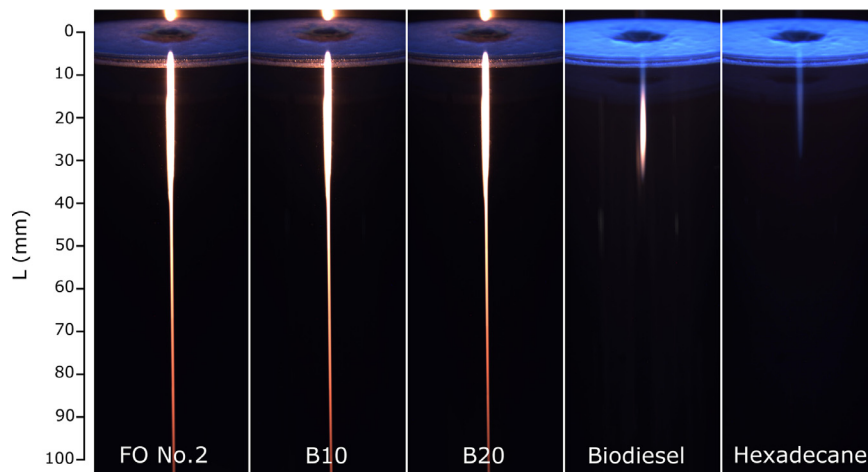

Fig. 6. Flame traces recorded for all the studied fuels at the 10% O_2 condition. The exposure time used for FO, B10 and B20 is 500 ms (12.5 injected droplets), whereas biodiesel and hexadecane required 2 s (50 injected droplets) for the bluish luminosity to become visible. (For interpretation of the references to color in this figure legend, the reader is referred to the web version of this article.)

through microgravity such as [17,23,24,26]. They are caused by the accumulation of soot aggregates at the radial position where thermophoresis and Stefan flux drag forces balance. The occurrence of soot shells is far less frequent for drop-tube droplet combustion tests, as any slip velocity droplet-coflow can sweep the soot particles away. As detailed in Appendix A (Supplementary materials), the experimental conditions used here minimize both forced and natural convection, allowing therefore the creation of quite spherical soot shells surrounding the droplets for high soot-yield conditions. Admittedly, the existence of small slip velocities and buoyancy-induced flows can drift away non-negligible quantities of soot particles, although this behavior also offers the advantage of avoiding, or at least delaying, the formation of dense soot crusts (which may even prevent drop size measurement, as it was found in studies with strictly controlled microgravity conditions and sooty fuels). However, it is important to note that, in the initial stages, the soot cloud always exhibits a good spherical symmetry, the elongated shape only appearing as the time progresses; this is a clear indication that the lack of sphericity of the shoot shell is only due to the lateral motion induced by the (very small) slip velocity, but not a symptom of non-uniform radial profiles. Therefore, it can be concluded from Figs. 7 and 8 that, although the experiments were performed at normal gravity, droplets can be assumed to evaporate at conditions close to spherical symmetry, at least for the radial profiles in the vicinity of the droplets. This facilitates the comparison with theoretical one-dimensional droplet combustion models and to extract related parameters like the diameter of the soot shell or the envelope flame.

Comparing Figs. 7 and 8, differences between both oxygen conditions become apparent, with thicker soot shells recorded as oxygen availability increases. For the 3% O_2 condition, the soot shells were so faint that no results could be accurately extracted from the pictures, and the 0% O_2 condition did not display soot shells at all. These differences are primarily ascribed to the already estimated temperature rise experienced by the envelope flame as oxygen availability increases. This higher flame temperature, in addition to its closer relative position to the droplet (as it will be discussed upon later), enhances soot formation within the reducing environment inside the envelope flame and, simultaneously, boosts to a large extent thermophoretic forces. These forces push soot agglomerates from their origin point (the high temperature region on the fuel side near the diffusion flame) towards the droplet, eventually reaching an equilibrium location with the outwardly directed drag forces, as already discussed. The fainter and farther away the flame front is, the weaker the thermophoretic forces in the droplet's vicinity are, and therefore a higher fraction of the newly formed soot particles would be drifted away as a result of any small flow within the envelope flame. This could explain the observed experimental trends, with thicker and more spherical soot shells as the oxygen availability increases.

For a given oxygen condition, qualitative differences can be observed between fuels. Whereas FO, B10 and B20 display very similar behaviors, no soot shells were detected for biodiesel or hexadecane at any of the studied conditions, although a recent work reported the formation of soot shells around biodiesel and hexadecane droplets in microgravity tests [17]. The non-appearance of soot shells in the current study might be in part related with the unavoidable flows (convective and buoyancy-induced) due to not having completely stagnant, low-gravity conditions around the droplet. For sooty fuels such as heating oil and its mixtures, these small flows might drift away some soot agglomerates, but even so there are enough soot particles reaching the soot shell equilibrium location. Therefore, it cannot be discarded that for fuels with much lower propensity to form soot, such as biodiesel or hexadecane, this drift could prevent the formation of a visible soot shell. However, the differences between both works could also be
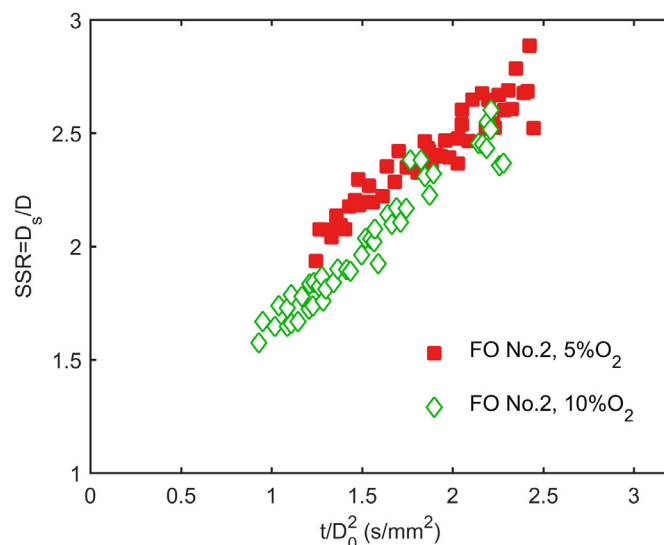

Fig. 9. Evolution of the soot standoff ratio (D_s/D) for FO No.2 at both oxygen conditions.

related to other dissimilar experimental conditions, primarily the initial droplet diameter. In fact, Pan et al. [17] found that, whereas a soot shell was clearly visible around biodiesel droplets of 528 μm, it was not detected for 445 μm droplets. The difference can be ascribed to the shorter residence time of soot precursors as droplet size decreases [17,27]. Hence, no soot shell would be expected either if 150 μm droplets were tested in the conditions of [17] and, so, there seems to be no contradiction between both works.

The diameters of soot shells in Figs. 7 and 8 were manually measured in order to analyze the evolution of their size with time. The soot standoff ratio (SSR), defined as the ratio between soot shell and droplet diameters, (D_s/D), is a widely used metric describing sooting behavior. The measured SSR for FO droplets in 5 and 10% O_2 atmospheres are displayed in Fig. 9.

The SSR curves begin when the nascent thin soot shell is considered sharp enough to be measured and they finish at the point where the soot shells disappear due to droplet extinction. For the 10% O_2 condition, the higher concentration of soot particles promotes clustering, and eventually big soot strings and agglomerates are formed, as displayed in Fig. 8. These agglomerates are not located at the equilibrium position dictated by the balance of forces, and therefore pictures where the soot shell was covered by such agglomerates were not measured. In spite of the uncertainties associated with manual measurements, the presented SSR values show discernible differences among oxygen conditions. Namely, for the 10% O_2 condition the shoot shell is found to appear earlier and is located closer to the droplet. These results are in accordance with the already mentioned boost of thermophoretic forces with oxygen availability, which appears to prevail over the expected effects due to the enhanced evaporation rate.

Although the experimental conditions used in this work are significantly different from other studies reporting SSR profiles, it is noteworthy that the extracted SSR values are in the range of those displayed, for instance, in [23] (580 μm Jet-A droplets in microgravity, room air) or [28] (1.15 mm n-decane droplets in microgravity, room air). Without taking into account inherent differences among fuels, these similarities in SSR values could be mainly ascribed to the combined effect of differences in three parameters: oxygen availability, initial droplet size and ambience temperature. According to Fig. 9, higher oxygen availability tends to reduce the SSR, as it promotes the inward thermophoretic forces; hence, this single difference would lead to larger SSR values in this work than

in tests with air (as in [23],[28]). Ambience temperature, on the other hand, was found in [28] (one of the very few works displaying soot shells for hot ambiences) to largely increase soot shell sizes, as it enhances the outward Stefan flow. Actually, SSR values found in [28] for hot ambiences at 21% O_2 are considerably larger than those of Fig. 9, which are quite similar to the cold ambience values. Finally, the effect of initial droplet size was reported in [28,29], with results pointing to a SSR increase with D_0, as larger flames reduce thermophoretic forces. The experimental conditions used in Fig. 9 (small 150 μm droplets in a 5–10% O_2 hot coflow), although very different from those of the cited works (bigger droplets in a 21% O_2 cold ambient) could therefore well be in the same range of values, mainly as a result of the much smaller initial droplet sizes, which compensates the effects of higher ambience temperatures and lower oxygen concentrations. Soot shells displayed in Figs. 7 and 8 were measured also for B10 and B20 in order to identify possible differences between fuels, but none were found, as variations in SSR were within the own dispersion of the data for each fuel (results not shown for brevity).

3.4. Flame evolution

In addition to the soot shell information provided by the backlighted camera, the synchronized shot of Camera 2 (Fig. 1) recorded the natural emission from the envelope flames which surrounded the droplets. Obviously, the flame information obtained through imaging methods depends on which part of the light emitted is actually recorded, and can therefore be somehow subjective when it comes to quantify the flame size, with different criteria regarding the flame positioning. A broadly accepted approach is to associate the flame region with the chemiluminescence emission from electronically excited hydroxyl radicals (OH*), occurring in the UV (around 308 nm), as this position has been reported to occur near the location of maximum flame temperature [30]. Another approach widely used in the droplet combustion literature is to extract the flame diameter by considering the outer boundary of the blue luminous zone, i.e. the combined chemiluminescent radiation stemming from different radicals emitting within the blue band (primarily CH*, [31,32]). Both approaches were compared in [29], where it was concluded that flame diameters based on the location of higher OH* intensity were consistently larger than those obtained by measuring the visible blue flame. For the case of sooty fuels, the thermal radiation emitted from incandescent soot particles further complicates flame measuring, as it can be orders of magnitude more intense than chemiluminescent emission. Although soot radiation is not a direct indicator of the regions where chemical reactions occur, it has been used in several droplet combustion works for indirectly measuring the flame position for sooty fuels (e.g., in [14] for diesel, or in [17] for hexadecane and biodiesel droplets). As the soot particles are formed on the fuel side of the envelope flame, it would be expected that flame diameters extracted from soot radiation would be somewhat smaller than those based on the actual chemiluminescent emission, as it can be visually verified in studies with relatively low sooting fuels and conditions (e.g., methyl-decanoate in [33] or butanol isomers in [34]).

Keeping in mind these differences, the present work uses two different approaches in order to define the flame position: whereas for non-sooty fuels and conditions the outer boundary of the chemiluminescent blue zone is considered as the flame front, for sooty cases the flame size is entirely obtained from the soot cloud thermal emission. Thus, there are two different sets of flame measurements, each one only comparable with data extracted with the same criteria. Due to the high propensity to soot of the studied fuels and the reducing atmospheres used, most of the flame information extracted in this work is based on the thermal radia-

tion of soot, much more intense than the chemiluminescent emission. Only hexadecane and biodiesel at the leaner condition (10% O_2) displayed measurable chemiluminescent flames, hexadecane throughout all the droplet combustion lifetime and biodiesel during the first half, with soot radiation predominating thereafter (see Fig. 6).

The aforementioned differences in flame appearance and intensity depending on the amount of soot present in the vicinity of the flame sheet are illustrated in Fig. 10 with a few selected flame images for all the studied fuels at the 10% O_2 condition. FO, B10 and B20 display much brighter flames due to intense soot emission, whereas biodiesel and hexadecane show weaker flames, as a result of their considerably lower sooting propensity.

As hexadecane did not show any soot emission for the 10% O_2 condition (Fig. 6), its flames in Fig. 10 are entirely ascribed to blue chemiluminescence. This causes the noisier aspect of the images, as the low signal is close to the detection limit of this high-sensitivity camera. The camera worked on binning mode (2×2), and the exposure time had to be increased to 1 ms. As a consequence, some axial blur can be noted in this kind of images, due to the motion of the free-falling droplets. This blur is not necessarily a problem when it comes to quantification, as flame diameter is measured in the spanwise direction. Biodiesel, on the other hand, displayed two well differentiated flame types: a first one caused by blue chemiluminescence (0.75 s/mm²), and a second one ascribed to soot emission (1.75 s/mm²). The intensity of the sooty flame is much higher, as it can be noted from the better quality of the image and from the fact that the exposure time could be reduced to 50 μs, and therefore the flame motion was effectively frozen. Both flames show quite good spherical symmetries, as happened with hexadecane.FO, B10 and B20 pictures show much more intense sooty flames, with indistinguishable behaviors between the three fuels. As a result of the dim backlight, the droplet and the soot shells are also visible, particularly for the first row (0.75 s/mm²). At 1.75 s/mm², the black body emission from soot is considerably more intense than the backlight, hindering to some extent droplet and soot shell visualization.

In addition to the discussed differences among fuels, the effect of oxygen availability on flame size and morphology was also ascertained. A representative selection of flame images for FO tested at the four studied oxygen conditions is presented in Fig. 11.

At a first glance, differences between oxygen conditions become apparent, with flames standing closer to the droplet and becoming brighter as oxygen availability increases. The shape of the incandescent soot clouds visible in the images presented in Fig. 11 show the effects of buoyancy, particularly for low oxygen ambiences. For the 0% O_2 condition the absence of an envelope flame means that droplet heating is entirely due to the hot coflow, and temperature gradients in the proximity of the droplet are lower. Soot particles, originated as fuel vapors move away from the droplet surface (thus entering the high-temperature coflow), are subjected to weaker inwardly-directed thermophoretic forces. As a result, they are easily dragged away by any convective flow. These results are in accordance with the absence of soot shells for this 0% O_2 case, even though it is obviously the condition with a higher soot yield. The other three conditions, with oxygen available in the coflow, display envelope flames which confine to some extent the formed soot particles within their fuel-rich side. As oxygen availability increases, flame diameter decreases, as displayed in Fig. 11. The location where soot particles are formed approaches therefore the droplet and this, added to the higher shell flame temperature (estimated in Section 3.1), enhances to a great extent thermophoretic forces in the droplets vicinity, as proven by soot shells appearance for the 5 and 10% O_2 conditions (Figs. 7 and 8). Still, the first case displays significant amounts of soot particles being dragged away by convective flows, as happened for the flameless 0% O_2 condi-
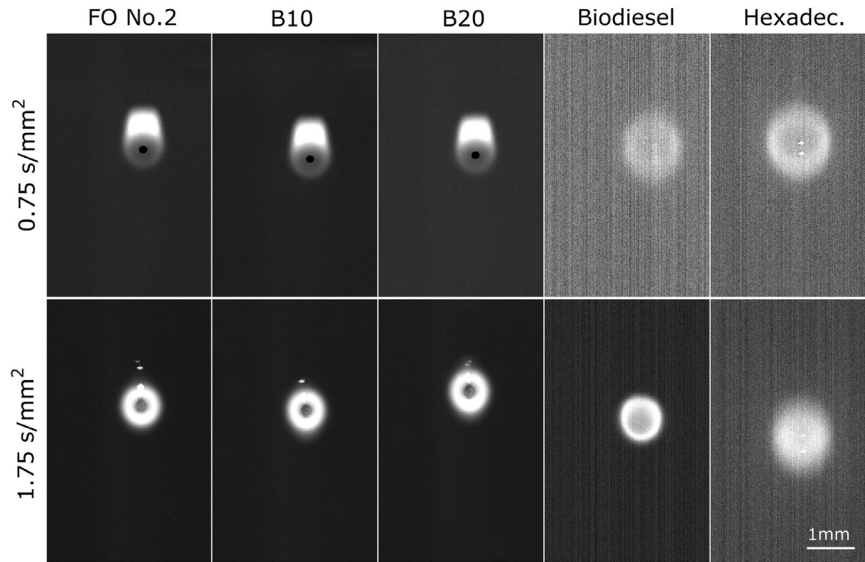
Fig. 10. Comparison of the flames recorded at two (normalized) timesfor different fuels and 10% O_2. All images are post-processed with contrast enhancement and background substraction. Due to the low intensity their flames, biodiesel and hexadecane pictures were binned (2×2) and their backlight switched off.
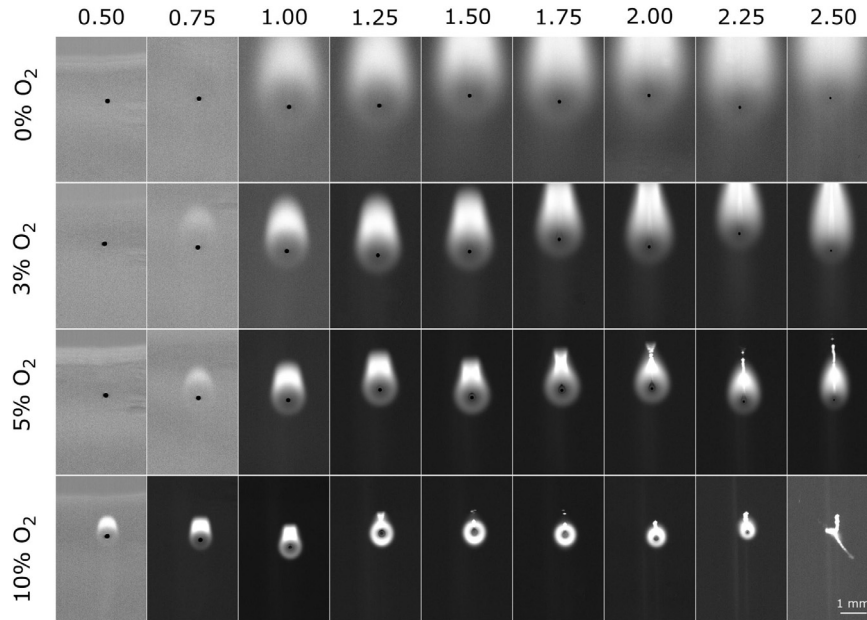

Fig. 11. Evolution of FO No.2 flames at the four studied oxygen conditions. Pictures are arranged according to their normalized time after injection: t/D_0^2 (s/mm²).

tion. For the 10% O_2, on the other hand, the sooty flame becomes much more spherical, and soot particles are retained within the (presumably) spherical chemiluminescent flame shell. In fact, the blue envelope flames detected for hexadecane and biodiesel at 10% O_2 kept a good spherical symmetry throughout all the combustion process, and therefore it seems plausible that, although not visible due to the strong soot radiation, the diffusion envelope flame maintained the same spherical symmetry as well for the FO images presented in Fig. 11 (regardless of the visible incandescent soot cloud behavior, heavily dependent on soot particles' dynamics). This would also be consistent with the spherical soot shells displayed in Fig. 8. As thermophoretic forces heavily depend on flame temperature, soot confinement is not equal among oxygen conditions, and the soot yield is not correlated with the soot shell density. This explains that conditions with a priori higher soot production display thinner soot shells.

Soot confinement within the diffusion flame for the 10% O_2 condition leads to the clustering of soot particles into big agglomerates, as observed in Fig. 8. These big agglomerates are much less affected by thermophoretic forces, and some of them can even exit the flame shell, slowly lagging behind. For the rest of oxygen conditions soot particles tended to be emitted out of the diffusion flame and therefore no big agglomerates were observed inside the flame shell. However, the emitted soot particles eventually gathered into a soot tail which followed the wake of the droplet. This soot tail can be clearly observed for the 5% O_2 condition in Fig. 11 and, although it can grow considerably in size, it has been thoroughly checked that it does not interact with the following droplet, as the provided interdroplet space is much longer than the soot tails observed for any oxygen condition. The soot particles composing the tail gradually clustered into string-shaped agglomerates as well, their oxidation with the ambient oxygen progressing much slower than the droplets themselves (as illustrated in Fig.
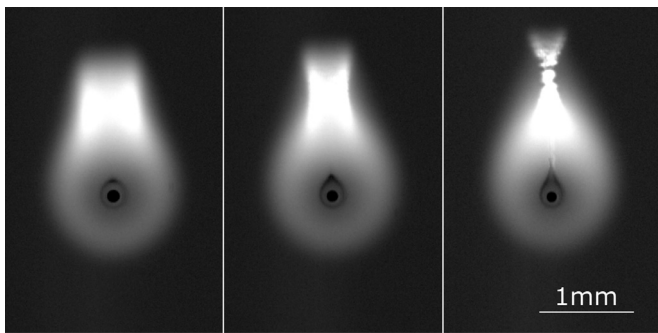
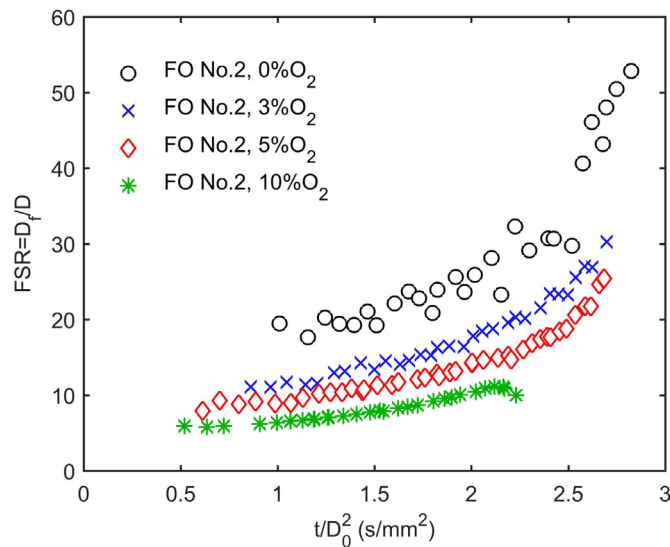**Fig. 12.** Enlarged images of FO No.2 flames at the 5% O_2 condition (1.50, 1.75 and 2.00 s/mm^2).

Fig. 13. Evolution of the flame standoff ratio (D_f/D) for FO at the 3, 5 and 10% O_2 conditions. Even though there is no actual flame for the 0% O_2 case, the border of the luminous zone has been identified as an artificial flame front.

Fig. 14. Evolution of the flame standoff ratio (D_f/D) for all fuels at the studied combustion conditions. For the 10% O_2 level, measurements based on the blue chemiluminescent front are marked with (C) for biodiesel and hexadecane. The rest of measurements are referred to the outer boundary of the sooty luminous zone.

6). An enlarged view of some of the pictures recorded for the 5% O_2 condition are displayed in Fig. 12, clearly showing the liquid droplet surrounded by the spherical soot shell and the incandescent soot cloud. The formation of a soot tail can be also observed as the combustion process proceeds.

In Fig. 11 it is also noteworthy the occurrence of a clear soot dispersion event at the droplet consumption point for the 10% O_2 case (2.50 s/mm^2). This behavior was also observed for B10 and B20 at the 10% O_2 condition, and is ascribed to the sudden release of the soot contained within the flame shell at the point of flame extinction. The abrupt removal of the flame barrier causes that the unoxidized soot particles come into contact with the oxidative hot coflow, producing the recorded brightness. Special attention was paid to the eventual fragmentation of the droplet in this final region, but no microexplosion was observed for any of the studied fuels.

The soot clouds presented in Fig. 11 were automatically measured in order to extract quantitative data regarding their size evolution with time. The flame diameter was measured as the largest dimension of the luminous zone in the spanwise direction. Analogously to the SSR, the relative position of the flame to the droplet surface (D_f/D), or flame standoff ratio (FSR) is displayed in Fig. 13 for FO subjected to the four examined oxygen conditions. The FSR values quantify the already commented behavior of sooty flames for these conditions. It is noteworthy that the first appearance of a visible flame is delayed as the oxygen availability decreases,
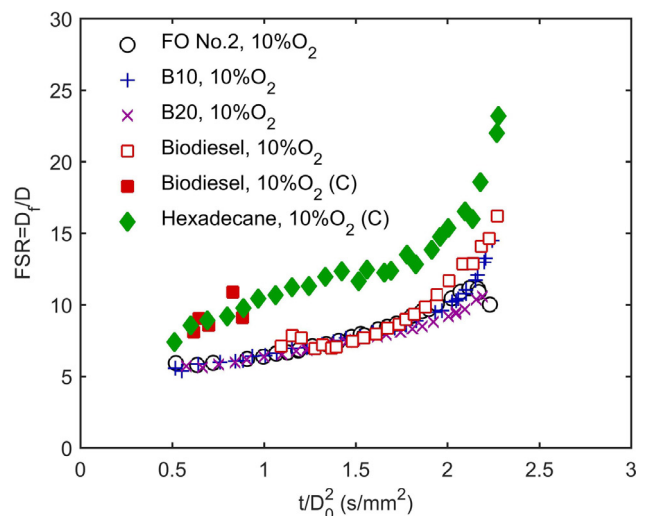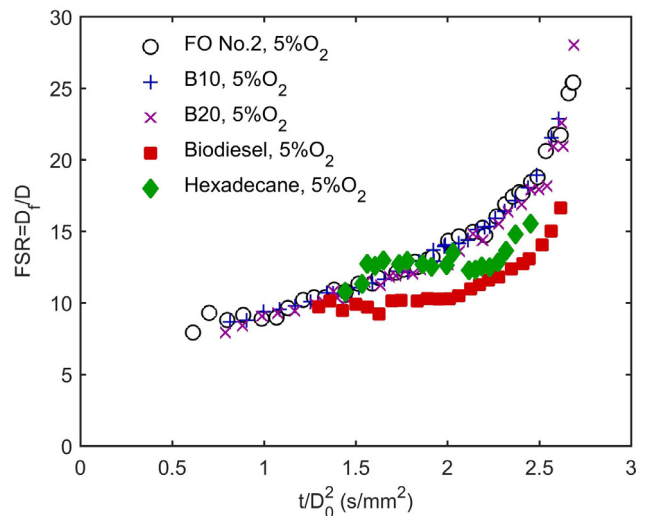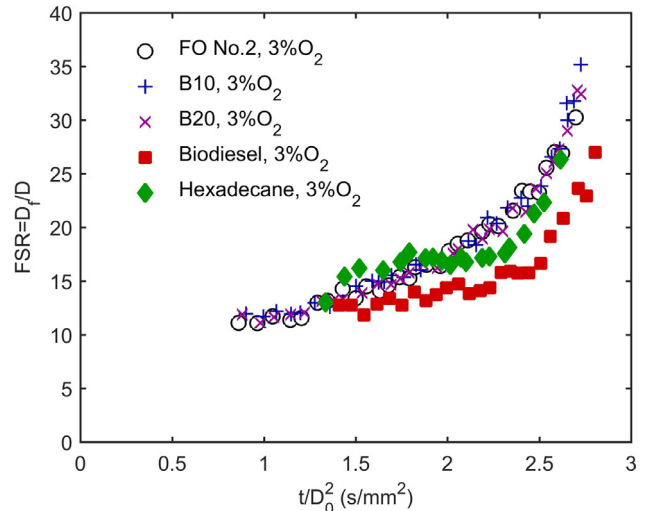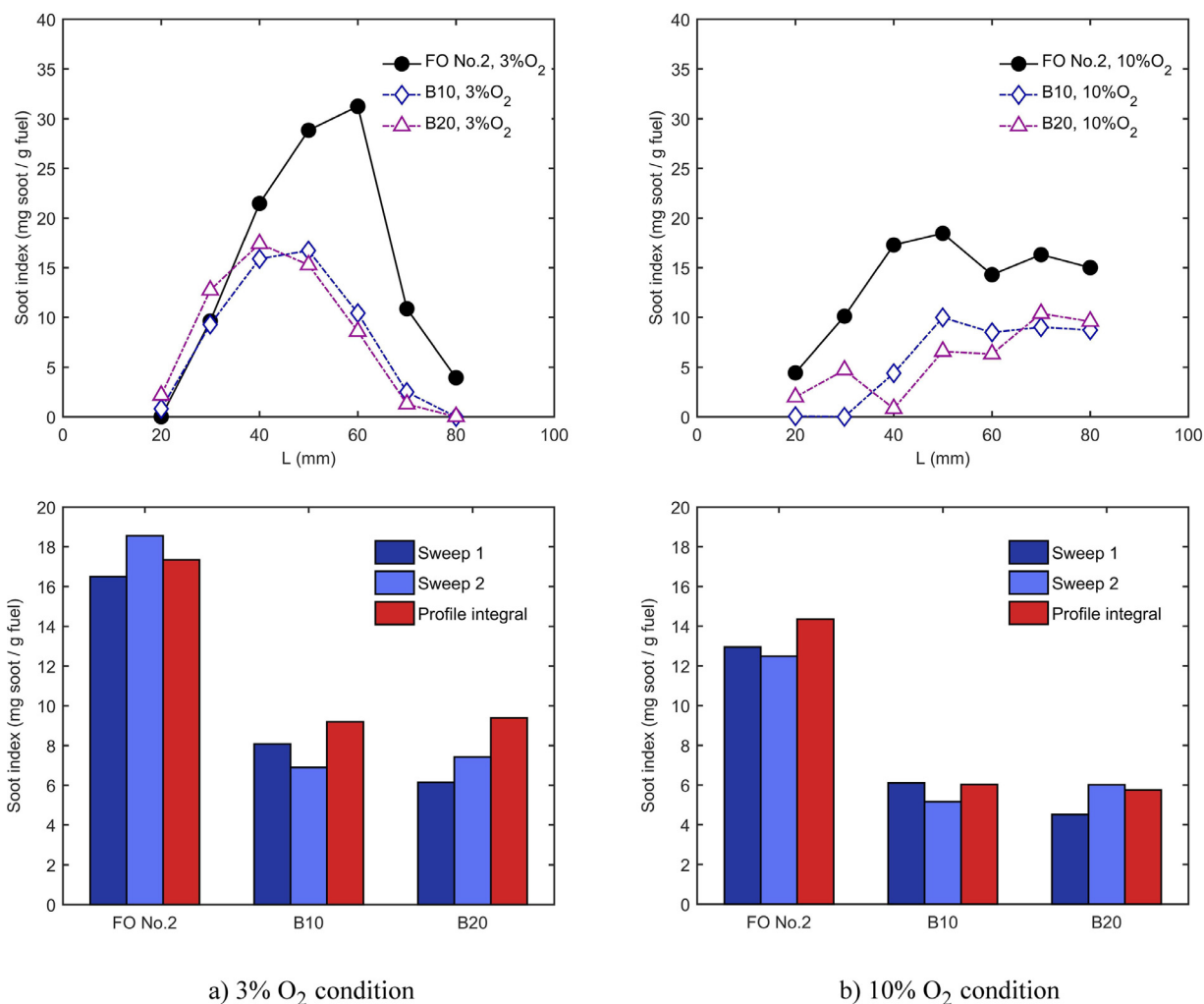
a) 3% O$_2$ condition   b) 10% O$_2$ condition

Fig. 15. Soot probe results for the 3% and the 10% O$_2$ condition. Droplets in these tests were 180 μm in initial diameter to increase soot yield. For each oxygen condition, soot index axial profiles are presented at the top, whereas the integrated values are displayed below.

as it can be observed in Fig. 11. According to the classical theory of droplet combustion, the FSR should remain constant with time. This is clearly not the case for the conditions where an actual flame exists (3, 5 and 10%), which display a sustained increase throughout all the combustion process. This behavior has been already reported in other droplet combustion studies with different fuels and experimental conditions (e.g., [17,23,24]), and it is ascribed to the well-known fuel vapor accumulation effect [35], especially relevant for low ambient oxidizer concentrations such as those used in this study.

A comparison between fuels for the three combustion conditions is presented in Fig. 14. As already commented, the approach followed for most fuels and conditions is to measure the outer boundaries of the soot clouds. Only for biodiesel and hexadecane at the 10% O$_2$ condition the flame diameters were measured based on their blue chemiluminescent emission ('C' tag in the legend).

FO, B10 and B20 displayed sooty flames for all the oxygen conditions, with differences between fuels being so small that no assertion can be safely made from the current data, as differences are within the measurement uncertainties.

Radiation from incandescent soot was also recorded for hexadecane at the 3 and 5% O$_2$ conditions, although it was much weaker than for the case of FO, B10 and B20. This can be noted in the delayed appearance of the first measurable point, and also in the higher variability of data, as a result of the lower signal-to-noise

ratio. For the 10% O$_2$ condition, hexadecane displayed no soot, and therefore the actual blue flame boundaries could be measured. Differences are apparent, with clearly higher FSR than those based on soot emission. As already stated, these results are in accordance with the fact that soot particles are located on the fuel-side of the envelope flame, and therefore flame diameters extracted from soot emission are expected to be smaller than those derived from actual chemiluminescent flame boundaries [14,29]. These differences in size between both kinds of flames can also be visually noted from the pictures displayed in Fig. 10.

Biodiesel presented sooty flames for the 3 and 5% O$_2$ conditions, with FSR values considerably smaller than those of FO and its mixtures. However, for the 10% O$_2$ case it displayed a mixed behavior, with completely blue flames (i.e. no soot yield) within the first part of the droplet lifetime and dominant soot radiation thereafter. Both types of pictures were presented in Fig. 10, where it can be seen that the emission due to soot is more intense and covers a slightly smaller diameter. FSR values determined from blue chemiluminescence for biodiesel within the first region are quite close to those of hexadecane. However, as soot emission eclipses the blue flame, the FSR referred to the soot cloud emission drops down, reaching values close to FO and its mixtures (which also have FSR values based on soot radiation). These results point to the importance of the flame measurement method, as differences between both kinds of flames might even exceed those related to

fuel behavior. In order to compare different fuels, the same kind of flames should be therefore utilized. Comparing the sooty flames of biodiesel with those of FO, B10 and B20, it is noteworthy that their FSR values appear to converge as oxygen availability increases; for the 3 and 5% cases, the flame sizes of biodiesel were considerable smaller than those of FO, whereas for 10% O_2 they display similar FSR values. In spite of obvious differences in fuels and experimental conditions, this trend is qualitatively in accordance with [14], where flame sizes for biodiesel were found to be slightly larger than those of diesel for a 21% O_2 condition.

3.5. Soot probe measurements

In addition to the presented results on droplet combustion behavior, asoot sampling method was used in order to characterize the sooting propensity of each fuel. For that purpose, the sampling probe described in Section 2.2 was used to locally capture soot particles at different distances from injection, determining thereby an axial profile of the amount of soot present along the flame traces. Two different oxygen conditions were studied, namely 3 and 10% O_2 in the coflow. Only FO, B10 and B20 produced enough soot to weight with accuracy on the analytical scale, and therefore only these three fuels were studied.

The obtained profiles for the two examined oxygen conditions are displayed in Fig. 15, where it can be seen that the collected amount for neat FO is clearly larger, pointing to a substantial soot reduction with biodiesel addition in both ambiences. As proposed in [14,15], this is probably a result of the aromatic fraction reduction in the resulting mixture in addition to the molecular oxygen content of biodiesel, capable of oxidizing soot precursors. The 3% O_2 profiles display dome-like curves, with soot yields close to zero some millimetres after droplet depletion (which occurs at $L\sim70$ mm). The 10% O_2 condition, on the other hand, presents a distinct behavior, with significant amounts of soot collected after the droplet depletion length. This is ascribed to the formation of relatively large soot agglomerates in tests with higher oxygen availability, as observed in Figs. 6 and 8. As a result, the specific surface area is reduced and, in spite of the high oxygen concentration, their oxidation rate decreases, causing high soot yields downstream of the droplet depletion length for the 10% O_2 case.

Anyhow, the axial evolution of soot mass is the outcome of formation and oxidation processes and these results do not intend to describe them, but rather to serve as a reference to evaluate the relative sooting tendency of the tested fuels at certain conditions. The cases can be better compared using a single parameter, representative of the soot collected over the whole trace. With that aim, sweep measurements were performed by continuously displacing the probe between the two flame trace limits ($L=20$ and $L=80$ mm). The displacement velocity of the soot probe was small enough (less than 1 mm/s) to prevent any possible interaction effect with droplet generation rate. The extracted soot mass was converted into a soot index, representative of the whole flame trace within that range ($L=20$–80 mm). This procedure was performed twice for each fuel and oxygen condition, and the extracted soot indices are plotted in Fig. 15. Besides, the values obtained by numerically integrating the already commented axial profiles are also represented (ideally, both integration methods should provide the same results).

Results displayed in Fig. 15 for both integration methods provide consistent results, pointing to the validity of the described sweep approach when it comes to provide a global indicator of sooting propensity. As already hinted by the axial profiles, the addition of biodiesel to FO clearly decreases the amount of soot generated, but differences between the 10% and 20% addition are not clear, with similar soot indices found for B10 and B20.

4. Conclusions

This work examines the droplet combustion and sooting characteristics of a UCO biodiesel, a heating oil and two mixtures of commercial interest, namely B10 and B20 (10 and 20% biodiesel by vol.). The experiments were designed to reproduce typical temperature and oxygen conditions in real boiler flames. Relative velocities between droplets and the surrounding gases were minimized, so that forced convection effects could be considered to be negligible. This, in addition to the small initial droplet size used (150 μm) explain the formation of nearly spherical soot shells and (when visible) blue envelope flames surrounding the droplets, proving therefore that droplets burnt in a practically 1-D configuration even when the tests were performed at normal gravity. Although some of the soot produced is dragged away by the relative flow, visually disturbing the spherical symmetry, an order-of-magnitude analysis demonstrates that heat and mass transfer processes remain dominated by molecular transport phenomena, indicating that radial profiles maintain an approximately 1-D configuration. The obtained experimental results may therefore be used to compare with theoretical one-dimensional droplet combustion models while, at the same time, being representative of the conditions faced by droplets in real applications.

All the examined droplet combustion characteristics for B10 and B20 (i.e. droplet size evolution, burning rates, SSR and FSR) were found to be practically indistinguishable from those of neat heating oil, whereas biodiesel displayed clearly differential behaviors, with longer heating transients and higher quasi-steady burning rates. Even though the studied biodiesel is highly unsaturated, no sign of polymerization of unsaturated FAMES was found for any of the tests, probably as a consequence of the short droplet lifetimes arisen from the realistic experimental conditions used. As expected, neat biodiesel displayed a much lower propensity to soot, and no soot shells were observed for any of the evaluated oxygen conditions. FSR were determined through the measurement of the incandescent soot cloud recorded for most fuels and conditions, being the actual chemiluminescent blue flame evaluated only for biodiesel and hexadecane at the leaner condition (10% O_2).

The effect of oxygen concentration on the droplet combustion process was also studied, with a clear enhancement of burning rates and smaller FSR as the oxygen volumetric fraction in the coflow increased. The confinement of soot was enhanced for higher oxygen levels and the amount of soot dragged away by the slip flow diminished, leading to a more spherical appearance of the soot shells. This is mainly ascribed to the increase in flame shell temperature, which enhances thermophoretic forces and, therefore, allows a better confinement of the soot particles within the reportedly spherical envelope flame.

Finally, a soot sampling method was applied for quantitatively measure the amount of soot produced by heating oil, B10 and B20. Results point to a significant decrease of soot collection with biodiesel addition, as pure heating oil yielded roughly two times higher soot indices than both mixtures. However, differences between B10 and B20 are not clear, with similar soot indices found between them. Neat biodiesel displayed a much lower propensity to soot, and it was not possible to accurately extract its soot index, as it was below the probe detection limit. This is in accordance with the much lower black-body luminosities recorded in the biodiesel flame images when compared to heating oil and its mixtures.

In summary, the practically identical droplet combustion characteristics of heating oil and its mixtures with biodiesel, as well as the lower propensity to soot of the latter support the suitability of such blends as replacement for conventional heating oil. The detailed experimental results obtained will be used at a later stage

to develop validated modeling tools for the prediction of evaporation and combustion of multicomponent droplets of practical fuels and their blends.

Acknowledgments

Supplementary materials

Supplementary material associated with this article can be found, in the online version, at doi:10.1016/j.combustflame.2019.02.014.

References

[1] M. Lapuerta, O. Armas, J. Rodriguez-Fernandez, Effect of biodiesel fuels on diesel engine emissions, Prog. Energy Combust. Sci. 34 (2008) 198–223.

[2] A. Datta, B.K. Mandal, A comprehensive review of biodiesel as an alternative fuel for compression ignition engine, Renew. Sustain. Energy Rev. 57 (2016) 799–821.

[3] P.M. Shameer, K. Ramesh, R. Sakthivel, R. Purnachandran, Effects of fuel injection parameters on emission characteristics of diesel engines operating on various biodiesel: a review, Renew. Sustain. Energy Rev. 67 (2017) 1267–1281.

[4] A. Macor, P. Pavanello, Performance and emissions of biodiesel in a boiler for residential heating, Energy 34 (2009) 2025–2032.

[5] J. González-González, A. Alkassir, J. San José, J. González, A. Gómez-Landero, Study of combustion process of biodiesel/gasoil mixture in a domestic heating boiler of 26.7 kW, Biomass Bioenergy 60 (2014) 178–188.

[6] A. Ghorbani, B. Bazooyar, A. Shariati, S.M. Jokar, H. Ajami, A. Naderi, A comparative study of combustion performance and emission of biodiesel blends and diesel in an experimental boiler, Appl. Energy 88 (2011) 4725–4732.

[7] B. Bazooyar, A. Ghorbani, A. Shariati, Combustion performance and emissions of petrodiesel and biodiesels based on various vegetable oils in a semi industrial boiler, Fuel 90 (2011) 3078–3092.

[8] S.W. Lee, T. Herage, B. Young, Emission reduction potential from the combustion of soy methyl ester fuel blended with petroleum distillate fuel, Fuel 83 (2004) 1607–1613.

[9] J.E. Batey, Combustion testing of a bio-diesel fuel oil blend in residential oil burning equipment, National Oilheat Research Alliance Technology Symposium (2003), p. 103.

[10] Y. Liu, Y. Xu, C. Avedisian, M. Hicks, The effect of support fibers on micro–convection in droplet combustion experiments, Proc. Combust. Inst. 35 (2015) 1709–1716.

[11] C. Chauveau, M. Birouk, I. Gökalp, An analysis of the d2-law departure during droplet evaporation in microgravity, Int. J. Multiph. Flow 37 (2011) 252–259.

[12] J. Ballester, C. Dopazo, Drop size measurements in heavy oil sprays from pressure-swirl nozzles, At. Sprays 6 (1996) 377–408.

[13] J. Ballester, C. Dopazo, Experimental study of the influence of atomization characteristics on the combustion of heavy oil, Combust. Sci. Technol. 103 (1994) 235–263.

[14] T. Li, D. Zhu, N. Akafuah, K. Saito, C. Law, Synthesis, droplet combustion, and sooting characteristics of biodiesel produced from waste vegetable oils, Proc. Combust. Inst. 33 (2011) 2039–2046.

[15] M. Botero, Y. Huang, D. Zhu, A. Molina, C. Law, Synergistic combustion of droplets of ethanol, diesel and biodiesel mixtures, Fuel 94 (2012) 342–347.

[16] M. Manjunath, V. Raghavan, P.S. Mehta, Vaporization characteristics of suspended droplets of biodiesel fuels of Indian origin and their diesel blends–An experimental study, Int. J. Heat Mass Transf. 88 (2015) 28–41.

[17] K.-L. Pan, J.-W. Li, C.-P. Chen, C.-H. Wang, On droplet combustion of biodiesel fuel mixed with diesel/alkanes in microgravity condition, Combust. Flame 156 (2009) 1926–1936.

[18] M. Zhu, Y. Ma, D. Zhang, Effect of a homogeneous combustion catalyst on combustion characteristics of single droplets of diesel and biodiesel, Proc. Combust. Inst. 34 (2013) 1537–1544.

[19] N. Hashimoto, H. Nomura, M. Suzuki, T. Matsumoto, H. Nishida, Y. Ozawa, Evaporation characteristics of a palm methyl ester droplet at high ambient temperatures, Fuel 143 (2015) 202–210.

[20] National Center for Biotechnology Information. PubChem Compound Database. https://pubchem.ncbi.nlm.nih.gov/compound/263 (accessed Nov. 16 2016).

[21] M. Angeloni, P. Remacha, A. Martínez, J. Ballester, Experimental investigation of the combustion of crude glycerol droplets, Fuel 184 (2016) 889–895.

[22] Á. Muelas, P. Remacha, A. Martínez, J. Ballester. Combustion behavior of jet a droplets and its blends with butanol. ASME Turbo Expo 2017: Turbomachinery Technical Conference and Exposition; 2017: American Society of Mechanical Engineers. p. V04AT04A073.

[23] Y.C. Liu, A.J. Savas, C.T. Avedisian, The spherically symmetric droplet burning characteristics of Jet-A and biofuels derived from camelina and tallow, Fuel 108 (2013) 824–832.

[24] Y.C. Liu, A.J. Savas, C.T. Avedisian, Spherically symmetric droplet combustion of three and four component miscible mixtures as surrogates for Jet-A, Proc. Combust. Inst. 34 (2013) 1569–1576.

[25] Y.C. Liu, A.J. Savas, C.T. Avedisian, Comparison of the burning characteristics of indolene and commercial grade gasoline droplets without convection, Energy Fuels 26 (2012) 5740–5749.

[26] Y. Xu, C.T. Avedisian, Combustion of n-butanol, gasoline, and n-butanol/gasoline mixture droplets, Energy Fuels 29 (2015) 3467–3475.

[27] A. Randolph, C. Law, Influence of physical mechanisms on soot formation and destruction in droplet burning, Combust. Flame 64 (1986) 267–284.

[28] G. Xu, M. Ikegami, S. Honma, K. Ikeda, X. Ma, H. Nagaishi, D.L. Dietrich, P.M. Struk, Inverse influence of initial diameter on droplet burning rate in cold and hot ambiences: a thermal action of flame in balance with heat loss, Int. J. Heat Mass Transf. 46 (2003) 1155–1169.

[29] Y.C. Liu, Y. Xu, M.C. Hicks, C.T. Avedisian, Comprehensive study of initial diameter effects and other observations on convection-free droplet combustion in the standard atmosphere for n-heptane, n-octane, and n-decane, Combust. Flame 171 (2016) 27–41.

[30] A. Marchese, F. Dryer, V. Nayagam, R. Colantonio, Hydroxyl radical chemiluminescence imaging and the structure of microgravity droplet flames, Symp. (Int.) Combust. (1996) 1219–1226.

[31] T. Farouk, Y. Liu, A. Savas, C. Avedisian, F. Dryer, Sub-millimeter sized methyl butanoate droplet combustion: microgravity experiments and detailed numerical modeling, Proc. Combust. Inst. 34 (2013) 1609–1616.

[32] F.E. Alam, Y. Liu, C. Avedisian, F. Dryer, T. Farouk, n-Butanol droplet combustion: numerical modeling and reduced gravity experiments, Proc. Combust. Inst. 35 (2015) 1693–1700.

[33] Y.C. Liu, T. Farouk, A.J. Savas, F.L. Dryer, C.T. Avedisian, On the spherically symmetrical combustion of methyl decanoate droplets and comparisons with detailed numerical modeling, Combust. Flame 160 (2013) 641–655.

[34] Y.C. Liu, F.E. Alam, Y. Xu, F.L. Dryer, C.T. Avedisian, T.I. Farouk, Combustion characteristics of butanol isomers in multiphase droplet configurations, Combust, Flame 169 (2016) 216–228.

[35] C. Law, S. Chung, N. Srinivasan, Gas-phase quasi-steadiness and fuel vapor accumulation effects in droplet burning, Combust. Flame 38 (1980) 173–198.

ELSEVIER
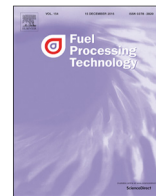
Research article

Production and droplet combustion characteristics of waste tire pyrolysis oil

Álvaro Muelas[a], María Soledad Callén[b], Ramón Murillo[b], Javier Ballester[c,*]

[a] *Laboratory of Research on Fluid Dynamics and Combustion Technologies (LIFTEC), CSIC – University of Zaragoza, Spain*
[b] *Instituto de Carboquímica (ICB-CSIC), Spain*
[c] *Fluid Mechanics Group/LIFTEC, CSIC-University of Zaragoza, Spain*

ABSTRACT

This work aims to study the pyrolysis of scrap tires as an end-to-end process, from its production to the combustion characteristics of the tire pyrolysis liquid (TPL) obtained. The TPL was produced in a continuous auger reactor (150 kWth) and its combustion characteristics were acquired through a drop tube facility, where the TPL burning behavior was compared to that of conventional heating oil (FO). The evaluated combustion characteristics included droplet and flame size evolution, burning rates, soot shell morphology, microexplosion occurrence and soot analysis. When compared to FO, TPL displayed considerably lower burning rates, although the consistent occurrence of microexplosions effectively shortened the TPL droplets lifetimes below those of FO. TPL also presented smaller flames and a higher propensity to soot. A TPL-FO blend of interest for heating applications (with only 5% of TPL due to its high sulfur content), was also tested, showing identical results to those of neat FO for all the studied combustion characteristics. The reported results are thought to provide valuable experimental data regarding the combustion behavior of a well characterized tire pyrolysis oil, which could also be used as the fuel-specific input data required for the simulation of realistic spray flames.

1. Introduction

The continuous growth in the amount of waste tires disposed worldwide is currently a major environmental problem, as a sustainable recovery and recycling of this residue presents significant technical difficulties, primarily due to the complex structure and composition of tire materials [1]. On the other hand, its disposal in landfills is not an option, as it can be a source of uncontrollable toxic fires and pollution. In fact, the disposal of waste tires in landfills is currently banned in the EU, according to the Council Directive 1999/31/EC. The dimensions of this environmental issue are substantial, as the number of end-of-life tires in the current decade has been estimated to be in the range of 1 billion units disposed per year worldwide [2–4].

One of the most promising alternatives to cope with this problem is to pyrolyze the scrap tires, as it has been highlighted in several works (e.g., [2,5,6]). Pyrolysis is a thermochemical process where a certain feedstock is heated at moderate temperatures (generally, between 400 °C and 800 °C) under inert environment at atmospheric pressure. Under these conditions, the raw material is converted into light gas, liquid and a carbonaceous solid or char [7]. Thus, this process transforms waste tires into new products with added value. In the case of rubber obtained from waste tires, a significant part of the material consists of carbon black (about 40%) that can be reused in the

production of new tires, as it has been recently demonstrated in [8]. As carbon black is usually synthesized through the incomplete combustion of oil heavy fractions, its recuperation by means of this process would significantly reduce the environmental impact of its production. Another main product of pyrolysis is the tire pyrolysis oil, corresponding to the liquid fraction. It should be noted that a substantial fraction of this oil ultimately comes from biomass, as around 50% of the rubber used in tire manufacturing originates from natural sources (hevea tree). Tire Pyrolysis Liquid (TPL) is mainly used for heat and power production, reducing therefore the needs for fossil fuels. In light of the huge amounts of waste tires disposed every year and the high calorific value of TPL (~40–44 MJ/kg, according to [2]), the potential for fossil fuel reduction is substantial. Finally, the non-condensable gas is typically used in situ to provide the energy needed for the pyrolysis process. Usually, all the plants incorporate a gas cleaning system to avoid sulfur compounds and particulate matter emissions, making the pyrolysis process globally clean. Despite the fact that commercial facilities and technology suppliers can be found all around the world, the practical applicability and economic viability of the products obtained from waste tire pyrolysis, and namely of TPL, remains nowadays with prospects of growth, with diverse studies addressing the production and combustion characterization of different oils obtained through the pyrolysis of waste tires, as it will be detailed down below. The economic

---

aspects, however, are beyond the scope of this work, which is aimed at improving the technical understanding of the production and combustion characteristics of this novel fuel.

Several works have examined the performance of TPL-diesel mixtures in both automotive [9–11] and non-automotive diesel engines [5,12,13]. Regarding the automotive application of TPL, an alternative fuel for diesel engines was produced from waste vehicle tires by the method of pyrolysis after the reduction of sulfur content with $Ca(OH)_2$ [14,15]. Different blends were tested in a diesel engine obtaining good performance in the case of low sulfur tire fuels. Frigo et al. [15] proved that mixtures up to 20% in TPL can be used in diesel engines without engine modifications, whereas mixtures with TPL from 20% to 40% need modifications of the injection to compensate the longer ignition delay.

As typical TPLs usually present substantially high sulfur contents, their use in internal combustion engines is seriously limited by fuel regulations. In fact, environmental restrictions associated with SO_2, NO_2 and CO emission levels higher than the acceptable limits prescribed by the European Air quality standard (EU2015/2193), restrict the use of TPL in automotive engines. As stated above, a possible alternative is their desulfurization by means of processes as those presented in [6,16]. A more straightforward approach is its use for heat generation in boilers, large stationary engines for heating and other energy-demanding industrial processes [1], as the sulfur limits regarding these applications are considerably more permissive than those set for automotive purposes (1000 ppm instead of 10 ppm, according to the Spanish Royal Decree 61/2006).

Concerning the application of TPL-diesel mixtures as a fuel in burners/boiler units, García-Contreras et al. [17] studied the replacement of diesel fuel by a blend (50%/50% by volume) of TPL-diesel in a residential boiler, obtaining the same performance as that achieved with diesel although with higher particulate matter emissions. However, all these studies have been mainly focused on the environmental impact without taking into account the combustion behavior.

The already cited studies on final applications provide insight into relevant fuel combustion characteristics from a realistic and applied point of view, and therefore are a usual method for determining the combustion features of a novel fuel such as TPL. However, the complexity of those combustion configurations makes it impossible to strictly control all the relevant parameters, and the obtained results might depend on slight changes in non-controlled variables such as the atomization characteristics or the fuel-air mixing within the combustion chamber. A dependency on the experimental setup used for the tests is thus inevitably introduced, being difficult to precisely determine whether certain combustion behavior is entirely attributable to the tested fuel or, on the contrary, is an indirect result of changes in another related process. By contrast, in the single droplet configuration, all the relevant variables influencing results can be well characterized, and the extracted combustion features are thus inherently ascribable to the studied fuels. This approach has been used in several works in order to characterize the combustion behavior of alternative fuels, with a special focus on biofuels and their blends with conventional, well-known petrofuels (e.g. [18] for butanol-gasoline or [19] for biodiesel-diesel mixtures) and also on different residual fuels (e.g. oil-water emulsions and coal-water slurries containing petrochemicals in [20,21]).

Single droplet combustion results are less common for pyrolysis oils than for other alternative fuels, although tire-derived oils have received very little attention and the currently available studies are mostly referred to bio-oils produced from lignocellulosic biomass. Yang and Wu [22] examined the droplet combustion characteristics of a pinewood bio-oil obtained from slow pyrolysis blended with butanol. They found that bio-oil addition consistently decreased butanol burning rates, while enhancing the formation of a solid residue and promoting the occurrence of microexplosions. Chen et al. [23] also registered microexplosions for a pyrolytic oil produced from castor seeds, which in turn underwent almost complete evaporation, leaving a negligible amount of solid residue. The works cited so far relied on the suspended droplet technique, where roughly ~1 mm sized droplets were suspended on ceramic fibers and burned. Garcia-Perez et al. [24] studied the combustion behavior of two different biomass vacuum pyrolysis oils under more realistic conditions, namely with ~60 μm sized droplets ignited in free fall (and therefore, without the possible interaction of the suspending fibers). Surprisingly, no microexplosions were registered for any of the studied bio-oils under such experimental conditions. Shaddix and Hardesty [25,26] also used a drop-tube facility with droplets in the range of ~350 μm, performing a thorough study on the combustion characteristics of flash pyrolysis oils produced from a variety of biofeedstocks. They found quite low burning rates for all of them, with values closer to those of heavy fuel oils than to heating oil. However, the consistent occurrence of microexplosions effectively shortened the bio-oil droplet lifespans, and consequently the overall lifetimes of the studied pyrolysis oils were quite similar to those of conventional heating oil.

As stated above, the cited studies evaluated the single droplet combustion characteristics of different pyrolysis oils produced from biofeedstocks. To the best of the authors' knowledge, this kind of study has not been addressed so far for TPL, even though its chemical composition and properties are entirely different to those of bio-oils. This work aims therefore to fill this gap by studying the single droplet combustion behavior of a well-characterized TPL, both neat and blended with conventional heating oil. The experimental conditions used are intended to be as close to those found in real applications as possible, with free-falling, small-sized droplets (150 μm) immersed in a gaseous coflow which simulates the temperature and coflow compositions found in real flames. Relative velocities between the free-falling droplets and the coflow were also minimized, so that droplets were only minimally disturbed by convective effects and burnt in a practically 1-D configuration, facilitating therefore comparison with theoretical one dimensional droplet combustion models.

2. Material and methods

2.1. Pyrolysis oil preparation and characterization

The TPL used in this research is the result of > 500 kg of granulated waste tires pyrolyzed in a continuous auger reactor plant of 150 kWth of nominal capacity and corresponding to technology readiness level 5 (TRL 5) described in detail elsewhere [9,27]. This experimental campaign was conducted in 13 experiments that gave as the result 100 h of continuous operation without any significant technical problem. The reaction temperature and pressure were 550 °C and 1 bara, respectively. N_2 was used as carrier gas at 5 NL/min. The waste tire mass flow rate was 6.7 ± 0.1 kg/h, and the residence time of the feedstock inside the reactor was 3 min. These conditions were selected as those maximizing both the liquid yield and the tire rubber conversion. As a consequence, yields to liquid, solid, and gas were 42.6 ± 0.1, 40.5 ± 0.3, and 16.9 ± 0.3 wt% respectively. Before characterization, TPL was subjected to decantation (30 days) in order to deposit possible fine char particles that could have been carried over from the reactor. The properties of the TPL have been previously reported [9,28] and are shown in Table 1.

The chemical composition of the TPL was also analyzed by GC–MS using a Varian CP-3800 gas chromatograph connected to a Saturn 2200 ion trap mass spectrometer. A capillary column, Agilent CP-Sil 8 CB, low bleed, 5% phenyl, 95% dimethylpolysiloxane, (60 m × 0.25 mm i.d. × 0.25 μm film thickness) was used. An initial oven temperature of 40 °C was maintained for 4 min. Then, a ramp rate of 4 °C/min was implemented to reach a final column temperature of 300 °C. This temperature was maintained for 21 min. The carrier gas was He (BIP quality) at a constant column flow of 1 mL/min. The injector, detector, and transfer line temperatures were 280, 200, and 300 °C, respectively. Samples volumes of 1 μL (50 μL diluted to a final volume of 500 μL in a

Table 1
Properties of the obtained TPL.

Property	Method	TPL
HHV (MJ/kg)	ASTM 240-09	42.70
LHV (MJ/kg)		40.49
C (wt%[a])		86.19
H (wt%[a])		10.33
O (wt%[a])		0.00
N (wt%[a])		0.79
S (wt%[a])		0.83
H/C atomic ratio		1.44
AFRst (kg/kg)	From elem. composition	13.46
Molar mass (kg/kmol)	From AspenTech HYSYS	142.5
Density at 15 °C (kg/m^3)	EN 12185	917
Kinematic viscosity at 40 °C (cSt)	EN 3104	2.39
Initial boiling point (°C)	EN 3405	82.2
T50 (°C)	EN 3405	231.1
Final boiling point (°C)	EN 3405	302.5
Final percent of distillate		80
Calculated cetane index (CCI)	ASTM D4737-04	17.6
Saturates (wt%)	From TLC	5.5
Aromatics (wt%)	ASTM 6379/04 for diesel	65.2
Polars (wt%)		29.3
Cold filter plugging point (°C)	EN 116	9
Lubricity (lm WS 1.4)	EN 12156	162.59
Water content (ppms[b])	EN 12937	689.9
Total acid number (mg/KOH)	From Mettler Toledo T50	5.0
Flash point (°C)	EN 3679	23.0
Smoke point (mm)	ASTM D1322	9
Oxidation stability (h)	EN 15751	16

TLC: thin layer chromatography.
[a] As received.
[b] On mass basis.

Table 2
Chemical composition and boiling point distribution by families of tire pyrolysis oil determined by GC–MS.

	Normalized peak area (%)	RSD (%)[a]	Boiling point (°C)[b]
Aromatics	75.37	0.33	97.1–278
Cyclic hydrocarbons	14.09	0.82	93.7–237
Linear paraffins	3.40	3.39	284–502
n-Alkenes	5.76	1.17	89.4–388
Esters	1.39	3.81	212–403

[a] RSD = relative standard deviation for samples injected by duplicated in the GC–MS.
[b] According to the simulated distillation with ASTM D2887.

mixture of 1:1 CH_2Cl_2:C_2H_6O) were injected applying a 25:1 split mode, with a solvent delay of 7.5 min. The MS was operated in electron ionization mode within a 35–550 *m/z* range. Each peak was assigned to selected compounds according to the corresponding m/z values, which were previously defined in the automatic library search NIST 2011. Each sample was analyzed by duplicate, and results were computed as an average. A total of 101 compounds identified in the liquid were divided in the following chemical families: aromatics (40 compounds) cyclic hydrocarbons (21 compounds), linear paraffins (18 compounds), n-alkenes (20 compounds) and esters (2 compounds) (Table 2). Some simplifications of the GC/MS analysis were assumed to determine the semi-quantitative composition of the different groups since, first, a unique response factor was used for all the identified compounds, and second, it was supposed that the whole sample was eluted and analyzed in the GC–MS chromatogram.

Each one of the main organic compounds present in the TPL were identified according to GC–MS. Regarding repeatability, good results were obtained for the different chemical families, with a RSD value lower than 5%. The major compounds were associated with aromatic compounds (75.37%), mainly constituted by a single aromatic ring with alkyls substituents where toluene and the mixture of xylenes showed

the highest percentages (14.65 and 17.45% respectively). Other heavier aromatic compounds were mainly associated with substituted naphthalene as well as indene. In addition to the aromatic compounds, D-limonene, a natural terpene included in the cycloalkanes family, represented 4.48% of the total in the TPL followed by o-cymene (3.96%), also an aromatic compound. This predominant aromatic composition and the relevant presence of limonene and cymene has already been reported in the literature [29] although in this case, these last compounds were not the major compounds in the TPL. Also, linear hydrocarbons both alkanes and alkenes were obtained, with percentages between 3 and 6% (Table 2) and with predominance of alkenes versus alkanes. The identified alkanes were hexadecane, heptadecane, octadecane, nonadecane, eicosane and tetracosane and some other high molecular weight alkanes. In addition to the main hydrocarbons, sulfur-containing compounds and nitrogen-containing compounds were also identified, with a low percentage of some oxygenated compounds in the form of esters.

2.2. Droplet combustion facility

The evaporation and combustion processes of the isolated droplets were characterized using LIFTEC's Droplet Combustion Facility (DCF). The main elements of the setup are shown in Fig. 1. A more detailed description can be found in previous works [30–32].

Droplets with an initial diameter (D_0) of 150 μm (150.1 ± 0.5 μm) were formed at a piezoelectric apparatus at a 25 Hz rate, providing an interdroplet spacing long enough ($> 100\ D_0$) to effectively avoid any significant interaction among droplets [19]. The free-falling droplets were introduced into a flat-flame burner's exhaust gases, providing thereby a controllable environment to study the evaporation and combustion processes of fuel droplets under temperature and gas compositions representative of those found in real flames. Since in actual applications oxygen concentration can significantly vary among regions within the flame, three different conditions were chosen, namely with a 0, 3 and 5% O_2 volumetric fraction (dry basis) in the gaseous coflow. These levels are thought to be representative of the oxygen range observed by droplets during their evaporation in boilers, where most of the liquid droplet evaporation occurs in a central, low-oxygen and fuel-rich core (e.g., see oxygen maps in [33,34]).

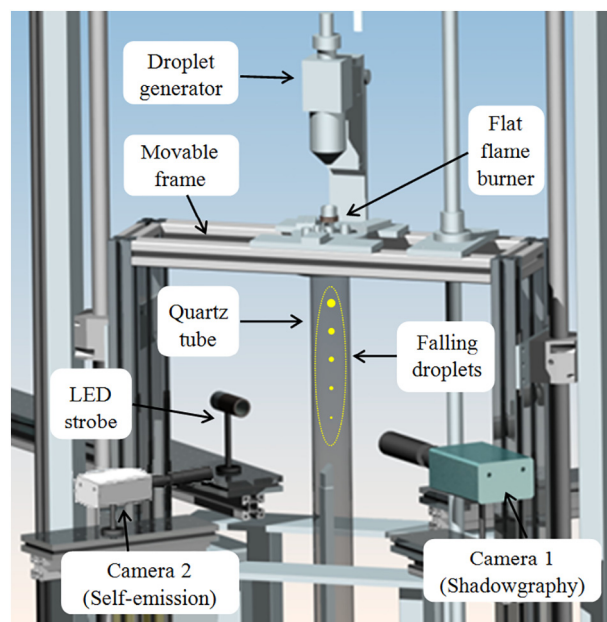The droplet combustion characteristics were completely determined

Fig. 1. Scheme displaying the main elements of the DCF.

by means of optical techniques. The droplet diameter and velocity were obtained from pictures recorded with a CCD camera (QImaging Retiga SRV, 12-bit) equipped with a telemicroscope and backlighted by means of a LED stroboscope. This optical system was synchronized to record two consecutive shots of the same free-falling droplet 500 µs apart. A second camera (Hamamatsu C11440-36U, 12-bit) recorded the light emitted from the envelope flames and soot particles. In order to high-light the droplet shadow, making it distinguishable from the flame, a weak backlight was included, capturing therefore in the same frame the droplet and its envelope flame. Images were post-processed in order to extract different droplet combustion characteristics in the most re-peatable way. This post-processing was performed in Matlab, using background subtraction, contrast enhancement and automatic edge detection algorithms.

Additionally to this close-up optical setup, the macroscopically visible flame traces were obtained through a third camera (Teledyne DALSA Genie Nano C4060) fitted with a DSLR lens. As such traces provide visual information regarding the amount of soot present in the combustion chamber, these pictures were also processed to extract in-formation concerning the sooting tendency of each fuel.

3. Results and discussion

Since the intended application of the obtained TPL is its combustion in boilers, information regarding its combustion characteristics seems most desirable. Due to its high sulfur content (0.83 wt% as received, Table 1), the pyrolysis oil must be diluted in order to fulfil the Spanish regulations, which establishes a limit of 1000 ppm for heating appli-cations. As conventional Spanish heating oil displays a low sulfur content (< 10 ppm, Table 3), a realistic blend would be 5% TPL in 95% (by weight) heating oil. This mixture, named TPL5, contains < 425 ppm of sulfur, complying therefore with the regulations. Blends with higher TPL content would still be possible, up to 12% by weight for this particular heating oil. The proposed mixture, however, is thought to be an interesting case of study because it is located at the mid-point of the suitable blending spectrum (i.e., different fuel-oils with higher sulfur content would allow for a lower TPL content in the mixture). TPL5 was therefore compared with pure tire pyrolysis oil (TPL) and with neat Spanish heating oil (FO). A pure and well-known compound such as n-Hexadecane (99% purity) was also included as a reference, since it has been used as a baseline for comparison in different works addressing diesel and heating oil combustion tests (e.g., in [19,30,35]). The main physicochemical properties of heating oil and hexadecane are sum-marized in Table 3 (for a more detailed description, the reader is re-ferred to [30]).

3.1. Droplet, soot shell and flame images

The combustion process of the studied fuels for the 5% O_2 condition is illustrated in Fig. 2. The depicted pictures are obtained from the backlighted Camera 1 (Fig. 1), and display the liquid fuel droplet sur-rounded by nearly-spherical soot shells for certain cases. Similar soot shells are reported in convection-free environments achieved through microgravity such as [18,35]. In these works, the soot particles pro-duced inside the envelope flame remain trapped at a certain radial lo-cation, where viscous drag and thermophoresis forces balance. The

onset of soot shells is, however, a quite infrequent event for droplet combustion tests at normal gravity, as any small relative velocity dro-plet-coflow (either caused by natural or by forced convection) would drag the small soot particles away. Slip velocities between droplets and the surrounding coflow were experimentally minimized in this work (Reynolds number < 0.4), enabling the onset of quite spherical soot shells for high soot-yield conditions. In the authors' opinion, the oc-currence of these spherical soot shells implies that even if test were conducted at normal gravity, droplets evaporate and burn under con-ditions close to spherical symmetry, especially in the droplet's vicinity, facilitating thus the comparison with theoretical 1-D droplet combus-tion models.

When comparing among fuels, the first significant difference is the occurrence of microexplosions for the pure pyrolysis oil (at 2.00 and 2.20 s/mm²) whereas the other fuels, including TPL5, evaporated smoothly until droplet extinction. In spite of the obvious differences between TPL and pyrolysis oils derived from bio-feedstocks, this dis-ruptive behavior was also noted by several authors when studying the single droplet combustion characteristics of different bio-oils (for in-stance, in [22,23,25,26,37]). The fact that TPL droplets also underwent these shattering events is a novel result, which nonetheless concurs with most of the previous characterizations performed on bio-oil dro-plets. The experimental setup used here, with non-suspended droplets is thought to provide reliable results in this regard, as the potential in-fluence of the solid filament (which can act as a heterogeneous nu-cleation site) is avoided. The wide differences in volatility between TPL compounds (as it can be observed in Tables 1 and 2), in addition to the high temperature coflow used in this work, could cause the bursting characteristics of TPL. The recorded microexplosions were quite violent and, in most cases, shattered the droplets in secondary disintegrations. TPL droplets consistently burst after a first period of smooth evapora-tion. However, the onset of microexplosion slightly varied within a short interval, typically not broader than 0.2 s/mm². The quantitative data extracted from these images, including droplet size measurements and microexplosion occurrence instants for each condition, shall be presented in the following section.

Regarding the already mentioned soot shells, further differences can be noted among fuels. Whereas FO, TPL5 and TPL display clearly visible soot shells, none was found for hexadecane, pointing to a much less sooty behavior of this fuel. The addition of a 5% TPL to conventional heating oil does not appear to significantly change its behavior, with nascent soot shells emerging by approximately the same normalized time as for neat FO (1.20 s/mm²), and maintaining similar thickness throughout all the droplet combustion lifespan. Pure TPL, on the other hand, already displays a distinguishable soot shell by 1.00 s/mm², pointing to a higher sooting tendency, at least in the earlier stages of droplet combustion. This higher soot yield can be ascribed to the aro-matic-rich nature of TPL, which displays a much higher aromatic composition than heating oil (75.37% of TPL consists on aromatics according to Table 2, whereas this figure is reduced to 29.16% in the studied heating oil [30]). For the 3% O_2 condition, the registered soot shells were much fainter, and the evaporation case (0% O_2) did not feature any soot shell. These differences can be primarily attributed to the temperature increase caused by the envelope flame as oxygen availability in the coflow rises [30].

Even though the majority of microexplosions effectively shattered

Table 3
Selected properties of heating oil (FO) and hexadecane.

Fuel	Molecular formula	C (wt%)	H (wt%)	S (ppm)	Boiling point (°C)	LHV (MJ/kg)	AFR (kg/kg)	Density at 20 °C (kg/m³)
FO	$C_{13.21}H_{24.63}$	86.5	13.5	< 10	271–352[b]	41.92	14.5	861
Hexadecane[a]	$C_{16}H_{34}$	84.9	15.1	0	286	44.20	14.9	773

[a] Extracted from [36].
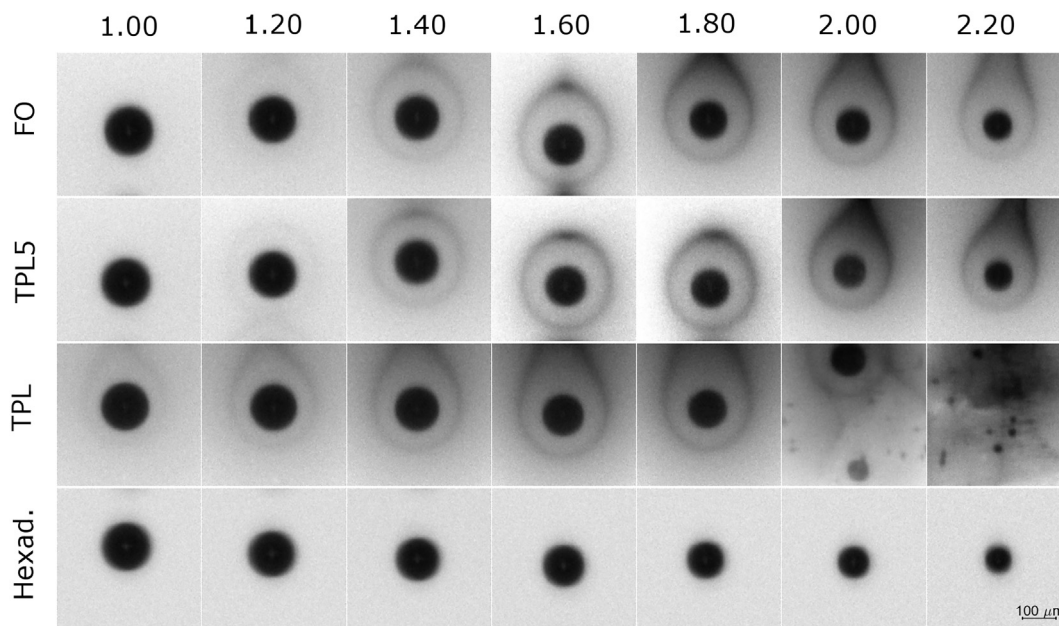[b] Distillation curve (20–80% mass distilled).

Fig. 2. Droplet and soot shell evolution for the examined fuels at the 5% O_2 condition. Images are organized in accordance with their normalized time after injection: t/D_0^2 (s/mm^2).
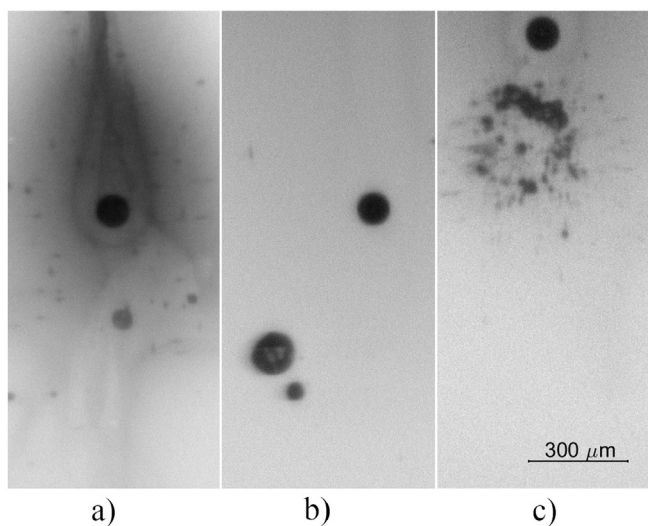

Fig. 3. Different microexplosion typologies registered with Camera 1: a) TPL droplet, L = 27 mm, 5% O_2; b) TPL droplet, L = 31 mm, 0% O_2; c) TPL droplet, L = 29 mm, 3% O_2.

the TPL droplets in a secondary atomization process (as those presented in Fig. 2), there were cases where these events displayed a lower intensity, with droplet puffing and swelling. The three main observed typologies are presented in Fig. 3, where the non-cropped double-shot images acquired with Camera 1 (Fig. 1) display the droplet just before the microexplosion (upper droplet), and the resulting smaller fragments after it. The time interval between shots is 500 μs, and therefore the characteristic time for the shattering event can be considered to be in the order of tens of microseconds. The LED pulse duration is of only 1 μs, effectively freezing such high-speed process. While Fig. 3a shows an efficient microexplosion, where the original droplet is shattered into much smaller fragments, the event displayed in Fig. 3b is rather a swelling and puffing phenomenon than a proper disintegration. In this case, the vapor accumulation inside the droplet does not lead to a sudden breakup, but causes a much slower droplet swelling coupled with puffing of small liquid fragments and a significant deviation from

the original droplet's free-falling path. Fig. 3c, on the other hand, displays a complete breakup of the initial droplet, as it happened in Fig. 3a, but without a trace of any especially relevantly sized sub-droplet. As, according to the well-known d²-law, droplet lifetime approximately scales with its diameter squared, the occurrence of microexplosions such as those displayed in Fig. 3a or c would effectively shorten the droplet combustion lifetime to practically a few instants after the disintegration event. Much less straightforward to predict is the combustion history of swelling droplets (Fig. 3b), as their random deviation made it extremely difficult to keep them in focus. Even though the images presented in Fig. 3 correspond to different oxygen conditions, no correlation was found between oxygen availability and mode of microexplosion. The occurrence of a complete fragmentation or a swelling process seemed to respond to apparently random patterns, as TPL droplets subjected to exactly the same conditions alternatively displayed both phenomena.

In addition to the droplet and soot shell data obtained by means of the backlighted camera, Camera 2 (Fig. 1) recorded the envelope flames around the droplets. A representative selection of these flame images for neat TPL tested with the three oxygen conditions is presented in Fig. 4.

Differences among oxygen conditions can be clearly observed, with smaller and brighter flames as oxygen availability increases. The studied pyrolysis oil displays a strong soot yield for all the studied oxygen conditions, and thus its flame characteristics are extracted from the soot continuous-spectrum emission. It is well known that soot is created in the inner side of the shell flame, and therefore the actual chemiluminescence flame would be located slightly farther from the droplet, although in these tests it remained eclipsed by the much stronger soot emission. Note that for the 0% O_2 case no combustion can take place, and the sooty emission presented in Fig. 4 is entirely ascribed to the thermal emission of the soot clouds when exposed to the high-temperature coflow. Analogous behaviors were found for FO and TPL5, although with slightly wider flames (flame sizes will be quantified in the following section). Hexadecane, on the other hand, displayed a much less pronounced sooty emission and, for the 5% O_2 condition, the actual chemiluminescence bluish flame was visible within the first stages of droplet combustion. It is noteworthy that, for higher oxygen availabilities than those used in this study (namely 10% O_2), the absence of any soot emission for hexadecane allowed the visualization of a
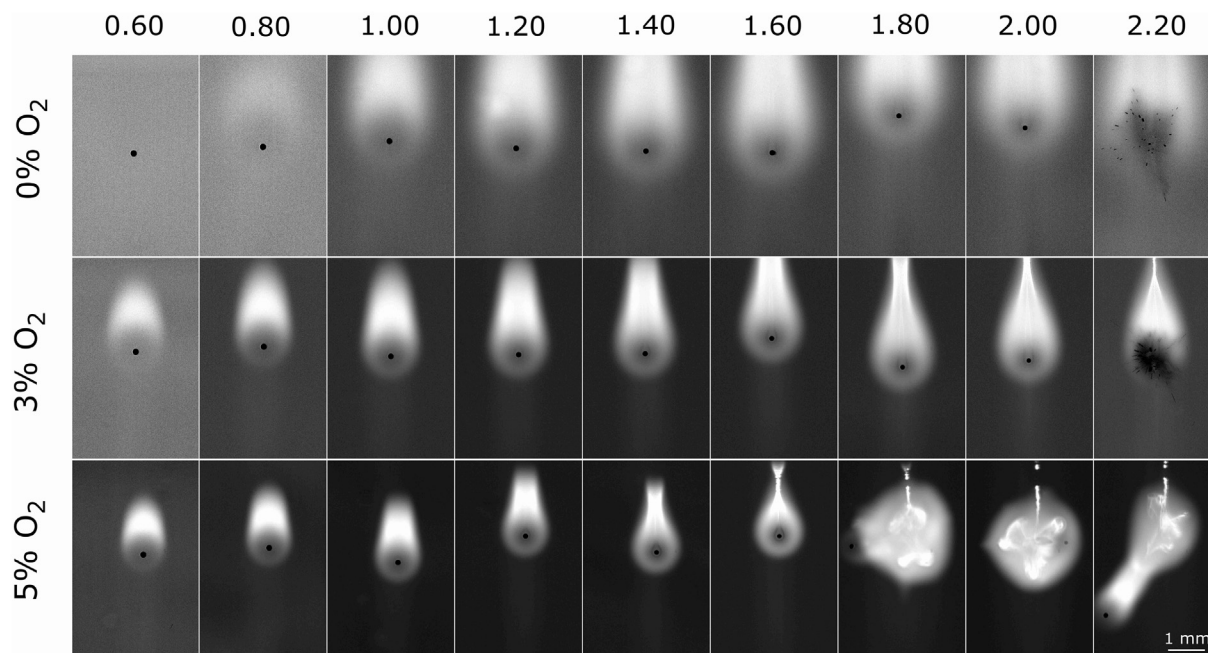
Fig. 4. TPL flame evolution at the three studied oxygen conditions. Images are organized in accordance with their normalized time after injection: t/D_0^2 (s/mm^2).

considerably spherical blue envelope flame throughout all the droplet lifetime, supporting therefore the already discussed 1-D configuration of the combustion process (in spite of the obvious buoyancy effects displayed by soot clouds in Fig. 4).

The different typologies of registered microexplosions can also be clearly observed in Fig. 4, where the TPL combustion process can either finish abruptly with a complete droplet shattering or proceed after an abrupt deviation of the droplet trajectory caused by the swelling and puffing event. This second situation can be clearly observed in two pictures of the 5% O$_2$ case, where the droplets appear to be violently propelled away from their original position.

3.2. Quantitative data

As stated above, the droplet combustion process was entirely characterized from the images presented in the previous section. These pictures were processed in order to extract their main combustion characteristics, namely their burning rates and their droplet and flame size evolutions with time, which shall be quantified and presented here. Since the droplet combustion process is intended to be studied under experimental conditions as representative of real flames as possible, tests were performed at 0, 3 and 5% O$_2$, covering therefore a typical range of oxygen availabilities around droplets in real flames, where the initial 21% practically only exists at the injection plane, before fresh air gets mixed with hot flame gases. The heating oil test at the 0% O$_2$ condition was performed twice to check the repeatability of the experimental procedure. Only a 0.5% relative difference was found for droplet burnout time, while a 0.7% difference was observed for the evaporation rate.

The extracted droplet size and burning rate evolution curves for the three selected oxygen conditions are presented in Fig. 5. The droplet size results are shown in the left column in terms of normalized diameter squared against normalized time. Normalization is applied with the initial droplet diameter (D_0). At a first glance, the curves are in accordance with the d^{2-} law and, after a significant heat-up transient period, the normalized size decreases linearly with time with a seemingly quite constant slope named burning rate (K). In order to gain insight into this relevant parameter, the D^2-t curves were fitted to a polynomial function (4th order), whose derivative provides the burning rate dependence with time: $K = -d(D^2)/dt$. These results are displayed

in the right column of Fig. 5, where it can be seen that, contrary to the notion of a nearly constant, time-independent burning rate which could be initially drawn from the D^2-t curves, all the calculated K-t curves display a gradual increase in K which spans for a substantial part of the droplets lifetimes before reaching a quasi-steady value. This progressive burning rate increase is primarily ascribed to the initial heating transient of the liquid phase.

The evaporation characteristics reported in Fig. 5 for FO and TPL5 are virtually identical over the course of the whole droplet lifespan. The small addition of TPL to heating oil does not appear to drive any significant change in the evaporative behavior (0% O$_2$), nor in combustion (3 and 5% O$_2$). Neat pyrolysis oil on the other hand, shows an earlier onset of vaporization, which can be clearly noted by the absence of initial droplet volumetric expansion. This is ascribed to the lower boiling point of the lightest fractions of the pyrolysis oil (Tables 1, 2) in comparison with those of heating oil (Table 3) or with the boiling point of hexadecane. Even though the TPL droplets start their vaporization earlier, their burning rates are soon surpassed by those of FO, TPL5 and hexadecane, fuels which also display clearly higher quasi-steady burning rates. These considerably lower K would induce longer droplet lifetimes for TPL in comparison with heating oil were they not altered by the microexplosion occurrence. In spite of the obvious differences among fuels, this behavior was also noted for several bio-oils in [25,26], where the onset of bursting events for the different pyrolysis oils substantially reduced their overall burnout times even below of those of a light fuel oil with a considerably higher (by a factor of 2–3) burning rate. Even though TPL also shows a lower K compared to FO (Fig. 5), this difference is much smaller than that noted in the referred works. This would point to considerably higher K values for tire-derived pyrolysis oils than for bio-oils, as it could be ascertained from a comparison of TPL and typical bio-oil composition and main thermophysical properties. For instance, TPL contains no water (bio-oils studied in [25] ranged 16–30% in water content), it has a substantially higher LHV (40.49 MJ/kg according to Table 1, whereas bio-oils in [25] displayed 16–19 MJ/kg) and also a significantly lower density (917 kg/m^3 in contrast to 1210–1230 kg/m^3 in [25]).

As it can be noted in Fig. 5, the TPL curves suddenly terminate at values in the range of $(D/D_0)^2 \approx 0.40$, precisely due to the apparition of the already described microexplosion events which, for a considerable fraction of the observed cases, shattered the droplets. This behavior was
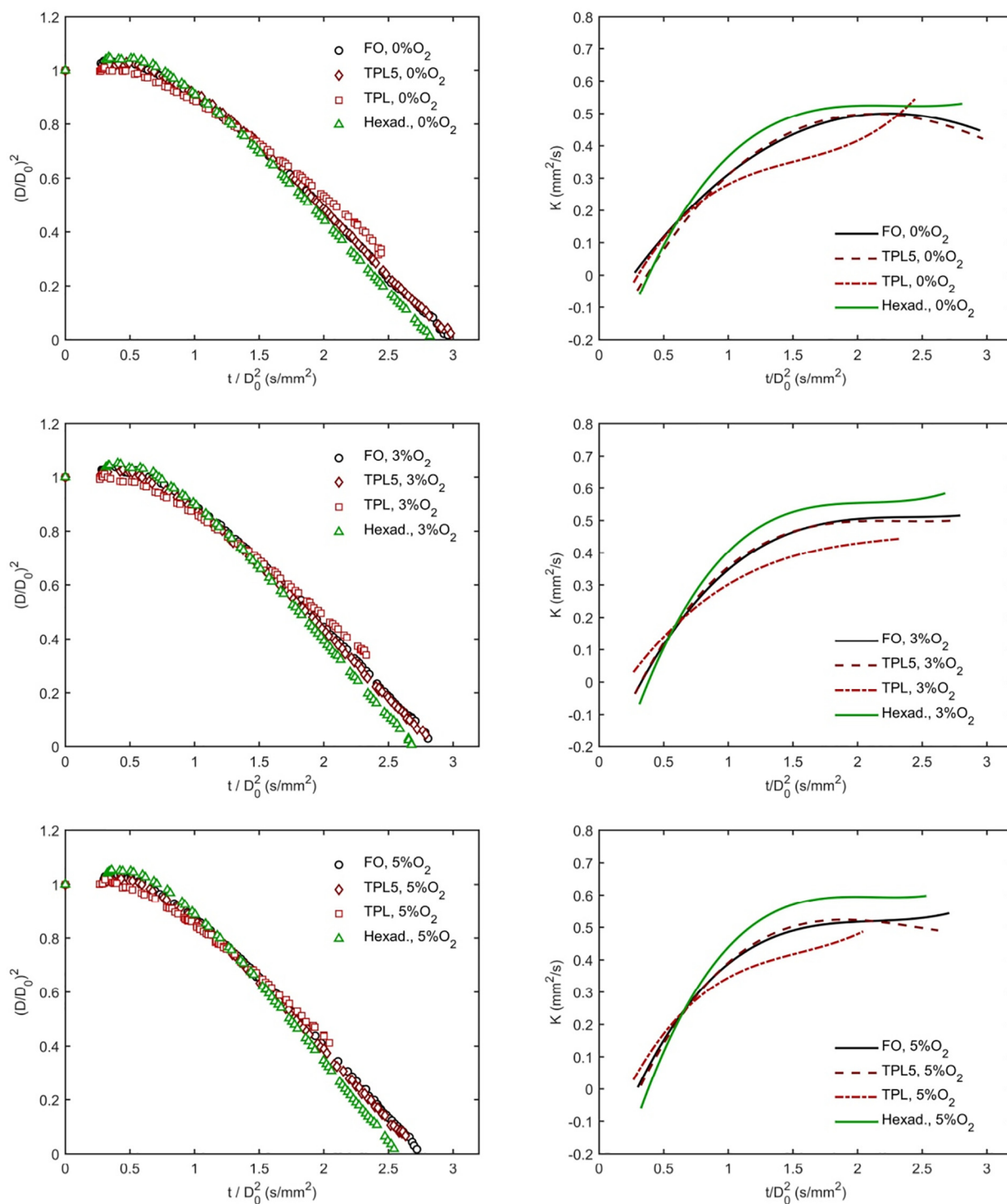
Fig. 5. Normalized droplet size and burning rate evolution for FO, TPL5, TPL and hexadecane at the three studied oxygen conditions.

Table 4
Observed intervals of microexplosion occurrence for TPL droplets.

	First microexplosion		Last microexplosion	
	$(D/D_0)^2$	t/D_0^2 (s/mm²)	$(D/D_0)^2$	t/D_0^2 (s/mm²)
0% O₂	0.40	2.3	0.33	2.4
3% O₂	0.44	2.1	0.34	2.3
5% O₂	0.51	1.8	0.41	2.0

registered for the three oxygen conditions, although with slight differences regarding the instant at which the droplets disintegrated. As stated above, microexplosions consistently occurred for TPL droplets, although this phenomenon could usually appear randomly within an interval of roughly 0.2 s/mm². Table 4 summarizes these intervals for the three studied oxygen conditions.

In addition to the presented results on droplet size and burning rates, the sooty flames captured by Camera 2 (Fig. 4) were also post-processed and analyzed to quantify their size evolution with time. The flame standoff ratio (FSR = D_f/D) is a widely used parameter in droplet combustion studies as a metric describing flame behavior. The
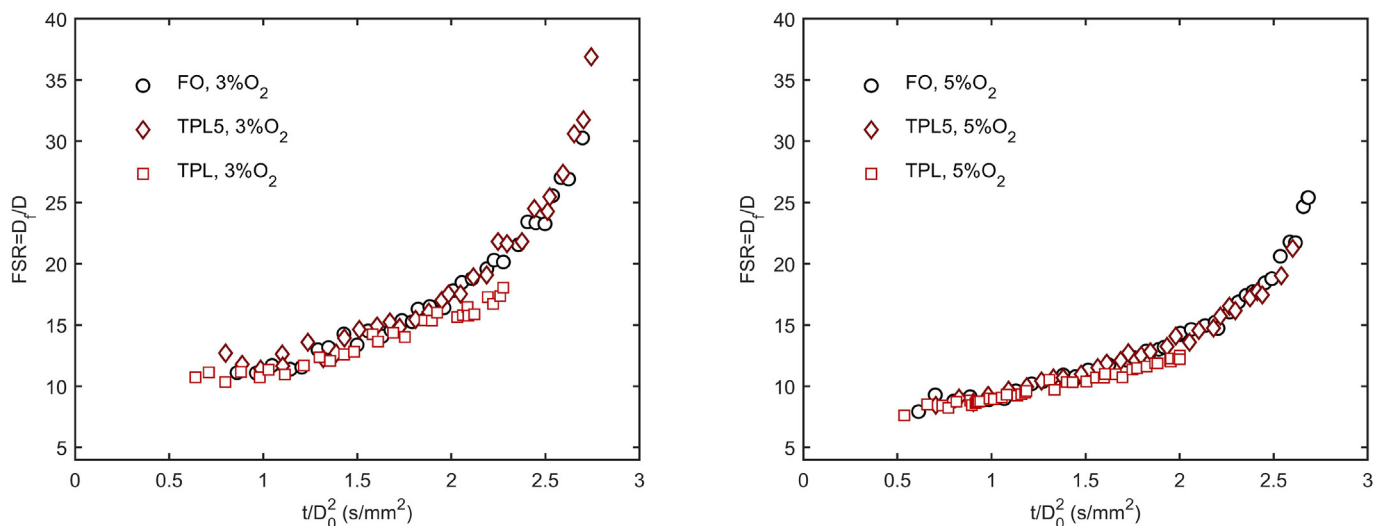
Fig. 6. Flame standoff ratio (D_f/D) evolution for all the studied fuels at the 3 and 5% O_2 condition.

measured FSR for both combustion conditions (3 and 5% O_2) are displayed in Fig. 6, showing a practically coincident behavior between heating oil and TPL5 for both oxygen conditions, whereas the pure pyrolysis oil displays a closer relative position of the flame to the droplet. The classical theory of droplet combustion dictates that the FSR is expected to be constant along the whole droplet combustion lifespan. Fig. 6, however, displays a steady increase of FSR with time. This experimental behavior is attributed to the accumulation of fuel vapor in the droplet's vicinity, effect which is enhanced when the oxygen fraction in the coflow is low [38]. When comparing both oxygen conditions, it is also worth noting that the first appearance of a measurable flame is delayed as the oxygen availability decreases, as it can be visually confirmed in Fig. 4.

3.3. Visual aspect and luminosity of flame traces

Besides the already presented droplet and flame pictures, long exposure images of the macroscopically visible flame streaks were captured with a color camera. These flame streaks are created by the combustion of the free-falling droplet stream, and they provide insight into the soot yielded for each fuel and condition, as incandescent soot radiates a characteristic luminosity. Fig. 7 compares the flame streaks

recorded for FO, TPL5, TPL and hexadecane (3% O_2 coflow condition), along with their extracted luminosity profiles.

For each long-exposure photograph, all pixels' values were added across a given cross section, providing thereby an axial evolution of luminosity for all the studied fuels. Even if the quantitative value of these results is not clear, the obtained profiles can be used to estimate relative differences in the soot yielded for various fuels at certain fixed and well know experimental conditions. It is important to note that the trace images displayed in Fig. 7 are significantly overexposed for a better visualization, and therefore the luminosity profiles were extracted from a different set of pictures, with much lower exposure values (namely, with higher f-stop numbers). The overexposure of the displayed images artificially enhances regions with very low signals, as it can be noted when comparing pictures and luminosity profiles. Whereas the images show noticeable luminosities throughout the displayed 100 mm, the signals recorded after 35 mm for TPL and after 50 mm for FO and TPL5 are negligible when compared with the upstream luminosity values, as demonstrated by the non-saturated profiles shown in Fig. 7.

The displayed pictures highlight clear differences among fuels, with hexadecane practically not showing any soot emission and FO, TPL5 and TPL presenting clear yellowish flame traces, as it was expected due
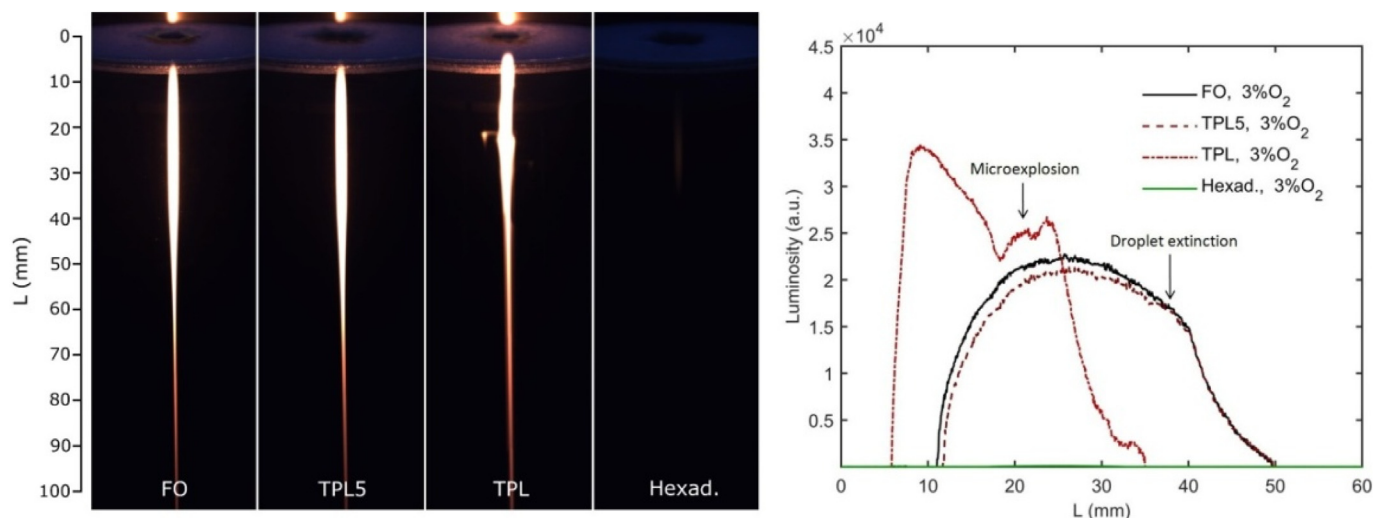

Fig. 7. Flame traces pictures and luminosity profiles for the 3% O_2 condition. The exposure time used in the displayed images is 200 ms (5 droplets injected during the exposure interval).

to their sooty behavior. Heating oil and TPL5 profiles can be considered to be alike, taking into account the qualitative kind of results that this optical method can provide. This similarity in luminosity profiles between FO and TPL5 is consistent with the already discussed identical behavior regarding soot shell appearance and thickness. Pure pyrolysis oil on the other hand, displays much higher luminosity values within the first millimetres after injection, in accordance with the earlier onset of soot shell illustrated in Fig. 2. This could point to a higher soot yield, particularly during the first stages of droplet combustion.

Another fundamental difference between the pure pyrolysis oil and the other fuels is microexplosion occurrence, as already stated. This difference can also be macroscopically observed in Fig. 7. Whereas FO and TPL5 profiles display a bell-shaped luminosity profile with a turning point in the region of droplet extinction, pure pyrolysis oil shows a bimodal, more abrupt profile, with the microexplosion location clearly marked by an increase in the registered soot emission.

4. Conclusions

This study used a continuous auger reactor on pilot scale (150 kWth of nominal capacity) in order to produce a tire pyrolysis liquid (TPL), which was later exhaustively characterized, including GC–MS analysis. As the intended use of the prepared TPL is its use in burners, its combustion characteristics were subsequently extracted by means of a droplet combustion facility. Single droplet combustion tests were performed to TPL, both pure and blended with conventional heating oil (5% TPL by weight). Neat heating oil and hexadecane were also studied.

All the examined droplet combustion characteristics (droplet size evolution, burning rates, flame standoff ratios, soot shells and flame luminosity profiles) were found to be practically identical for pure heating oil and TPL5, pointing to virtually indistinguishable combustion behaviors between both fuels. On the contrary, pure TPL showed an earlier onset of vaporization, ascribed to the lower boiling point of its lightest fractions as compared to those of heating oil. TPL also displayed significantly lower burning rates and flames located slightly closer to the droplet surface. Droplet microexplosions occurred consistently for droplet sizes in the order of $(D/D_0)^2 \approx 0.40$, effectively shortening the lifetimes of TPL droplets even below those of conventional heating oil. Although most of the recorded microexplosions effectively shattered the TPL droplets into small fragments, swelling and puffing events were alternatively observed in some cases. As droplets subjected to exactly the same conditions displayed both phenomena, this behavior is thought to respond to apparently random patterns. No correlation was found between microexplosion mode and oxygen availability, although it was determined that ambiences richer in oxygen promoted an earlier occurrence of these events. Neat TPL exhibited higher values of flame luminosity, pointing to a higher soot emission (and therefore a higher soot yield). This behavior is in accordance with the earlier onset of a distinguishable soot shell for TPL in comparison with heating oil and TPL5. No solid residue was found for any of the studied fuels or blends, although the occurrence of microexplosions for TPL hindered droplet tracking downstream the disintegration location.

The reported results are thought to contribute to the scarce available data regarding the combustion behavior of a well characterized tire pyrolysis oil. As the single droplet tests were performed under strictly controlled experimental conditions, which also intend to be representative of those found in real applications, the provided data could be used for the simulation of realistic spray flames as well as for the design of adapted combustion equipment.

Acknowledgements

References

[1] M. Sienkiewicz, H. Janik, K. Borzędowska-Labuda, J. Kucińska-Lipka, Environmentally friendly polymer-rubber composites obtained from waste tyres: a review, J. Clean. Prod. 147 (2017) 560–571.

[2] J.D. Martínez, N. Puy, R. Murillo, T. García, M.V. Navarro, A.M. Mastral, Waste tyre pyrolysis–a review, Renew. Sust. Energ. Rev. 23 (2013) 179–213.

[3] E.B. Machin, D.T. Pedroso, J.A. de Carvalho, Energetic valorization of waste tires, Renew. Sust. Energ. Rev. 68 (2017) 306–315.

[4] R. Singh, S. Mondal, B. Ruj, A. Sadhukhan, P. Gupta, Interaction of three categories of tyre waste during co-pyrolysis: effect on product yield and quality, J. Anal. Appl. Pyrolysis (2019), https://doi.org/10.1016/j.jaap.2019.05.007.

[5] C. İlkılıç, H. Aydın, Fuel production from waste vehicle tires by catalytic pyrolysis and its application in a diesel engine, Fuel Process. Technol. 92 (5) (2011) 1129–1135.

[6] T.-C. Chen, Y.-H. Shen, W.-J. Lee, C.-C. Lin, M.-W. Wan, An economic analysis of the continuous ultrasound-assisted oxidative desulfurization process applied to oil recovered from waste tires, J. Clean. Prod. 39 (2013) 129–136.

[7] I.I. Enagi, K. Al-Attab, Z. Zainal, Liquid biofuels utilization for gas turbines: a review, Renew. Sust. Energ. Rev. 90 (2018) 43–55.

[8] J.D. Martínez, N. Cardona-Uribe, R. Murillo, T. García, J.M. López, Carbon black recovery from waste tire pyrolysis by demineralization: production and application in rubber compounding, Waste Manag. 85 (2019) 574–586.

[9] J.D. Martínez, J. Rodríguez-Fernández, J. Sánchez-Valdepeñas, R. Murillo, T. García, Performance and emissions of an automotive diesel engine using a tire pyrolysis liquid blend, Fuel 115 (2014) 490–499.

[10] W.-C. Wang, C.-J. Bai, C.-T. Lin, S. Prakash, Alternative fuel produced from thermal pyrolysis of waste tires and its use in a DI diesel engine, Appl. Therm. Eng. 93 (2016) 330–338.

[11] K. Tudu, S. Murugan, S. Patel, Effect of diethyl ether in a DI diesel engine run on a tyre derived fuel-diesel blend, J. Energy Inst. 89 (4) (2016) 525–535.

[12] O. Doğan, M.B. Çelik, B. Özdalyan, The effect of tire derived fuel/diesel fuel blends utilization on diesel engine performance and emissions, Fuel 95 (2012) 340–346.

[13] S. Murugan, M. Ramaswamy, G. Nagarajan, Assessment of pyrolysis oil as an energy source for diesel engines, Fuel Process. Technol. 90 (1) (2009) 67–74.

[14] H. Aydın, C. Ilkılıç, Analysis of combustion, performance and emission characteristics of a diesel engine using low sulfur tire fuel, Fuel 143 (2015) 373–382.

[15] S. Frigo, M. Seggiani, M. Puccini, S. Vitolo, Liquid fuel production from waste tyre pyrolysis and its utilisation in a Diesel engine, Fuel 116 (2014) 399–408.

[16] T.-C. Chen, Y.-H. Shen, W.-J. Lee, C.-C. Lin, M.-W. Wan, The study of ultrasound-assisted oxidative desulfurization process applied to the utilization of pyrolysis oil from waste tires, J. Clean. Prod. 18 (18) (2010) 1850–1858.

[17] R. García-Contreras, J.D. Martínez, O. Armas, R. Murillo, T. García, Study of a residential boiler under start-transient conditions using a tire pyrolysis liquid (TPL)/diesel fuel blend, Fuel 158 (2015) 744–752.

[18] Y. Xu, C.T. Avedisian, Combustion of n-butanol, gasoline, and n-butanol/gasoline mixture droplets, Energy Fuel 29 (5) (2015) 3467–3475.

[19] T. Li, D. Zhu, N. Akafuah, K. Saito, C. Law, Synthesis, droplet combustion, and sooting characteristics of biodiesel produced from waste vegetable oils, Proc. Combust. Inst. 33 (2) (2011) 2039–2046.

[20] G. Kuznetsov, K.Y. Vershinina, T. Valiullin, P. Strizhak, Differences in ignition and combustion characteristics of waste-derived oil-water emulsions and coal-water slurries containing petrochemicals, Fuel Process. Technol. 179 (2018) 407–421.

[21] K.Y. Vershinina, N.E. Shlegel, P.A. Strizhak, Influence of the initial temperature of coal water slurries containing petrochemicals on their ignition characteristics, Appl. Therm. Eng. 138 (2018) 591–602.

[22] S. Yang, M. Wu, The droplet combustion and thermal characteristics of pinewood bio-oil from slow pyrolysis, Energy 141 (2017) 2377–2386.

[23] G.-B. Chen, Y.-H. Li, C.-H. Lan, H.-T. Lin, Y.-C. Chao, Micro-explosion and burning characteristics of a single droplet of pyrolytic oil from castor seeds, Appl. Therm. Eng. 114 (2017) 1053–1063.

[24] M. Garcia-Perez, P. Lappas, P. Hughes, L. Dell, A. Chaala, D. Kretschmer, et al., Evaporation and combustion characteristics of biomass vacuum pyrolysis oils, IFRF Combust. J. 200601 (2006) 1–27.

[25] C.R. Shaddix, D.R. Hardesty, Combustion Properties of Biomass Flash Pyrolysis Oils: Final Project Report (No. SAND99–8238), Sandia National Labs, 1999.

[26] C.R. Shaddix, P.J. Tennison, Effects of char content and simple additives on biomass pyrolysis oil droplet combustion, Symp. Combust. 27 (2) (1998) 1907–1914.

[27] E. Aylón, A. Fernández-Colino, R. Murillo, M. Navarro, T. García, A. Mastral, Valorisation of waste tyre by pyrolysis in a moving bed reactor, Waste Manag. 30 (7) (2010) 1220–1224.

[28] J.D. Martínez, M. Lapuerta, R. García-Contreras, Rn Murillo, T. García, Fuel properties of tire pyrolysis liquid and its blends with diesel fuel, Energy Fuel 27 (6) (2013) 3296–3305.

[29] E.R. Umeki, C.F. Oliveira, R.B. Torres, R.G. Santos, Physico-chemistry properties of fuel blends composed of diesel and tire pyrolysis oil, Fuel 185 (2016) 236–242.

[30] Á. Muelas, P. Remacha, J. Ballester, Droplet combustion and sooting characteristics

of UCO biodiesel, heating oil and their mixtures under realistic conditions, Combust. Flame 203 (2019) 190–203.

[31] M. Angeloni, P. Remacha, A. Martínez, J. Ballester, Experimental investigation of the combustion of crude glycerol droplets, Fuel 184 (2016) 889–895.

[32] Á. Muelas, P. Remacha, A. Martínez, J. Ballester, Combustion Behavior of Jet A Droplets and its Blends With Butanol. ASME Turbo Expo 2017, American Society of Mechanical Engineers, 2017 (V04ATA073).

[33] J. Ballester, C. Dopazo, Experimental study of the influence of atomization characteristics on the combustion of heavy oil, Combust. Sci. Technol. 103 (1–6) (1994) 235–263.

[34] J.M. Ballester, N. Fueyo, C. Dopazo, Combustion characteristics of heavy oil-water emulsions, Fuel 75 (6) (1996) 695–705.

[35] K.-L. Pan, J.-W. Li, C.-P. Chen, C.-H. Wang, On droplet combustion of biodiesel fuel mixed with diesel/alkanes in microgravity condition, Combust. Flame 156 (10) (2009) 1926–1936.

[36] National Center for Biotechnology Information, PubChem compound database, Available from https://pubchem.ncbi.nlm.nih.gov/compound/11006 , Accessed date: 29 May 2019.

[37] S.-S. Hou, F.M. Rizal, T.-H. Lin, T.-Y. Yang, H.-P. Wan, Microexplosion and ignition of droplets of fuel oil/bio-oil (derived from lauan wood) blends, Fuel 113 (2013) 31–42.

[38] C. Law, S. Chung, N. Srinivasan, Gas-phase quasi-steadiness and fuel vapor accumulation effects in droplet burning, Combust. Flame 38 (1980) 173–198.

energy&fuels

Article

Properties and Combustion Characteristics of Bio-Oils from Catalytic Co-Pyrolysis of Grape Seeds, Polystyrene, and Waste Tires

Álvaro Muelas,* Diego Aranda, María Soledad Callén, Ramón Murillo, Alberto Veses, Mohamad Asrardel, and Javier Ballester

Read Online

ACCESS | 📊 Metrics & More | 📖 Article Recommendations | 🆂🅸 Supporting Information

ABSTRACT: This work aims to study the bio-oils obtained from the catalytic co-pyrolysis of waste polymers and a residual biomass (grape seeds, GS). For that purpose, the organic liquid fractions produced in an auger reactor were thoroughly characterized in two steps, obtaining in the first place their main physicochemical properties as well as their chemical compositions, and second, their droplet combustion behaviors. Both the polymer type (waste tires or polystyrene, WT and PS, respectively) and the nature of the low-cost, calcium-based catalyst used (Carmeuse limestone, calcined dolomite, or an inert material such as sand) were studied. A significant improvement in the physicochemical properties of the bio-oils was obtained when using a catalyst, with lower viscosity, density, and oxygen content. These beneficial effects were more marked for the bio-oil produced with the Carmeuse catalyst, presumably due to the higher prevalence of aromatization and hydro-deoxygenation reactions. When changing the polymer source from WT to PS, a considerable increase in the aromatic content and a viscosity reduction were noted. The droplet combustion tests revealed the consistent occurrence of microexplosions for all of the studied bio-liquids, these bursting events being more violent for the GS—PS oil. Regarding the evaporation behavior, this liquid also yielded significantly higher burning rates during the initial heat-up phase, in agreement with its richer composition in volatile compounds such as styrene. These results point to this fuel as the one with the best global combustion behavior from all of the explored bio-oils. The GS—WT liquids showed much closer features among them, although with noticeable differences depending on the catalyst used. A more volatile behavior was observed for GS—WT Carmeuse, followed by GS—WT dolomite and GS—WT sand, strengthening thus the previously reported improvements in physicochemical properties. Finally, the propensity to form soot of these bio-oils was characterized through a soot probe, which revealed a higher soot yield for the bio-liquids produced with the Carmeuse catalyst.

1. INTRODUCTION

The use of biomass as a feedstock in a pyrolysis process is a well-known and promising technology to reduce the current dependence on fossil fuels while also being a renewable and carbon-neutral energy source.[1,2] The pyrolysis of biomass yields biochar, gases, and vapors[3] that after cooling can be condensed into a liquid product known as bio-oil or, alternatively, pyrolysis liquid or pyrolysis oil. Bio-oil has been extensively studied in the literature, either as a standalone fuel or as a mixture, in diverse applications such as boilers, furnaces, diesel engines, or even turbines (e.g., see refs 4—6). Studies regarding computational simulation of waste and biomass pyrolysis have also been carried out in different types of reactors.[7—9] However, some bio-oil properties imply important drawbacks, which severely hinder their use in many combustion applications:[2,3,10,11] high acidity and corrosivity, low heating value (LHV), high water content, immiscibility with conventional fuels, and high viscosity. Moreover, bio-oils typically display a significant content of solid particles and a bad storage behavior due to aging. Most of these undesirable properties arise from the high oxygen content of the fuel, which generally ranges between 35 and 60 wt %.[2] It would be most desirable, therefore, to remove the oxygenated compounds, upgrading the bio-oil properties. Different upgrading strategies, such as hydro-deoxygenation, fast catalytic pyrolysis,

hydrogenation, catalytic cracking, and molecular distillation, are considered to be promising technologies, which can overcome these challenges.[12,13]

An alternative strategy to obtain an upgraded bio-oil is the co-pyrolysis of biomass with other carbon-rich wastes, such as waste tires or plastics, allowing for the production of a stable oil.[14] Recent reviews such as refs 2 and 15 provide valuable information on this technology, which can produce a better quality fuel when compared with the traditional fast pyrolysis of neat biomass, primarily because of the much lower oxygen content and higher heating value of these co-pyrolysis liquids.[13,16] A further advantage of this approach is that the polymer wastes used as a feedstock in the pyrolysis plant are valorized through this process. This is especially beneficial for the case of using waste tires, as they pose a major environmental problem due to the huge number of end-of-life tires produced every year (in the range of 1 billion units worldwide[17]), the technical difficulties involved in their

recovery and recycling,[18] and the high risks associated with their disposal in landfills (which, in fact, is banned in the European Union in accordance with the Council Directive 1999/31/EC).

In spite of these advantages, the bio-oils obtained through co-pyrolysis of biomass and waste polymers still require further upgrading to be considered as drop-in fuels for most combustion applications.[13,19] A significant improvement of the oil properties can be obtained when using a suitable catalyst within the co-pyrolysis process. This strategy appears to be a promising option for upgrading the bio-liquids while keeping the production process in a single step, as it is detailed in recent reviews such as refs 19 and 20. In fact, the use of low-cost calcium-based catalysts has been studied by this group for the catalytic co-pyrolysis of grape seeds and two different waste polymers (waste tires and polystyrene) in previous works, both in a lab-scale reactor[21,22] and in a technology readiness level 5 (TRL-5) auger reactor.[13,23] The encouraging results obtained in these studies support this technology for obtaining high-quality bio-oils with a heating value comparable to that of conventional fossil fuels and very low oxygen content, suitable thus for direct use in certain combustion applications.

Since the main final use of these bio-oils is their energetic valorization, an assessment of their combustion characteristics is thought to be a valuable addendum to the more standard physicochemical analysis. For that purpose, the isolated droplet configuration has proven to be a useful benchmark for gaining knowledge on the combustion behavior of liquid fuels. The simplicity of this setup, with a single, isolated liquid droplet burning under fixed and well-characterized conditions, allows for a precise knowledge of all of the relevant parameters that affect the process. In comparison with the much more complex configurations occurring in real applications such as engines or boilers, this simplicity greatly facilitates the analysis of the underlying physics in fundamental studies, as well as allows for a precise characterization of the combustion behavior for different fuels in more applied works. This approach has been used in the literature for evaluating the combustion characteristics of many conventional and alternative fuels, such as diesel and biodiesel,[24,25] kerosene and aviation bio-fuels,[26] or gasoline and butanol,[27] among many others. For the case of bio-oils, it can be said that most of the effort has been directed to study the droplet combustion characteristics of liquids produced through conventional pyrolysis of lignocellulosic biomass. Extensive studies by Shaddix et al.[28,29] explored the droplet combustion behaviors of a wide variety of flash pyrolysis liquids obtained from different feedstock (pine, oak, poplar, etc.). They obtained consistent microexplosions (i.e., a burst of the liquid droplet due to internal vaporization), which effectively shortened the droplet life span. However, the burning rates were significantly lower than those of a fuel oil no. 2, as it would be expected in light of the bio-oil properties displayed in ref 28. It is noteworthy that these studies were performed in a drop tube facility, where the 350 μm droplets were heated and ignited in free fall, without the influence of a suspending fiber, which could promote heterogeneous nucleation of the vapors inside the droplet. A similar setup, although with considerably smaller droplets (in the range of 60 μm), was used by Garcia-Perez et al.[30] for evaluating the combustion characteristics of biomass vacuum pyrolysis liquids. Similarly to refs 28 and 29, the bio-oil burning rates were noticeably lower than those of a fuel oil no. 2, but in this case, the authors did not observe complete microexplosions,

reportedly because of the lower heating rates and smaller droplet sizes. Interestingly, Garcia-Perez et al.[30] studied the formation of residual carbonaceous solids, with sizes that could even surpass that of the initial droplet diameter. On the other hand, Shaddix et al. highlighted in ref 28 the important role of the reported microexplosions in reducing or even eliminating the production of coke cenospheres, which can be highly problematic for many combustion applications. Other single-droplet works such as refs 31−33 relied on the suspended droplet technique, with puffing and bubbling phenomena rather than the proper microexplosions reported in refs 28 and 29. It is important to note, therefore, that the experimental conditions used in the droplet combustion tests can significantly modify the observed behaviors.

As pointed out, bio-oils produced through conventional pyrolysis show wide differences in chemical composition and properties when compared with liquids obtained by means of more novel technologies. A previous work[34] highlighted these differences for a tire pyrolysis liquid (TPL), which was found to display a much quicker conversion than the aforementioned bio-oils, with microexplosions and burning rates comparable to those extracted for a Spanish heating oil (i.e., fuel oil no. 2). To the best of the authors' knowledge, this kind of droplet combustion characterization has not been performed for co-pyrolysis liquids of biomass and waste polymers. In light of the promising results of this technology to yield high-quality and upgraded bio-oils, this study aims to evaluate the main combustion characteristics of different liquid fractions yielded from the catalytic co-pyrolysis of grape seeds and two kinds of waste polymers (residual tires and polystyrene). In doing so, this work intends to provide data regarding the single-droplet combustion behavior of these novel fuels under experimental conditions close to those occurring in real flames. Additionally, the effect of the catalyst used in the co-pyrolysis process will be also assessed, namely by comparing the droplet combustion behaviors of three bio-oils obtained under exactly the same experimental conditions, with the only change of the catalyst. Two different calcium-based catalysts will be tested for this purpose, in addition to a reference case where no catalyst was used in the co-pyrolysis. Besides the more common droplet combustion characteristics, such as the droplet and flame size evolution curves or the burning rates, the experimental results will also report complementary behaviors, which are thought to be of special relevance for this kind of fuels, such as the occurrence and typology of microexplosions, the potential formation of carbonaceous solid residues, and a quantification of the soot yielded for each oil under high temperature and reducing conditions.

2. MATERIALS AND METHODS

2.1. Biomass, Waste Materials, and Catalysts. The biomass used was grape seeds (GS) (*Vitis vinifera*), a residue from the wine industry of the north-east area of Spain. Prior to its use, it was dried by reducing moisture content below 2 wt %. Regarding the waste materials, two different feedstocks were utilized. On the one hand, polystyrene (PS) (Acteco Productos y Servicios S.L.), which was obtained from food packaging and, on the other hand, rubber produced in the shredding of passenger car tires (WT), which was received in granulated form, without the steel thread and textile netting. It is worth mentioning that the particle sizes of the three materials were similar, around 2−4 mm.

The main properties (proximate and ultimate analysis and heating value) of the different feedstocks are summarized in Table 1. The proximate analysis of the raw material was determined according to

Table 1. Main Properties of Grape Seeds (GS), Polystyrene (PS), and Waste Tires (WTs)

|	GS[a]	PS[a]	WT[a]
moisture (wt %)	6.3	0.3	0.9
ash (wt %)	4.3	0.9	7.0
volatile matter (wt %)	65.1	98.4	63.0
fixed carbon (wt %)	24.3	0.4	29.3
ultimate analysis (wt %)			
C	53.9	92.1	84.1
H	6.6	7.75	7.4
N	2.2	0.12	0.5
S	0.1	0.0	1.7
O	37.2	0.03[b]	3.4
HHV (MJ/kg)	22.1	41.1	37.3
LHV (MJ/kg)	20.5	39.4	35.7

[a]As received (air-dried basis). [b]Calculated from the ultimate analysis by difference.

UNE-EN ISO 18134-3, UNE-EN ISO 18122, and UNE-EN ISO 18123 for moisture, the proportion of ashes, and the volatile matter, respectively. The fixed carbon was calculated by difference. The ultimate analysis of the different materials was determined according to UNE-EN 5104 in a Thermo Flash 1112, and the oxygen content was obtained by difference. The calorific value (LHV) was measured experimentally using an IKA-2000 calorimetric pump according to the Spanish standard procedure UNE 164001 EX. As it can be observed in Table 1, remarkable differences among the three raw materials were observed. Whereas GS were characterized by a high oxygen content (37.2 wt %), involving a low LHV (20.5 MJ/kg), WT and PS showed a high carbon content and a low oxygen content, implying heating values similar to or even higher than those obtained from fossil fuels.

In this study, two different calcium-based catalysts (particle size distribution ranged between 300 and 600 μm) obtained from the calcination at 900 °C of limestone (Carmeuse) and dolomite were selected based on their low cost, environmental friendliness (CO_2 capture effect inherent to these catalysts), and reusability nature. Both low-cost catalysts were commercially available and were purchased through different private companies located in Spain. These catalysts have been previously described[13,23] by the following techniques: X-ray diffraction (XRD), N_2-physisorption, mercury porosimetry,[35,36] temperature-programmed desorption of ammonia (NH_3-TPD), temperature-programmed desorption of carbon dioxide (CO_2-TPD),[37] and inductively coupled plasma-optical emission spectroscopy (ICP-OES). Detailed information about catalyst properties can also be found in the Supporting Information (Tables S.1 and S.2).

In this research, two different variables that affect the catalytic co-pyrolysis of biomass and waste polymers were studied. First, the influence of the polymer type was assessed performing co-pyrolysis experiments with GS−WT and GS−PS (80:20 mass ratio for the two feed mixtures). Process conditions were identical for both feedstocks, and the same catalyst was used (Carmeuse). In addition, the influence
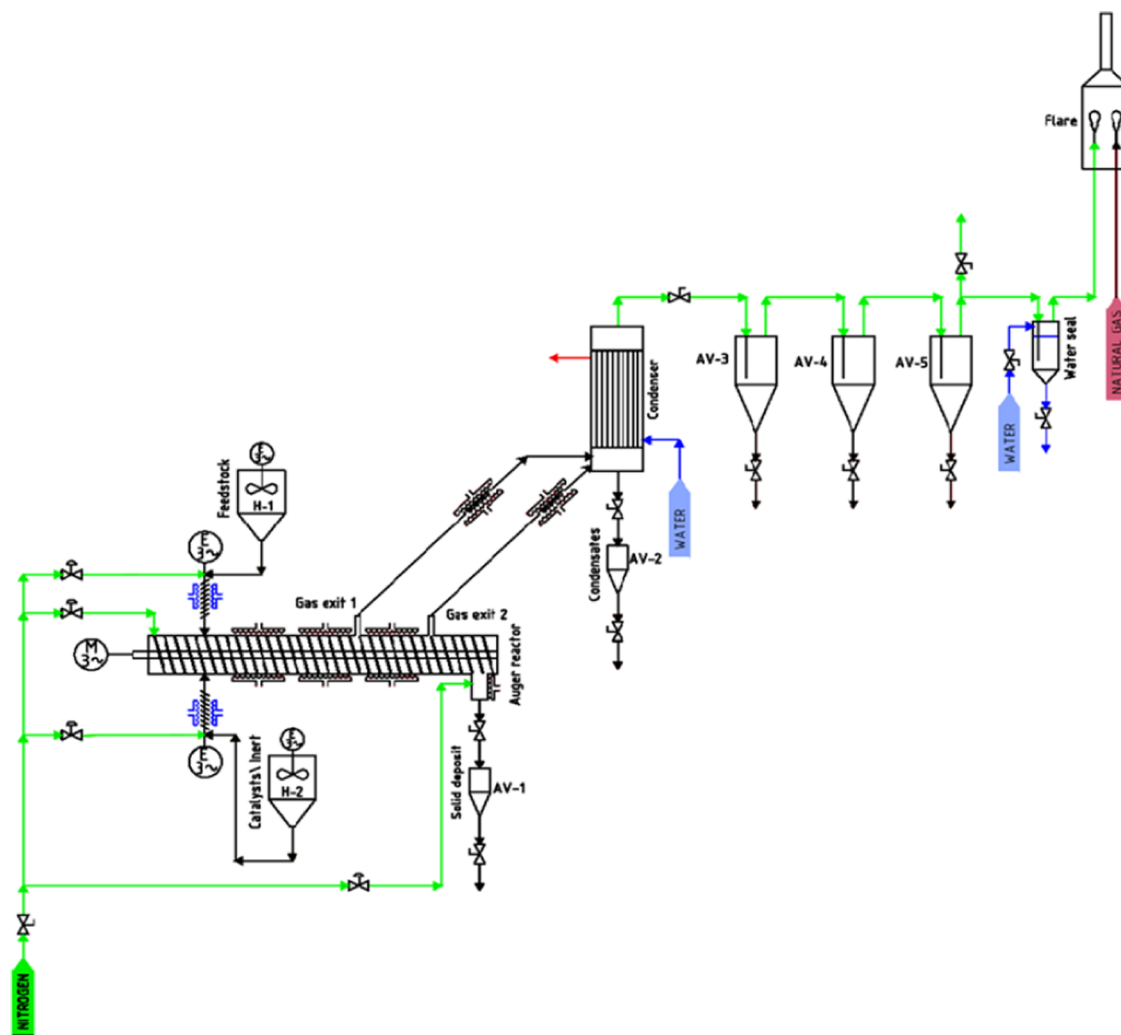
Figure 1. Process flow drawing of the pilot plant used for catalytic co-pyrolysis experiments.
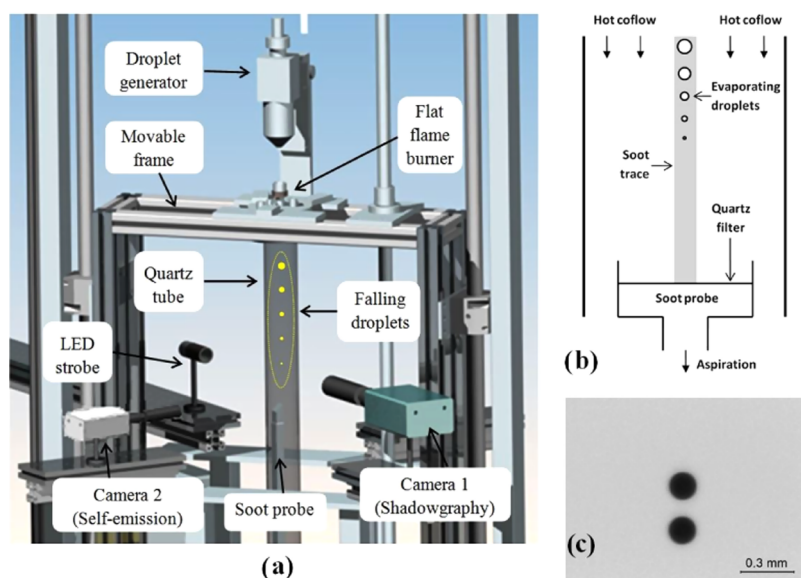
Figure 2. Droplet combustion facility (DCF) scheme, displaying its main components (a); diagram depicting the soot probe operation (b); double-exposure photograph of a free-falling GS–PS oil droplet (c).

of catalyst nature was also studied, performing three tests with the same feed mixture (GS–WT mixture, 80:20 mass ratio) and using the two low-cost catalysts (Carmeuse and dolomite) (fuel to catalyst ratio, 2:1 mass basis) as well as sand (particle size distribution between 2 and 6 mm), which acted as a blank reference to ascertain the effect of not using any catalyst.

2.2. Pilot Plant. All experiments were performed in a pyrolysis pilot plant (100 kW$_{th}$) consisting of an auger reactor working at atmospheric pressure, using N$_2$ as the carrier inert gas, with a feedstock feeding of 2 kg/h at 550 °C. The duration of each experiment was set at 2 h, and the solid residence time was 7 min. To guarantee the repeatability of the tests, two runs were performed, ensuring a relative standard deviation (RSD) <5%. Extended information about the pilot plant can be found elsewhere.[13] Briefly, two independent stirred hoppers provided with screw feeders regulate the mass flow of the different feedstocks (Figure 1). One of them is used to feed the mixture composed of GS and waste polymer and the other one feeds the low-cost catalyst. Prior to the experiments, the feeding was carefully mixed and then was added to the hopper, ensuring a good homogeneity. Based on the maximum deoxygenation rate reached in the organic fraction, a feedstock-to-catalyst ratio of 2 was fixed for catalytic tests. Particularly, the catalysts were diluted with sand, keeping a (sand + catalyst)-to-feedstock ratio of 3:1. This stock of solids has been calculated as the minimum amount of heat carrier required for a self-sustainable process from an energy perspective.[38,39] Three independent electrical resistances surrounding the reactor provide the energy needed for the pyrolysis process. In addition, a control and acquisition system allowed monitoring 4 pressure transducers and 10 thermocouples located in strategic points of the pilot plant. While the remaining solid after pyrolysis is collected in a closed hopper, the released gas leaves the reactor and is conducted to a condenser where the pyrolytic oil is collected. The noncondensable gas is cleaned and conducted to a flare. All conversion products but gas are weighed and stored in closed containers or bottles under inert conditions for further use and analysis.

2.3. Product Characterization. The three conversion products (liquid, solid, and gas) obtained after the co-pyrolysis experiments were characterized. Because details regarding the gas and solid fractions have been previously reported,[13,23] this research was mainly focused on the liquid fraction analysis and use. Hence, the liquid fraction was a heterogeneous sample composed of two differentiable phases: organic and aqueous. These phases were separated after centrifugation at 2000 rpm for 10 min and further decanted (organic phase at the top and aqueous phase at the bottom). The organic

phase was analyzed, according to standard methods, to determine different physicochemical properties. The ultimate composition (Carlo Erba EA1108), calorific value (IKA C-2000), water content by Karl Fischer titration (Crison TitroMatic) according to ASTM E 203-96, pH (Mettler Toledo T50), and density (gravimetric method) were determined in triplicate.

The chemical composition of the organic phase was obtained by using gas chromatography coupled to mass spectrometry (GC-MS) (Varian CP-3800 gas chromatograph and a Saturn 2200 ion trap mass spectrometer). A CP-Sil 8 CB low-bleed capillary column composed of 5% phenyl and 95% dimethylpolysiloxane was used (60 m, i.d. 0.25 mm, film thickness 0.25 μm). The injected samples were subjected to the following temperature/time program: 40 °C for 4 min and a heating rate of 4 °C/min until reaching a final temperature of 300 °C for 21 min. BIP-quality helium was used as the carrier gas at a constant column flow of 1 N mL/min, and the respective temperatures for the injector, source, and transfer line were 280, 200, and 300 °C. In all cases, 1 μL of sample was injected, where 1:25 wt % was mixed with CH$_2$Cl$_2$/C$_2$H$_6$O (1:1 vol). A split ratio of 25:1 and a solvent delay of 6.4 min were applied. Electron ionization mode at 70 eV and a range of 35–550 m/z was operated by the MS. Individual peaks were identified with the 2011 NIST library, and each peak was quantified according to the corresponding m/z by normalization area (area of each peak versus the total area) to finally group compounds by different families. The samples were injected by duplicate, and relative standard deviations for the different families varied between 0.15 and 17%.

2.4. Droplet Combustion Facility (DCF). After production and characterization of the different co-pyrolysis liquid fractions, their most relevant evaporation and combustion features were explored by means of single-droplet combustion tests. These tests were performed on a drop tube rig developed at LIFTEC and described in detail in a previous work.[40] A scheme depicting the main elements of the setup is presented in Figure 2.

A stream of free-falling droplets was generated in a piezoelectric device, which achieved initial nominal diameters (d_0) of 150 μm and a separation between consecutive droplets always greater than 100 diameters. This separation, in combination with the low relative velocity droplet coflow, ensured that each droplet remained unaffected by the others during its whole life span. The hot coflow was provided by a McKenna premixed flat-flame burner, the free-falling droplets being directly introduced within its combustion products by means of an injection orifice passing through the sintered burner plug. Once surrounded by this hot coflow, the droplets

Table 2. Properties of the Organic Fractions after the Noncatalytic and Catalytic Co-Pyrolysis Processes[a]

experiment	properties				elemental analysis (wt %)					
	H_2O (wt %)	pH	viscosity (mPa·s)	density (g/mL)	C	N	H	S	O	LHV (MJ/kg)
GS−WT (80:20) sand	1.07 ± 0.1	9.5	16.3 ± 0.8	1.11	83.6 ± 0.9	2.6 ± 0.2	9.5 ± 0.2	0.4 ± 0.02	3.9 ± 0.2	38.8 ± 1.2
GS−WT (80:20) Carmeuse	0.62 ± 0.1	9.1	3.5 ± 0.2	0.91	87.0 ± 0.8	2.5 ± 0.1	9.6 ± 0.2	0.4 ± 0.02	0.5 ± 0.1	40.7 ± 1.5
GS−WT (80:20) dolomite	0.76 ± 0.1	9.1	5.6 ± 0.3	0.98	84.9 ± 0.4	2.8 ± 0.2	10.0 ± 0.1	0.6 ± 0.03	1.8 ± 0.2	40.1 ± 1.4
GS−PS (80:20) Carmeuse	0.74 ± 0.1	8.7	2.3 ± 0.1	0.94	88.6 ± 0.6	1.8 ± 0.1	8.5 ± 0.1	0.1 ± 0.01	1.0 ± 0.1	40.9 ± 1.6

[a]LHV = lower heating value.

evaporated and burned along a cylindrical quartz combustion chamber axis. The burner was fed with methane, and air in different proportions depending on the oxygen availability desired in the coflow. As this work intends to study the evaporation and combustion behavior of the different oils under conditions as representative as possible of those occurring in final applications such as boilers, a realistic environment was sought in terms of both gas temperature and composition. Thus, three different oxygen levels were used for this study, namely, a pure evaporation condition (i.e., 0% O_2) and two combustion cases, with 3 and 5% O_2 (vol, dry basis) in the coflow. The first condition was obtained through the burning of a stoichiometric mixture of methane and air at the flat-flame burner, whereas for the latter cases, a slight air excess was employed to yield unburned O_2 in the flue gas. The temperature profiles for these three conditions can be found in Appendix C of the Supporting Information of ref 40 where it can be observed that most of the droplet evolution occurs under gas temperatures of the order of 1600−1700 K.

The droplet evaporation and burning processes were recorded by means of three different optical setups, each of them aiming to capture different features. A backlit charge-coupled device (CCD) camera (QImaging Retiga SRV, camera 1 in Figure 2a) fitted with a telemicroscope was used to obtain the droplet size and velocity by working through the double-exposure technique, as displayed in Figure 2c. This kind of picture was processed in Matlab to extract the data in an accurate and repeatable way. Additionally, a complementary metal oxide semiconductor (CMOS) camera (Hamamatsu C11440-36U; camera 2 in Figure 2a) recorded the diffusion flame formed around each droplet, as will be shown in Section 3.2. A third optical setup captured the macroscopic flame traces created by the free-falling droplets, as will also be displayed in Section 3.2. This rig consisted of a Teledyne DALSA Genie Nano C4060 fitted with a NIKKOR 18−105 mm f/3.5−5.6G ED lens.

Besides exploring the evaporation and burning behaviors of the different oil samples, their propensity to form soot was also characterized through a particle sampling probe. This probe was developed and described in detail in ref 41, and therefore, only its main features are summarized here. A scheme depicting its operation is presented in Figure 2b, where it can be observed that the probe collects all of the soot particles, which are formed along the droplet life span. To prevent soot oxidation, these tests were always performed at the 0% O_2 condition, and therefore, the collected soot particles correspond to the pyrolysis of the fuel's vapors within an inert, hot coflow, which allowed soot formation but inhibited its consumption. The soot agglomerates were retained on a quartz microfiber filter, which was subsequently dried at 110 °C for over 24 h. The weighing of the dried filter with and without soot provided the soot mass collected during the test. Due to the small amount of soot weighed, special care was taken to prevent that room humidity could affect the results, as it was found that the quartz filter was hygroscopic. For that reason, the weighing procedure was performed inside a controlled-humidity room, with relative humidity levels always in the order of 15%. The analytical scale used was a Sartorius CP225D with a repeatability of ±20 µg. As introduced in ref 41, a soot index named isolated droplet soot yield (IDSY) and expressing the weight of soot produced per unit of injected fuel was obtained for each oil, providing

therefore a quantitative metric regarding their propensity to form soot.

3. RESULTS AND DISCUSSION

3.1. Properties and Chemical Composition of the Organic Fractions. Although the main aim of this research was focused on studying the combustion of the organic fractions, it was also interesting to relate them with the properties and the chemical composition based on two different effects: on the one hand, the influence of the catalyst on the co-pyrolysis GS−WT with an inert heat carrier like sand and with two different low-cost catalysts: Carmeuse lime and dolomite; on the other hand, the influence of two different waste materials, WT and PS, in the co-pyrolysis with GS, using the same catalyst: GS−WT Carmeuse and GS−PS Carmeuse. The main properties of the organic fraction for the different samples and catalysts are shown in Table 2.

Table 2 shows how the water content of the organic fraction depends on the catalyst type for the same co-pyrolysis mixture GS−WT. A decrease in the water content is observed with the Carmeuse catalyst compared to that of the noncatalytic process, whereas very similar results were obtained with the other catalyst, dolomite. This is directly related to the promotion of dehydration reactions by materials containing calcium with poor total basicity and pure CaO crystalline phase without impurities.[13] According to the characterization techniques, the Carmeuse catalyst was a high-purity material composed of CaO in a high percentage, 95 wt %, whereas dolomite was mainly formed by CaO (47.6 wt %) and MgO (33.2 wt %).[13] In addition, a lower total basicity of the Carmeuse catalyst (0.04 mmol CO_2/g at 550 °C) compared to that of the dolomite catalyst (0.11 mmol CO_2/g at 598 °C) would also justify the higher reduction in the water content. It was also observed that the addition of CaO in the co-pyrolysis of GS and WT rubber produced a remarkable decrease of the oxygen content (Table 2) compared to the noncatalytic process, sand. This fact corroborated the CaO dehydration capacity and the improvement of the organic phase by using this catalyst.[13,23] Therefore, an increase of the heating value was reached, confirming that the co-pyrolysis of GS and WT rubber (80:20) with this Carmeuse catalyst provided better quality bio-oils.

When the same catalyst was compared for a different co-pyrolysis feedstock (GS−WT versus GS−PS), quite similar results were obtained for both. This could be justified by the similar nature of the materials, as WT is a copolymer of styrene and butadiene.

The influence of the catalyst on the viscosity (see Table 2) for the GS−WT experiments showed that both calcium-based catalysts produced a remarkable decrease on this property

Table 3. Chemical Composition of the Organic Fractions Analyzed by GC-MS in the Co-Pyrolysis and Catalytic Co-Pyrolysis Processes[a]

experiment	aromatics	olefins	linear HC	cyclic HC	phenols	esters	ketones	fatty acids	others
GS−WT (80:20) (sand)	64.5	2.7	0.4	23.6	5.0	0.8	0.1	1.0	1.8
GS−WT (80:20) (Carmeuse)	70.9	2.3	0.9	16.0	1.4	1.5	2.1	1.6	3.6
GS−WT (80:20) (dolomite)	58.0	5.0	1.8	18.1	3.9	2.9	3.9	2.5	4.0
GS−PS (80:20) (Carmeuse)	96.9		0.2		0.3	0.4	0.8	0.2	1.2

[a]HC: hydrocarbons.
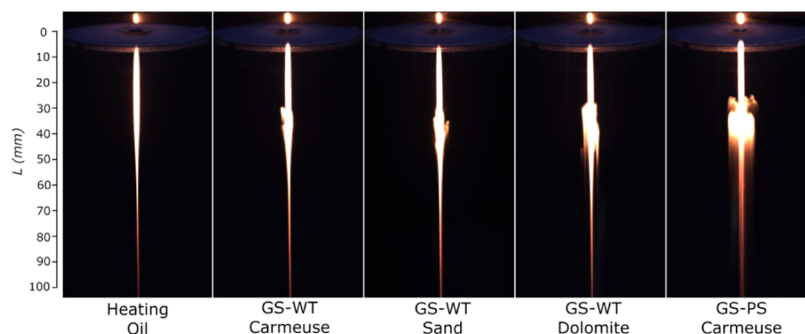
Figure 3. Long-exposure flame traces pictures captured for all fuels at the 3% O_2 coflow. The exposure time for all images is 200 ms (five droplets injected during the exposure interval).

compared to sand, this effect being most considerable for Carmeuse. When the influence of the waste material on the viscosity was compared, it was observed that lower viscosity was obtained for the co-pyrolysis of GS and PS than for the GS and WT mixtures using the same catalyst, Carmeuse, indicating that this polymer, PS, improved the quality of the oil obtained versus the WT. As the bio-oil viscosity is widely dependent on the feedstock and pyrolysis conditions,[42,43] this improvement in the viscosity for the co-pyrolysis experiments could be explained based, on the one hand, on the feedstock (PS consists of volatile matter and almost no fixed carbon (Table 1), whereas that WT is made of styrene−butadiene copolymer, natural rubber, and polybutadiene) and, on the other hand, on the nature and chemical composition of the bio-oils as shown in the next paragraphs.

According to the composition of the organic phase using GC-MS, a semiquantitative identification of the compounds (relative area percentage) was carried out, as shown in Table 3. A total of nine different families were identified for the co-pyrolysis of GS−WT rubber without catalyst (sand) and independently of the catalyst used. These families were aromatics, olefins, linear hydrocarbon HC, cyclic HC, phenols, esters, ketones, fatty acids, and others. The aromatics constituted the group with higher percentage, the main compounds[13] being styrene, ethylbenzene, toluene, xylene, and benzene.[13]

The effect of the catalyst on the composition of the organic phase was reflected on the reduction of cyclic HC compared to the experiment with no catalyst (sand). In addition, an increase in the ketone family was observed. The Carmeuse catalyst increased the aromatic content compared to dolomite and to the noncatalyst experiment (sand), indicating that this type of catalyst promoted the aromatization and hydro-deoxygenation through ketonization and esterification reactions[13] producing a highly aromatic bio-oil and enhancing the potential use of the bio-oil as a source of chemical products or as a drop-in fuel.

When the comparison was based on the type of waste material used, WT and PS, it was observed that the GS−PS co-

pyrolysis produced mainly aromatics,[22] with a low contribution of the other families (linear HC, phenols, esters, ketones, fatty acids, and others). With regard to the aromatic compounds, styrene, ethylbenzene, and toluene were the main compounds identified in the organic fraction (see Table S2, Supporting Information in ref 23), all of them being low-molecular-weight aromatic compounds. As previously mentioned, these results could have a remarkable impact on the further use of this liquid, not only as a drop-in fuel but also as a source of chemical products. The thermal scission of PS, linked to the promotion of H_2 transfer reactions, and the CaO effect, mainly attached to the dehydration and decarboxylation effects, seemed to justify the reduction of phenols and esters through the hydro-deoxygenation route, being more remarkable in the case of GS−PS compared to the GS−WT Carmeuse experiment, obtaining a richer aromatic and more deoxygenated liquid. In addition, this effect was more remarkable in the case of GS−PS versus GS−WT due to the pure nature of the PS, whereas WT is composed of styrene−butadiene copolymer, natural rubber, and polybutadiene. This composition for both the GS−PS and the GS−WT bio-oils with the Carmeuse catalyst, associated with more low-molecular-weight components, could also explain the lowest viscosity obtained[44,45] and the synergetic positive effects due to the presence of plastics and calcium-based catalyst. At this point, the great improvement of bio-oil properties and chemical composition after the catalytic process should be remarked. Thus, some of the main properties aforementioned were similar to those found for other commercial liquid fuels such as diesel.[46]

3.2. Droplet Combustion Results. This section aims to explore the single-droplet combustion behavior of each fuel by means of the droplet combustion facility (DCF) described in Section 2.4. Besides the already presented four co-pyrolysis oils, this study will also include results for heating oil, which is considered a good representative of conventional fossil fuels used in many industrial and residential applications. This fuel was thoroughly characterized in previous works, where its main
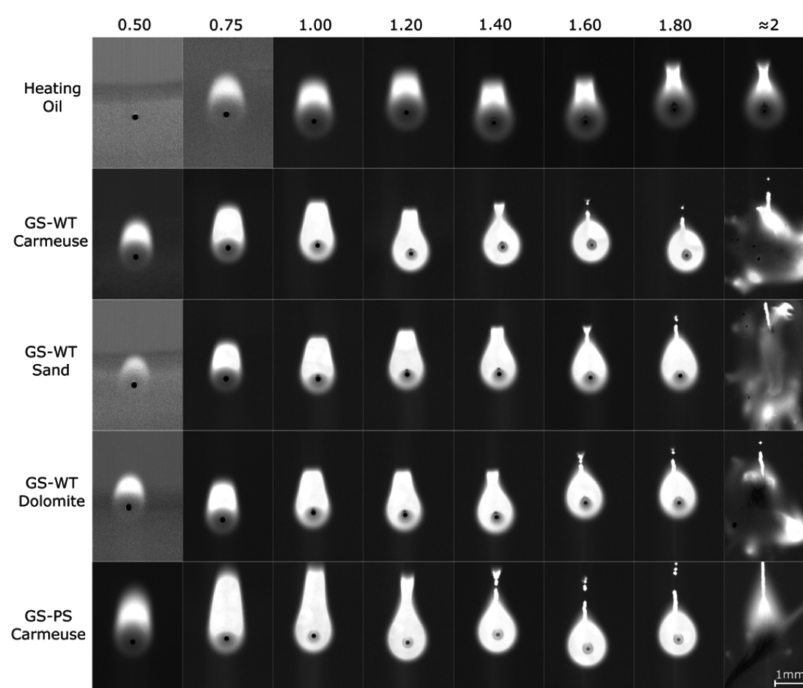
Figure 4. Individual droplets surrounded by their diffusion flames captured for all fuels at the 5% O_2 condition. The images are organized in accordance with their normalized time after injection: t/d_0^2 (s/mm^2).

isolated droplet characteristics were explored in detail[40] and even some surrogates were formulated to match them.[41] As the organic fractions obtained in this work are primarily intended for their burning in applications such as boilers, their comparison with heating oil seems appropriate, putting into perspective the behavior of these oils when compared with a well-characterized reference baseline. This fuel was the only one whose droplet evaporation experiment was repeated to check for the procedure repeatability. As detailed in ref 40, the comparison of both experimental runs yielded differences of 0.5% in droplet burnout times and 0.7% in time-averaged evaporation rates.

3.2.1. Droplet, Flame, and Trace Images. As it was described in Section 2.4, most information regarding the droplet combustion process is extracted from different optical setups. The first kind of pictures corresponds to the flame traces captured with a color camera operating with a long-exposure time. Since all of the studied fuels yield a significant amount of soot when exposed to the high-temperature conditions applied at the DCF, these images display bright and orangish streaks caused by the black body radiation emitted from incandescent soot particles. The exposure time of these images is several times longer than the droplet generation period (40 ms), and therefore, the integrated luminosity of multiple droplets is accumulated in the image, creating the flame traces that are presented in Figure 3 for all fuels at the 3% O_2 condition.

A first substantial difference can be noted in Figure 3 between heating oil and the rest of fuels. Whereas the former displays a smooth luminosity profile throughout all of the combustion chamber, the four co-pyrolysis oils show abrupt microexplosions around 30 mm after the injection point. These microexplosions, which will be studied in detail later on in this same section, completely shattered the droplets, causing a second atomization, which can be noted in Figure 3 as an irregular broadening of the sooty luminous area. Among the

four co-pyrolysis oils, GS−PS Carmeuse displayed the most violent microexplosions for all of the oxygen conditions, with soot agglomerates being propelled further away from the combustion chamber's centerline. On the other hand, the three oils obtained from GS and WT yielded similar microexplosion intensities, although with slight differences regarding their occurrence point, as will be detailed below. It is worth to note that these relative behaviors were maintained regardless of the O_2 condition explored.

The second kind of images are those captured with camera 2 (Figure 2a), which aimed to record the individual envelope flames that surrounded the droplets. As was discussed in a previous work,[40] the black body radiation emitted from soot particles is considerably more intense than the chemiluminescence emission from electronically excited radicals such as OH* or CH*, which are the most broadly accepted light-emitting species when it comes to establishing the flame position.[47−49] Given the high sooting tendency of the fuels studied here, soot emission heavily predominated in this kind of images, and therefore, it would be more correct to speak of soot clouds rather than flame pictures. Soot particles are formed on the inner side of the shell flame, and therefore, the light emission from excited radicals produced in chemical reactions would be located slightly further away from the droplet. In spite of this, and given the difficulty to capture this weak chemiluminescence emission for sooty fuels, several droplet combustion studies have indirectly estimated the flame position from the sooty emission (e.g., refs 24 and 25). This will also be the case in this work, as its main objective is to obtain relative differences among the different bio-liquids, the same kind of sooty flames being captured (and measured) for all of them. A representative selection of these envelope flames is displayed in Figure 4 for all fuels under the 5% O_2 condition. The pictures are arranged in terms of their residence time normalized by the initial droplet diameter squared (t/d_0^2), as it
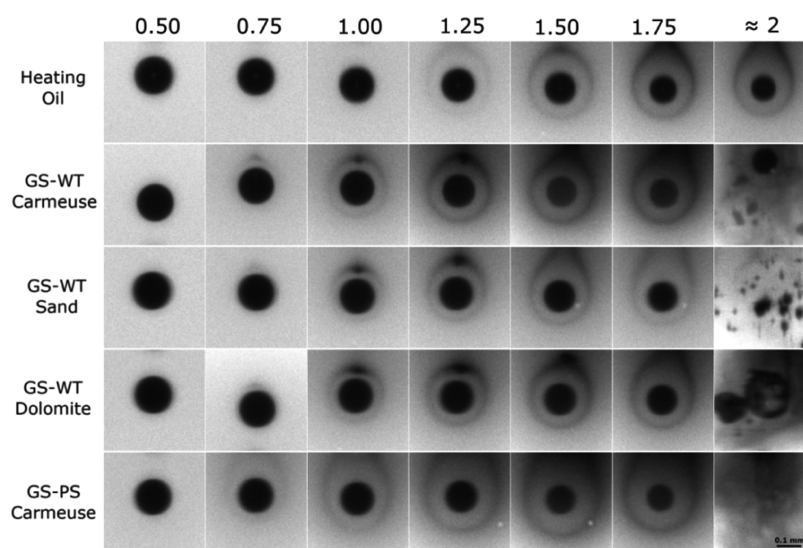
Figure 5. Individual droplets surrounded by soot shells for all fuels at the 5% O$_2$ condition. The images are cropped from the original double-exposure photographs and organized in accordance with their normalized time after injection: t/d_0^2 (s/mm^2).

is common practice in the droplet combustion literature to minimize the differences arising from slight variations in d_0.

Envelope flames in Figure 4 show distinct behaviors among fuels. The first and more obvious one is the occurrence of microexplosions for all of the co-pyrolysis liquids around 2 s/mm^2 after injection, whereas heating oil displays a smooth evaporation until droplet depletion, as is noticed in Figure 3. Regarding the onset of the flame, GS−PS Carmeuse displays a clearly more intense sooty emission already at 0.50 s/mm^2, followed by the GS−WT oils. No emission can be observed at that time for heating oil, whose ignition is in general delayed with respect to all pyrolysis oils. This points to a more volatile behavior of the GS−PS lighter fractions, which evaporate and ignite earlier than the rest of the fuels. Likewise, GS−WT Carmeuse would ignite slightly earlier than GS−WT dolomite and GS−WT sand, as inferred by the higher signal-to-noise ratio of its first picture (i.e., the flame appears brighter and less noisy, whereas the background shifts to a darker tone after the contrast enhancement procedure). These observations concerning droplet ignition are consistent with the earlier onset of a flame trace in Figure 3.

Figure 4 also provides some qualitative information regarding the sooting propensity of each fuel. Even though quantitative data will be provided in the next section, it seems interesting to analyze these features to prove if they are consistent with the subsequent soot probe measurements. For any given residence time, the GS−PS oil displays a more intense light emission. This envelope flame luminosity becomes brighter than that due to the backlight used with camera 2, and therefore, the liquid droplet becomes progressively eclipsed (as it can be observed by the clearer shade of the droplet). Additionally, GS−PS pictures display the longest soot trail for a given residence time while also showing an earlier clustering of the soot trail's particles into thicker agglomerates. These soot agglomerates appear to exit the diffusion flame, forming an elongated soot tail, which lags behind the free-falling droplet. The residence time when this clustering event happens is different for each fuel: GS−PS is the first one (1.40 s/mm^2), followed by GS−WT Carmeuse, GS−WT dolomite, and GS−WT Arena. Heating oil shows the onset of this soot clustering event only in its last picture ($\approx$2 s/

mm^2). Ranking the fuels according to this feature appears to provide very similar results as when sorting them in terms of sooty luminosity or even in soot trail length for a given residence time. This fact would suggest a higher soot yield for all of the co-pyrolysis oils when compared with that of heating oil, pointing also to noticeable differences among them. These qualitative observations will be validated below with quantitative soot yield measurements.

The third kind of pictures obtained at the DCF are the backlighted, double-exposure droplet images captured with camera 1 (Figure 2). The main aim of these pictures is to characterize the droplet size evolution, as will be detailed in the next section. However, through these close-up images, it is also possible to obtain valuable information regarding interesting phenomena such as microexplosion occurrence or the tendency to form soot particles. These two features can be observed in Figure 5, where a set of representative droplet images are presented according to their normalized residence time for all fuels at the 5% O$_2$ condition.

An interesting characteristic shared by all fuels in Figure 5 is the appearance of nearly spherical soot shells surrounding the droplets. As discussed in previous works (e.g., refs 34 and 40), the apparition of these soot shells is quite infrequent for droplet combustion tests at normal gravity, being generally a feature explored in experiments under microgravity conditions such as refs 24, 26, and 27. However, the droplet sizes and small slip velocities applied in this work significantly reduced natural and forced convection effects, allowing for the formation of these structures (as detailed in ref 40). The regions with a greater density of soot particles in Figure 5 reveal the places where the inwardly directed thermophoretic force is balanced by the outward viscous drag. As can be noticed in Figure 5, the resulting soot shells are considerably spherical, pointing to a configuration close to spherical symmetry in the vicinity of the droplet. The influence of natural or forced convection on the evaporation results presented in this work is thus expected to be negligible, which greatly facilitates comparison with one-dimensional (1-D) droplet evaporation and combustion models (as assessed in Appendix A of the Supporting Information of ref 40 for a set of tests performed under the same experimental conditions). It is
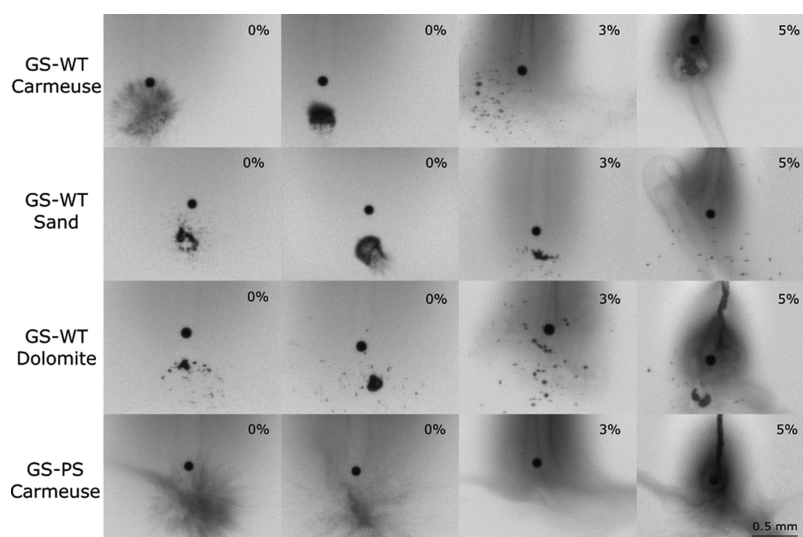
Figure 6. Double-exposure pictures of individual droplets microexploding for the bio-oils evaporating and burning under all oxygen conditions (O_2 level indicated for each image).

also worth mentioning that these soot shells only occur under oxidizing atmospheres, being absent in the pure evaporation case (the lack of an envelope flame lowers thermal gradients, causing much weaker thermophoretic forces). Likewise, the higher the O_2 availability in the coflow is, the stronger thermophoresis becomes, yielding thicker and more spherical soot shells (e.g., see ref 40).

On the other hand, it is also clear that, contrary to droplet combustion works under strictly controlled microgravity conditions, in the current study, not all of the soot particles are gathered at the radial equilibrium location, even for the 5% O_2 case depicted in Figure 5. The occurrence of a small slip velocity, in addition to buoyancy, tends to drag soot particles toward the trails analyzed in Figure 4. This fact has the advantage of clearing the camera view from an excessive amount of soot particles, which could hinder droplet identification and measurement (as, for example, occurred in ref 26 for a kerosene). The analysis of the soot shells presented in Figure 5 should, however, take into account this soot leakage toward the droplet wake, complicating an assessment of the soot tendency based on the shell's thickness. If this leakage is assumed to be similar among fuels, the soot shells presented in Figure 5 would indicate a considerably lower soot production for heating oil in comparison with the co-pyrolysis liquids, as the soot shell onset is considerably delayed for this fuel.

Consistently with Figures 3 and 4, another main difference noted in Figure 5 between the studied fuels is the occurrence of microexplosions for all of the pyrolysis oils, whereas heating oil droplets evaporate smoothly until liquid depletion. This bursting feature will be explored in detail through a collection of representative double-exposure images in Figure 6 for all of the fuels that showed this phenomenon.

Each of the 16 double-exposure pictures arranged in Figure 6 was captured with a delay between shots of 500 μs, and therefore, it can be considered that during that short time lapse the parent droplet evolves from a completely spherical shape to a collection of smaller droplets created through a second atomization process caused by the sudden internal vaporization of the lighter bio-oil fractions. To the best of the authors' knowledge, this kind of result is novel for liquid fuels obtained through the co-pyrolysis of a biomass residue (GS) and waste

polymers (WT and PS). When comparing the microexplosion images displayed in Figure 6 with those available in the literature for pyrolysis oils produced from biomass and waste tires, it seems clear that the droplet combustion experimental setup plays a relevant role. The sudden droplet breakups in Figure 6 show similarities with those reported at the same experimental facility for a tire pyrolysis liquid (TPL) in ref 34 or with the bio-oils tested in ref 28 under a similar drop tube setup where unsupported, free-falling droplets were also exposed to a high-temperature gaseous coflow. On the other hand, most of the experimental results available in the literature for bio-oils were obtained in setups where the droplet was attached to a solid filament. In these kinds of studies (e.g., refs 31−33), the microexplosion typology was reported to be quite different. Internal bubbling and puffing events swelled the droplet but were not enough to trigger a second atomization into many child droplets, as was noticed in the drop tube tests. In this regard, the influence of the solid filament (which can act as a heterogeneous nucleation site), as well as the larger droplets typically used in suspended droplet studies, is thought to be relevant regarding the occurring microexplosion typologies.

When comparing among the different co-pyrolysis oils in Figure 6, it seems clear that most of the reported microexplosions shattered the parent droplet, although with varying degrees of success. All of the fuels were exposed to exactly the same experimental conditions, and therefore, the different modes of microexplosions can be attributed to differences in the oil composition and properties. GS−PS displayed more intense microexplosions, in most occasions the parent droplet being atomized into a fine spray, without a hint of any relevantly sized child droplet. This differential behavior is consistent with the more violent disruption event displayed in the flame traces of Figure 3.

The oils obtained from co-pyrolysis of GS and WT, on the other hand, displayed on average less violent secondary atomizations, the liquid mass being dispersed in a poorer manner for all of them compared to GS−PS. As a result, in Figure 6, it is possible to observe relatively big subdroplets, which could even be measured from these pictures. These kinds of microexplosions for GS−WT oils are quite similar to
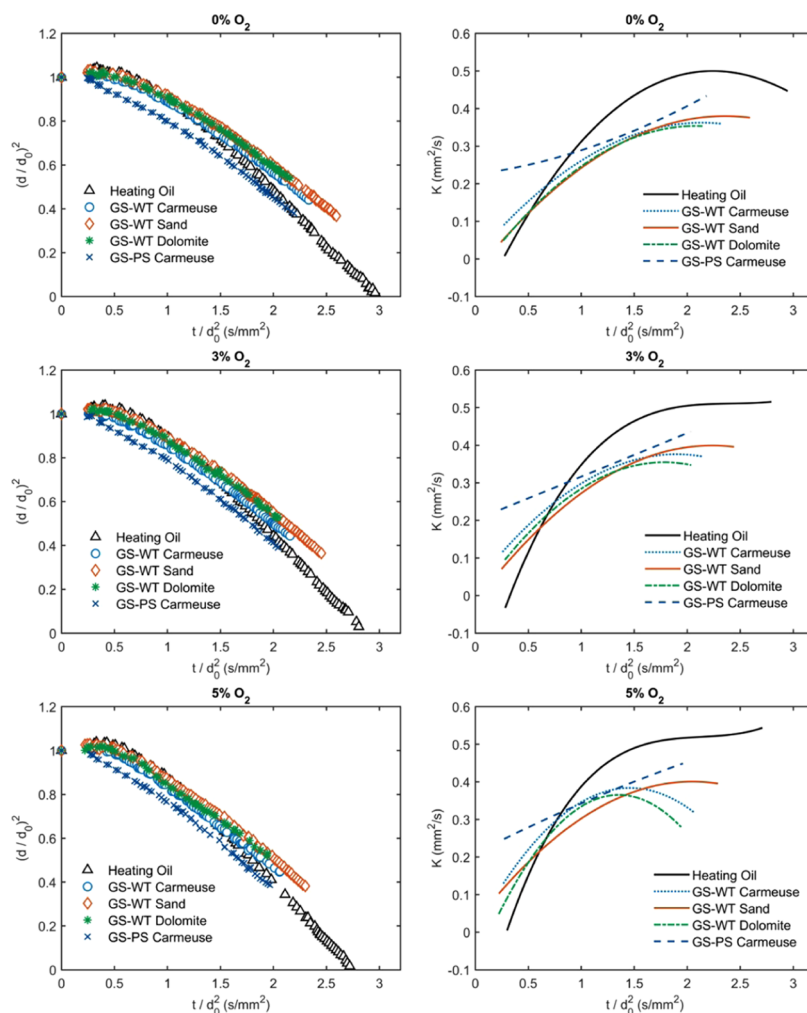
Figure 7. Normalized droplet size (left) and burning rate (right) evolution curves for all of the fuels at the three studied oxygen conditions.

those presented in ref 34 for a TPL. As was reported in that previous work, no correlation was observed between the mode of microexplosion and the oxygen availability in the coflow (the pictures presented in Figure 6 correspond indistinctly to 0, 3, and 5% O_2 conditions). Thus, the differences noted in Figure 6 for a given fuel appear to follow random patterns. This can be clearly noticed, for instance, for GS−WT Carmeuse, which shows an atomization spectrum ranging from a very efficient microexplosion (comparable to that described for GS−PS) to a situation more similar to a swelling and puffing event. These wide differences in the microexplosion mode for a given fuel at a fixed condition underscore the importance of stochastic aspects in this process, which become even more important for small-sized droplets such as those used in this study.[50]

3.2.2. Quantitative Data. As detailed in Section 2.4, the images recorded with cameras 1 and 2 (Figure 2) were processed to quantify the main combustion characteristics of the studied fuels in the most repeatable manner. The evolution of droplet size with time and the burning rate are presented in Figure 7 for the three oxygen conditions studied in this work (0, 3, and 5%). As introduced before, the first one corresponds to a pure evaporation case under oxygen-free and high-temperature conditions, whereas the other two study the droplet combustion at oxygen levels, which are representative of real combustion conditions in boilers (as it can be observed,

e.g., in the oxygen maps experimentally measured in ref 51). Results in Figure 7 are normalized by the initial droplet diameter (d_0), so that any small difference in d_0 between runs is minimized. Droplet size evolution curves are presented in the left column in terms of the normalized square diameter versus normalized time, whereas the burning rates ($K = -d(d^2)/dt$) are displayed in the right column, also in terms of normalized time. The K values were calculated by fitting the $d^2−t$ curves to a polynomial function, which was subsequently derived with respect to time, yielding the temporal evolution of the burning rate. The fitting was performed through a least-squares regression, with the polynomial order being chosen as the minimum that allowed us to correctly capture the data trend without introducing numerical artifacts unrelated to the problem physics (i.e., order 3 for the pyrolysis oils and 4 for heating oil).

As can be observed in Figure 7, all of the studied fuels show a steady decrease in droplet size until a complete liquid depletion for heating oil or until a sudden interruption occurs in the experimental curves for the pyrolysis liquids. This sudden interruption indicates the instant of droplet bursting, which consistently occurred for all of the pyrolysis oils as described in Figure 6. Similarly to the reported data for a tire pyrolysis liquid in ref 34, the instant of microexplosion was not completely fixed but occurred randomly within an interval of the order of 0.1−0.2 s/mm². In that sense, the last
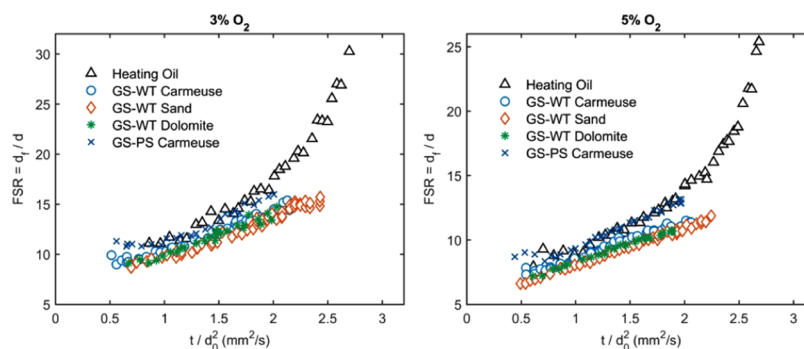
Figure 8. Flame standoff ratio evolution curves for all fuels at both combustion conditions.

experimental point for each run in Figure 7 corresponds to the last axial position where complete (and measurable) droplets were found.

Heating oil, on the other hand, displays a more conventional evaporation behavior, with an initial droplet heating-up phase followed by a quasi-steady evaporation stage. During the first one, the liquid increases its temperature without practically any mass loss due to the low vapor pressure of heating oil when cold (the distillation curve of this fuel was experimentally measured in ref 41, with an initial distillation point of 233 °C). This droplet heating without significant evaporation causes a slight increase in the droplet size during that first region since the liquid density decreases with temperature. As the temperature increases, the onset of a strong evaporation starts to significantly reduce the droplet size, and the droplet progressively transitions toward the quasi-steady phase predicted by the well-known d^2-law. This transition can be better noticed in the $K-t$ plot, where the burning rate of heating oil steadily increases until reaching a quite constant value.

The droplet evaporation behavior for the bio-oils reveals significant differences when compared with that of heating oil. In light of the heavy fragmentation incurred by the droplets at the bursting instant (Figure 6), it is expected that a total conversion of all of the pyrolysis liquids occurs before that of heating oil. Even for low-efficiency microexplosions, where certain child droplets still display a relevant size, the strong dependency of evaporation time on droplet diameter (consumption times scale with the squared diameter) implies that the total conversion is expected to occur close to the microexplosion instant. On the other hand, all of the pyrolysis oils (and particularly GS−PS) appear to display higher evaporation rates during the initial heating-up stage, which does not show the thermal volumetric expansion noted for heating oil. This would mean a higher vapor pressure in cold conditions, as probably these liquids contain light fractions with relatively low boiling points. In spite of this faster evaporation onset, pyrolysis liquids increase their burning rates at a slower pace than heating oil, their quasi-steady burning rate values also being lower. However, as previously noted, the occurrence of a secondary atomization greatly enhances the liquid conversion through a sudden increase in the gas−liquid contact surface.

When comparing among the different pyrolysis liquids in Figure 7, GS−PS Carmeuse shows the most differential behavior, with a substantial higher evaporation during the initial stage (i.e, higher K values for short residence times). This would point to a richer composition in compounds with

low boiling point when polystyrene is used as polymer source in comparison with waste tires. However, the increase in K is slower than for GS−WS oils, the burning rates being relatively similar in the final stages prior to the microexplosion.

A comparison between the evaporation curves for GS−WS liquids reveals small differences among them, the effect of the catalyst used in the co-pyrolysis process being clearly less influential than that of the polymer feedstock. The GS−WT liquids also display quite similar evaporation behaviors to those reported in ref 34 for a tire pyrolysis oil. This result was not initially expected, as the liquids evaluated in the current work are obtained by a co-pyrolysis of only 20% in mass of waste tires with 80% of grape seeds. In spite of the relatively small differences noted among GS−WT liquids, it is noteworthy that the product obtained when Carmeuse was used as a catalyst shows a noticeable faster conversion, followed by GS−WT dolomite and GS−WT sand. Relevant differences were also noted when it comes to the microexplosion occurrence size, with GS−WT dolomite bursting at slightly larger normalized droplet sizes than GS−WT Carmeuse. The co-pyrolysis liquid obtained without any catalyst (GS−WT sand) displayed a slower conversion as well as a more delayed microexplosion onset (i.e., the break-up occurred for smaller droplet sizes).

On a final note regarding the evaporation characteristics, it is also worth to mention that all of the trends and behaviors extracted from Figure 7 are maintained for all of the studied oxygen conditions, keeping the same relative behaviors between fuels irrespective of oxygen availability in the coflow. On the other hand, when comparing a given fuel at different oxygen conditions, it is clear that the enhanced heat transfer due to the apparition of the diffusion flame accelerates the evaporation process, significantly increasing the burning rates.

In addition to the evaporation characteristics, the sooty envelope flames recorded by means of camera 2 (Figure 2) and displayed in Figure 4 were also postprocessed, and their flame size (d_f) was extracted for both combustion conditions. As it is common in the droplet combustion literature, these results are presented in Figure 8 in terms of the flame standoff ratio (FSR = d_f/d) evolution with normalized residence time.

The FSR values presented in Figure 8 point to noticeable differences among the studied fuels, with wider flames for heating oil and smaller ones for the GS−WT liquids. This result is consistent with ref 34, where a tire pyrolysis oil was found to display envelope flames closer to the droplet surface than those of heating oil. GS−PS Carmeuse, on the other hand, shows FSR values intermediate between those of heating oil and GS−WT. For all of the studied fuels, the flame standoff ratio shows a sustained growth with the droplet residence time,

in disagreement with the classical droplet combustion theory (which predicts a constant FSR value). This feature is caused by the fuel vapor accumulation effect, described in ref 52 and enhanced for low oxygen availabilities such as those occurring in the current work. A comparison for a given fuel at both oxygen conditions reveals, as expected, an approaching of the flame front to the droplet surface when increasing the O_2 availability in the gaseous coflow, in addition to a lower uncertainty in the experimental data (i.e., lower scattering) due to an improved image quality.

Finally, the soot probe method described in Section 2.4 was applied for all of the fuels, obtaining for each of them their corresponding isolated droplet soot yield (IDSY), defined in ref 41 as the soot produced per unit of fuel mass injected under fixed DCF evaporation conditions (150 μm droplets evaporating and pyrolyzing in 0% O_2 coflow). Samples of the particles collected on the filter were analyzed under a scanning electron microscope (SEM) to check that the weighed solids corresponded entirely to soot agglomerates and not to other solids, which could potentially be formed in the process (e.g., coke particles). A visual analysis of these SEM samples corroborated that virtually all of the collected solids are indeed soot agglomerates, without any hint of carbonaceous residues formed through liquid-phase reactions. The soot collection tests were repeated at least three times for each fuel, so that a measure of the experimental uncertainty could be estimated. The average IDSY obtained for each fuel is presented in Figure 9, along with uncertainty bars calculated as twice the measurements' standard deviation (σ).
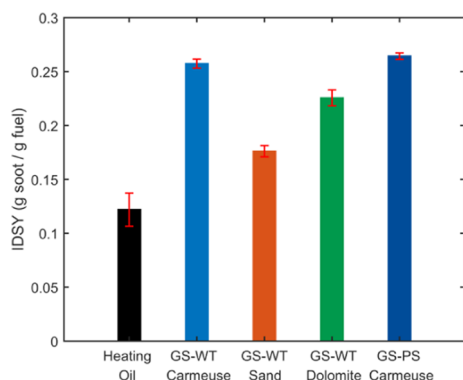

Figure 9. Isolated droplet soot yield (IDSY) obtained for each fuel through the aspirating soot probe tests. The uncertainty bars indicate ±2σ of the experimental measurements.

The quantitative results presented in Figure 9 are quite consistent with the qualitative observations in Section 3.2.1. As suggested in Figure 4 by the more luminous shell flames, the longer soot trails, and the earlier clustering of these trails into thick agglomerates observed for GS−PS Carmeuse, Figure 9 confirms that this oil showed the highest propensity to form soot. This result is also consistent with the GC-MS analysis presented in Table 3, where it was shown that this oil displays the largest amount of aromatic compounds (96.9%). On the other hand, GS−WT Carmeuse appears to produce a soot yield quite close to that of GS−PS, even if its aromaticity is noticeably lower (70.9%). It is, however, worth to note that the distribution of single- and multiringed aromatics plays a major role in the soot yielded by a fuel, as there are wide differences between the sooting tendency of single-ringed aromatics and

that of multiringed (e.g., see ref 53). Thus, it could be possible that even if GS−WT Carmeuse has a considerably lower total aromatic fraction, it has a higher multiring/single-ring ratio. This fuel was also found in Figure 4 to display the second longest soot trails as well as the second earliest clustering of these soot trails into agglomerates. The latter observation seems to concur remarkably well with the soot probe results for all of the studied fuels, as it can be observed by comparing Figures 9 and 4. The GS−WT oil produced without any catalyst (GS−WT sand) yielded the lowest amount of soot among all of the co-pyrolysis oils, with GS−WT dolomite displaying an ISDY value in between those of GS−WT Carmeuse and sand. All of these liquids yielded a significant higher soot weight when compared with heating oil, as can be corroborated in Figure 9. This is ascribed to the noticeably higher aromatic content of the co-pyrolysis liquids (58.0−96.9% according to Table 3 vs only 26.2% in heating oil, as presented in ref 41).

4. CONCLUSIONS

In this work, different bio-oils were produced in an auger reactor, aiming to study both the effect of changing the polymer type in the feedstock and the nature of the catalyst for a given biomass−polymer ratio. The physicochemical analysis performed to these organic fractions concluded that the introduction of a catalyst significantly decreased the liquid viscosity and density, this effect being more marked when using Carmeuse than when employing dolomite. GS−WT Carmeuse also displayed a noticeable lower oxygen content than GS−WT dolomite and GS−WT sand, as well as a lower water fraction. This is thought to be caused by the CaO dehydration capacity, which also enhances the heating value of the liquids obtained with this catalyst. Regarding the chemical composition, the introduction of the Carmeuse catalyst increased the aromatic content compared to dolomite and sand, as a result of aromatization and hydro-deoxygenation reactions. From these data, the use of a catalyst (and, more specifically, the Carmeuse type) seems to significantly improve the bio-liquid characteristics. The second variable of study was the polymer type. In this regard, the main difference between GS−WT Carmeuse and GS−PS Carmeuse was the considerably higher aromatic content and the viscosity reduction when using PS as polymer source. This is thought to be caused by the thermal scission of PS, which seemed to heavily reduce phenol and ester contents through the hydro-deoxygenation route in GS−PS compared to that in GS−WT.

The second part of this study analyzed the main droplet combustion characteristics of the aforementioned liquids. The main characteristic of all of the bio-oils studied is the occurrence of microexplosions, which achieved in most cases a second atomization of the droplet. This feature is beneficial for liquid conversion in the combustion chamber, as it significantly shortens the droplet life span even below that of a conventional heating oil. Among the four studied liquids, the larger differences were found when changing the polymer source. Namely, GS−PS Carmeuse displayed a considerably more volatile behavior during the initial stage, probably caused by a richer composition in compounds with low boiling point. This fuel also showed the most efficient microexplosions, and therefore, its evaporation behavior is considered to be, in global terms, the best among all of the explored bio-oils. The GS−WT oils displayed more similar behaviors among them, which are also found to be akin to that of a tire pyrolysis liquid

(TPL) studied under the same experimental conditions in a previous work. Smaller yet noticeable differences were found between the three GS−WT liquids, with a more volatile behavior for GS−WT Carmeuse, a slower conversion for the oil produced without the catalyst (GS−WT sand), and an intermediate behavior for GS−WT dolomite.

Regarding the propensity to form soot, all of the explored bio-liquids displayed a substantially higher soot yield than heating oil, as verified by the aspirating soot probe tests and the imaging observations. These results are consistent with the high aromatic content of the bio-liquids and could be a drawback when it comes to their combustion in boilers. In this regard, the highest soot yield was measured for both fuels using the Carmeuse catalyst, whereas the liquid obtained without the catalyst (GS−WT sand) produced the lowest soot tendency, probably due to its lower aromaticity and higher oxygen content. In spite of these high sooting levels, a quite positive feature common to all of the studied bio-oils is the fact that a SEM analysis of the collected solid particles only revealed soot agglomerates, without any hint of carbonaceous coke-like solids, a common issue when burning certain bio-oils, and which is reported to be detrimental to most combustion applications.

■ ASSOCIATED CONTENT

ⓢ Supporting Information

The Supporting Information is available free of charge at https://pubs.acs.org/doi/10.1021/acs.energyfuels.0c02257.

Data on the properties of the two calcium-based catalysts used in this study, namely, their ICP-OES and structural characterization (Table S.1) and the amount of CO_2 and NH_3 desorbed from the TPD-CO_2 and TPD-NH_3 profiles (Table S.2) (PDF)

■ AUTHOR INFORMATION

Corresponding Author

Álvaro Muelas − *Laboratory of Research on Fluid Dynamics and Combustion Technologies (LIFTEC), CSIC−University of Zaragoza, Zaragoza 50018, Spain;* ⓞ orcid.org/0000-0003-1337-0310; Phone: 976506520; Email: amuelas@liftec.unizar-csic.es

Authors

Diego Aranda − *Laboratory of Research on Fluid Dynamics and Combustion Technologies (LIFTEC), CSIC−University of Zaragoza, Zaragoza 50018, Spain*

María Soledad Callén − *Instituto de Carboquímica (ICB—CSIC), Zaragoza 50018, Spain;* ⓞ orcid.org/0000-0001-6063-7386

Ramón Murillo − *Instituto de Carboquímica (ICB—CSIC), Zaragoza 50018, Spain*

Alberto Veses − *Instituto de Carboquímica (ICB—CSIC), Zaragoza 50018, Spain*

Mohamad Asrardel − *Laboratory of Research on Fluid Dynamics and Combustion Technologies (LIFTEC), CSIC−University of Zaragoza, Zaragoza 50018, Spain*

Javier Ballester − *Fluid Mechanics Group/LIFTEC, CSIC−University of Zaragoza, Zaragoza 50018, Spain*

Complete contact information is available at:
https://pubs.acs.org/10.1021/acs.energyfuels.0c02257

Notes

■ REFERENCES

(1) Ahtikoski, A.; Heikkilä, J.; Alenius, V.; Siren, M. Economic viability of utilizing biomass energy from young stands—the case of Finland. *Biomass Bioenergy* **2008**, *32*, 988−996.

(2) Abnisa, F.; Daud, W. M. A. W. A review on co-pyrolysis of biomass: an optional technique to obtain a high-grade pyrolysis oil. *Energy Convers. Manage.* **2014**, *87*, 71−85.

(3) Imran, A.; Bramer, E. A.; Seshan, K.; Brem, G. An overview of catalysts in biomass pyrolysis for production of biofuels. *Biofuel Res. J.* **2018**, *5*, 872−885.

(4) Bridgwater, A.; Meier, D.; Radlein, D. An overview of fast pyrolysis of biomass. *Org. Geochem.* **1999**, *30*, 1479−1493.

(5) Van de Beld, B.; Holle, E.; Florijn, J. The use of pyrolysis oil and pyrolysis oil derived fuels in diesel engines for CHP applications. *Appl. Energy* **2013**, *102*, 190−197.

(6) Bridgwater, A. V. Review of fast pyrolysis of biomass and product upgrading. *Biomass Bioenergy* **2012**, *38*, 68−94.

(7) Xiong, Q.; Yang, Y.; Xu, F.; Pan, Y.; Zhang, J.; Hong, K.; Lorenzini, G.; Wang, S. Overview of computational fluid dynamics simulation of reactor-scale biomass pyrolysis. *Chem. Eng.* **2017**, *5*, 2783−2798.

(8) Ding, K.; Xiong, Q.; Zhong, Z.; Zhong, D.; Zhang, Y. CFD simulation of combustible solid waste pyrolysis in a fluidized bed reactor. *Powder Technol.* **2020**, *362*, 177−187.

(9) Aramideh, S.; Xiong, Q.; Kong, S.-C.; Brown, R. C. Numerical simulation of biomass fast pyrolysis in an auger reactor. *Fuel* **2015**, *156*, 234−242.

(10) Bridgwater, A. V. Renewable fuels and chemicals by thermal processing of biomass. *Chem. Eng. J.* **2003**, *91*, 87−102.

(11) Czernik, S.; Bridgwater, A. Overview of applications of biomass fast pyrolysis oil. *Energy Fuels* **2004**, *18*, 590−598.

(12) Baloch, H. A.; Nizamuddin, S.; Siddiqui, M.; Riaz, S.; Jatoi, A. S.; Dumbre, D. K.; Mubarak, N.; Srinivasan, M.; Griffin, G. Recent advances in production and upgrading of bio-oil from biomass: A critical overview. *J. Environ. Chem. Eng.* **2018**, *6*, 5101−5118.

(13) Sanahuja-Parejo, O.; Veses, A.; López, J. M.; Murillo, R.; Callén, M. S.; García, T. Ca-based Catalysts for the Production of High-Quality Bio-Oils from the Catalytic Co-Pyrolysis of Grape Seeds and Waste Tyres. *Catalysts* **2019**, *9*, No. 992.

(14) Alvarez, J.; Amutio, M.; Lopez, G.; Santamaria, L.; Bilbao, J.; Olazar, M. Improving bio-oil properties through the fast co-pyrolysis of lignocellulosic biomass and waste tyres. *Waste Manage.* **2019**, *85*, 385−395.

(15) Uzoejinwa, B. B.; He, X.; Wang, S.; Abomohra, A. E.-F.; Hu, Y.; Wang, Q. Co-pyrolysis of biomass and waste plastics as a thermochemical conversion technology for high-grade biofuel production: Recent progress and future directions elsewhere world-wide. *Energy Convers. Manage.* **2018**, *163*, 468−492.

(16) Martínez, J. D.; Veses, A.; Mastral, A. M.; Murillo, R.; Navarro, M. V.; Puy, N.; Artigues, A.; Bartrolí, J.; García, T. Co-pyrolysis of biomass with waste tyres: Upgrading of liquid bio-fuel. *Fuel Process. Technol.* **2014**, *119*, 263−271.

(17) Martínez, J. D.; Puy, N.; Murillo, R.; García, T.; Navarro, M. V.; Mastral, A. M. Waste tyre pyrolysis—A review. *Renewable Sustainable Energy Rev.* **2013**, *23*, 179—213.

(18) Sienkiewicz, M.; Janik, H.; Borzędowska-Labuda, K.; Kucińska-Lipka, J. Environmentally friendly polymer-rubber composites obtained from waste tyres: A review. *J. Cleaner Prod.* **2017**, *147*, 560—571.

(19) Zhang, L.; Bao, Z.; Xia, S.; Lu, Q.; Walters, K. B. Catalytic pyrolysis of biomass and polymer wastes. *Catalysts* **2018**, *8*, No. 659.

(20) Zhang, X.; Lei, H.; Chen, S.; Wu, J. Catalytic co-pyrolysis of lignocellulosic biomass with polymers: a critical review. *Green Chem.* **2016**, *18*, 4145—4169.

(21) Sanahuja-Parejo, O.; Veses, A.; Navarro, M.; López, J.; Murillo, R.; Callén, M.; García, T. Catalytic co-pyrolysis of grape seeds and waste tyres for the production of drop-in biofuels. *Energy Convers. Manage.* **2018**, *171*, 1202—1212.

(22) Sanahuja-Parejo, O.; Veses, A.; Navarro, M. V.; López, J. M.; Murillo, R.; Callén, M. S.; García, T. Drop-in biofuels from the co-pyrolysis of grape seeds and polystyrene. *Chem. Eng. J.* **2018**, *377*, No. 120246.

(23) Veses, A.; Sanahuja-Parejo, O.; Navarro, M.; López, J.; Murillo, R.; Callén, M.; García, T. From laboratory scale to pilot plant: Evaluation of the catalytic co-pyrolysis of grape seeds and polystyrene wastes with CaO. *Catal. Today* **2020**, DOI: 10.1016/j.cattod.2020.04.054.

(24) Pan, K.-L.; Li, J.-W.; Chen, C.-P.; Wang, C.-H. On droplet combustion of biodiesel fuel mixed with diesel/alkanes in microgravity condition. *Combust. Flame* **2009**, *156*, 1926—1936.

(25) Li, T.; Zhu, D.; Akafuah, N.; Saito, K.; Law, C. Synthesis, droplet combustion, and sooting characteristics of biodiesel produced from waste vegetable oils. *Proc. Combust. Inst.* **2011**, *33*, 2039—2046.

(26) Liu, Y. C.; Savas, A. J.; Avedisian, C. T. The spherically symmetric droplet burning characteristics of Jet-A and biofuels derived from camelina and tallow. *Fuel* **2013**, *108*, 824—832.

(27) Xu, Y.; Avedisian, C. T. Combustion of n-butanol, gasoline, and n-butanol/gasoline mixture droplets. *Energy Fuels* **2015**, *29*, 3467—3475.

(28) Shaddix, C. R.; Hardesty, D. R. *Combustion Properties of Biomass Flash Pyrolysis Oils: Final Project Report*, No. SAND99-8238; Sandia National Laboratories: Albuquerque, NM, 1999.

(29) Shaddix, C. R.; Tennison, P. J. Effects of char content and simple additives on biomass pyrolysis oil droplet combustion. *Symp. (Int.) Combust.* **1998**, 1907—1914.

(30) Garcia-Perez, M.; Lappas, P.; Hughes, P.; Dell, L.; Chaala, A.; Kretschmer, D.; Roy, C. Evaporation and combustion characteristics of biomass vacuum pyrolysis oils. *IFRF Combust. J.* **2006**, No. 200601.

(31) Yang, S.; Wu, M. The droplet combustion and thermal characteristics of pinewood bio-oil from slow pyrolysis. *Energy* **2017**, *141*, 2377—2386.

(32) Chen, G.-B.; Li, Y.-H.; Lan, C.-H.; Lin, H.-T.; Chao, Y.-C. Micro-explosion and burning characteristics of a single droplet of pyrolytic oil from castor seeds. *Appl. Therm. Eng.* **2017**, *114*, 1053—1063.

(33) Hou, S.-S.; Rizal, F. M.; Lin, T.-H.; Yang, T.-Y.; Wan, H.-P. Microexplosion and ignition of droplets of fuel oil/bio-oil (derived from lauan wood) blends. *Fuel* **2013**, *113*, 31—42.

(34) Muelas, Á.; Callén, M. S.; Murillo, R.; Ballester, J. Production and droplet combustion characteristics of waste tire pyrolysis oil. *Fuel Process. Technol.* **2019**, *196*, No. 106149.

(35) Veses, A.; Puértolas, B.; Callén, M.; García, T. Catalytic upgrading of biomass derived pyrolysis vapors over metal-loaded ZSM-5 zeolites: Effect of different metal cations on the bio-oil final properties. *Microporous Mesoporous Mater.* **2015**, *209*, 189—196.

(36) Puértolas, B.; Veses, A.; Callén, M. S.; Mitchell, S.; García, T.; Pérez-Ramírez, J. Porosity—acidity interplay in hierarchical ZSM-5 zeolites for pyrolysis oil valorization to aromatics. *ChemSusChem* **2015**, *8*, 3283—3293.

(37) Stefanidis, S.; Karakoulia, S.; Kalogiannis, K.; Iliopoulou, E.; Delimitis, A.; Yiannoulakis, H.; Zampetakis, T.; Lappas, A.;

Triantafyllidis, K. Natural magnesium oxide (MgO) catalysts: a cost-effective sustainable alternative to acid zeolites for the in situ upgrading of biomass fast pyrolysis oil. *Appl. Catal., B* **2016**, *196*, 155—173.

(38) Veses, A.; Aznar, M.; Martínez, I.; Martínez, J. D.; López, J. M.; Navarro, M. V.; Callén, M. S.; Murillo, R.; García, T. Catalytic pyrolysis of wood biomass in an auger reactor using calcium-based catalysts. *Bioresour. Technol.* **2014**, *162*, 250—258.

(39) Veses, A.; Aznar, M.; Callén, M. S.; Murillo, R.; García, T. An integrated process for the production of lignocellulosic biomass pyrolysis oils using calcined limestone as a heat carrier with catalytic properties. *Fuel* **2016**, *181*, 430—437.

(40) Muelas, Á.; Remacha, P.; Ballester, J. Droplet combustion and sooting characteristics of UCO biodiesel, heating oil and their mixtures under realistic conditions. *Combust. Flame* **2019**, *203*, 190—203.

(41) Muelas, Á.; Aranda, D.; Ballester, J. Alternative Method for the Formulation of Surrogate Liquid Fuels Based on Evaporative and Sooting Behaviors. *Energy Fuels* **2019**, *33*, 5719—5731.

(42) Pereira, L. G. G.; Pires, C. A. M. Bio-oil viscosity of sisal residue: process and temperature influence. *Energy Fuels* **2018**, *32*, 5115—5124.

(43) Elliott, D. C.; Oasmaa, A.; Meier, D.; Preto, F.; Bridgwater, A. V. Results of the IEA Round Robin on Viscosity and Aging of Fast Pyrolysis Bio-oils: Long-Term Tests and Repeatability. *Energy Fuels* **2012**, *26*, 7362—7366.

(44) Diebold, J. P. A Review of the Chemical and Physical Mechanisms of the Storage Stability of Fast Pyrolysis Bio-oils. In *Fast Pyrolysis of Biomass: A Handbook*; Bridgwater, A. V., Ed.; CPL Press: Newbury, 2002; Vol. 2, pp 243—292.

(45) Ringer, M.; Putsche, V.; Scahill, J. *Large-Scale Pyrolysis Oil Production: A Technology Assessment and Economic Analysis*, NREL/TP-510-37779; National Renewable Energy Laboratory: Golden, Colorado, 2006.

(46) Martínez, J. D.; Lapuerta, M.; García-Contreras, R.; Murillo, R.; García, T. Fuel properties of tire pyrolysis liquid and its blends with diesel fuel. *Energy Fuels* **2013**, *27*, 3296—3305.

(47) Marchese, A.; Dryer, F.; Nayagam, V.; Colantonio, R. Hydroxyl radical chemiluminescence imaging and the structure of microgravity droplet flames. *Symp. (Int.) Combust.* **1996**, 1219—1226.

(48) Farouk, T.; Liu, Y.; Savas, A.; Avedisian, C.; Dryer, F. Sub-millimeter sized methyl butanoate droplet combustion: Microgravity experiments and detailed numerical modeling. *Proc. Combust. Inst.* **2013**, *34*, 1609—1616.

(49) Liu, Y. C.; Xu, Y.; Hicks, M. C.; Avedisian, C. T. Comprehensive study of initial diameter effects and other observations on convection-free droplet combustion in the standard atmosphere for n-heptane, n-octane, and n-decane. *Combust. Flame* **2016**, *171*, 27—41.

(50) Mikami, M.; Kojima, N. An experimental and modeling study on stochastic aspects of microexplosion of binary-fuel droplets. *Proc. Combust. Inst.* **2002**, *29*, 551—559.

(51) Ballester, J.; Dopazo, C. Experimental study of the influence of atomization characteristics on the combustion of heavy oil. *Combust. Sci. Technol.* **1994**, *103*, 235—263.

(52) Law, C.; Chung, S.; Srinivasan, N. Gas-phase quasi-steadiness and fuel vapor accumulation effects in droplet burning. *Combust. Flame* **1980**, *38*, 173—198.

(53) Das, D. D.; John, P. C. S.; McEnally, C. S.; Kim, S.; Pfefferle, L. D. Measuring and predicting sooting tendencies of oxygenates, alkanes, alkenes, cycloalkanes, and aromatics on a unified scale. *Combust. Flame* **2018**, *190*, 349—364.

Combustion of crude glycerol and its blends with acetals

A. Muelas[a], P. Remacha[a], A. Pina[a], J. Barroso[a], A. Sobrino[a], D. Aranda[a], N. Bayarri[b], C. Estévez[b], J. Ballester[a,*]

[a] LIFTEC, Universidad de Zaragoza/CSIC, María de Luna 10, 50018 Zaragoza, Spain
[b] Inkemia IUCT Group, Álvarez de Castro, 63, 08100 Mollet del Vallés, Spain

ARTICLE INFO

ABSTRACT

In spite of its relevance, the prospective energetic valorization of crude glycerol (CG), a major by-product of biodiesel production, remains nowadays unfulfilled in the industry because of the significant challenges posed by its combustion properties. Besides some basic post-treatments such as desalting (to obtain desalted crude glycerol, DG), its blending with other industrial by-products could improve crude glycerol properties, while maintaining the renewable nature of the fuel. A secondary product obtained from the FAGE process, consisting in a mixture of acetals named GF*, has been proposed in this work as a suitable fuel for this purpose. The combustion characteristics of these by-products have been tested along with different CG-GF* and DG-GF* blends by employing single droplet combustion experiments and semi-industrial furnace tests. Single droplet results point to widely different behaviors between GF* and the glycerols, the latter displaying much lower burning rates and violent microexplosions ascribed to salt content as well as to the broad differences in their constituent's boiling points. Relevant differences were noted between DG and CG modes of microexplosion, presumably due to the lower salt content of the former. Both CG-GF* and DG-GF* mixtures presented similar behaviors to CG, although with a noticeably faster conversion. The furnace tests revealed that GF* addition widened the range of stable conditions in the burner, significantly improving flame stability and reducing CO emissions. NOx emissions slightly increased, although they could be reduced through burner aerodynamics optimization, facilitated by the improvement in flame stability. The reported results support the potential use of GF* as auxiliary fuel for enhancing the combustion behaviors of crude glycerol.

1. Introduction

The extensive manufacture of biodiesel during the last decades has indirectly increased the production of glycerol, a by-product of the transesterification process, where vegetable oils or animal fats react with short-chained alcohols. The obtained glycerol stream, usually denominated crude glycerol, is far from being chemically pure, typically consisting of a mixture of glycerol, water, alcohol, soap, FAMEs and alkaline catalyst residues [1,2]. These impurities severely hinder its use in high added value processes, being crude glycerol (CG) of very little economic value nowadays [1,2]. In view of the large surplus of this by-product, and as viable high-end alternatives are very limited with the current refining technologies and market position, its energetic valorization in industrial boilers has been proposed as a feasible solution to the large amounts of CG produced in biodiesel plants.

In principle, the characteristics of CG are compatible with its potential use as fuel in industrial power plants, either completely replacing or co-fired with fossil fuels. Some works in the literature reported favorable results in terms of the co-combustion of glycerol with other fuels (e.g., biomass [1]). Most of those studies analyzed the effect of using glycerol (or other bioliquids) as fuels in small-scale test facilities on the combustion characteristics (specially emitted pollutants) with respect to those obtained from burning traditional fuels (e.g., [3–8]). However, there are still relatively few studies on the use of crude bioliquids in commercial heat/power generation plants [9] due to the modifications required for existing systems [10]. In the case of CG, there are significant differences between its physicochemical properties and those of conventional fossil fuels, namely: low calorific value, high water content, high autoignition temperature, production of toxic acrolein gases, high viscosity at room temperature and high mineral content. These properties significantly hinder the use of CG in combustion-related applications [3,4] or may involve significant

modifications in existing burners [8,11]. In particular, the lower calorific value of CG (~16 MJ/kg) compared to that of fossil fuels (e.g. 44 and 46 MJ/kg for diesel and propane, respectively), forces to consume a significant amount of an auxiliary fuel, typically natural gas or propane, to ensure a good quality combustion with stable flame.

An alternative option to overcome the challenges posed by burning neat CG is to blend it with other liquid by-products which can improve its combustion behavior. In doing so, the obtained fuel would be entirely considered as waste-derived, as opposed to its prospective blending with conventional petro-fuels such as diesel. A novel process, described in [12,13], has been developed to produce Fatty Acid Glycerol formal Esters (FAGE), a fuel of similar characteristics to that of the widespread FAME. This process is reported to yield a by-product consisting in a mixture of acetals, being glycerol formal (GF) the predominant one. This by-product stream is reported to display much more suitable physicochemical properties for its combustion when compared with CG [13], and therefore their potential blending could significantly improve the prospects of a successful valorization of the crude glycerol surplus, while also consuming the aforementioned FAGE by-products. In addition, as detailed in [12,13], the FAGE manufacture process uses glycerol as feedstock, even further increasing therefore its consumption.

In this work, the combustion characteristics of crude glycerol (as received from a biodiesel plant and also desalted), an acetal mixture (GF*) and their blends were experimentally studied at two different scales. Their combustion properties were obtained under well controlled conditions in single droplet experiments, whereas their behaviors under realistic conditions were assessed from tests in a semi-industrial furnace. The objective was to characterize the behavior of those fuels and to determine the potential benefits of blending crude glycerol, which has been reported to display significant difficulties for its appropriate stand-alone combustion, with GF*.

2. Experimental method

2.1. Fuels investigated

A crude glycerol sample (CG) provided by Mercuria Biofuels as a by-product of their biodiesel manufacture was, after a proper homogenization and filtration process, physicochemically characterized prior to its combustion tests. The main results of this characterization are outlined in Table 1.

As introduced before, this work aims to explore the possibility of improving the CG combustion characteristics by blending it with a FAGE by-product, consisting in a series of acetal compounds denoted GF and GFOMOM. For the interested reader, information regarding the FAGE, GF and GFOMOM production and characteristics can be found in [12,13]. A mixture of both by-products was supplied by Inkemia IUCT, in a proportion of industrial relevance for the FAGE production process.

Table 1
Main chemical components and properties of the crude glycerol (CG) studied.

Parameter	Value
Glycerol (% m/m)	81.4
Water (% m/m)	2.8
Methanol (% m/m)	0.1
NGOM[a] (% m/m)	7.5
Sulfur (% m/m)	1.1
HHV (MJ/kg)	12.7–15.8[b]
Density, 30 °C (kg/m^3)	1290
Viscosity, 80 °C (cP)	67

[a] Non-glycerol organic matter.
[b] The higher heating value was determined four times, with a significant data dispersion (standard deviation of 1.63 MJ/kg). Thus, the upper and lower values, rather than their average, are displayed.

This blend was named GF*, and its behavior will be explored along with that of different CG-GF* mixtures, both in single droplet combustion tests and in the furnace. Three CG-GF* blends were prepared for the droplet experiments, with 7, 15 and 30 vol% of GF*. In addition, neat glycerol (Panreac, 99.5% purity) was also included in order to provide a reference baseline.

It is well known that the high mineral content of CG can seriously damage the combustion facilities [5] and for that reason, the 'raw' crude glycerol was processed to remove most of its salt content. Dissolved salts in the CG were removed by solvent precipitation followed by filtration of the solid salts. The solvent was recovered by distillation and reused. With this procedure, the salt content can be reduced up to 80%, depending on the nature of the solvent. The advantage of salt precipitation with respect to the alternative process of glycerin distillation is the lower capital cost of the process equipment. Furthermore, the operating cost of solvent desalting is also lower than glycerin distillation, even if its industrial implementation has several disadvantages (the main one being the need to manipulate the solid salt in the presence of a volatile solvent). Further process optimization is needed in order to successfully scale-up the desalting technology. Even so, this process was applied to a batch of CG, obtaining a representative sample of desalted crude glycerol (DG), whose salt content analysis is compared to that of the original CG in Table 2. Namely, an ICP-AES (Inductively Coupled Plasma Atomic Emission Spectroscopy) analysis was performed at ICB-CSIC in order to quantify the main cations present in both glycerols. This information was complemented with that of the total ash content, measured by means of a burner and a muffle-type furnace. Using this latter parameter as a global indicator of salt presence, the desalination process achieved a reduction of 64.3% of the total ash content initially present in the CG sample. Once obtained and characterized, the combustion of DG, both neat and blended with GF*, was also analyzed in the droplet facility and in the semi-industrial furnace.

2.2. Droplet combustion facility

The single-droplet evaporation and combustion characteristics of the examined fuels were obtained through the Droplet Combustion Facility (DCF) developed at LIFTEC. These experiments provide insight into the intrinsic behavior of each fuel when tested under fixed and well characterized conditions. As these conditions are exactly the same for each sample, the observed differences are completely attributable to the studied fuels, and relative behaviors among them can be extracted in a simplified configuration. A detailed description of the experimental rig used for this purpose can be found elsewhere [14,15].

The isolated, freely-falling droplets were originated at a piezoelectric device with initial diameters of 151.1 ± 1.9 μm and subsequently injected within a hot coflow, where their evaporation and burning processes were recorded by optical means. In order to decrease the viscosity of the glycerol samples, the droplet generator had to be heated to temperatures up to 100 °C. An interdroplet separation larger than 100 droplet diameters effectively prevented any interaction between droplets [16,17]. In order to obtain a gaseous ambience representative of those found in real flames, a hot coflow consisting in the

Table 2
Salt content in the crude and desalted glycerol samples.

Parameter	CG	DG
Al (g/kg)	0.013	< D.L.[a]
Ca (g/kg)	0.041	< D.L.[a]
K (g/kg)	25.67	6.00
Na (g/kg)	3.86	3.80
P (g/kg)	1.46	0.38
Ash (% m/m)	7.15	2.55

[a] Detection limit.

combustion products flowing out of a flat-flame burner was used. By adjusting the burner's feed flow rates, the composition and temperature of its exhaust gases could be modified, providing therefore different atmospheres for studying the droplet combustion process. Three conditions were selected, with 0, 3 and 10% of oxygen molar fraction (dry basis) in the coflow. As in real flames the oxygen availability can significantly vary within flame regions, the chosen conditions are thought to cover a varied range of common ambiences observed by droplets within real spray flames.

The single droplet evaporation and combustion characteristics were entirely gained by means of optical methods. A CCD camera (QImaging Retiga SRV) fitted with a telemicroscope and backlighted through a LED stroboscope used the double exposure technique in order to extract not only the droplets size but also its velocity. With a delay of 500 μs between the LED's shots, a given droplet could be recorded multiple times in the same picture. This is used for measuring the droplet velocity, but also for characterizing other features such as the occurrence of microexplosions. Additionally, a color DSLR camera (Nikon D5000) recorded the visible flame streak formed by the freely-falling droplets, which provided insight into some macroscopically observable features.

2.3. Semi-industrial furnace

The second stage of the combustion tests was conducted in a semi-industrial furnace, under conditions representative of those found in real boilers. The experimental facility has been described in detail in previous works [18,19] and only their main characteristics will be summarized here.

The combustion chamber is cylindrical and vertically oriented, with a total length of 3.5 m and a diameter of 0.83 m in the upper half, where the burner and the flame are located. All furnace elements are cooled by individual water jackets and their inner walls are refractory lined over the whole chamber length. Fig. 1 shows the geometry of the

burner installed in the furnace roof. It was designed to provide a broad flexibility, in order to adapt to different fuels or to implement low-NOx measures (more details in [19]). The combustion air is injected through two concentric ducts, in adjustable proportions; the split was fixed at 68%/32% of primary/secondary air. The liquid fuels were preheated to 80 °C and injected by means of an air-assist atomizer. Due to the well-known difficulties to achieve a stable flame with crude glycerol, the facility allowed for the use of an auxiliary fuel (propane), which was injected through 16 injectors installed in the periphery of the burner throat (see Fig. 1). Although the spray characteristics were not determined, mean spray sizes are typically in the order of several tens of microns, with the distribution tail reaching the order of a hundred microns, as it can be confirmed in [20,21], where the spray characteristics of a heavy oil tested at this same furnace were analyzed. Thus, the droplet sizes used in the single droplets experiments (~150 μm) are expected to be close to the tail of the spray distribution obtained in the current furnace tests.

The main objective of these tests was to evaluate the stability and emissions achievable with crude glycerol (both neat and desalted) and its blends with GF*. Flue gas composition was measured with individual on-line analyzers for O_2, CO and NOx (repeatability < 1%, 0.5% and 0.5% of their respective full scale values). Given the lack of generally-accepted methods to evaluate flame stability, some indices were extracted from flame images and radiation. A video camera and a photomultiplier tube fitted with a bandpass filter at 310 ± 5 nm (OH* chemiluminescence band) were installed at one of the side windows with that purpose.

3. Tests in droplet combustion facility

3.1. Base fuels

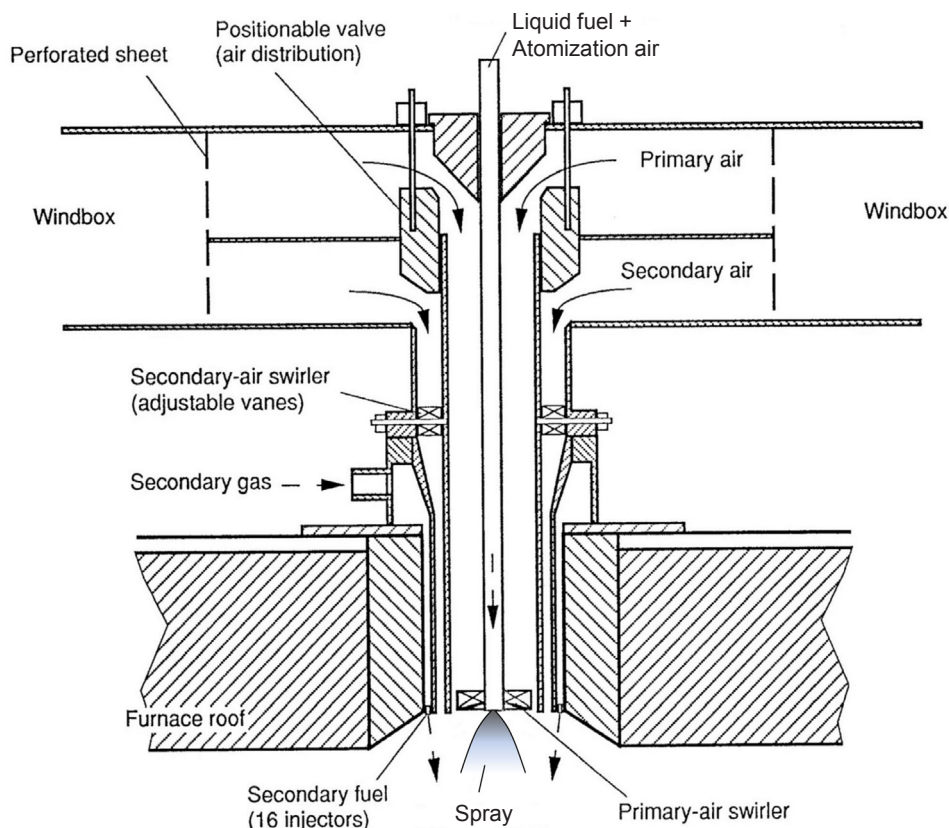As introduced in Section 2.1, the droplet evaporation and

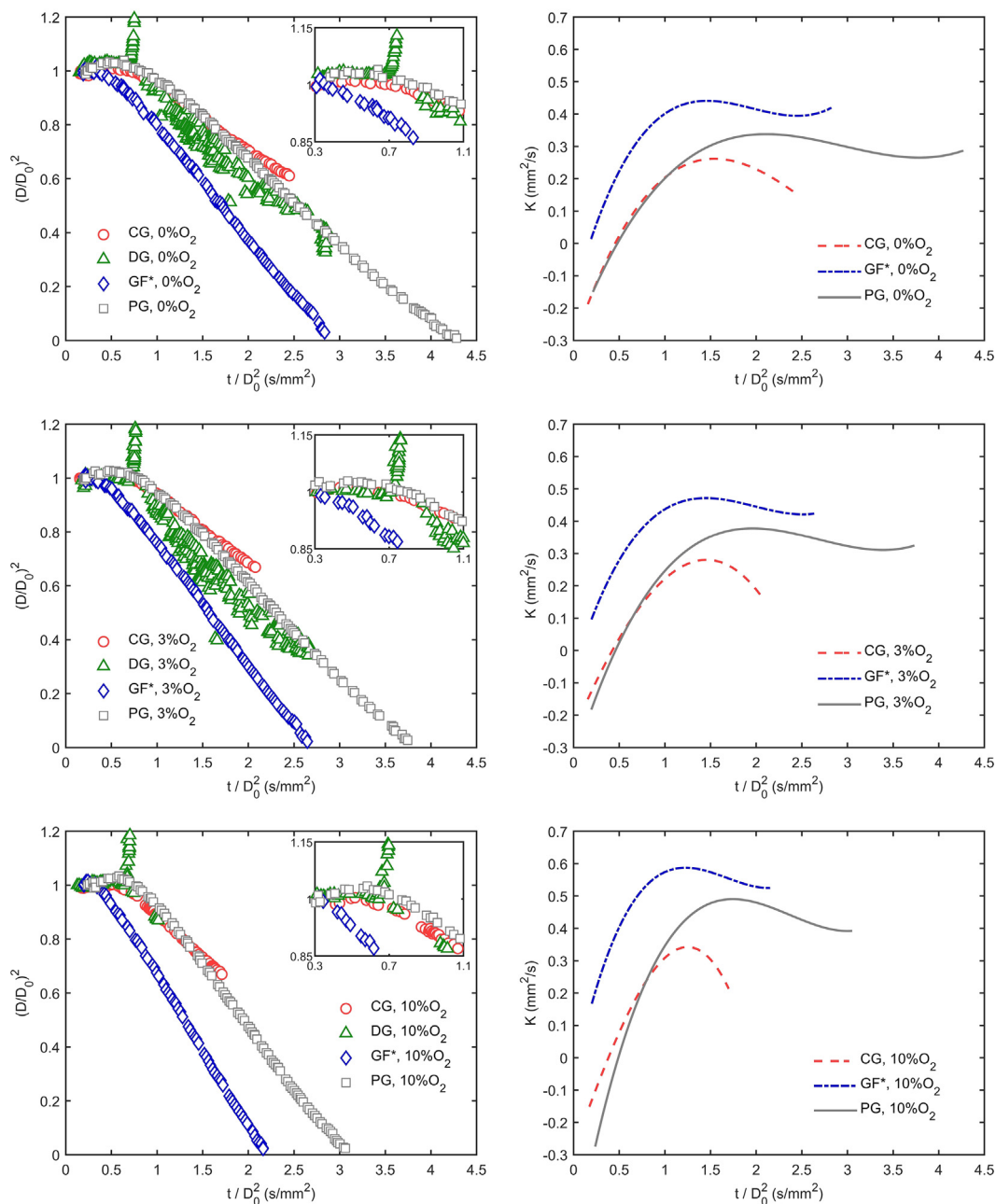**Fig. 1.** Burner used for combustion tests in the semi-industrial furnace.

Fig. 2. Normalized droplet size and burning rate evolution for the three studied base fuels at different oxygen conditions (top: 0%, centre: 3%, bottom: 10%).

combustion characteristics of the industrial by-products CG, DG and GF* were extracted along with those of pure glycerol (PG) by means of single droplet tests. These fuels are categorized as 'base fuels', to distinguish them from the CG-GF* and DG-GF* mixtures, which shall be presented in Section 3.2. Results are displayed in Fig. 2, with the droplet size evolution curves showed in the left column and the subsequently extracted burning rates ($K = -d(D^2)/dt$) provided in the right one. It should be noted that the droplet size curves are normalized by the initial droplet diameter (D_0), so that any small difference in D_0 among tests is automatically corrected. The K-t/D_0^2 curves are obtained as the time-derivatives of the size curves. For this purpose, the latter data was fitted to a 4th order polynomial, which was subsequently derived with respect to time. Regarding the uncertainty of the displayed curves, the error bars for a given droplet residence time have not been included because they are smaller than the symbols used in Fig. 2. Pure glycerol tests were repeated one month after their first run in order to check the procedure repeatability, providing a 6.80, 1.75 and 0.24%

difference in time-averaged evaporation rate for the 0, 3 and 10% O_2 conditions, respectively. The first value is unusually high for these tests, which typically show a repeatability in the order of 1% for the time-averaged evaporation rate (e.g., 0.7% for a heating oil vaporization test in [15]). This lower repeatability is thought to respond to the significantly higher initial droplet velocities found for the PG repetition tests (especially for the 0% O_2 case), which would cause a quicker transit of the droplet along the gas coflow temperature profile. Any difference in the gas temperature around the droplet for a given residence time would have a bigger impact in the evaporation experiment, more sensitive towards this parameter because of the absence of a diffusion flame surrounding the droplet. In any case, all the experimental data presented in this work were obtained with initial droplet velocities much closer together than that of PG at the 0% O_2, and therefore their repeatability is expected to be considerably better.

Fig. 2 illustrates very similar evaporative behaviors between CG and PG during approximately the first half of the droplet lifespan for all the
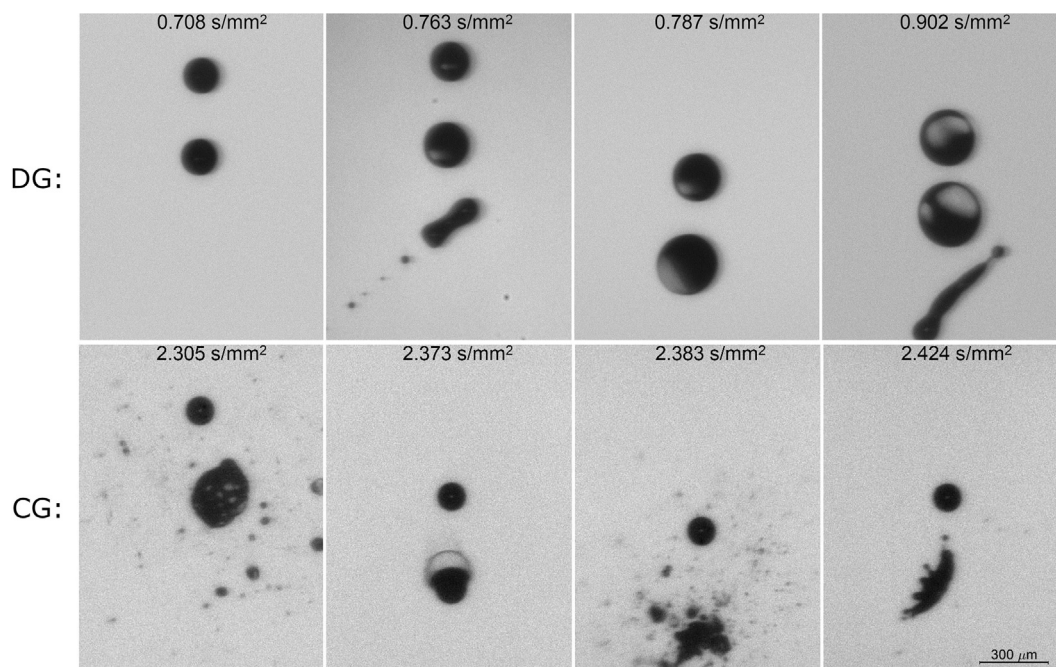
Fig. 3. Droplet swelling and microexplosion sequences for DG (upper row) and CG (lower row) at the 0% O_2 condition. For each sequence, the normalized time after injection (t/D_0^2) for the upper droplet is provided.

studied oxygen conditions. This is ascribed to the high content of glycerol in the studied CG (81.4%, according to Table 1). Both fuels display a prolonged initial heat-up transient with some thermal swelling (i.e., an increase of the droplet size due to its density decrease), primarily caused by their low tendency to evaporate at the droplet's injection temperatures. However, CG appears to show a more volatile behavior in that initial region, with slightly smaller normalized sizes and somewhat higher burning rates. The vaporization of the small fractions of NGOM and water present in the CG (Table 1) is thought to account for these differences. Over the course of this heat-up period, the PG droplets gradually increase their burning rate until reaching a quasi-steady value which is kept approximately constant until the droplet is completely vaporized, as stated by the well-known d^2-law. The CG curves, by contrast, are suddenly interrupted much before the droplet burnout time due to the onset of violent microexplosions which shattered the droplets. This kind of event was also observed in a previous work on crude glycerol droplet combustion [14], and it is ascribed to the formation of internal vapor bubbles which disrupt the liquid droplet upon their violent release. These disintegrations are reported to be beneficial for the fuel conversion efficiency in real applications, as a secondary atomization would not only significantly shorten the droplets' burnout time, but also improve the fuel-gas mixing within the combustion chamber and reduce pollutant emissions [14,22]. Just before the microexplosion occurrence, the CG burning rates appear to abruptly decay, departing from the PG behavior. This subtle feature was also noticed in [23] for ethanol-TTIP mixtures, although relevant differences between the microexplosion mechanisms might hamper comparison with the CG case (TTIP was found to hydrolyze creating a solid shell at the surface). A hypothesis which might explain this abrupt decay in *K* in the present work is based on the results presented by Wang et al. for binary alkane mixtures [17], where it was found that the onset of the first internal vapor bubble occurs much before this event can be inferred from alterations in the droplet size, as the initial bubble size is too small to cause a significant change in the droplet diameter. This initial bubble was reported to grow rather slowly until reaching a turning point, where its size abruptly increased, causing the shattering of the droplet. The progressive decay in the burning rate observed for CG in Fig. 2 could thus be ascribed to the formation of small bubbles

inside the droplets just prior to their fragmentation.

On the other hand, the desalted crude glycerol displays a completely different behavior when compared to both CG and PG. As illustrated in Fig. 2, DG droplets underwent an abrupt swelling just after completing their initial heat-up transient. This swelling could rapidly increase the droplet size by a factor of 2 prior to a puffing event or a weak microexplosion. For most cases at the 0 and 3% O_2 conditions, these events achieved to propel some small liquid fragments away from the parent droplet, significantly decreasing its size. After this phenomenon, the DG droplets evaporated smoothly until reaching a new microexplosion, this one analogous to that described for CG, which completely shattered the droplet. Because of the variable intensity of the weak microexplosions, the DG droplet measurements displayed in Fig. 2 should only be regarded as a sample of the range of sizes observed after this event. Depending on the puffing intensity, the mass loss of the parent droplet varied, explaining therefore the high dispersion found for this particular fuel. This high dispersion hindered the extraction of evaporation and burning rates for DG in Fig. 2. For DG at the 10% O_2 condition, the puffing event was significantly more intense than those described for the 0 and 3% and, for most cases, achieved to shatter the parent droplet into several child droplets of roughly the same size. This fact hampered droplet measurements after the fragmentation point for DG at 10% O_2, as displayed in Fig. 2.

Finally, the acetal mixture GF* presents a much shorter initial heating transient than the glycerols, with substantially higher burning rates throughout the droplet lifespan. Contrary to CG and DG, GF* droplets do not experience microexplosions, and their size evolution curves proceed until the droplets are completely evaporated. In spite of their considerably higher volatility, the total conversion of the GF* droplets is expected to occur slightly after that of crude glycerol, as the shattering of the latter would drastically reduce their consumption time afterwards (combustion time roughly scales with D^2, as it can be noticed in Fig. 2).

When comparing among oxygen conditions for a given fuel, it is clearly ascertained from Fig. 2 that higher oxygen availability accelerates the droplet conversion process, enhancing burning rates and reducing droplet burnout times. This is due to the formation of an envelope flame surrounding the droplet when oxygen is available. If the
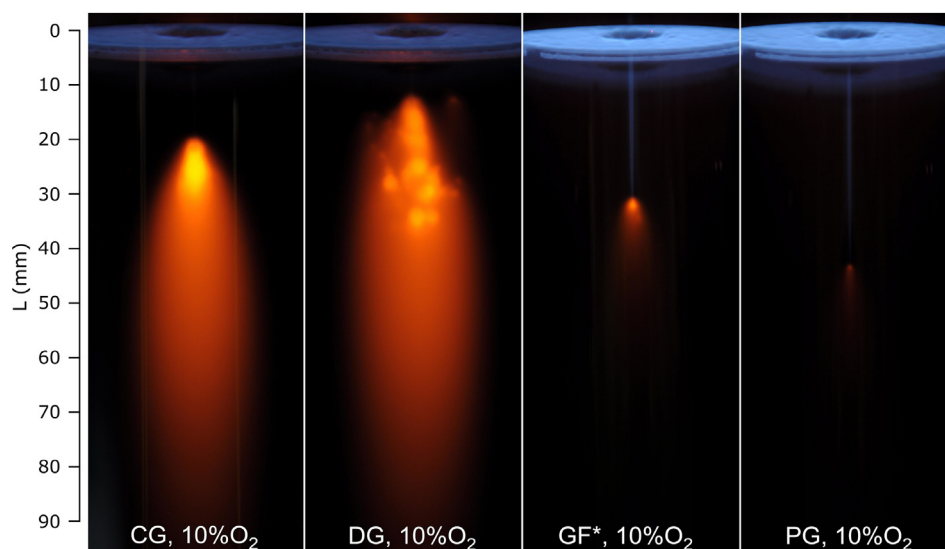
Fig. 4. Macroscopic flame traces created by the freely-falling droplets of the studied base fuels. An exposure time of 2 s was used for GF* and PG, whereas CG and DG pictures were captured with 1/3 s due to their higher luminosity.

oxygen fraction in the gaseous coflow is increased, the envelope flame displays a higher temperature and is located closer to the droplet surface. Both effects significantly enhance the heat transfer towards the liquid phase, accelerating therefore the droplet evaporation process and the microexplosion occurrence.

Fig. 3 illustrates an overview of some microexplosion sequences recorded for CG and DG at the evaporation condition (0% O_2 coflow). As detailed in Section 2.2, each picture displays multiple sequential shots of the same freely-falling droplet 0.5 ms apart. The upper row shows the already described DG swelling and puffing events, whereas the lower one illustrates the CG abrupt microexplosions. The first obvious difference between both is their occurrence point, considerably delayed for CG as it can be confirmed in Fig. 3. The DG swelling starts just after its heat-up period, with droplet sizes in the order of D_0 (e.g., 153 μm for $t/D_0^2 = 0.708$ s/mm^2 in Fig. 3) gradually increasing their diameter during the following few milliseconds (~2–4 ms) prior to their break-up and puffing, which can be observed in the triple-exposure pictures at $t/D_0^2 = 0.763$ and 0.902 s/mm^2. On the other hand, microexplosions recorded for CG occur after a significant evaporation has already taken place (droplet sizes ~120 μm), with a much shorter characteristic time than the swelling and puffing events observed for DG. In the case of CG the upper droplets appear to be totally spherical, without any sign of microexplosion, whereas the lower ones are completely shattered by the bursting of the inner vapors. Therefore, the characteristic time for the recorded fragmentation events would be considerably lower than 0.5 ms for this fuel, even though the initial bubbles might have been building up during a longer time lapse (as observed for a different fuel in [17]). As already pointed out, an additional difference between the two kinds of microexplosions presented in Fig. 3 is the fact that CG microexplosions completely shattered the droplets, whereas the DG break-up phenomena was much weaker, with considerably larger child droplets which could even be tracked and measured downstream the bursting point for the 0 and 3% O_2 conditions (Fig. 2).

The CG microexplosions illustrated in the lower row of Fig. 3 display exactly the same features as those reported in [14] for a different crude glycerol sample, although also with significant differences when compared to [24], another of the few available works on CG droplet combustion. The broad differences between both experimental setups are thought to be responsible for the aforementioned discrepancies, as [24] employed a suspended droplet technique with bigger droplet sizes and lower ambience temperatures. The CG microexplosion typology

reported here, with fast (< 0.5 ms) and violent droplet shattering, also differs from those described in several works on different mixtures and emulsions of alkanes, alcohols and water (e.g., [17,25–27]). All the referred studies, performed by means of the freely-falling technique and avoiding therefore the potential influence of the solid filament, reported the occurrence of significant droplet swelling before its shattering. For instance, binary heptane-hexadecane droplets in [17] were found to increase their diameter by more than 60% prior to droplet burst, with a characteristic time in the order of a few milliseconds. Both microexplosion features appear to closely concur with the DG break-up phenomena illustrated in Fig. 3. Since the experimental configuration used in this work is analogous to that employed in [17,25–27], the reported DG microexplosions are thought to respond to the same mechanisms proposed in those works, i.e., the homogeneous nucleation of the liquid mixture within the droplet. This local vaporization of the more volatile components (NGOM, water, methanol, even some non-recovered desalination solvent) would create a gas bubble within the liquid phase, whose growth explains the droplet swelling which precedes its break-up. As already discussed, a different case would be that of CG, whose fast and violent microexplosions concur with [14], where the droplet shattering was ascribed to the decomposition of alkali salts rather than to the evaporation of its lighter compounds, following therefore a different mechanism than those governing homogeneous nucleation between liquids. The fact that crude glycerol modifies its original abrupt microexplosions for the slower swelling-induced break-ups after the desalination process also suggests that salt content plays a relevant role in the droplet bursting mode. However, further investigation is clearly needed in order to better ascertain the differences between both microexplosion typologies.

The broad differences noted between the studied base fuels also lead to macroscopically observable distinct behaviors. This can be clearly ascertained from Fig. 4, where the flame traces formed by the combustion of the free-falling droplets are presented by means of long-exposure photographs. All of them display a subtle blue streak stemming from the chemiluminescent emission of the droplets' envelope flames. However, whereas for pure glycerol and GF* this blue streak spans for the whole droplet burnout time, for CG and DG it is abruptly interrupted by a much more intense orangish emission. This luminosity was analyzed by a spectrometer (Ocean Optics HR2000), which found a marked peak at 589 nm, determining therefore that most of this radiation stems from the emission of excited sodium ions, released after the droplet shattering. This can be verified in Fig. 5, where the
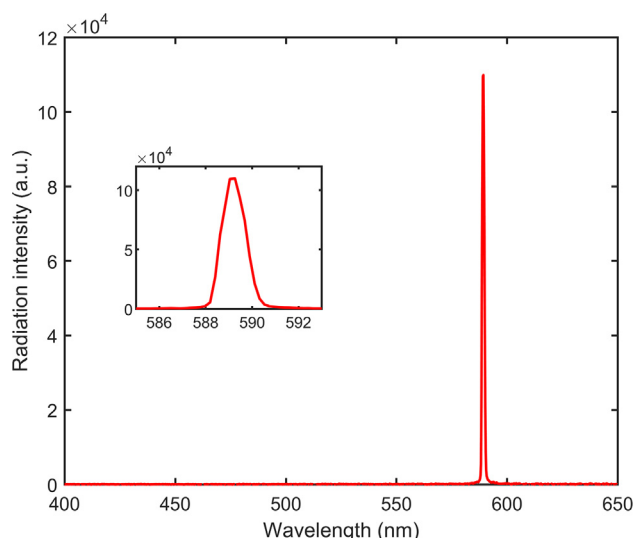
Fig. 5. Emission spectrum recorded in the combustion test of CG-GF*7 droplets (10% O_2 condition).

spectrum recorded for CG-GF*7 is presented. Thus, the onset of the orangish umbrella in Fig. 4 indicates the point of the first recorded microexplosion for the set of droplets captured in the long-exposure picture. In accordance with the curves presented in Fig. 2, DG droplets experience an earlier occurrence of microexplosions, although this difference is reduced compared to the 0% O_2 condition displayed in Fig. 3. The different modes of droplet shattering can also explain the noticeable differences found between both orangish umbrellas: whereas the CG sodium emission is more centered around a clearly more intense spot, the weaker microexplosions of DG provide a more distributed and asymmetrical sodium release along the child droplets trajectories.

The droplet burnout lengths for GF* and PG can also be clearly distinguished in Fig. 4, as they feature an orangish spark at the point of droplet depletion. The spectra recorded determined that these sparks were also caused by sodium emission, and therefore their occurrence is due to small contents of sodium in the GF* and PG, which are released into the hot ambience after the liquid has completely evaporated. This sodium can either be contained within the original fuel samples or be a result of cross-contamination. In any event, the amount of sodium present in GF* and PG is estimated to be negligible, as the orangish luminosity does not arise until the very instant of droplet depletion. Both the visible flame traces and the recorded spectra point to a negligible soot yield for all the studied fuels, as the characteristic blackbody continuum emission ascribed to soot is absent (e.g., see the spectrum recorded for CG-GF*7 in Fig. 5).

3.2. Glycerol - acetal mixtures

As introduced before, one of the main objectives of this work is to evaluate the effects of GF* addition on the evaporation and combustion characteristics of crude glycerol. To this end, the tests described in the previous section were performed on different CG-GF* and DG-GF* mixtures at the 3% O_2 coflow condition. The droplet size and burning rate curves are displayed in Fig. 6 for both kinds of blends.

It is noteworthy that CG and its mixtures with GF* show very similar behaviors throughout all the droplets combustion history. The three studied blends presented the same microexplosion typology than that described for CG in Fig. 3, and their macroscopically observable flame traces were also akin to those recorded for the neat crude glycerol (Fig. 4). Regarding the quantitative evaporation data, it can be inferred from Fig. 6 that GF* addition slightly accelerated the droplet evaporation process, although this effect is barely noticeable for the mixtures with lower GF* content, being clearer for the CG-GF*30 blend.

On the contrary, the addition of GF* drove relevant changes in the combustion features of DG, such as the suppression of the swelling and puffing stages. In [25–27] it was experimentally concluded that, for homogeneous nucleation to occur, the initial concentration of the most volatile constituents (e.g., water, NGOM, non-recovered desalination solvent or methanol in the case of DG) must be within a limited range defined by the relation of the homogeneous superheat limit of the mixture to the boiling point of the less volatile compounds. If, as it was proposed in Section 3.1, the swelling events displayed by DG are indeed caused by homogeneous nucleation within the droplet, the addition of a compound such as GF* could shift the mixture to a concentration range out of the superheat limits, hindering therefore the initial swelling and puffing phenomena. As it can be noticed in Fig. 6, DG-GF* droplets vaporized smoothly until $(D/D_0)^2 \sim 0.45$, where an abrupt microexplosion led to a complete droplet breakup such as those observed for CG and its mixtures. These kind of microexplosions are ascribed to salt content, and therefore the lower salt concentration of DG is consistent with the delayed occurrence of the droplet shattering for DG-GF* in comparison with CG-GF*, which burst around $(D/D_0)^2 \sim 0.66$. As it was observed for CG mixtures, the burning rate enhancement with GF* blending is more pronounced for a 30% GF* addition, being the evaporation process of DG-GF*7 and DG-GF*15 virtually the same. These results would be in accordance with the behaviors reported for the base fuels in Section 3.1, where the considerably higher volatility of GF*, both in terms of higher burning rates and shorter heat-up periods, was highlighted.

4. Tests in semi-industrial furnace

The combustion characteristics of crude glycerol have been also investigated in a configuration representative of industrial facilities by means of tests performed with CG, DG and their blends with GF* in a semi-industrial furnace. The study has focused on analyzing the range of conditions allowing a stable combustor performance and the need of a support fuel to ensure flame stability. In the tests, the mass flow rate of glycerols, CG-GF* and DG-GF* mixtures was fixed at ~17 kg/h. Propane was used as auxiliary fuel, with flow rates in the range 0–3 Nm^3/h.

A first, basic requirement concerns the stability of the flame, as in many cases glycerol burners need to be supplied with a secondary fuel in order to achieve a stable, attached flame [4,5,7]. Thanks to its broad flexibility, the burner used in this study (Fig. 1) could be adjusted to maintain a stable flame without any support fuel. Nevertheless, the operating range and the combustion quality (e.g. in terms of CO emissions) varied with the fuels fed to the burner. For example, in the case of unblended desalted glycerol, DG, a minimum of 5.8% excess oxygen (by vol., dry basis) was needed when no propane was used; this limit gradually decreased with the amount of propane fed through the secondary injectors (see Fig. 1), so that it was below 1.4% for 1 Nm^3/h of propane. The addition of GF* also had a clearly beneficial effect in this respect: the minimum of 5.8% excess oxygen dropped to 2.4% and < 3.3%[1] when the proportion of GF* in the liquid fuel was 15% and 30%, respectively. This is a first evidence of the positive effect of blending with GF*, as it could alleviate the need for premium fuels to stabilize the flame.

The CO and NOx emissions measured for the different tests with DG are represented in Fig. 7 and provide a clear picture on the effect of either propane or GF* addition. A limit of 100 ppm was arbitrarily selected as a threshold between 'good' and 'bad' combustion qualities (the legal limit of 1000 ppm is too high for this purpose). Due to the

---

[1] Actually, good flame stability was verified with 30% GF* down to 1.5% oxygen, but this was measured in a test with a higher fuel flow rate. Although this does not necessarily affect the result, it was preferred not to include this lower limit in Fig. 7.
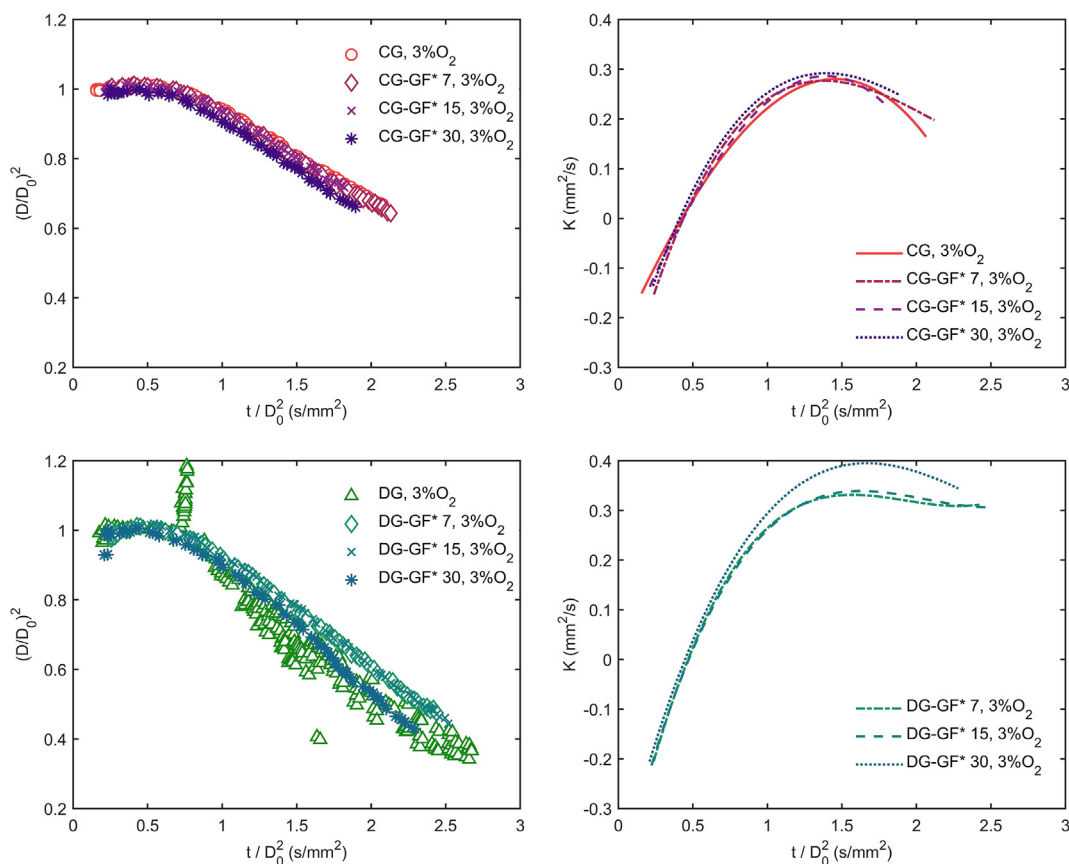
Fig. 6. Normalized droplet size and burning rate evolution for CG-GF* and DG-GF* blends at the 3% O_2 condition.
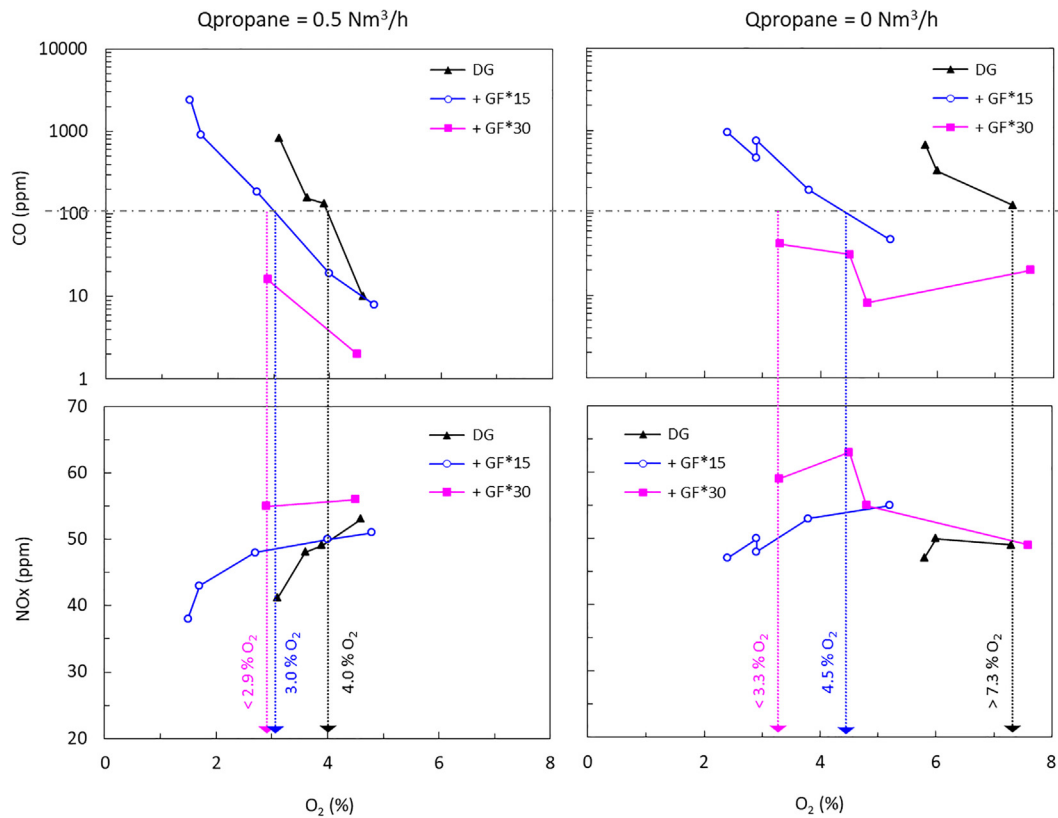

Fig. 7. Emissions of CO (top) and NOx (bottom) measured in the tests with DG and its blends with GF* when burning with 0.5 (left) and 0 Nm^3/h (right) of propane. The excess oxygen required in each case for quality combustion (CO < 100 ppm) are also indicated.

wide range of CO emissions, a logarithmic scale has been used. It should be noted, however, that this magnifies the region of very low emissions (let's say, < 20 ppm), where the variations may be due to minor experimental uncertainties and, hence, not always are meaningful.

The use of 0.5 Nm^3/h of propane (Fig. 7, left) leads in all cases to lower CO emissions than if DG or its blends are burned alone. Given the strong influence of excess oxygen on CO and the fact that its range not always overlapped for the different fuels, a direct method to compare the various situations is to determine the oxygen concentration required to keep CO emissions below the 100 ppm threshold. The addition of 0.5 Nm^3/h of propane diminishes in all cases the excess air required to reach the CO limit, the reduction being more marked for DG (< 7.3% to 4% O$_2$) than for DG + 15%GF* (4.5% to 3%) and DG + 30%GF* (< 3.3% to < 2.9%). This gradation seems logical, as the margin for improvement is larger for unblended desalted glycerol and gradually narrows as the amount of GF* increases. The positive effect of GF* on combustion quality can be clearly observed by comparing the different curves for fixed propane. The excess oxygen required to keep CO below 100 ppm is a useful index for this purpose: by adding 15% GF*, the oxygen concentration decreases from 4% to 3% for 0.5 Nm^3/h of propane and from > 7.3% to 4.5% when no support fuel is used. If the proportion of GF* is increased to 30%, an additional displacement of CO curves to lower excess oxygen is evident for both test series.

NOx emissions tend to increase with the amount of GF*. This can perfectly be the consequence of a 'better' combustion (higher temperature, better dispersion of fuel vapor in the air flow). In principle, this could be compensated by modifying the burner aerodynamics (e.g., the split between primary and secondary air), especially when the fuel allows a relatively wide range of stable flame operating conditions, but this was not the objective of the study and no attempt in this regard was made.

As in the case of single droplets tests, the behavior of unblended crude (not desalted) glycerol and the effect of acetals addition were also

investigated in the semi-industrial furnace. The results obtained are displayed in Fig. 8 in terms of the CO and NOx emissions measured for the different test series performed with CG, DG ant their corresponding blends with GF*30. The curves show that CG combustion is also improved by GF* addition but this effect is much less intense (for 0.5 Nm^3/h of propane, excess oxygen decreases only from < 3.4% to 2.5%) than in the tests with DG where a reduction of several orders of magnitude in the CO levels is achieved (Fig. 7).

Conversely, it is observed that the desalting process seems to have a negative effect on glycerol combustion as it rises significantly the CO levels, especially when no auxiliary fuel is used: whereas for CG less than 4.7% oxygen is enough to keep CO emissions below the 100 ppm threshold, it must be increased over 7.3% when burning DG. Although the great differences in scale of the facilities used in this work prevents a direct comparison of the results here discussed, this effect could be related to the distinct combustion behavior noticed in the DG droplet tests. As previously explained, DG droplets undergo an initial period characterized by both swelling and puffing events not observed with CG, but the final shattering due to microexplosions is delayed with respect to CG. This is expected to result in a slower and delayed production of fuel vapor in the DG flame, which may also negatively affect the fuel-air mixing and explain the higher excess oxygen required to achieve good flame stability and a nearly-complete conversion to CO$_2$. In any case, further research would be needed to ascertain these phenomena which are out of the scope of this work.

Information about the flame configuration and appearance was gained from color images recorded with a video camera. The acquisition rate was fixed at 117 fps, resulting in 351 snapshots for each condition, which were subsequently processed to derive a representative mean image. Fig. 9 is an example of the flame appearance for the three fuels tested. The images reflect the commented differences in the combustion behavior, showing brighter flames as the acetal percentage in the mixture is increased. As found for the droplet tests
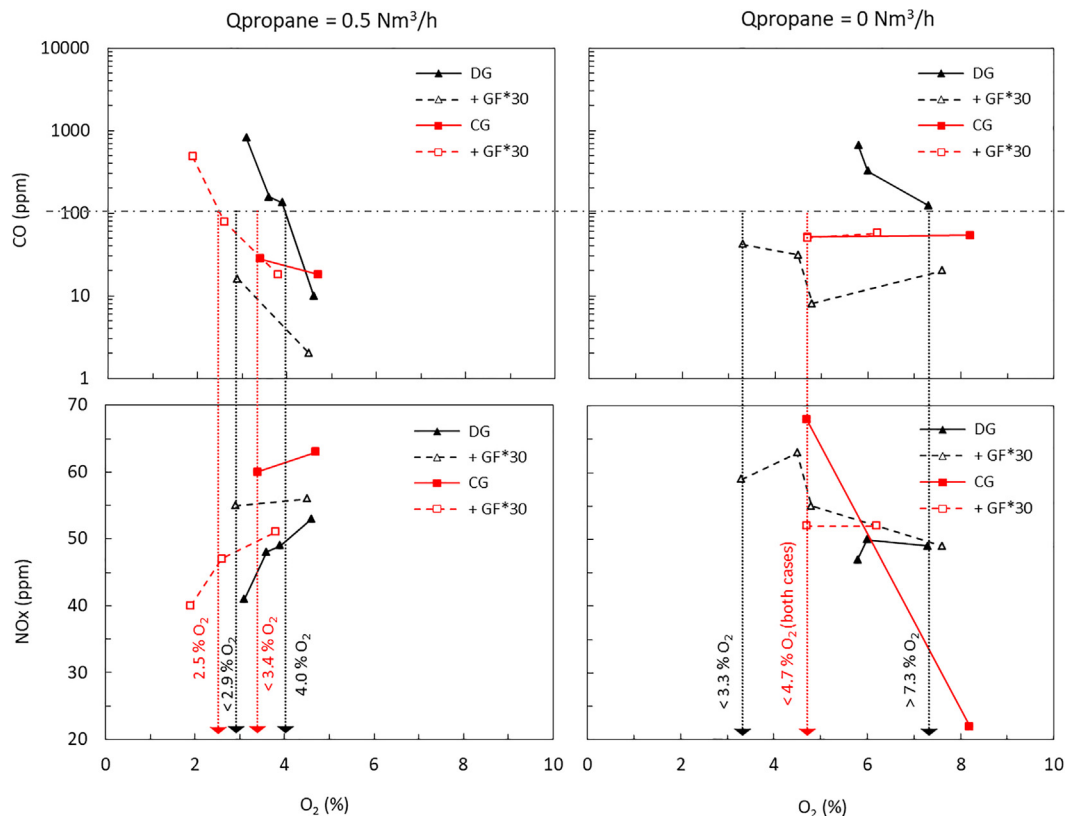

Fig. 8. Emissions of CO (top) and NOx (bottom) measured in the tests with crude and desalted glycerol (CG and DG, respectively) and their blends with 30% GF* when burning with 0.5 (left) and 0 Nm^3/h (right) of propane. The excess oxygen required in each case for quality combustion (CO < 100 ppm) are also indicated.
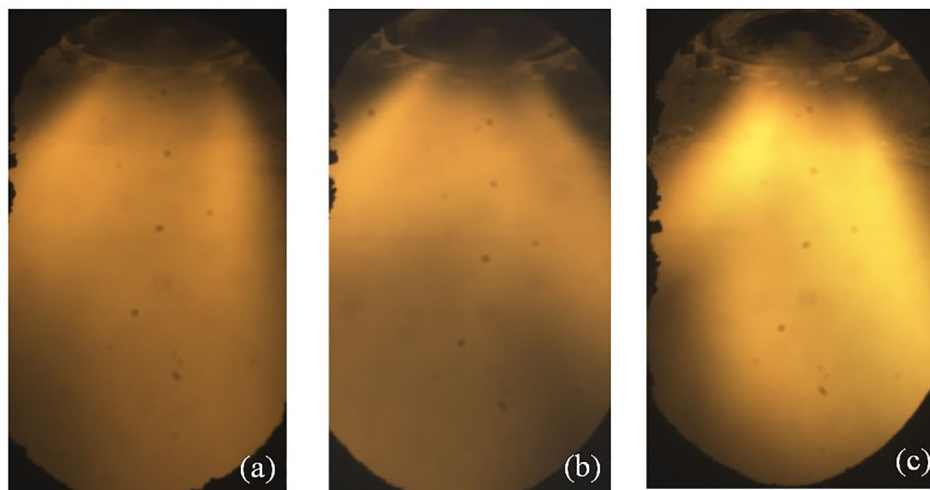
Fig. 9. Flame images with DG (a) and its blends with 15% GF* (b) and 30% GF* (c). 0.5 Nm³/h of propane in all cases. Oxygen concentrations were 3.6, 4.0 and 2.9%, respectively.

(Fig. 5), the spectrograph confirmed that the orangish color corresponds to the emission band of excited sodium.

The intensity distribution of each flame image was analyzed and the corresponding axial position of the center of mass was calculated. This parameter, represented in Fig. 10, is indicative of the location of the region where glycerol is burned (since luminosity is dominated by the orange emission due to sodium). In general, the addition of GF* tends to shorten that distance, which seems consistent with an enhanced flame stability. However, it should be noted that when GF* increases from 15% to 30%, the opposite trend is observed; a similar change appears when propane is added. The longer average distance when propane or a high amount of GF* is used might reflect the preferential burning of those more reactive fuels, whereas glycerol combustion (the main origin of the luminosity) is delayed. Therefore, in this case, the location of the visible flame may not always be a reliable stability index. An additional analysis was performed in terms of the amplitude of the oscillations of radiation in the OH* band measured by a photo-multiplier. Fig. 10 shows the rms of the photomultiplier signal, normalized by the mean value. In all cases, the amplitude of the oscillations consistently decreased when either propane or GF* was added, as further confirmation of the improved stability achieved when using a supporting secondary fuel or blending glycerol with acetals.

5. Conclusions

The combustion characteristics of an industrial crude glycerol sample, both as received from a biodiesel plant (CG) and desalted (DG), were studied along with those of a mixture of acetals named GF* and obtained as a by-product of FAGE production. The effect of GF* addition on the combustion of glycerol was studied at two different scales, namely through single-droplet combustion tests and by means of experiments in a semi-industrial furnace.

The single-droplet combustion tests showed that CG displayed very similar evaporation and burning rates to those of pure glycerol, although the consistent occurrence of microexplosions effectively reduced the CG droplet consumption times. The shattering events were reported to be considerably fast (< 0.5 ms) and violent, with the droplets being practically disintegrated afterwards. Desalted crude glycerol on the other hand, exhibited a completely different behavior, with droplet swelling and puffing just after completing the initial heat-up period, and with a characteristic time in the order of a few milliseconds. These phenomena concur with other single droplet works on liquid mixtures and emulsions under similar experimental conditions, and is therefore ascribed to the homogeneous nucleation of the most volatile compounds within DG. By contrast, CG microexplosion typology is consistent with that of a previous work, where the salt content was found to be responsible for the shattering events. The acetal mixture GF* displayed a more conventional behavior, with markedly higher burning rates, shorter heat-up initial transients and a smooth and sustained evaporation which lasted until droplet burnout. The addition of GF* did not appear to drive drastic changes in the studied single droplet combustion behaviors for CG, although it suppressed the swelling and
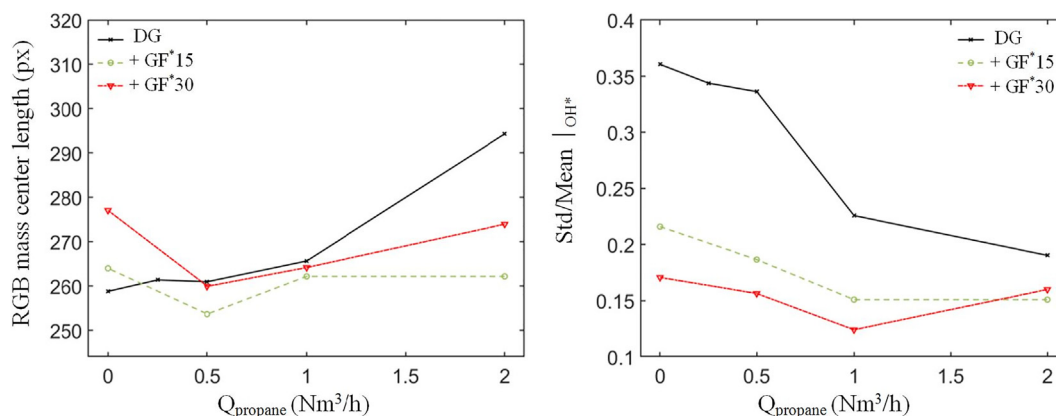

Fig. 10. Axial location of the centre of mass in flame images (left) and the fluctuations level (right) for the flames of DG and its blends with 15% GF* and 30% GF* for different mass flow rates of auxiliary gas (propane). Oxygen concentrations ranged from 2.9% to 6.0%.

puffing stages for DG. In both cases, it progressively increased the burning rates and slightly accelerated the microexplosion onset favoring glycerol conversion.

The combustion behavior of the same fuels (CG, DG and mixtures with GF*) were also tested in a semi-industrial furnace. The results confirmed that the addition of GF* widened the range of stable combustion, significantly reduced CO emissions and notably improved flame stability (as determined from its flickering amplitude), especially in the case of DG. The blends showed a slight increase of NOx emissions, although this might be compensated by optimizing burner aerodynamics (facilitated by the enhanced flame stability). These benefits can also be interpreted from the perspective of a partial or total reduction in the use of premium fuels (natural gas, propane), as GF* can also act as a support fuel, with the advantage of being of renewable nature. In contrast, the results showed that glycerol desalting may result in some increase in the CO levels and, therefore, in the excess oxygen required to reach optimal flame stability and combustion efficiency.

Acknowledgements

References

[1] J.C. Thompson, B.B. He, Characterization of crude glycerol from biodiesel production from multiple feedstocks, Appl. Eng. Agric. 22 (2006) 261–265.

[2] S. Hu, X. Luo, C. Wan, Y. Li, Characterization of crude glycerol from biodiesel plants, J. Agric. Food. Chem. 60 (2012) 5915–5921.

[3] B. Metzger, Glycerol Combustion, MSc. Thesis, North Carolina State University Raleigh, NC, USA, 2007.

[4] M.D. Bohon, B.A. Metzger, W.P. Linak, C.J. King, W.L. Roberts, Glycerol combustion and emissions, Proc. Combust. Inst. 33 (2011) 2717–2724.

[5] S.A. Steinmetz, J.S. Herrington, C.K. Winterrowd, W.L. Roberts, J.O. Wendt, W.P. Linak, Crude glycerol combustion: particulate, acrolein, and other volatile organic emissions, Proc. Combust. Inst. 34 (2013) 2749–2757.

[6] P. Queirós, M. Costa, R. Carvalho, Co-combustion of crude glycerin with natural gas and hydrogen, Proc. Combust. Inst. 34 (2013) 2759–2767.

[7] L. Jiang, A.K. Agrawal, Combustion of straight glycerol with/without methane using a fuel-flexible, low-emissions burner, Fuel 136 (2014) 177–184.

[8] W.-C. Huang, S.-S. Hou, T.-H. Lin, Combustion characteristics of a 300 kWth oil-fired furnace using castor oil/diesel blended fuels, Fuel 208 (2017) 71–81.

[9] H. Pawlak-Kruczek, M. Ostrycharczyk, J. Zgóra, Co-combustion of liquid biofuels in PC boilers of 200 MW utility unit, Proc. Combust. Inst. 34 (2013) 2769–2777.

[10] A. Krutof, K. Hawboldt, Blends of pyrolysis oil, petroleum, and other bio-based fuels: a review, Renew. Sustain. Energy Rev. 59 (2016) 406–419.

[11] J.S.J. Alonso, C. Romero-Ávila, L.S.J. Hernández, A.-K. Awf, Characterising biofuels and selecting the most appropriate burner for their combustion, Fuel Process. Technol. 103 (2012) 39–44.

[12] M. Lapuerta, J. Rodríguez-Fernández, C. Estevez, N. Bayarri, Properties of fatty acid glycerol formal ester (FAGE) for use as a component in blends for diesel engines, Biomass Bioenerg. 76 (2015) 130–140.

[13] M. Lapuerta, I. González-García, I. Céspedes, C. Estévez, N. Bayarri, Improvement of cold flow properties of a new biofuel derived from glycerol, Fuel 242 (2019) 794–803.

[14] M. Angeloni, P. Remacha, A. Martínez, J. Ballester, Experimental investigation of the combustion of crude glycerol droplets, Fuel 184 (2016) 889–895.

[15] Á. Muelas, P. Remacha, J. Ballester, Droplet combustion and sooting characteristics of UCO biodiesel, heating oil and their mixtures under realistic conditions, Combust. Flame 203 (2019) 190–203.

[16] T. Li, D. Zhu, N. Akafuah, K. Saito, C. Law, Synthesis, droplet combustion, and sooting characteristics of biodiesel produced from waste vegetable oils, Proc. Combust. Inst. 33 (2011) 2039–2046.

[17] C. Wang, X. Liu, C. Law, Combustion and microexplosion of freely falling multi-component droplets, Combust. Flame 56 (1984) 175–197.

[18] J. Ballester, J. Barroso, L. Cerecedo, R. Ichaso, Comparative study of semi-industrial-scale flames of pulverized coals and biomass, Combust. Flame 141 (2005) 204–215.

[19] J. Ballester, C. Dopazo, N. Fueyo, M. Hernández, P.J. Vidal, Investigation of low-NOx strategies for natural gas combustion, Fuel 76 (1997) 435–446.

[20] J. Ballester, C. Dopazo, Drop size measurements in heavy oil sprays from pressure-swirl nozzles, At. Sprays 6 (1996) 377–408.

[21] J. Ballester, C. Dopazo, Experimental study of the influence of atomization characteristics on the combustion of heavy oil, Combust. Sci. Technol. 103 (1994) 235–263.

[22] C.R. Shaddix, D.R. Hardesty, Combustion properties of biomass flash pyrolysis oils, Report No. SAND99-8238, Sandia National Laboratories, 1999.

[23] H. Li, C. Rosebrock, N. Riefler, T. Wriedt, L. Mädler, Experimental investigation on microexplosion of single isolated burning droplets containing titanium tetra-isopropoxide for nanoparticle production, Proc. Combust. Inst. 36 (2017) 1011–1018.

[24] H.Y. Setyawan, M. Zhu, Z. Zhang, D. Zhang, Ignition and combustion characteristics of single droplets of a crude glycerol in comparison with pure glycerol, petroleum diesel, biodiesel and ethanol, Energy 113 (2016) 153–159.

[25] J. Lasheras, A. Fernandez-Pello, F. Dryer, Experimental observations on the disruptive combustion of free droplets of multicomponent fuels, Combust. Sci. Technol. 22 (1980) 195–209.

[26] J. Lasheras, A. Fernandez-Pello, F. Dryer, Initial observations on the free droplet combustion characteristics of water-in-fuel emulsions, Combust. Sci. Technol. 21 (1979) 1–14.

[27] J. Lasheras, A. Fernandez-Pello, F. Dryer, On the disruptive burning of free droplets of alcohol/n-paraffin solutions and emulsions, Symp. (Int.) Combust. 18 (1980) 293–305.

Pyrolysis effects during high-temperature vaporization of alkane droplets

Álvaro Muelas [a,*], Jaime Carpio [b], Javier Ballester [c], Antonio L. Sánchez [d], Forman A. Williams [d]

[a] Laboratory of Research on Fluid Dynamics and Combustion Technologies (LIFTEC), CSIC–University of Zaragoza, Spain
[b] E. T. S. I. Industriales, Universidad Politécnica de Madrid, Madrid 28006, Spain
[c] Fluid Mechanics Group/LIFTEC, School of Engineering and Architecture, CSIC-University of Zaragoza, María de Luna, 3, Zaragoza 50018, Spain
[d] Dept. Mechanical and Aerospace Engineering, University of California San Diego, La Jolla, CA 92093-0411, USA

ABSTRACT

The temporal evolution of the droplet radius is measured experimentally in high-temperature inert atmospheres for three different alcohols (ethanol, n-butanol, and glycerol) and three alkanes (n-heptane, n-dodecane, and n-hexadecane). It is shown that, while accompanying theoretical predictions of droplet-radius variations show excellent accuracy for the three alcohols, the three alkanes exhibit vaporization rates that are significantly smaller than those predicted theoretically. The accompanying observation of significant soot formation suggests that endothermic fuel pyrolysis may be responsible for the diminished vaporization rate. The quantification of this phenomenon is investigated here using a one-step irreversible reaction with an Arrhenius rate to model the fuel decomposition. It is shown how an analytical description developed on the basis of activation-energy asymptotics can be used in combination with the experimental measurements of the temporal droplet-radius evolution to adjust the fuel-pyrolysis kinetics, embodied at leading order in an effective pyrolysis temperature, which is obtained for n-heptane, n-dodecane, and n-hexadecane.

1. Introduction

Because of its numerous related applications, the problem of individual-droplet vaporization has been studied at length (see, e.g., [1,2] for reviews). Although the initial work focused on isothermal evaporation of a drop surrounded by an atmosphere at the same temperature, attention soon turned to the problem of a droplet vaporizing in a hot atmosphere [3,4], that being especially of interest in combustion applications. Useful analytical expressions for the rate of droplet vaporization were reported by Godsave and Spalding at the fourth combustion symposium [5,6]. These early modeling efforts have been complemented over the years to account for effects of relative droplet-gas motion, multi-component composition of liquid fuels, and internal circulation of the liquid, as described, for example, in [7].

In most spray-combustion applications, droplets primarily burn in a group-combustion regime, with the fuel that originates from the vaporizing droplets burning with the ambient oxygen in a flame that surrounds the droplet cloud (see [8] for a recent review of spray combustion). Since fuel oxidation in the atmosphere surrounding each individual droplet (i.e. at distances of the order of the droplet radius) is negligibly small in the group-combustion regime, theories addressing droplet vaporization in a hot inert atmosphere [9] provide adequate quantification of the resulting droplet vaporization rate for spray-combustion computations. The present paper explores vaporization-rate departures encountered in liquid-hydrocarbon droplets when the ambient thermal conditions promote significant pyrolysis of the fuel vapor. As explained below, this effect becomes significant at high ambient temperatures exceeding about 1000 K, often encountered in liquid-fuel burners, when the characteristic time of thermal hydrocarbon decomposition becomes comparable to the characteristic diffusion time around the droplet. Under those conditions, a significant fraction of the heat transferred from the hot atmosphere is employed to pyrolyze the fuel, thereby reducing the amount of heat available to heat up and vaporize the liquid fuel.

The motivation for the present study is to help to ascertain how accurately classical theories of droplet vaporization can be applied in describing the spray combustion processes that occur in the group-combustion regime. Since transient droplet evaporation is

likely to be of relevance in the interior of groups under such conditions, experiments were designed under which time-dependent effects are significant. Comparisons of measured and computed histories can test how well the theoretical descriptions perform. For some fuels, soot formation through fuel pyrolysis may occur during group combustion in the outer portions of the group, where the temperatures of the gases surrounding the droplets are higher. Excessive soot formation generally is detrimental, and the extent to which it may be present and interact with the droplet vaporization processes is poorly understood. Soot-production chemistry may occur either in the inner quasi-steady zone that develops around a droplet during the later stages of evaporation or in outer fully transient zones [10] farther away from the droplets in the spray. The present investigation addresses, for the first time, the first of these two possibilities, offering a new theoretical simplification that may prove useful in future analyses of spray combustion in the group-combustion regime. The new theoretical description, motivated by the present experimental measurements, may impact future computational investigations of spray combustion, leading to improved fidelity in combustor designs.

The paper begins by presenting illustrative experimental results corresponding to alcohol and alkane droplets vaporizing in a hot inert atmosphere. The measured temporal variation of the droplet radius is compared with standard predictions based on a chemistry-free droplet-vaporization model, yielding excellent agreement for alcohol vaporization. For the alkane droplets, however, the predictions show significant departures from the experimental measurements, with relative differences being more pronounced for heavier fuel molecules and also at higher ambient temperatures. The reduced vaporization rate measured in the experiments is attributed here to decreased rates of heat transfer to the liquid caused by endothermic fuel pyrolysis, consistent with the appearance of soot, which was observed in all alkane experiments. In an effort to improve quantification of the process, a new theory of droplet vaporization in the presence of fuel pyrolysis is developed here. The strong temperature sensitivity of the pyrolytic reactions is exploited in our large-activation-energy analysis, with the fuel decomposition occurring in a thin layer at a fixed pyrolysis temperature, a property of the fuel whose approximate value is evaluated from the vaporization rate measured experimentally.

2. Experimental measurements

Six different fuels were employed in this study, namely three alcohols (ethanol, n-butanol, and glycerol) and three alkanes (n-heptane, n-dodecane, and n-hexadecane). All the samples used in the tests were above 99.0% in purity. The evaporation process of these liquid-fuel droplets was studied in the Droplet Combustion Facility (DCF) available at LIFTEC, represented schematically in Fig. 1. Since a detailed description of this facility can be found in a recent publication [11], only its most relevant features will be given below.

A stream of free-falling droplets was generated at a piezoelectric device, with droplet initial radii (a_0) of 72.5 µm for ethanol and butanol and 75 µm for the rest of fuels. It is noteworthy that these radii are in a range often encountered in practical applications, while larger droplets often had to be employed in other experimental investigations. The droplet-generation frequency was fixed at 25 Hz, providing interdroplet distances large enough to avoid interactions between droplets [12]. The droplet-generation steadiness was thoroughly checked, primarily at the first position that allowed optical access to the combustion chamber (i.e., 3 mm below the droplet injection point), yielding a deviation in a_0 as low as 0.3 µm throughout the course of the experiments (rms value for all the tests). Glycerol had to be

preheated to 100° C prior to its atomization in order to lower its viscosity, whereas the rest of the fuels were atomized at room temperature.

The droplets were injected into the inert combustion products of a McKenna flat-flame burner, which provided the inert hot coflow required for the liquid-fuel evaporation and pyrolysis. This burner was fed with different stoichiometric mixtures of CH_4, H_2, O_2, CO_2, and air, as to provide a coflow gas mixture of N_2, CO_2, and H_2O at the desired temperature T_∞. Since the droplets are injected through an orifice, this target temperature T_∞ is achieved at a finite distance of the order of 10 mm from the burner. Further downstream the temperature along the droplet trajectory remains equal to T_∞, as verified in temperature measurements with a thin S-type thermocouple having a 50-µm diameter (see Appendix C of the Supplementary materials of [11] for details of the temperature profile).

All fuels were tested for a target temperature $T_\infty = 1730$ K. Additionally, hexadecane was also tested at a lower target temperature, $T_\infty = 1311$ K, achieved by modifying the reactant feed to the flat-flame burner. In these inert gas mixtures, the vaporization of alcohol droplets proceeds with negligible chemical activity. For alkane droplets, however, significant fuel pyrolysis is present at the high temperatures employed in the experiments, as revealed by the appearance of visible soot traces, shown in Fig. 1b for heptane and dodecane. As discussed below, the endothermic fuel decomposition has an important effect on the resulting vaporization rate.

The coflow velocity was measured for the standard coflow condition $T_\infty = 1730$ K by means of the PIV technique using a Nd:YAG laser with Al_2O_3 0.3 µm particles as tracers, thereby allowing quantification of the relative droplet-coflow velocity. The optical setup was fixed, the flat-flame burner being moved vertically to vary the residence time of the droplet in the hot gas prior to measurement. The droplet vaporization process was measured by images acquired with a backlit CCD camera (QImaging Retiga SRV) fitted with a long-distance microscope, which was employed to determine both the size and velocity histories of the free-falling droplets. The spatial resolution for this optical setup was 1.4 µm/pixel, allowing us to capture with good accuracy droplets above 25 µm in diameter. The backlight used was an LED stroboscope programmed to shoot sequential flashes every 0.5 ms. This, in combination with the exposure time of the camera, permitted recording of two sequential shots of the same droplet in each photograph, as displayed in Fig. 1c. Subsequent automatic post-processing of these images was carried out in Matlab to extract the droplet sizes and velocities in a precise and repeatable way. Associated Reynolds numbers for the flow around the droplet were found to be smaller than 0.5 throughout the entire recorded droplet lifetimes, with typical values on the order of 0.2 during most of the droplet vaporization history. The results of the droplet measurements provide the variation of the squared droplet radius a^2 with the residence time t in the hot gas, represented by symbols in Fig. 2 for the six fuels considered here (the accompanying curves in the figure correspond to theoretical predictions, to be discussed below).

As can be inferred from the curves in Fig. 2, vaporization is negligible during the initial droplet heat-up period, which is longer for fuels with higher boiling temperature (i.e. glycerol, dodecane, and hexadecane). For these fuels, the decrease in the liquid-fuel density associated with the temperature increase leads to a noticeable increase in the droplet radius during this stage. Vaporization begins once the droplet-surface temperature reaches a value close to the boiling temperature and continues until the droplet disappears. As expected, most of the vaporization occurs with a constant slope da^2/dt, achieved when the droplet reaches a uniform constant temperature.
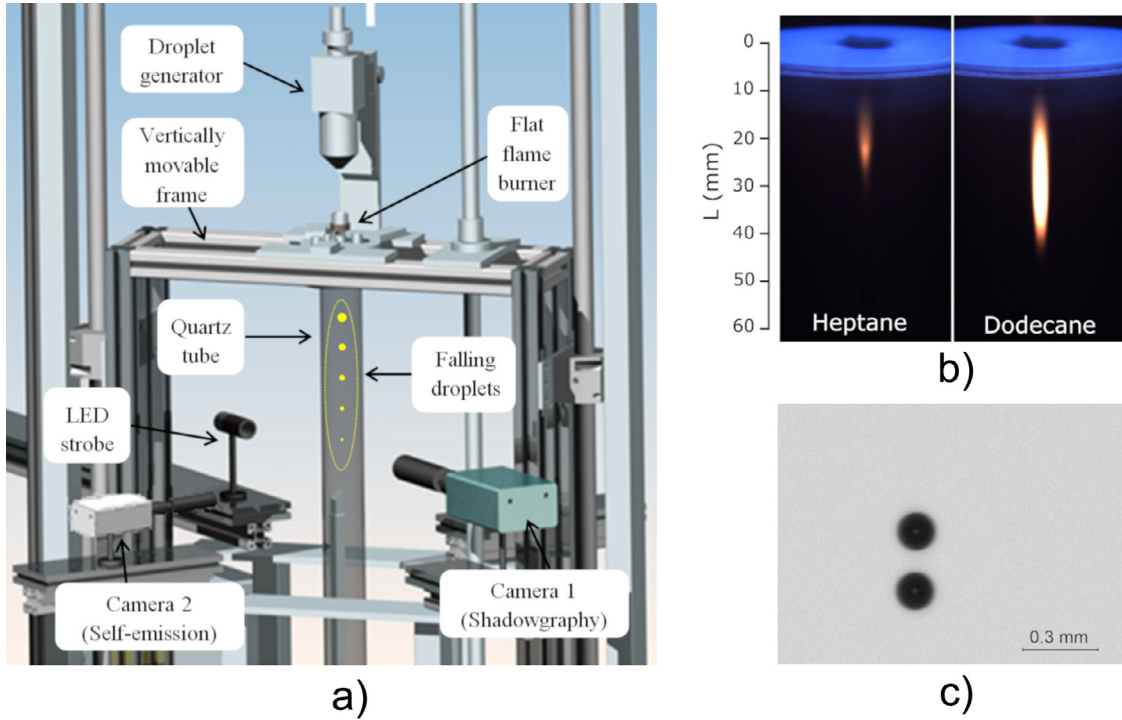
Fig. 1. A schematic view of the experimental facility employed in this paper (a). The pictures on the right-hand side corresponds to macroscopically visible traces created by soot thermal emission for the heptane and dodecane tests (b) and to double-exposure photography of a free-falling hexadecane droplet (c).

3. Predictions of droplet vaporization

The experimental measurements of the droplet-radius temporal evolution $a(t)$ were compared with theoretical predictions obtained following the standard theory of droplet vaporization in an inert environment at temperature T_∞ [7]. For the small values of the droplet Reynolds number found in the experiments, corrections associated with forced-convection effects remain negligibly small, so that the flow is effectively spherico-symmetrical. Correspondingly, all variables are functions of the time t and the radial distance $\tilde{r}$ to the droplet center. The evolution of the temperature inside the droplet $T_l(\tilde{r}, t)$ from its initial uniform value $T_l(\tilde{r}, 0) = T_0$ was computed by integration of the energy equation

$$\rho_l c_l \frac{\partial T_l}{\partial t} = \frac{1}{\tilde{r}^2} \frac{\partial}{\partial \tilde{r}} \left(\kappa_l \tilde{r}^2 \frac{\partial T_l}{\partial \tilde{r}} \right) \begin{cases} \tilde{r} = 0: & \frac{\partial T_l}{\partial \tilde{r}} = 0 \\ \tilde{r} = a: & 4\pi \kappa_l a^2 \frac{\partial T_l}{\partial \tilde{r}} = \dot{q}_d \end{cases} \quad (1)$$

while the droplet radius $a(t)$ is computed from the integrated form of the continuity equation

$$\frac{d}{dt} \left(4\pi \int_0^a \rho_l \tilde{r}^2 d\tilde{r} \right) = -\dot{m}, \quad (2)$$

subject to the initial condition $a(0) = a_0$. The density ρ_l, specific heat c_l, and thermal conductivity κ_l of the liquid fuel are functions of the temperature.

The droplet vaporization rate $\dot{m}$ and the droplet heating rate $\dot{q}_d$ appearing above are determined from the analysis of the quasi-steady spherico-symmetrical structure of the gas flow surrounding the droplet, which can be described in terms of the gas temperature T and fuel-vapor mass fraction Y. For the cases considered here, corrections arising from unsteady gas-phase effects, scaling with the inverse square root of the liquid-to-ambient density ratio [10], remain small, and have been correspondingly neglected in our analysis. The solution depends on the value of the droplet-surface temperature T_s, related to the surface value of the fuel-vapor mass

fraction Y_s by the Clasius–Clapeyron relation

$$Y_s = \left[Y_s + \frac{M_F}{M_I} (1 - Y_s) \right] \exp \left[\frac{L_v}{R_F T_B} - \frac{L_v}{R_F T_s} \right] \quad (3)$$

involving the molecular masses of the fuel and the inert M_F and M_I, the boiling temperature T_B, the latent heat of vaporization L_v, and the fuel constant $R_F = R_o/M_F$, with R_o representing the universal gas constant. To facilitate the description, the analysis is carried out by assuming that the gas thermal conductivity κ, specific heat at constant pressure c_p, and fuel Lewis number $L = \kappa/(\rho c_p D)$, with D denoting the fuel-vapor diffusivity, take uniform values, obtained with use of the so-called "1/3 rule" [13], as explained below. The accuracy of this widely used approximation in describing alcohol and alkane droplet vaporization was tested by comparisons with numerical integrations accounting for the variation of κ, c_p, and L with temperature and composition. For the conditions considered below, the observed differences in resulting vaporization rates were found to be negligibly small, in agreement with early findings [13], thereby justifying the adoption of this constant-property simplification.

Integration of the energy and fuel-vapor conservation equations, subject to the boundary conditions $T = T_s$ and $Y = Y_s$ at $\tilde{r} = a$ and $T = T_\infty$ and $Y = 0$ as $\tilde{r} \to \infty$, leads to the familiar expressions

$$\lambda = \frac{\dot{m}}{4\pi \kappa a/c_p} = \frac{1}{L} \ln \left(\frac{1}{1 - Y_s} \right) \quad (4)$$

for the dimensionless vaporization rate λ and

$$\frac{\dot{q}_d}{4\pi \kappa a L_v/c_p} = \lambda \left[\frac{c_p (T_\infty - T_s)/L_v}{e^\lambda - 1} - 1 \right] \quad (5)$$

for the dimensionless droplet heating rate.

The above expressions (4) and (5), supplemented with (3), are used in integrating (1) and (2). Following standard practice [13], properties of the fuel-inert gas mixture are evaluated using reference values of the temperature $T_{\text{ref}} = T_s + (T_\infty - T_s)/3$ and fuel
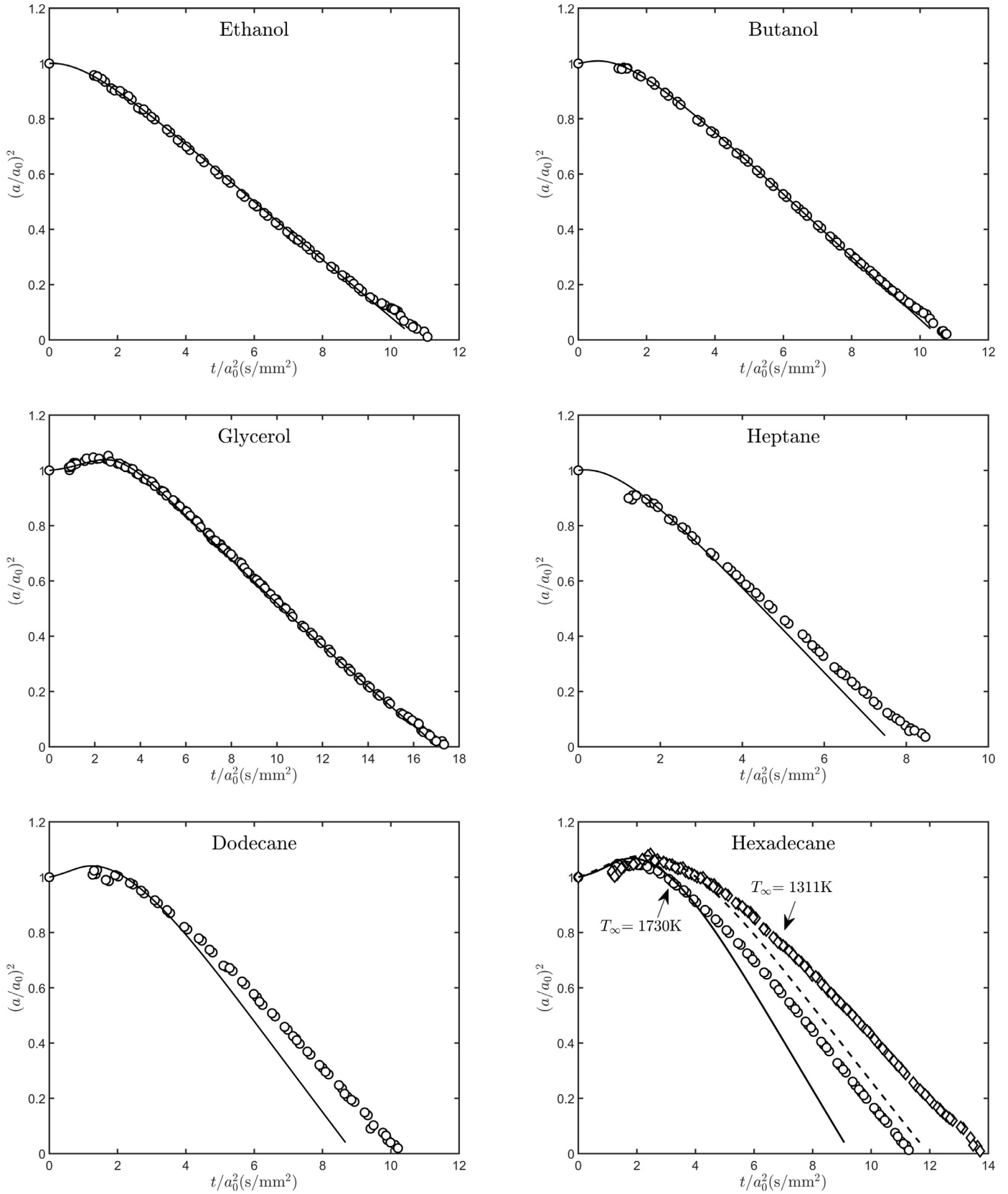
Fig. 2. The variation with time of the droplet radius as obtained from post-processing the images taken at different distances from the injection point (symbols) and as obtained with the theoretical predictions corresponding to vaporization of a spherical droplet in a quasi-steady chemically frozen gaseous atmosphere. In all cases, the target temperature of the gaseous coflow was $T_\infty = 1730$ K, with additional results given for hexadecane at $T_\infty = 1311$ K.

mass fraction $Y_{\text{ref}} = 2Y_s/3$. For example, the density ρ is computed at T_{ref} as that of an ideal gas mixture of fuel and inert with mass fractions Y_{ref} and $1 - Y_{\text{ref}}$, respectively. The thermal conductivity κ and the fuel diffusivity D are evaluated using mixture-average expressions [14], with the thermal conductivity of each gaseous species and the binary diffusivity of the fuel into each inert species evaluated at the reference temperature T_{ref}. The specific heat c_p is taken to be that of the fuel vapor at T_{ref} [13].

The evolution of the droplet radius with time, obtained from integrations of the above problem for the six fuels considered here, is shown in the curves of Fig. 2, where the small effects of initial departures from the target temperature T_∞ have been taken into account. As can be anticipated from (3), since $L_v \gg R_F T_B$ for all fuels tested here, with the injection droplet temperature T_0 being significantly below the boiling temperature T_B (i.e. for $(T_B - T_0)/T_B \gg [L_v/(R_F T_B)]^{-1}$), the fuel-vapor mass fraction at the droplet surface is initially negligible. During this initial stage it is thus found from (4) that $\lambda \simeq 0$, while the droplet heating rate is $\dot{q}_d = 4\pi \kappa a (T_\infty - T_s)$, as follows from (5). During this heat-up period the droplet mass, $4\pi \int_0^a \rho_l \tilde{r}^2 d\tilde{r}$, remains constant, but its radius increases as a result of the decreasing liquid-fuel density $\rho_l(T_l)$. Significant vaporization begins to occur as T_s reaches values such that $(T_B - T_s)/T_B \sim [L_v/(R_F T_B)]^{-1}$. As vaporization proceeds further, a stage is reached in which the temperature inside the droplet reaches a constant uniform value equal to T_s and the reduced vaporization rate reaches the familiar Spalding value [5,6]

$$\lambda = \ln\left(1 + \frac{c_p(T_\infty - T_s)}{L_v}\right), \tag{6}$$

as follows from (5) when $\dot{q}_d = 0$, with corresponding constant values of T_s and Y_s, determined from (3) and (4). During this final vaporization stage the mass-conservation Eq. (2) reduces to the so-called d^2−law

$$\frac{da^2}{dt} = -\frac{2\kappa}{\rho_l c_p}\lambda, \tag{7}$$

so that the curves representing the variation with time of the square of the droplet radius become straight lines with negative slope.

As can be observed in Fig. 2, the agreement between the droplet vaporization model and the experiments is remarkably good for the three alcohols, whereas for alkanes the model tends to over-predict the vaporization rate, with over-predictions becoming larger for larger molecular weight. The departures are especially noticeable during the final stage, with the model consistently over-predicting the constant slope $-da^2/dt$. In order to quantify these deviations, the curves shown in Fig. 2 were fitted to straight lines using the least-squared method to extract the quasi-steady vaporization rates of the different fuels. The selected interval for this fitting was $0.2 \le (a/a_0)^2 \le 0.6$, a convenient intermediate region, where the initial heating transient can be considered to be essentially completed while the droplet radius is large enough to avoid the higher experimental uncertainties related to the measurement of very small droplets. The values of $-da^2/dt$ extracted from the experiments are listed in Table 1 along with the theoretical predictions. It can be seen in the table that the theoretical predictions and the experimentally measured values are in excellent agreement for the three alcohols, with relative errors remaining below 5% in all three cases. By way of contrast, the experimentally measured values for the three alkanes differ significantly from the corresponding theoretical predictions. The largest departures correspond to hexadecane at high temperature.

The reduced vaporization rate seems to indicate that the alkane droplets effectively see an ambient temperature that is lower than the actual ambient temperature of the coflow. This, along with the

observation of soot formation, is consistent with the presence of endothermic pyrolysis. The needed theoretical description of the problem is given below.

Values of $-da^2/dt$ (mm^2/s)		
Fuel	Experiments	Theoretical predictions
Ethanol	0.1001	0.1049
Butanol	0.1093	0.1137
Glycerol	0.0781	0.0756
Heptane	0.1363	0.1537
Dodecane	0.1337	0.1639
Hexadecane ($T_\infty = 1730$ K)	0.1329	0.1771
Hexadecane ($T_\infty = 1311$ K)	0.1156	0.1352

4. A model for droplet vaporization with fuel-vapor pyrolysis

If the ambient temperature is high enough, the gaseous alkane molecules C_nH_{2n+2} may decompose into smaller molecules through an endothermic process that lowers the gas temperature. The associated thermal kinetics is known to involve numerous elementary reactions [15]. The dominant pathway and the resulting products arising from decomposition of a given fuel depend on the combustion conditions. All of these complicating details do not need to be accounted for in our analysis, focused on global effects arising from the endothermic nature of the thermal hydrocarbon pyrolysis chemistry. Instead, for our purposes it suffices to model the pyrolytic kinetics with a single irreversible reaction, with the associated energetics evaluated by assuming that C_2H_4 is the main product of pyrolysis. Depending on the number of carbon atoms n present in the alkane molecule, the overall reaction is either $C_nH_{2n+2} \rightarrow \frac{n-1}{2}C_2H_4 + CH_4$ (when n is odd) or $C_nH_{2n+2} \rightarrow \frac{n-2}{2}C_2H_4 + C_2H_6$ (when n is even). The amount of heat needed to pyrolyze a unit mass of fuel vapor q can be correspondingly obtained from the enthalpies of formation of C_nH_{2n+2}, C_2H_4, CH_4, and C_2H_6 to give, for instance, $q = (2.70, 2.75, 2.90)$ MJ/kg for heptane, dodecane, and hexadecane, respectively. These values are much smaller than the associated heat of combustion, slightly above 47 MJ/kg for all three fuels, but much larger than their latent heat of vaporization at T_B, given by $L_v = (0.313, 0.261, 0.224)$ MJ/kg for heptane, dodecane, and hexadecane.

The fuel decomposition rate ω (mass of fuel consumed per unit volume per unit time) will be modeled with the Arrhenius expression

$$\omega = \rho BY \exp\left(-\frac{E_a}{R_o T}\right), \tag{8}$$

where ρ is the density and B and E_a are the preexponential frequency factor and activation energy, respectively. For constant values κ, c_p, and $L = \kappa/(\rho c_p D)$ the problem reduces to that of integrating

$$\frac{\lambda}{r^2}\frac{dY}{dr} - \frac{1}{L}\frac{1}{r^2}\frac{d}{dr}\left(r^2\frac{dY}{dr}\right) = -\frac{B}{\kappa/(\rho c_p a^2)}Y\exp\left(-\frac{E_a}{R_o T}\right), \tag{9}$$

$$\frac{\lambda}{r^2}\frac{d}{dr}(c_p T/q) - \frac{1}{r^2}\frac{d}{dr}\left(r^2\frac{d}{dr}(c_p T/q)\right)$$
$$= -\frac{B}{\kappa/(\rho c_p a^2)}Y\exp\left(-\frac{E_a}{R_o T}\right), \tag{10}$$

with boundary conditions

$$T(1) - T_s = Y(1) - Y_s = 0 \quad \text{and} \quad T(\infty) - T_\infty = Y(\infty) = 0. \tag{11}$$

Here $r = \tilde{r}/a$ represents the radial distance to the center of the droplet scaled with the droplet radius. The rescaled vaporization rate λ defined in the first equation of (4) appears as an eigenvalue,

to be determined with the additional mass-conservation condition

$$\lambda = \lambda Y_s - \frac{1}{L}\frac{dY}{dr}\bigg|_{r=1} \tag{12}$$

at the droplet surface, where energy conservation provides

$$\frac{\dot{q}_d}{4\pi \kappa a L_v/c_p} + \lambda = \frac{c_p}{L_v}\frac{dT}{dr}\bigg|_{r=1}, \tag{13}$$

which serves to determine $\dot{q}_d$, thereby completing the solution. In solving (9)–(11) it is sometimes convenient to replace either (9) or (10) by the chemistry-free combination

$$\frac{d}{dr}\left\{\lambda\left[\frac{c_pT}{q}-Y\right] - \frac{d}{dr}\left[r^2\left(\frac{c_pT}{q}-\frac{Y}{L}\right)\right]\right\} = 0, \tag{14}$$

to be used later in the course of the solution. As expected, the above formulation reproduces the classical droplet-vaporization results in the absence of chemical reaction, when (9) and (10) can be readily integrated to give the expressions

$$\frac{Y}{Y_s} = \frac{1-e^{-L\lambda/r}}{1-e^{-L\lambda}} \quad \text{and} \quad \frac{T-T_\infty}{T_s-T_\infty} = \frac{1-e^{-\lambda/r}}{1-e^{-\lambda}}, \tag{15}$$

which can be used in (12) to yield (4) for the dimensionless vaporization rate and in (13) to yield (5) for the droplet heating rate.

5. Solution for large activation energies

5.1. Preliminary considerations

As seen in the dimensionless Eqs. (9) and (10), the relative importance of the chemical reaction is measured by the ratio of the characteristic diffusion time in the gas surrounding the droplet $La^2/[\kappa/(\rho c_p)] = a^2/D$ to the characteristic value of the fuel-consumption time $\{B\exp[-E_a/(R_oT)]\}^{-1}$. For large values of the activation energy E_a the chemical reaction displays a strong dependence on the temperature, so that for configurations with $T_\infty - T_s \sim T_\infty$, the case considered here, the fuel-consumption rate increases by many orders of magnitude as the temperature increases from T_s to T_∞.

For low ambient temperatures such that

$$B\exp\left(-\frac{E_a}{R_oT_\infty}\right) \ll \frac{D}{a^2} \tag{16}$$

the effect of pyrolysis is entirely negligible and the familiar results given in (4) and (5) are recovered. The following analysis considers instead the limiting case

$$B\exp\left(-\frac{E_a}{R_oT_s}\right) \ll \frac{D}{a^2} \ll B\exp\left(-\frac{E_a}{R_oT_\infty}\right), \tag{17}$$

when pyrolysis occurs in a thin layer centered at $r = r_f$ where the temperature is close to a value $T = T_f$, intermediate between T_s and T_∞. The thin reaction layer separates an inner region for $1 \le r < r_f$ where the flow is chemically frozen from an outer region for $r > r_f$ where the flow is in chemical equilibrium. The reciprocal of the dimensionless activation energy

$$\varepsilon = \left(\frac{E_a}{R_oT_f}\right)^{-1} \ll 1 \tag{18}$$

determines the characteristic thickness of the reaction layer $r - r_f \sim \varepsilon$ as well as the associated characteristic values of the fuel mass fraction $Y \sim \varepsilon$ and temperature variation $T - T_f \sim \varepsilon T_f$. Diffusion and chemical reaction are balanced in the reaction layer, a condition that leads to

$$\frac{B}{D/a^2}\left(\frac{E_a}{R_oT_f}\right)^{-2}\exp\left(-\frac{E_a}{R_oT_f}\right) \sim 1. \tag{19}$$

As revealed by the above order-of-magnitude estimate, in the limit of large activation energies the occurrence of the reaction at temperatures close to T_f implies that the frequency factor takes exponentially large values.

The solution in terms of matched-asymptotic expansions requires in principle introduction of the expansions

$$Y^- = Y_0^-(r) + \varepsilon Y_1^-(r) + \cdots \quad \text{and} \quad T^- = T_0^-(r) + \varepsilon T_1^-(r) + \cdots \tag{20}$$

in the frozen region $1 \le r \le r_f$ and

$$Y^+ = Y_0^+(r) + \varepsilon Y_1^+(r) + \cdots \quad \text{and} \quad T^+ = T_0^+(r) + \varepsilon T_1^+(r) + \cdots \tag{21}$$

in the equilibrium region $r_f \le r < \infty$, together with the reaction-layer expansions

$$Y = 0 + \varepsilon\varphi_1(\zeta) + \cdots \quad \text{and} \quad T = T_f + \varepsilon\theta_1(\zeta) + \cdots \tag{22}$$

involving the rescaled coordinate $\zeta = (r - r_f)/\varepsilon$. The analyses of the outer and inner regions are to be presented separately below.

5.2. The outer solution

For the specific case treated here the solution simplifies considerably. In particular, the existence of a positive temperature gradient $dT^+/dr|_{r=r_f} > 0$ on the equilibrium side of the reaction layer prevents fuel leakage at all orders, with the result that $Y_0^+ = Y_1^+ = \cdots = 0$. On the other hand, defining the pyrolysis-zone position r_f as the apparent fuel-depletion point as seen from the frozen region yields

$$\frac{\lambda}{r^2}\frac{dY^-}{dr} - \frac{1}{L}\frac{1}{r^2}\frac{d}{dr}\left(r^2\frac{dY^-}{dr}\right) = 0\begin{cases}Y^-(1) = Y_s \\ Y^-(r_f) = 0\end{cases}. \tag{23}$$

Substitution of the expansion for Y^- followed by integration of the problems found at increasing orders in powers of ε provides

$$\frac{Y^-}{Y_s} = \frac{Y_0^-}{Y_s} = \frac{e^{-L\lambda/r_f}-e^{-L\lambda/r}}{e^{-L\lambda/r_f}-e^{-L\lambda}}, \tag{24}$$

with all higher-order terms becoming identically zero (i.e. $Y_1^- = Y_2^- = \cdots = 0$). The result can be used in (12) to give

$$\lambda = \frac{\ln[1/(1-Y_s)]}{L(1-1/r_f)}, \tag{25}$$

relating the droplet vaporization rate $\lambda = \lambda Y_s - L^{-1}dY^-/dr|_{r=1}$, equal to the fuel pyrolysis rate $-(r_f^2/L)dY/dr|_{r=r_f}$, with the flame location r_f. Formally, the asymptotic problem in the limit $\varepsilon \ll 1$ is posed as that of finding the value of B that leads to a given value of r_f (or λ).

The outer temperature functions $T_n^\pm$ for $n = 0, 1, 2, \ldots$ satisfy the linear equations

$$\frac{\lambda}{r^2}\frac{dT_n^\pm}{dr} - \frac{1}{r^2}\frac{d}{dr}\left(r^2\frac{dT_n^\pm}{dr}\right) = 0, \tag{26}$$

obtained by neglecting the chemical term in (10). The boundary conditions on the frozen side are $T_0^- - T_s = T_1^- = T_2^- = \cdots = 0$ at $r = 1$ and $T_0^- - T_f = T_1^- - \theta_1^- = T_2^- - \theta_2^- = \cdots = 0$ at $r = r_f$, while the boundary conditions on the equilibrium side are $T_0^+ - T_\infty = T_1^+ = T_2^+ = \cdots = 0$ as $r \to \infty$ and $T_0^+ - T_f = T_1^+ - \theta_1^- = T_2^+ - \theta_2^- = \cdots = 0$ at $r = r_f$, where the constants θ_1^-, θ_1^+, etc are to be determined by matching the outer solution with the inner reactive layer. Straightforward integration of (26) provides

$$\frac{T_0^- - T_s}{T_f - T_s} = \frac{T_1^-}{\theta_1^-} = \frac{T_2^-}{\theta_2^-} = \cdots = \frac{e^{-\lambda/r}-e^{-\lambda}}{e^{-\lambda/r_f}-e^{-\lambda}} \tag{27}$$

and

$$\frac{T_\infty - T_0^+}{T_\infty - T_f} = \frac{T_1^+}{\theta_1^+} = \frac{T_2^+}{\theta_2^+} = \cdots = \frac{1 - e^{-\lambda/r}}{1 - e^{-\lambda/r_f}}. \tag{28}$$

The temperature description on the frozen side (27) can be used in (13) to evaluate the droplet heating rate, yielding at leading order

$$\frac{\dot{q}_d}{4\pi\kappa a L_v/c_p} = \lambda\left[\frac{c_p(T_f - T_s)/L_v}{e^{\lambda(1-1/r_f)} - 1} - 1\right]. \tag{29}$$

Additional useful equations, relating the different terms in (20) and (21), can be obtained by integrating once (14) and evaluating the result on both sides of the reaction layer, at intermediate distances $\varepsilon \ll |r - r_f| \ll 1$ where the outer expansions are valid. At leading order it is found that

$$\left.\frac{dT_0^+}{dr}\right|_{r=r_f} = \left.\frac{dT_0^-}{dr}\right|_{r=r_f} - \frac{q/c_p}{L}\left.\frac{dY_0^-}{dr}\right|_{r=r_f}, \tag{30}$$

while at the following order

$$\lambda T_1^-\big|_{r=r_f} - r_f^2\left.\frac{dT_1^-}{dr}\right|_{r=r_f} = \lambda T_1^+\big|_{r=r_f} - r_f^2\left.\frac{dT_1^+}{dr}\right|_{r=r_f}. \tag{31}$$

Eq. (30), stating that a fraction

$$\gamma = -\frac{q/c_p}{L}\left.\frac{dY_0^-}{dr}\right|_{r=r_f}\bigg/\left.\frac{dT_0^+}{dr}\right|_{r=r_f} < 1 \tag{32}$$

of the heat reaching the reaction layer by conduction from the hot equilibrium region is employed to pyrolyze the fuel (the remaining heat being conducted towards the frozen region), can be evaluated with use made of (24), (27), and (28) to yield

$$\frac{T_f - T_s}{T_\infty - T_s} = \frac{e^{-\lambda/r_f} - e^{-\lambda}}{1 - e^{-\lambda}}\left[1 - \frac{q(e^{\lambda/r_f} - 1)}{c_p(T_\infty - T_s)}\right], \tag{33}$$

which can be used, together with (25), to determine T_f as a function of r_f. Similar evaluations of (31) and (32) provide

$$\frac{-\theta_1^-}{e^\lambda - e^{\lambda/r_f}} = \frac{\theta_1^+}{e^{\lambda/r_f} - 1}, \tag{34}$$

and

$$\gamma = \frac{q(e^{\lambda/r_f} - 1)}{c_p(T_\infty - T_f)}, \tag{35}$$

to be used in the following analysis.

5.3. The inner region

The problem in the inner region reduces to a reaction-diffusion balance, which can be described by rewriting (9) and (14) in terms of the rescaled variables, producing at leading order

$$\frac{d^2 y_1}{d\zeta^2} = \frac{BL}{\kappa/(\rho c_p a^2)}\left(\frac{E_a}{R_o T_f}\right)^{-2}\exp\left(-\frac{E_a}{R_o T_f}\right)y_1 e^{\theta_1/T_f}, \tag{36}$$

$$\frac{d^2}{d\zeta^2}\left(\theta_1 - \frac{q/c_p}{L}y_1\right) = 0. \tag{37}$$

Note that the factor affecting the reaction term reflects the anticipated scaling (19). Matching with the outer solutions provides the boundary conditions

$$y_1 = \left(\left.\frac{dY_0^-}{dr}\right|_{r=r_f}\right)\zeta; \quad \theta_1 - \left(\left.\frac{dT_0^-}{dr}\right|_{r=r_f}\right)\zeta = \theta_1^- \quad \text{as} \quad \zeta \to -\infty, \tag{38}$$

$$y_1 = 0; \quad \theta_1 - \left(\left.\frac{dT_0^+}{dr}\right|_{r=r_f}\right)\zeta = \theta_1^+ \quad \text{as} \quad \zeta \to +\infty. \tag{39}$$

Integrating (37) readily yields

$$\theta_1 - \frac{q/c_p}{L}y_1 = \left(\left.\frac{dT_0^+}{dr}\right|_{r=r_f}\right)\zeta + \theta_1^+$$

$$= \left(\left.\frac{dT_0^-}{dr}\right|_{r=r_f} - \frac{q/c_p}{L}\left.\frac{dY_0^-}{dr}\right|_{r=r_f}\right)\zeta + \theta_1^-, \tag{40}$$

relating the temperature and fuel mass fraction in the reaction layer. The condition $\theta_1^+ = \theta_1^-$, stemming from the above expression and (30), and that stated in (34) can be simultaneously satisfied only if $\theta_1^+ = \theta_1^- = 0$, revealing that, just like the fuel mass fraction, the temperature has zero first-order corrections in the frozen and equilibrium regions.

Using (40) with $\theta_1^+ = \theta_1^- = 0$ and introducing for convenience the rescaled variables

$$\varphi = \frac{q}{c_p T_f}\frac{y_1}{L} \quad \text{and} \quad \eta = \frac{\lambda}{r_f^2}\frac{q}{c_p T_f}\zeta \tag{41}$$

along with the rescaled Damköhler number

$$\Delta = \frac{B}{D/a^2}\left(\frac{E_a}{R_o T_f}\right)^{-2}\left(\frac{\lambda}{r_f^2}\right)^{-2}\left(\frac{q}{c_p T_f}\right)^{-2}\exp\left(-\frac{E_a}{R_o T_f}\right) \tag{42}$$

results in the boundary-value problem

$$\frac{d^2\varphi}{d\eta^2} = \Delta\varphi e^{\varphi+\eta/\gamma}; \quad \begin{cases}\varphi + \eta = 0 \text{ as } \eta \to -\infty \\ \varphi = 0 \text{ as } \eta \to +\infty\end{cases}. \tag{43}$$

Note that the condition $\varphi + \eta = 0$ as $\eta \to -\infty$ effectively implies that $d\varphi/d\eta - 1$ must approach zero, so that for a given γ the above second-order equation must satisfy three boundary conditions, which is possible only for a single value of $\Delta(\gamma)$, the eigenvalue of the problem. The mathematical problem defined in (43) is similar to that encountered in Liñán's classical premixed-flame regime of nonpremixed combustion [16]. Despite the similarity, however, reduction to the same canonical form in general is not feasible, the only exception being the limit $\gamma \ll 1$, in which the solution to (43) can be related at leading order to one of the limiting cases considered by Liñán, as shown below.

5.4. Solution to the canonical problem

For a given positive value of $\gamma < 1$, defined in (32), the profiles of $\varphi(\eta)$ and corresponding values of Δ were obtained by a shooting integration scheme initiated at $-\eta \gg 1$. The resulting variation of Δ with γ is shown in Fig. 3 along with selected profiles of $\varphi(\eta)$ for $\gamma = 0.2$ and $\gamma = 0.99$. The numerical integration is more difficult for $\gamma \ll 1$, when the reaction layer becomes very thin, and also for $1 - \gamma = (dT_0^-/dr|_{r=r_f})/(dT_0^+/dr|_{r=r_f}) \ll 1$, when the temperature gradient on the frozen side is very small, with the consequence that the reaction extends far into the frozen region. Useful analytic predictions for $\Delta(\gamma)$ in these two limiting cases are presented below.

For $\gamma \ll 1$, introducing the rescaled variables $\bar{\varphi} = \varphi/\gamma$, $\bar{\eta} = \eta/\gamma$, and $\bar{\Delta} = \gamma^2\Delta$ and neglecting small terms of order γ reduces (43) to the linear problem

$$\frac{d^2\bar{\varphi}}{d\bar{\eta}^2} = \bar{\Delta}\bar{\varphi}e^{\bar{\eta}}; \quad \begin{cases}\bar{\varphi} + \bar{\eta} = 0 & \text{as } \bar{\eta} \to -\infty \\ \bar{\varphi} = 0 & \text{as } \bar{\eta} \to +\infty\end{cases}, \tag{44}$$
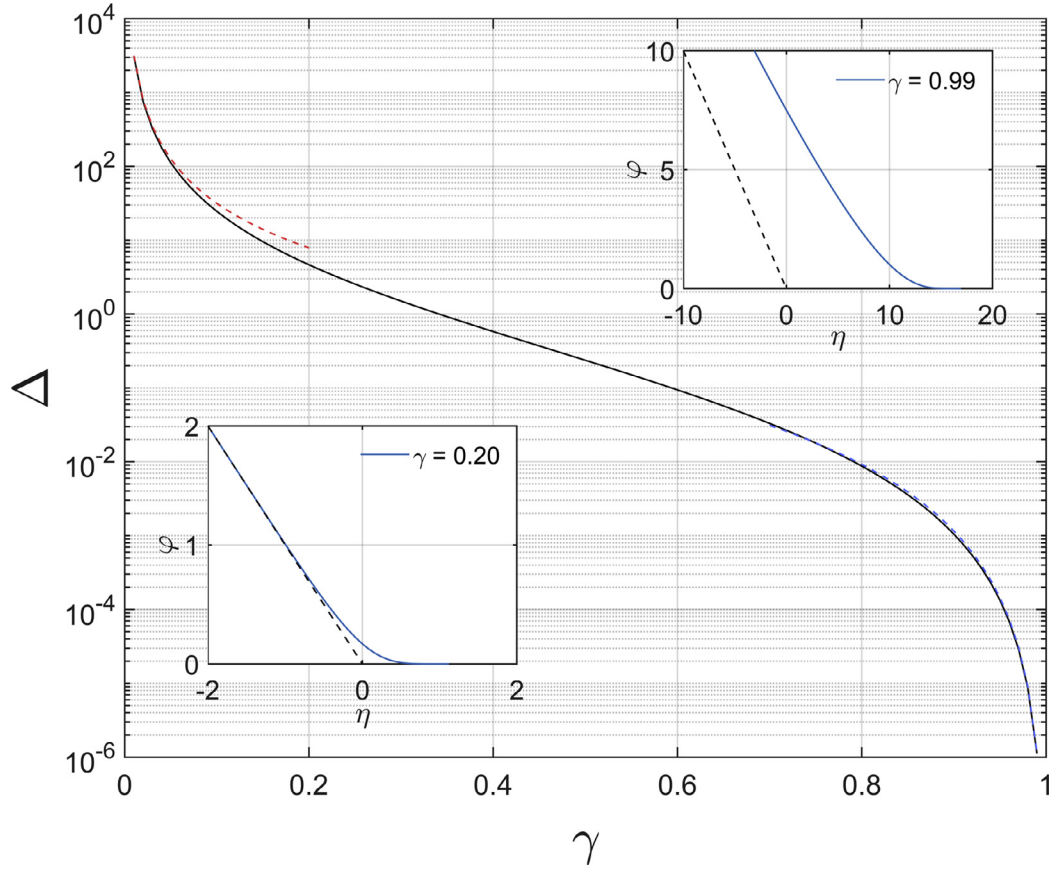
which can be written in the standard form

Fig. 3. The variation of Δ with γ as obtained from numerical integration of the eigenvalue problem (43) (solid curve) and the asymptotic predictions $\Delta = 0.315236\gamma^{-2}$ for $\gamma \ll 1$ and $\Delta = 1.1517(1-\gamma)^3$ for $1-\gamma \ll 1$ (dashed curves). The insets show the profiles of reduced fuel mass fraction $\varphi(\eta)$ for $\gamma = 0.2$ and $\gamma = 0.99$, with the dashed lines representing the asymptotes $\varphi = -\eta$.

$$\frac{d^2\bar{\varphi}}{dz^2} + \frac{1}{z}\frac{d\bar{\varphi}}{dz} - \bar{\varphi} = 0; \quad \begin{cases} \bar{\varphi} = -2\big[\ln(z/2) - \ln(\bar{\Delta})/2\big] & \text{as } z \to 0 \\ \bar{\varphi} = 0 & \text{as } z \to \infty \end{cases},$$

$$\text{(45)}$$

involving $z = 2\sqrt{\bar{\Delta}e^{\bar{\eta}}}$ as independent variable. The general solution to the above equation can be expressed as a linear combination of the modified Bessel functions of zeroth order, $\bar{\varphi} = C_K K_0(z) + C_I I_0(z)$, involving the constants of integration C_K and C_I. The boundary condition as $z \to \infty$ requires that $C_I = 0$, while the boundary condition as $z \to 0$ provides $C_K = 2$ and

$$\bar{\Delta} = e^{-2\gamma_E} \simeq 0.315236, \tag{46}$$

where $\gamma_E \simeq 0.577215$ represents Euler's constant. It is worth noting that the same mathematical problem was encountered by Liñán in one of the limiting solutions to the premixed-flame regime, namely, the limit $-m \to \infty$ discussed in Appendix C of [16]. As seen in the comparison of Fig. 3, the leading-order result $\Delta = 0.315236\gamma^{-2}$ predicts the Damköhler number for $\gamma \ll 1$ with small relative errors of order γ.

As illustrated in the upper inset of Fig. 3, for $1 - \gamma \ll 1$ the solution exhibits a fuel-depletion layer with order-unity thickness centered about $\eta = \eta_o \gg 1$. As is apparent from (43), this displacement is consistent with a small value of $\Delta \ll 1$, such that $\eta_o \sim \ln(1/\Delta)$, as needed to enable a diffusion-reaction balance to be preserved. The rescaled fuel mass fraction, of order $\varphi \sim 1$ for $\eta - \eta_o \sim 1$, increases towards the frozen side, giving characteristic values of $\varphi + \eta \sim \ln(1/\Delta)$ at distances $-\eta \sim 1$. The chemical reaction continues in a region that extends for $-\eta \sim (1-\gamma)^{-1} \gg 1$ with $\varphi + \eta \sim 1$. In this weakly reactive region, which ultimately determines the value of Δ, the diffusion-reaction equation takes

the form

$$\frac{d^2\hat{\varphi}}{d\hat{\eta}^2} = -\hat{\Delta}\hat{\eta}e^{\hat{\varphi}+\hat{\eta}} \tag{47}$$

when written in terms of the rescaled variables $\hat{\varphi} = \varphi + \eta$, $\hat{\eta} = (1-\gamma)\eta$, and $\hat{\Delta} = \Delta/(1-\gamma)^3$. The solution must satisfy $\hat{\varphi} = 0$ and $d\hat{\varphi}/d\hat{\eta} = 0$ as $\hat{\eta} \to -\infty$ and must match as $\hat{\eta} \to 0$ with the solution encountered for $-\eta \sim 1$.

Integration of (47) from $-\hat{\eta} \gg 1$ reveals that for $\hat{\Delta}$ larger than a critical value $\hat{\Delta}_c \simeq 1.1517$ the solution develops a singularity before reaching $\hat{\eta} = 0$, i.e. $\hat{\varphi} \to +\infty$ at a negative value of $\hat{\eta}$, while for $\hat{\Delta} < \hat{\Delta}_c$ the integration reaches $\eta = 0$ with $\hat{\varphi} \sim 1$. It is clear that a consistent asymptotic description, including matching with the solution in the intermediate region $-\eta \sim 1$ where $\hat{\varphi} \sim \ln(1/\Delta) \gg 1$, is only possible for $\hat{\Delta} = \hat{\Delta}_c \simeq 1.1517$, for which the singularity of the outer solution develops exactly at $\hat{\eta} = 0$. The analysis of the weakly reactive region therefore provides the asymptotic prediction $\Delta = \hat{\Delta}_c(1-\gamma)^3$ for $1-\gamma \ll 1$. It is remarkable how this leading-order result can be derived without analyzing in detail the multi-layer structure of the solution near $\eta = 0$. Such an analysis would be necessary, however, in deriving higher-order corrections, but these do not appear to be needed, in view of the excellent accuracy of the leading-order prediction $\Delta = 1.1517(1-\gamma)^3$, demonstrated by the comparison seen in Fig. 3.

6. The pyrolysis temperature

For known values of the pyrolysis-rate parameters B and E_a, the preceding description of the quasi-steady gas flow surrounding the droplet can be coupled with (1) and (2), describing the

temperature variation inside the droplet $T_d(\tilde{r}, t)$ and the droplet radius $a(t)$, to enable predictions of droplet-vaporization histories to be made. In the calculation, the Clasius-Clapeyron Eq. (3) is used to determine Y_s as a function of the instantaneous droplet-surface temperature T_s. The result can be used in solving (25), (29), (33), (35), and (42), supplemented by the function $\Delta(\gamma)$ shown in Fig. 3, to determine λ, $\dot{q}_d$, r_f, T_f, γ, and Δ. The analysis simplifies at the end of the droplet-heating period, when the droplet temperature reaches a uniform constant value $T_d = T_s$, close to T_B when $L_v/(R_F T_B) \gg 1$. During this stage the droplet heating rate $\dot{q}_d$ is identically zero, while λ, Y_s, T_s, r_f, T_f, γ, and Δ reach values that remain almost constant, with the square of the droplet radius changing linearly with time according to (7). This constant slope is clearly visible in the plots of Fig. 2.

The calculation procedure outlined above can be simplified by exploiting further the strong temperature sensitivity of the chemical reaction, entering in the theoretical description through the exponential present in (42). It can be reasoned that for large values of the dimensionless activation energy $E_a/(R_o T_f) \gg 1$ the relative changes in T_f are limited to small values of order $[E_a/(R_o T_f)]^{-1} \ll 1$. Therefore, at leading order in the limit $E_a/(R_o T_f) \gg 1$ the pyrolysis temperature T_f of a given fuel becomes a constant kinetic parameter, which takes the same value regardless of the droplet radius a or ambient temperature T_∞, with pyrolysis becoming negligible when $T_\infty < T_f$.

The value of T_f can be obtained from measurements of the constant slope of the curve da^2/dt reached at the end of the droplet-heating period. The computation begins by writing (7) in the form

$$\lambda = -\frac{\rho_l c_p}{2\kappa} \frac{da^2}{dt},$$ (48)

while setting $\dot{q}_d = 0$ in (29), and combining the result with (33) provides

$$\frac{T_f - T_s}{L_v/c_p} = \frac{(q + L_v)(e^\lambda - 1) - c_p(T_\infty - T_s)}{q + c_p(T_\infty - T_s) - L_v(e^\lambda - 1)}$$ (49)

and

$$r_f = \lambda \ln^{-1}\left[1 + \frac{c_p(T_\infty - T_s) - L_v(e^\lambda - 1)}{q}\right].$$ (50)

The above three equations, together with (3) and (25), constitute a coupled system of equations that determine T_f along with the associated values of λ, Y_s, T_s, and r_f. The solution can be obtained by a simple iterative scheme. Since κ has a very weak dependence on Y_s, while $T_B - T_s \ll T_B$, as follows from (3) when $L_v/(R_F T_B) \gg 1$, one may use (48) with ρ_l, c_p, κ evaluated with use made of $T_s = T_B$ and an estimated value of Y_s to compute λ, which can be substituted into (49) to determine T_f in the first approximation. A correction can be obtained by using the value of r_f given by (50) to evaluate Y_s from (25) and substituting the result into (3) to obtain T_s. These new values of Y_s and T_s can then be used in (48) to recompute λ, leading to a more accurate evaluation of T_f from (49).

This simple iterative procedure was used to determine the values of T_f corresponding to the three alkanes of Fig. 2 from the slope of the curve da^2/dt corresponding to $T_\infty = 1730$ K, yielding the values $T_f =(1080$ K, 912 K, 841 K) for heptane, dodecane and hexadecane, respectively, with associated reaction-zone standoff radii given by $r_f = (7.34, 4.95, 4.14)$. Because of the strong temperature sensitivity of the pyrolysis reaction, it is expected that the values of T_f evaluated from the experiments at a different value of T_∞ should differ by a small relative amount of order $[E_a/(R_o T_f)]^{-1}$ from the values given above, whereas the corresponding value of r_f could in principle differ by an amount of order unity. To check for consistency, the values of T_f and r_f corresponding to hexadecane were recomputed using the slope $-da^2/dt$ corresponding to

$T_\infty = 1311$ K, yielding $T_f = 969$ K and $r_f = 9.86$, to be compared with the values $T_f = 841$ K and $r_f = 4.14$ obtained at high temperature. The differences in T_f, 128 K, appear to be consistent with the effective dimensionless activation energy being on the order of $E_a/(R_o T_f) \sim 10$ for hexadecane.

The fraction γ of the heat conducted from the ambient atmosphere that is employed in fuel pyrolysis, as defined in (32) and calculated from (35), is appreciable, being (0.486, 0.591, 0.670) for heptane, dodecane and hexadecane, respectively at $T_\infty = 1730$ K. This is consistent with the pyrolysis energy q being large compared with the heat of vaporization L_v and with T_f not being very much less than T_∞, so that the discontinuity in the temperature gradient at the pyrolysis zone is mild, that zone being situated far enough from the surface of the droplet that its standoff radius r_f, which depends strongly on T_f, is not small in these experiments. The corresponding "pyrolysis dip" observed in liquid-fuel combustion is much closer to the liquid surface, remaining, however, similarly small, the pyrolysis energy being typically much less than heats of combustion. The concept of a pyrolysis temperature in fact may also find application on the fuel side of diffusion flames in combustion experiments, although this application has not been explored yet. The interest in the present work, however, is restricted to vaporization.

7. The modified Spalding law

With errors of order $[E_a/(R_o T_f)]^{-1}$, predictions of droplet vaporization histories based on treating T_f as a fixed kinetic property of the fuel can make use of (25) and (33) to obtain λ and r_f for given values of T_s, Y_s, and T_∞, with $\dot{q}_d$ following from (29). In particular, the constant value of λ reached when $\dot{q}_d = 0$ at the end of the droplet-heating period is given by

$$\lambda = \ln\left[1 + \frac{c_p(T_\infty - T_s)}{L_v} - \left(\frac{q}{L_v}\right)\left(\frac{c_p(T_\infty - T_f)}{q + L_v + c_p(T_f - T_s)}\right)\right],$$ (51)

as can be seen by solving (49) for λ. If the approximation $T_s = T_B$ is used, then the above expression allows us to quantify directly the reduced vaporization rate associated with fuel pyrolysis, which enters as a correction proportional to q/L_v that vanishes at $T_\infty = T_f$.

In interpreting the result, it is convenient to rewrite (51) in the alternative form

$$\lambda = \ln\left[1 + \frac{c_p(T_a - T_s)}{L_v}\right],$$ (52)

where the apparent temperature of the atmosphere is

$$T_a = \alpha T_f + (1 - \alpha)T_\infty$$ (53)

with

$$\alpha = \frac{q}{L_v + c_p(T_f - T_s) + q}.$$ (54)

As can be seen by comparing the above expression with the classical Spalding solution (6), the presence of pyrolysis results in the modified effective ambient temperature T_a, intermediate between T_f and T_∞. As seen in (54), the weighting factor α is the ratio of the amount of heat involved in the fuel pyrolysis to the total amount needed to vaporize the liquid fuel, heat up the resulting vapor to the pyrolysis temperature T_f, and pyrolyze it. The values of α corresponding to $T_f =(1080$ K, 912 K, 841 K) can be evaluated using an approximate specific heat $c_p = 3.7 \times 10^3$ J/(kg K) along with $T_s = T_B =(371$ K, 489 K, 560 K) to give $\alpha = (0.48, 0.60, 0.70)$ for heptane, dodecane, and hexadecane, respectively (evaluations of α accounting for departures of T_s from T_B and using the "1/3 rule" [13] for computing c_p yield values that differ by about 1 % from those given above). As can be seen, the effect of pyrolysis is

more important for heavier alkanes, for which the apparent temperature is closer to the pyrolysis temperature, thereby having a larger impact on the vaporization rate (52).

As a further check on the accuracy of the T_f =constant approximation, the value of $\alpha = 0.70$ evaluated for hexadecane with $T_f = 841$ K (the value obtained from the experiments at $T_\infty = 1730$ K) was used in (52) to provide a prediction for the vaporization rate at $T_\infty = 1311$ K. The associated slope $-\mathrm{d}a^2/\mathrm{d}t$, evaluated from (7), was found to be $-\mathrm{d}a^2/\mathrm{d}t = 0.1049$ mm^2/s, which differs by 9.2 % from the value $-\mathrm{d}a^2/\mathrm{d}t = 0.1156$ mm^2/s determined experimentally. This small departure is again consistent with the errors, of order $[E_a/(R_oT_f)]^{-1}$, present in the leading-order description considered here.

8. Concluding remarks

The experimental results reported here have shown how fuel-pyrolysis effects reduce vaporization rates of normal alkanes, to an increasing extent with increasing chain length of the fuel molecule. A new theory of droplet vaporization has been developed to quantify the resulting vaporization-rate decrease. The needed one-step endothermic activation-energy analysis differs markedly from previous activation-energy analyses, which considered only exothermic reactions. It involves complexities that may not initially be anticipated, such as an extended weakly reactive layer in the inner zone when a large fraction of the heat conducted from the ambient atmosphere is required for pyrolysis. The kinetically controlled pyrolysis temperature T_f is seen to emerge as a useful kinetic approximation that replaces at leading order the Arrhenius parameters B and E_a. Determination of E_a and subsequently B from measurements of vaporization rates at different T_∞ would require accuracies of 1% or better because of their strong sensitivity to vaporization-rate changes. This underscores the importance of the kinetically controlled pyrolysis temperature in interpreting experimental droplet-vaporization results.

The analysis reveals that pyrolysis effects are absent for droplets vaporizing in low-temperature atmospheres with temperatures T_∞ below T_f. Formulas are developed for the vaporization and heating rates of droplets vaporizing in high-temperature atmospheres with $T_\infty > T_f$. At the end of the heat-up period, when the droplet temperature reaches a constant value, the equation for the vaporization rate accounting for the presence of pyrolysis can be cast in the classical form (52) originally derived by Godsave and Spalding [5,6], with the ambient temperature T_∞ replaced by the apparent ambient temperature $T_a = \alpha T_f + (1 - \alpha)T_\infty$, involving the fuel-specific energetic weighting factor α defined in (54). Clearly, additional experiments involving different levels of ambient temperature and different alkanes should be considered in future work to test the accuracy of the predictive formulae derived here and improve the evaluation of the pyrolysis temperature T_f. Besides droplet experiments, counterflow systems involving liquid fuel pools or prevaporized alkane jets and preheated inert gases can be useful in that respect, providing insightful information free from transient effects.

Declaration of Competing Interest

The authors declare that they do not have any financial or non-financial conflict of interests

Acknowledgments

References

[1] W.A. Sirignano, Fuel droplet vaporization and spray combustion theory, Prog. Energ. Combust. Sci. 9 (4) (1983) 291–322.
[2] C.K. Law, Recent advances in droplet vaporization and combustion, Prog. Energ. Combust. Sci. 8 (3) (1982) 171–201.
[3] G. Godsave, Combustion of droplets in a fuel spray, Nature 164 (4173) (1949) 708.
[4] D.B. Spalding, Combustion of liquid fuels, Nature 165 (4187) (1950). 160–160
[5] G. Godsave, Studies of the combustion of drops in a fuel spraythe burning of single drops of fuel, Proc. Combust. Inst., 4, Elsevier (1953), pp. 818–830.
[6] D. Spalding, The combustion of liquid fuels, Proc. Combust. Inst., 4, Elsevier (1953), pp. 847–864.
[7] W.A. Sirignano, Fluid dynamics and transport of droplets and sprays, 2, Cambridge University Press, 2010.
[8] A.L. Sánchez, J. Urzay, A. Liñán, The role of separation of scales in the description of spray combustion, Proc. Combust. Inst. 35 (2) (2015) 1549–1577.
[9] B. Abramzon, W. Sirignano, Droplet vaporization model for spray combustion calculations, Int. J. Heat Mass Transf. 32 (9) (1989) 1605–1618.
[10] A. Crespo, A. Liñán, Unsteady effects in droplet evaporation and combustion, Combust. Sci. Technol. 11 (1-2) (1975) 9–18.
[11] Á. Muelas, P. Remacha, J. Ballester, Droplet combustion and sooting characteristics of uco biodiesel, heating oil and their mixtures under realistic conditions, Combust. Flame 203 (2019) 190–203.
[12] T. Li, D. Zhu, N. Akafuah, K. Saito, C.K. Law, Synthesis, droplet combustion, and sooting characteristics of biodiesel produced from waste vegetable oils, Proc. Combust. Inst. 33 (2) (2011) 2039–2046.
[13] G. Hubbard, V. Denny, A. Mills, Droplet evaporation: effects of transients and variable properties, Int. J. Heat Mass Transf. 18 (9) (1975) 1003–1008.
[14] R.J. Kee, G. Dixon-Lewis, J. Warnatz, M.E. Coltrin, J.A. Miller, A fortran computer code package for the evaluation of gas-phase multicomponent transport properties, Sandia National Laboratories Report SAND86-8246 13 (1986). 80401–1887
[15] P.E. Savage, Mechanisms and kinetics models for hydrocarbon pyrolysis, J. Anal. Appl. Pyrol. 54 (1-2) (2000) 109–126.
[16] A. Liñán, The asymptotic structure of counterflow diffusion flames for large activation energies, Acta Astronautica 1 (7-8) (1974) 1007–1039.

energy&fuels

Alternative Method for the Formulation of Surrogate Liquid Fuels Based on Evaporative and Sooting Behaviors

Álvaro Muelas,[†] Diego Aranda,[†] and Javier Ballester*,[‡]

[†]Laboratory of Research on Fluid Dynamics and Combustion Technologies (LIFTEC) and [‡]Fluid Mechanics Group/LIFTEC, CSIC—University of Zaragoza, 50018 Zaragoza, Spain

S *Supporting Information*

ABSTRACT: This study proposes a novel approach to design and evaluate surrogates for liquid fuels, aimed at replicating their evaporative and sooting behaviors. The method was demonstrated for a commercial heating oil. The lack of surrogates found in the literature for this relevant fuel, in addition to its physicochemical complexity, was the primary reason for its choice to test the proposed method. A first surrogate aiming to emulate the evaporative behavior of the target fuel was designed through the combination of a theoretical evaporation model and experimental tests. The second surrogate was formulated to replicate the sooting behavior of heating oil, whereas a third surrogate aimed to match the physicochemical properties relevant for both processes. The so-designed surrogates were validated afterward by means of single-droplet evaporation tests under high-temperature conditions. The obtained evaporation curves served as a benchmark for evaluating the evaporative characteristic, whereas an aspirating probe collecting all of the soot produced at a high-temperature and reducing atmosphere was used for the validation of the sooting tendency. It was found that surrogates specifically designed to match the evaporative and sooting behaviors of the target fuel displayed a remarkably good agreement when validated against experimental data for heating oil. Overall, the obtained results confirmed the validity of the methodologies proposed for surrogate formulation, combining predictive methods and droplet evaporation tests at high temperatures.

1. INTRODUCTION

The optimization and efficient use of the energy contained in fuels is a major challenge in combustion science, as it can significantly mitigate its impact in environmental aspects such as pollutant emissions or climate change. A substantial complication in the design of combustion optimization strategies arises due to the physicochemical complexity of most conventional petroleum-derived fuels, which usually display a marked multicomponent character with hundreds of different constituents. It is nearly impossible to identify all of the individual molecules and compositions and, even if it could be attainable, the combustion modeling of such a mixture would be unfeasible due to the lack of detailed data and huge computation costs.[1] In addition to this, real petroleum-based fuels typically display an extensive variability depending on the nature of the crude, the manufacturer, or even the season.[2] In light of these limitations, the most followed approach to simulate the combustion performance of real fuels is through the use of surrogates, i.e., mixtures of a few well-characterized pure compounds of known chemical species and mixture fractions that mimic certain physical and chemical properties of the target fuel.[2,3] These simpler blends not only ease computational studies, but also provide time-invariant reference fuels for experimental studies[4] and facilitate insight into the underlying combustion-related processes.[2,4] With appropriate blending strategies, a surrogate might match a set of desired design properties, and therefore, its behavior in certain related combustion processes can emulate those of the target fuel. By increasing the number of constituents in the surrogate, it is possible to match a greater number of design properties, although at the cost of increasing its complexity.[2]

Much work has been done regarding the design and testing of surrogates for transportation fuels and, particularly, for diesel and gasoline (e.g., see review refs 5 and 6, respectively). It can be seen that most of the effort has been focused on emulating gas-phase chemistry properties (ignition, extinction, sooting propensity, etc.), with only a few studies trying to match physical behaviors.[4] The cited gas-phase features are undoubtedly of critical importance for most combustion-related applications, particularly for those in which the fuel is completely vaporized prior to its intake in the combustion chamber. However, for applications where the fuel enters the combustion chamber in liquid state (typically in the form of a spray), matching also certain liquid physical properties such as volatility, density or viscosity, as well as its evaporative behavior can be of critical relevance for a complete description of the target fuel.[4,6] This would be particularly true for the case of the combustion of heating oil in boilers, as well as for diesel in compression−ignition engines[4] or even for gasoline in gasoline direct injection engines.[6]

In spite of the wide range of applications where the fuel is injected in liquid form into the combustion chamber, the use of configurations taking into account the phase-change process is a minority within the surrogate literature, and most work has been performed at configurations with completely prevaporized fuel.[7,8] Due to the multicomponent character of real liquid fuels, there are certain behaviors that are intrinsic and most relevant to spray burning in real applications but cannot be

accounted for in tests with prevaporized fuel.[7] For instance, it is generally accepted that the light-end components of the fuel preferentially evaporate near the injection point, whereas the heavier, less volatile compounds become predominant downstream. These differences among liquid and vapor compositions throughout the combustion chamber can have a significant impact in relevant application-related aspects such as emissions or burner flame stability. The use of combustion configurations that incorporate the phase change of the fuel is therefore an appropriate approach for a complete description of real, multicomponent liquid fuels.[7] For this purpose, the simplified single-droplet configuration has been found in several recent works to be particularly useful in the design and evaluation of a wide range of surrogates for liquid fuels, both by conducting experimental tests[7−9] and through the use of multicomponent droplet evaporation models.[10−14] This configuration has the advantage of incorporating the aforementioned particularities associated with liquid fuels while also keeping a much simpler analysis and modeling compared to the stochastic environment of real spray flames.

At this point, it seems important to distinguish between surrogate design and its subsequent evaluation. Different methodologies have been used for both processes in the literature, and although it is not the objective here to exhaustively review all of them, a brief description of the approaches employed so far for some relevant design properties seems appropriate to place the current work in context.

When it comes to surrogate design, a well-established approach consists in matching a set of properties that are relevant for certain combustion aspects (e.g., cetane number for chemical kinetics, molecular weight for diffusive properties, or H/C for flame temperature in ref 15). By matching the former set of properties, the surrogates obtained through this methodology are thought to be able to emulate the latter features and, therefore, the desired complex combustion behaviors (e.g., the gas-phase combustion kinetic phenomena in ref 15). A comparatively small amount of studies have formulated surrogate fuels aiming to match the evaporative behavior of the target fuel, even though (as discussed above) it is a most relevant design property for applications where the fuel enters the combustion chamber in liquid state. Among them, the most followed approach is to use the distillation curve as design property representative of the evaporative behavior (e.g., in refs 4, 10, 14, 16). Even though the distillation curve certainly provides valuable information regarding the evaporative characteristics of multicomponent fuels, droplets evaporating in real combustion environments may exhibit different behaviors from those observed in a batch distillation process because of the low mass diffusion rate of species within the liquid.[17,18] An alternative and application-oriented description of the evaporation behavior of a multicomponent fuel could be achieved by means of the simplified single-droplet configuration. It is noteworthy that any surrogate formulation process always needs a method for estimating the design property value in terms of the mixture composition. This would lead to the use of single-droplet multicomponent models as a predictive tool for surrogate formulation, as it has been done in some recent works such as refs 12, 13. The target fuels in those works were, however, mixtures of discrete and well-identified chemical components (a FACE A gasoline comprising 66 species in ref 12, and a light naphtha containing 15 constituents in ref 13). This allows for the simulation of the

target fuel's evaporative behavior, providing therefore a target value to formulate surrogates. However, to the authors' knowledge, this approach has not been applied to more conventional petro-fuels such as regular gasoline or diesel, comprising hundreds of unknown species. Besides the evaporative behavior, the propensity to soot of the target fuel is also found to be a relevant feature in many liquid combustion applications. In this regard, and taking into account the inherent complexity of soot chemistry, the most followed approach has been to use experimentally obtained indices such as the threshold sooting index[19,20] or the yield sooting index (YSI).[21,22]

Once a surrogate has been formulated, different methodologies can be applied for evaluating its adequacy. A good example of straightforward surrogate evaluation would be the case of a surrogate designed for matching a certain property such as the derived cetane number, where a simple cetane number test would reveal its suitability. As numerous studies on surrogates seek to match gas-phase chemistry characteristics of the target fuel, common evaluation methods comprise gas-phase tests such as shock tubes, rapid compression machines, or reactors designed for flame speed measurements. Regarding physical surrogates, and more particularly surrogates formulated to match the evaporative behavior, the most followed validation method involves the distillation curve extraction, with comparatively fewer studies testing the surrogate's adequacy through the use of the single-droplet evaporation/combustion approach. The already cited works by Elwardany et al.[11−13] evaluated the ability of several physical surrogates to emulate different target fuels' evaporative behaviors by means of a single-droplet evaporation model. When it comes to experimental validations, Liu et al. used a single-droplet apparatus to evaluate the combustion characteristics of surrogates designed to match certain gas-phase combustion properties of Jet A,[7] and also to compare some standard reference fuels for gasoline (such as indolene or heptane—isooctane mixtures) with a commercial gasoline.[8,9] The use of models for the design and validation of surrogates of practical fuels entails some difficulties since the accurate modeling of multicomponent fuels is still a challenging objective and also requires a detailed characterization of their composition as well as the physicochemical properties of their components. In those cases, experimental characterizations by means of evaporation/combustion tests offer some advantages, providing reliable data without requiring a comprehensive description of the fuel properties. A recent work by Chen et al.[14] combines both approaches for validating the evaporative behavior of a Jet A surrogate, comparing the droplet vaporization curves of the target fuel (experimentally obtained) and that of a four-component surrogate (estimated through a multicomponent evaporation model). Regarding the sooting tendency, a vast majority of studies evaluate the surrogate's soot yield in a gas-phase configuration (e.g., in ref 21), with no reported work validating a surrogate's soot yield through the use of the single-droplet configuration, where the reducing conditions in the droplet's proximity and concentration effects may play a significant role.

In summary, the single-droplet configuration clearly offers a suitable environment and some interesting and unexplored opportunities of study toward the development of surrogates for real liquid fuels. The main objective of this work consists therefore in using this approach to formulate and subsequently validate new surrogates that match the evaporative and sooting

behaviors of a light heating oil. This approach combines modeling and experimental work on a single droplet evaporating under conditions representative of real flames. Both design properties are considered to be critical for the target fuel's main application, i.e., its combustion in boilers, and therefore different surrogates were designed with the aim of emulating them.

A first surrogate matching the heating oil's evaporative characteristics was formulated based on a combination of single-droplet evaporation tests at high temperature (required to obtain the behavior of the complex target fuel) and a multicomponent evaporation model (needed to estimate the characteristics of the different surrogate mixtures). The subsequent evaluation of surrogate blends was also experimentally obtained through droplet evaporation tests. A second surrogate was designed to emulate the heating oil's soot tendency. Its formulation was based on the well-known YSI indicator, whereas its validation was experimentally gained by means of soot sampling at the single-droplet evaporation tests. The third and last surrogate was designed following a well-established and common methodology, as it is the matching of a group of rather simple physicochemical properties that are related with the more complex evaporation and sooting behaviors. The so-formulated surrogate can thus be considered to be a reference case, and it was also validated through the aforementioned single-droplet tests at the droplet combustion facility (DCF). Compared to prior works, the current study proposes novel approaches on both the formulation and evaluation sides. The use of DCF tests to provide the target behavior (required in the formulation phase) extends the use of theoretical droplet evaporation models as a tool for the design of surrogates for target fuels with unknown composition. Furthermore, there is no precedent of this kind of experimental validation applied for surrogates designed ad hoc to precisely match the target fuel's single-droplet evaporation behavior. The validation method proposed for estimating the sooting tendency would not only serve as a novel approach to evaluate the adequacy of liquid surrogate fuels, but it would also provide insight into the possibility of using the YSI as a soot predictor for the single-droplet configuration (a case of study significantly different from that used in YSI tests[21,22]).

As it has been introduced, the main objective of this work is to develop and test novel approaches that can contribute to the recent surrogate formulation and validation developments based on the use of the isolated single-droplet configuration. By applying these methodologies with the aim of matching the evaporative and sooting behaviors of heating oil, a quite unexplored fuel within the surrogate literature, the second main objective of the current study would be attained. In spite of the significant advance of natural gas during the last decades, the share of light heating oil still accounts for roughly 17% of the EU domestic heating market, reaching more than 40% of all households in certain countries such as Switzerland or Ireland.[23] Due to its geographical reach, this liquid fuel can be readily transported to off-grid regions, and therefore, its use in residential and rural areas is expected to remain predominant in the near future. In view of its magnitude, the development of surrogate fuels matching heating oil's relevant behaviors seems most desirable for the design of combustion optimization strategies. However, to the authors' knowledge, no previous study has addressed this issue, and therefore, the surrogates

obtained here aiming to match the evaporative and sooting behaviors of heating oil would contribute to fill this gap.

2. EXPERIMENTAL AND PREDICTIVE METHODS

2.1. Fuels Investigated. A commercial Spanish heating oil (fuel oil No. 2) was used as target fuel. A complete characterization was performed at the Instituto de Carboquimica (ICB-CSIC) to determine its most significant properties, which are listed in Table 1. The distribution by families is presented in Appendix A of the Supporting Information for the sake of completeness.

Table 1. Main Properties of the Studied Heating Oil

molecular formula	$C_{13.21}H_{24.63}$	LHV (MJ/kg)	41.92
$\overline{MW}$ (g/mol)	184.5	density at 20 °C (kg/m³)	861
C/H (-)	0.54	viscosity at 40 °C (cP)	3.43

In addition to the presented properties, the distillation curve of heating oil was also measured by means of a distillation apparatus similar to that featured in ref 16, that is, following the advanced distillation curve (ADC) methodology developed by Bruno[24] rather than using the more common ASTM D86 technique.[25] The ADC method was chosen because by measuring kettle temperatures inside the liquid, the provided points are thermodynamically consistent and representative of the liquid−vapor equilibrium. The classical D86 apparatus, on the other hand, measures the vapor temperature in the distillation head, providing therefore somewhat lower temperatures than the actual thermodynamic state points.[4,6,16,24] Two sequential ADC atmospheric distillation curves were acquired for heating oil, both displayed in Figure 1 along with their least-squares fitting.
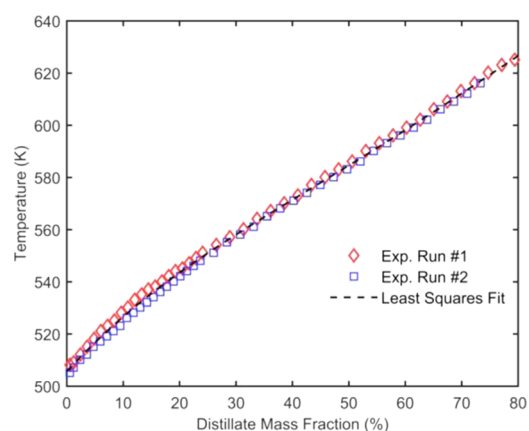

Figure 1. Experimental distillation curves extracted for the target heating oil.

Two pure fuels were used in this work as surrogate palette compounds: *n*-eicosane (EICO, $C_{20}H_{42}$, >99% purity) and 1-methylnaphtalene (MNP, $C_{11}H_{10}$, >95% purity). The criteria for choosing these two compounds will be addressed below.

2.2. Droplet Combustion Facility. As the formulation and subsequent evaluation of surrogates is intended to be based on the evolution of fuel droplets in a high-temperature environment, a set of experiments were performed at LIFTEC's droplet combustion facility (DCF). This facility has already been described in detail in previous works,[26−28] and therefore, only a brief exposition will be provided here. A schematic showing the main parts of the DCF is displayed in Figure 2 along with representative pictures of the droplet evaporating and burning processes.

A piezoelectric device at the top of the facility generated a monosized stream of free-falling droplets, with a nominal diameter of 150 μm. This is considered to be a good compromise between satisfactory experimental accuracies and real sizes found in sprays. The interdroplet space was always over 100 diameters, and thus
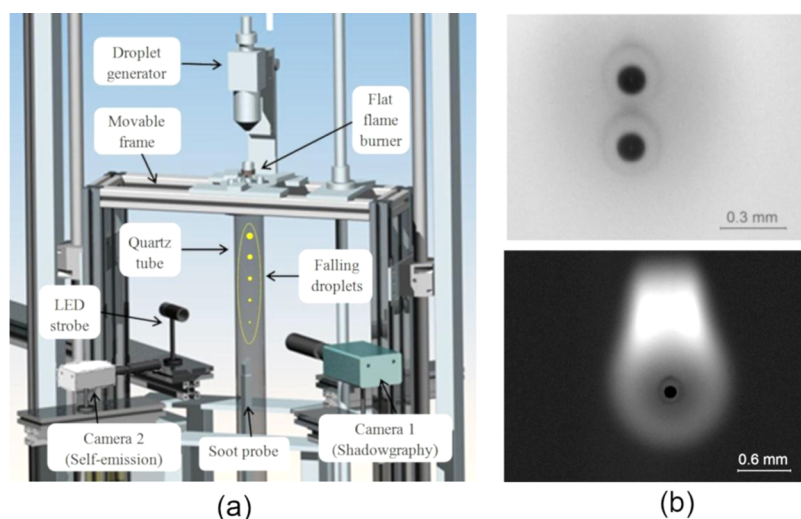
Figure 2. Schematic of the droplet combustion facility (a) and representative pictures captured with both cameras for the combustion of heating oil droplets showing the droplet surrounded by the soot shell and the envelope flame (b).
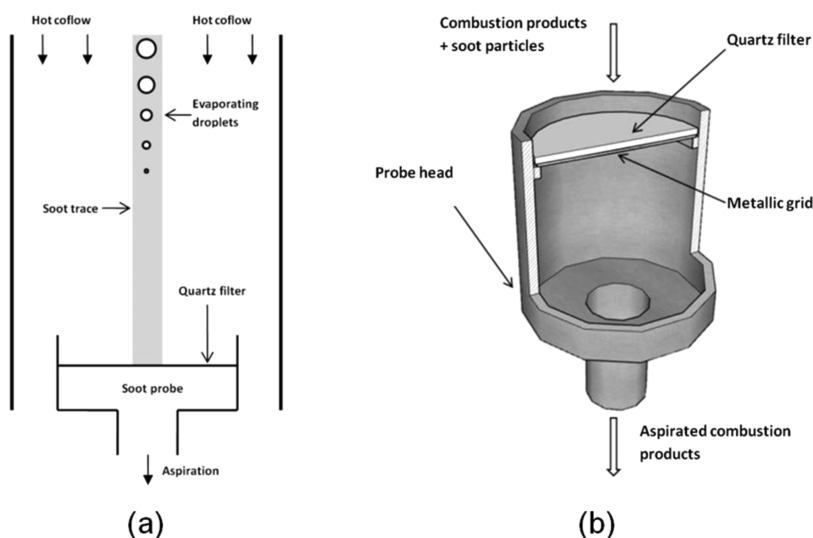

Figure 3. Soot sampling probe: (a) diagram depicting its operation; (b) schematic detailing the main parts.

interaction between droplets can be considered as negligible.[29] The droplet generator device possesses a heating system that allows for the dosing of fuels with high pour point or that are too viscous. The monosized, isolated droplets were introduced into the exhaust gases produced by a flat-flame burner (McKenna) fed with methane and air. This allows for the vaporization and (if oxygen is available) burning of the small droplets in an atmosphere representative of those found in real flames. As this work intends to study the vaporization process of the droplets rather than their combustion, the feed flows of methane and air were adjusted stoichiometrically, and therefore, the flat-flame combustion products contained no oxygen. As the experimental conditions of this gaseous coflow are critical for the validity of the experimental droplet evaporation results and their subsequent modeling, both the coflow temperatures and velocities were thoroughly measured along the tube centerline, as detailed in ref 28.

The droplet vaporization process of different fuels was characterized through the images acquired with a CCD camera (QImaging Retiga SRV, "Camera 1" in Figure 2a). This camera was synchronized with the droplet generator and with a light-emitting diode (LED) strobe, allowing the use of the double-shot technique. The LED strobe emitted very short (<1 μs) pulses of light every 500 μs, freezing the motion of the backlighted, free-falling droplets. By working with an exposure time of 1200 μs, the same droplet was recorded twice in a

single frame, as illustrated by Figure 2b (top). These images were post-processed to extract the size and velocity evolution of droplets along the axial coordinate in a precise and repeatable way. For the cases when oxygen is available in the coflow and the droplets are surrounded by a diffusion flame, a high-sensitivity CMOS camera (Hamamatsu C11440-36U, "Camera 2" in Figure 2a) captures the light spontaneously emitted from the flame region (Figure 2b, bottom).

As discussed above, one of the main advantages of the single-droplet configuration is its simplicity. The ideal case of study would be that of a single, isolated droplet evaporating (or burning) in a completely quiescent ambience without any convective effects, neither forced nor buoyancy-induced. This would create a completely one-dimensional (1D) configuration, whose easier modeling and analysis favors its application as a canonical case for developing and testing liquid surrogate fuels.[7,8] For this reason, the experimental conditions used in this work were chosen to minimize both forced and natural convection, as detailed in ref 28. The Reynolds number based on the droplet-coflow relative velocity was estimated to remain always below 1 for all of the studied cases.

The propensity to soot of the studied fuels was characterized by means of a sampling probe which collected the total amount of soot produced in the combustion chamber, as illustrated in Figure 3. As the

experimental conditions applied in this work were intended for studying the vaporization process of droplets rather than their combustion, the absence of oxygen in the hot coflow (with temperatures up to 1450 °C) greatly enhanced soot formation through the pyrolyzation of the fuel vapors. The formed soot agglomerates descended unoxidized along the tube centerline (as depicted in Figure 3a), and were retained on a quartz microfiber filter. The soot collected throughout a certain amount of time (typically around 15 min) was dried at 110 °C for over 24 h and then weighed on an analytical scale (Sartorius CP225D; repeatability, ±20 μg). A soot index, named as isolated droplet soot yield (IDSY) and expressing the weight of soot per unit of injected fuel, was calculated, providing thereby quantitative information regarding the sooting behavior of different fuels.

2.3. Distillation Model. A simple batch distillation model was developed to simulate the distillation curves of different liquid mixtures. The liquid blend is assumed to be heated to its bubble point, where an infinitesimal amount of vapor is removed, providing therefore a new composition in the liquid phase, which yields a different (higher) bubble point. By removing sufficiently small quantities of vapor at a constant flow rate, the distillation curve for the evaluated mixture is calculated. As the model assumes that all of the vapor leaving the boiling flask is stored in a total condenser, the distillation process has no reflux and, by the end of the procedure, the totality of the initial liquid mixture is distilled. The model assumes the following liquid−vapor equilibrium[30,31]

$$f_i^{\mathrm{L}} = f_i^{\mathrm{V}} \tag{1}$$

with f_i^{L} and f_i^{V} being the fugacities of the component i in the liquid and vapor phases, respectively. The liquid fugacity is calculated through the following expression

$$f_i^{\mathrm{L}} = \gamma_i x_i P_i^0 \Phi_i^0 K_i \tag{2}$$

with γ_i being the activity coefficient of component i in the liquid mixture, x_i the molar fraction of i in the liquid, P_i^0 the vapor pressure of pure i at the evaluated temperature, Φ_i^0 the fugacity of pure i at the evaluated temperature and vapor pressure, and K_i the Poynting correction factor (close to 1 for atmospheric pressure). The vapor fugacity is obtained through

$$f_i^{\mathrm{V}} = \Phi_i^{\mathrm{V}} y_i P \tag{3}$$

with Φ_i^{V} being the fugacity coefficient for i in the vapor mixture, y_i the molar fraction of i in the vapor, and P the total pressure of the system.

By combining eqs 1−3, the liquid−vapor equilibrium can be calculated for each mixture component at a given temperature and total pressure. This model considers the vapor as a real gas and takes into account the nonideality of the liquid mixture. The well-known expression $y_i P = x_i P_i^0$ would be a particular case of (1), where the total pressure is low ($K = 1$), the gas is considered to be ideal ($\Phi = 1$) and the liquid mixture behaves also as an ideal solution ($\gamma = 1$). The described distillation model was satisfactorily validated by comparison with experimental and simulation results of binary mixtures presented in ref 32.

2.4. Multicomponent Droplet Vaporization Model. The droplet vaporization process was modeled following the classical, transfer number-based approach widely used in droplet vaporization and combustion works. The implemented model takes into account nonunitary Lewis number in the gas film, variable thermophysical properties, and the effect of Stefan flow on the vaporization process.[33] It also assumes complete spherical symmetry, quasi-steady gaseous phase, and liquid−vapor equilibrium considering ideal gas and liquid mixtures (i.e., Dalton's and Raoult's laws apply at the interface).

Regarding the liquid phase, the effects of finite liquid thermal conductivity and species diffusivity within the droplet are taken into account through the well-known effective thermal conductivity[33] and effective diffusivity models,[34] respectively. These models solve the transient heat and diffusion equations within the spherical droplets

$$\frac{\partial T}{\partial t} = \alpha_{\mathrm{l}} \left(\frac{\partial^2 T}{\partial r^2} + \frac{2}{r} \frac{\partial T}{\partial r} \right) \tag{4}$$

$$\frac{\partial Y_{\mathrm{li}}}{\partial t} = D_{\mathrm{l}} \left(\frac{\partial^2 Y_{\mathrm{li}}}{\partial r^2} + \frac{2}{r} \frac{\partial Y_{\mathrm{li}}}{\partial r} \right) \tag{5}$$

where T is temperature, r the radial distance to the center, α_{l} the liquid thermal diffusivity, D_{l} the liquid mass diffusivity, and Y_{li} the liquid mass fraction of the component i. The values of α_{l} and D_{l} were obtained from refs 30, 31 for both palette compounds. The transport coefficients for a given binary mixture were calculated according to the Li correlation for the liquid thermal conductivity (described in detail in ref 30) and to the Wilke−Chang estimation method, followed by the Sanchez and Clifton correlation for the liquid mass diffusivity (both methods thoroughly presented in ref 31).

Equations 4 and 5 were numerically calculated by using a 1D parabolic−elliptic PDE solver in Matlab (pdepe solver, based on ref 35). The effect of internal recirculation for moving droplets is taken into account by replacing α_{l} and D_{l} in eqs 4 and 5 with

$$\alpha_{\mathrm{eff}} = X_{\mathrm{T}} \alpha_{\mathrm{l}} \tag{6}$$

$$D_{\mathrm{eff}} = X_{\mathrm{D}} D_{\mathrm{l}} \tag{7}$$

As X_{T} and X_{D} increase from 1 to 2.72 when the Péclet number (either thermal or mass transfer based) increases from 0 to infinity, the enhanced transport coefficients in the heat and diffusion equations account for the effects of internal convection on both processes. This model cannot solve in detail the actual temperature and species distributions inside the droplet, but it is considered to correctly predict their average surface values, which are critical properties in the droplet evaporation process.[12,34]

The implemented model was successfully validated for different fuels and conditions, including literature data as well as experimental results from the DCF. However, the agreement between the model and n-eicosane (one of the proposed surrogate palette compounds, as outlined below) was not as good as for other compounds, with predicted burning rates consistently higher than those displayed in the experimental tests. The reasons behind this behavior are not entirely understood, but a literature search revealed similar results for heavy alkanes subjected to combustion conditions.[36,37] Even though refs 36, 37 dealt with the droplet combustion process rather than its evaporation, the high coflow temperatures used in the current work (up to 1450 °C; Section 2.2) are thought to be representative of a combustion environment, keeping in mind the obvious difference that the high temperatures are here caused by the hot gaseous inert coflow rather than by a diffusion flame. In ref 36, the agreement of classical droplet theoretical models with experimental data was studied for a wide range of fuels, coming to the conclusion that theories progressively overestimated the burning rate as the fuel molecular weight increased, possibly as a consequence of gas-phase fuel decomposition near the droplet surface, more readily produced for heavier hydrocarbons. These gas-phase endothermic reactions would reduce the evaporation rate of the droplet in the experimental tests, while their absence in the classical models would explain the divergences found between observed and predicted burning rates.[36] Another possible explanation was proposed in ref 38, where the variable property models commonly used were found to approximate in a poorer way fuels with high molecular weight. In any case, ascertaining the cause for these deviations is not within the scope of this work, and an empirical fitting was performed on the described droplet vaporization model to calibrate it for each particular fuel. This was done by adding an energy sink (in the form of a constant endothermic heat of reaction) in the droplet evaporation transfer number. The value for this heat of reaction was empirically adjusted for each fuel as to achieve the best possible agreement between simulations and experiments. Such agreement can be observed in Figure 4, where the droplet vaporization curves experimentally obtained at the DCF for two pure compounds (eicosane and 1-methylnaphtlene) are compared with their respective simulations after
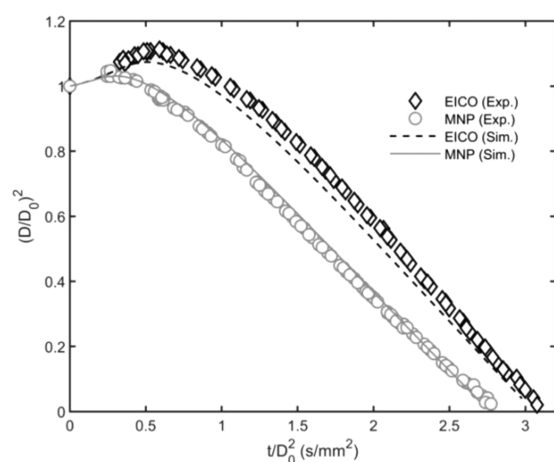
Figure 4. Comparison of the droplet vaporization curves experimentally obtained for pure eicosane (EICO) and 1-methylnaphtlene (MNP) along with the simulations provided by the model for both compounds after the empirical calibration.

applying the aforementioned empirical calibration. Results are displayed in terms of normalized diameter squared versus normalized time, using the droplet diameters at injection as references for normalization.

In spite of the empirical calibration, some differences can still be noted between the experimental and model results for eicosane. This is ascribed to the fact that eicosane droplets entered the combustion chamber partially frozen, due to the high freezing point of this fuel (36.5 °C). In the DCF tests, the freely falling droplets travel several centimetres at ambient temperatures prior to their intake in the combustion chamber. This could cause a partial freezing of the small droplets, which were initially heated at 50 °C at the droplet generator device for proper dosing. Even if this effect slightly distorts the ability of the model to reproduce eicosane behavior, this is a relatively minor effect that is expected to significantly decrease and eventually disappear as eicosane is mixed with 1-methylnaphtalene. The proposed combination of droplet evaporation tests and modeling results is therefore found to be valid for the binary mixtures designed and evaluated in Section 3.

3. RESULTS AND DISCUSSION

3.1. Surrogate Palette Choice. A critical step when designing surrogates is the definition of the surrogate palette, i.e., the set of pure compounds that are mixed together to create a surrogate fuel. These palette compounds should ideally be representative of the chemical families found in the target fuel,[4] display well-known design properties in the range of those found for the target fuel, and, at the same time, be readily available. The higher the number of palette compounds, the better agreement can be obtained for a certain design property, in addition to having the possibility of matching a greater number of them. However, as already stated, a greater number of palette compounds significantly increases the complexity of the process, not only in computational terms but also when it comes to result analysis. As the present work intends to explore new methodologies for the formulation and evaluation of surrogates, the surrogate palette was decided to consist only of two compounds: *n*-eicosane (EICO) and 1-methylnaphtalene (MNP). Each one is a representative of the two main chemical families found in the heating oil (see Appendix A): linear alkanes and aromatics. The choice of these two compounds in particular was based on their main properties, which were found to be in the range of those extracted for the target fuel in Table 1. Particular attention was

paid to the ability of these two compounds to properly reproduce the distillation curve of the heating oil (Figure 1), as both boiling temperatures are approximately terminal points of the extracted heating oil's distillation curve (517 and 616 K for MNP and EICO, respectively).

3.2. Formulation of Surrogates. As introduced above, a total of three different formulations, derived from different surrogate design approaches, were defined aiming to emulate the evaporation and sooting behavior of the target heating oil.

3.2.1. SR1 Formulation: Evaporation Behavior. The first surrogate, named SR1, was formulated by means of a novel methodology that intends to capture the evaporation behavior of the target fuel through the combined use of experimental and modeling exercises based on the single-droplet vaporization configuration.

The first step consists in experimentally characterizing the vaporization behavior of heating oil, a chemically complex fuel comprising hundreds of hydrocarbons. As a proper simulation of such a fuel by means of theoretical evaporation models would be unfeasible, this characterization is achieved by means of the DCF tests described in Section 2.2. The evolution of droplet diameter displayed in Figure 5 constitutes a valuable description of the evaporative behavior of the target heating oil when subjected to conditions representative of real flames.
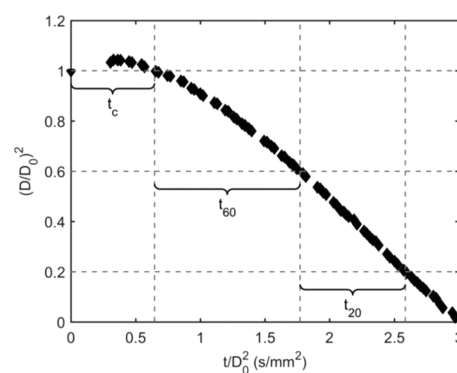

Figure 5. Experimental droplet vaporization curve obtained in the DCF for heating oil along with its extracted characteristic times t_c, t_{60}, and t_{20} (0.645, 1.126, and 0.813 s/mm² respectively).

As it can be observed in Figure 5, three characteristic times are defined for the measured vaporization curve. These times intend to describe the vaporization behavior of the fuel so that they can be used as design properties. The first one (t_c) describes the initial transient region, where the liquid droplet heats up, displaying a significant volumetric expansion (i.e., normalized droplet sizes greater than 1) due to thermal swelling. The second one (t_{60}) is intended to characterize the transition region where the droplet is already under vigorous vaporization, but the process has not reached its quasi-stationary behavior due to the liquid-phase unsteadiness. This region exhibits a sustained increase in the evaporation rate K, i.e., in the slope of the displayed droplet vaporization curve, $K = -d(D^2)/dt$. As the shape of the curve in this region can significantly vary among fuels and conditions, the design property is arbitrarily simplified to t_{60}, that is, the normalized time that it takes to the droplet to reach a normalized diameter squared of 60% its initial value. After this point, the droplet can be assumed to have reached the quasi-steady region, where the evaporation rate K remains approximately constant. The design property chosen for describing this region is t_{20}, as it is

graphically reflected in Figure 5. The curve points after $(D/D_0)^2 = 0.2$ are not included in any design property due to the higher experimental uncertainties for very small droplets.

The extracted characteristic times are therefore the property targets that the surrogates would have to match. To predict the value of the proposed design parameters (t_c, t_{60}, and t_{20}) for different mixtures of the surrogate palette, it is essential to use theoretical droplet vaporization models that can accurately simulate the droplet evaporation process under the experimental conditions of the DCF tests. The droplet vaporization curves simulated by the model described in Section 2.4 for different binary blends of the proposed palette compounds (EICO and MNP) are presented in Figure 6. The empirical
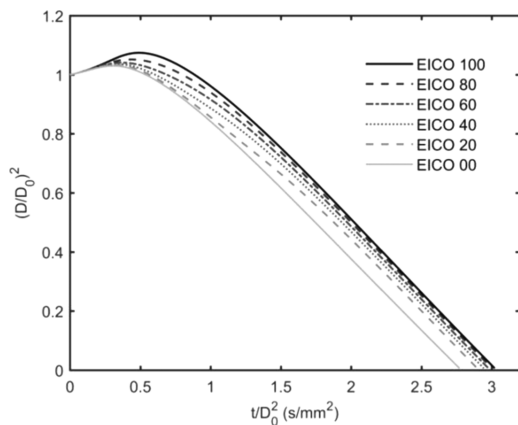
Figure 6. Droplet vaporization curves calculated by the model for different binary blends of eicosane (EICO 100) and 1-methyl-naphtlene (EICO 00) at the same conditions as those experimentally registered for the heating oil DCF test.

adjustment factors introduced for both pure compounds are also added to the simulation of their mixtures by weighting them according to the relative mass flow rate evaporated from each component.

As it can be observed in Figure 6, both palette compounds show well-differentiated features, with EICO displaying a much slower heat-up initial period and also a slightly higher quasi-steady evaporation rate (i.e., a steeper slope in the final regions). As expected, the evaluated blends show intermediate behaviors between the pure liquids, with more pronounced and longer initial volumetric expansion as the EICO content is increased. Quantification of the described behaviors can be done by means of the already presented characteristic times. For that purpose, simulations were run for a higher number of EICO–MNP blends, and their extracted characteristic times are presented in Figure 7 in terms of the EICO content in the mixture.

Among the three studied characteristic times, t_c is the most sensitive toward binary composition, showing a significant and sustained increase as the mixture is enriched in EICO. A domelike behavior is predicted for t_{60}, whereas t_{20} remains quite flat, as the quasi-steady evaporation rates calculated are quite close for both pure palette compounds. The increase of t_{20} for blends containing small amounts of EICO is ascribed to the fact that the transition from preferential vaporization of MNP to EICO is delayed toward the end of the curve, within the region assigned to t_{20}. The sensible heat necessary for rising up the droplet temperature would be responsible for the mentioned increase in t_{20} for such mixtures. Therefore, these
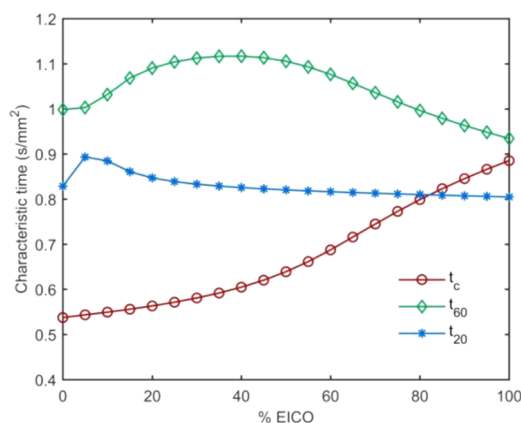

Figure 7. Characteristic times extracted for the simulation of EICO–MNP mixtures in terms of their EICO content (% mass).

characteristic times are representative of different aspects affecting the evaporation curve and, for a given surrogate blend, can be compared to those of the target fuel (Figure 5) so that any of them could be selected as the design parameter depending on the particular goal. However, if the objective is to determine the EICO–MNP blend that best reproduces the global evaporation behavior, the optimization problem should be based on a combination of the various characteristic times. With that purpose, the following global error for evaporation (e_{ev}) is calculated for each mixture i

$$e_{ev_i} = \sqrt{\left(\frac{t_{c_i} - t_{c_{ho}}}{t_{c_{ho}}}\right)^2 + \left(\frac{t_{60_i} - t_{60_{ho}}}{t_{60_{ho}}}\right)^2 + \left(\frac{t_{20_i} - t_{20_{ho}}}{t_{20_{ho}}}\right)^2}$$

(8)

with $t_{c_{ho}}$, $t_{60_{ho}}$, and $t_{20_{ho}}$ being the characteristics times of the target fuel (heating oil). The evolution of e_{ev} with the binary mixture composition is presented in Figure 8. Although
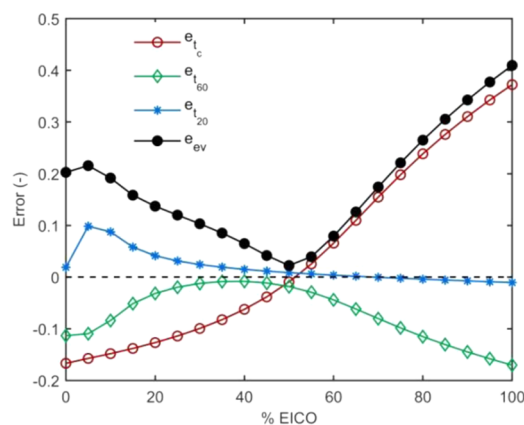

Figure 8. Errors in the various calculated characteristic times for all of the studied EICO–MNP blends along with the global error for evaporation (e_{ev}).

individual times display different trends, the combined error e_{ev} shows a well-defined minimum value for the EICO-51 mixture (51% eicosane). This blend was named SR1, aimed to emulate the evaporative behavior of the target heating oil. The adequacy of SR1 in achieving this goal will be experimentally evaluated in Section 3.3.1.

3.2.2. SR2 Formulation: Sooting Behavior. A second surrogate, named SR2, was formulated aiming to match the sooting behavior of the target heating oil. In this case, the formulation was based on a well-known soot indicator such as the yield soot index (YSI),[21,22] whereas the subsequent evaluation of its adequacy was obtained through experimental tests developed in the DCF (Section 3.3.2).

On the formulation side, the YSI was chosen as design property because of the availability of consistent and reliable data for a wide variety of compounds in the range of diesel fuel, including both palette components (EICO and MNP). In principle, it would be necessary to experimentally measure the YSI of the heating oil sample to obtain the required target YSI value. However, as the YSI of different jet and diesel fuels were found in ref 21 to correlate well with their total aromatic content (given that the fuel chemical distribution between single-ringed and multiringed aromatics remains close between fuels), an extrapolation using these data was performed to estimate the YSI of the target heating oil based on its total aromatic fraction. As Spanish light heating oil displays significant chemical closeness with diesel when it comes to its aromatic distribution (single-ring/multiring aromatic ratio of 2.9:1 in weight; see Appendix A in the Supporting Information), this approximation is thought to be adequate for the studied fuel. This extrapolation is illustrated in Figure 9,
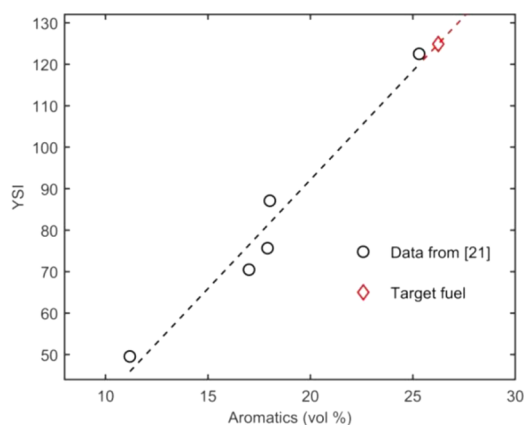

Figure 9. Experimental data and linear fit obtained from ref 21 for different jet and diesel fuels, along with the extrapolation that provides an estimation of the YSI value for the heating oil.

where the linear fit presented in ref 21 is slightly extrapolated beyond its upper limit to estimate the YSI of the target fuel, which contains 26.24% in volume of aromatics. The YSI so obtained (124.9) will be used as the target value for SR2 formulation.

Once the target YSI value is obtained, the process of formulating SR2 from the selected surrogate palette compounds can be done by applying the following mixing rule presented in ref 21

$$\text{YSI}_{\text{mix}} = \sum_{i=1}^{M} W_i \, \text{YSI}_i \tag{9}$$

with W_i being the mass fraction of compound i and YSI_i its YSI value as a pure fuel. By applying this mixing rule and extracting from ref 21 the YSI values of pure EICO (14.1) and MNP (471.2), the surrogate mixture which would match the target value of the heating oil is EICO-76. This blend will be named

SR2, designed to emulate the sooting propensity of the target fuel. The adequacy of SR2 in achieving this aim will be experimentally tested in Section 3.3.2.

3.2.3. SR3 Formulation: Physicochemical Properties. The third surrogate aims to match a set of physicochemical properties that are thought to be relevant for the evaporation and sooting behaviors. The surrogate design methodology followed here consists in a multiproperty regression algorithm, similarly to the approach used in ref 4 for diesel or in ref 39 for jet fuel surrogates. The design properties chosen for this study were YSI, liquid density, molecular weight, C/H ratio, and distillation curve. Even though some design properties are not directly connected with the evaporation and sooting behaviors, they are thought to be relevant for the aforementioned processes, and by matching them, the droplet evaporative and sooting behaviors of the formulated surrogate could be expected to get close to that of the target fuel, although there is no guarantee that matching a set of basic design properties will produce identical behavior in complex applications.[4] The YSI and C/H ratio are properties with a clear connection with the propensity to soot, whereas the distillation curve has been widely used to describe the evaporative behavior of multicomponent fuels. The liquid density displays a considerable impact on the droplet evaporation process, and it was proposed in ref 7 as a relevant target for surrogates aiming to emulate the evaporation and burning behaviors of complex liquid fuels. The molecular weight, on the other hand, is closely linked to the diffusive properties of the fuel, and therefore, it is also expected to be relevant for matching its evaporation behavior.

All of the property targets were experimentally obtained for heating oil through the already described initial characterization (see Section 2.1), except for the YSI, which was estimated to be 124.9 as outlined in Section 3.2.2.

Once the target values are known for the five design properties, the next step involves estimating the values that would display different blends of the proposed surrogate palette:

- YSI: as explained in Section 3.2.2.
- Liquid density (ρ): using the following mixing rule[31]

$$\rho_{\text{mix}} = \frac{1}{\sum_{i=1}^{M} W_i/\rho_i} \tag{10}$$

- Molecular weight (MW) and C/H ratio: from simple stoichiometric calculations.
- Distillation curve (DC): by means of the distillation model described in Section 2.3.

By knowing both the target values and the estimation methods, the relative errors found for each design property P between the calculated and target values for all of the EICO−MNP composition range can be obtained. For the simpler design properties, this relative error is calculated as follows

$$e_{P_i} = \sqrt{\left(\frac{P_i - P_{\text{ho}}}{P_{\text{ho}}}\right)^2} \tag{11}$$

with i being the evaluated EICO−MNP mixture, ho the target heating oil, and P any design property (YSI, ρ, MW, or C/H ratio). The relative error for the distillation curve is evaluated for the ensemble of the curve by averaging the deviations at all of the points

$$e_{DC_i} = \sqrt{\frac{1}{N_j} \sum_{j=1}^{N_j} \left(\frac{T_{i,j} - T_{ho,j}}{T_{ho,j}} \right)^2} \qquad (12)$$

with j denoting a point in the evaluated distillation curve (for instance, the point for 50% distilled mass), N_j the total number of evaluated points for each curve, and $T_{i,j}$ and $T_{ho,j}$ the temperature at point j for the blend i and the heating oil, respectively.

It is noteworthy that for most design properties (YSI, ρ, MW, and C/H ratio), a binary mixture EICO−MNP can be found that makes the corresponding e_P equal to zero, that is, a blend that perfectly matches the corresponding target value for the property P. The distillation curve, on the other hand, is composed of several points, and therefore, the simultaneous emulation of all of them would involve a high number of degrees of freedom, whereas the possible formulations only allows for one adjustable parameter which is the EICO/MNP proportion. This can be clearly inferred from Figure 10, where
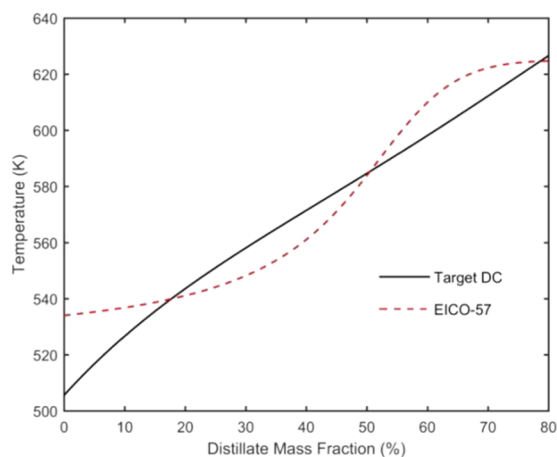
Figure 10. Comparison of the target distillation curve experimentally extracted for heating oil and the binary mixture EICO−MNP which minimizes the value of e_{DC} (EICO-57).

the distillation curve experimentally obtained for heating oil (see Section 2.1) is compared with the simulated curve of the EICO−MNP mixture, which minimizes the value of e_{DC} (EICO-57).

The optimal mixture EICO-57 displays significant differences compared to the heating oil experimental curve, with a clear sigmoid behavior that was not observed for the target DC. This is an expected result, as it is highly unlikely that a bicomponent mixture can adequately approximate the whole distillation curve of a real fuel containing hundreds of components.[16] However, as the aim here is not to closely match the distillation curve of the target fuel but rather to evaluate different methodologies for surrogate formulation, the distillation curve has been incorporated to the set of design properties, considering that even if the optimal blend does not achieve to closely emulate the DC of the target fuel, it still adjusts it better than the rest of possible mixtures.

Even though the errors e_{Pi} are expressed in relative form, each design property varies within a characteristic range, and while some properties display relatively small variations along the possible EICO−MNP mixtures, others are much more sensitive to the binary mixture composition. For instance, whereas the maximum relative error found for the density is

18.5%, the maximum deviation for the YSI rises up to 277%. An objective function that directly adds these relative errors would result in an unbalanced surrogate, which preferably matches those design properties with higher variability. A widely used approach to balance objective functions is through the use of weighting factors that can be adjusted for the purpose of achieving a surrogate that matches all design properties within certain previously defined tolerances. Alternatively, the relative errors can be divided by its maximum deviation so that all of the resulting normalized errors span from 0 to 1, and can be therefore compared in equal terms. This approach will be followed in this work, as it is thought that the obtained objective function considers the different design properties in an unbiased manner. The normalized errors (ε) are calculated as follows

$$\varepsilon_{P,i} = \frac{e_{P_i}}{\max(e_P)} \qquad (13)$$

with i being the evaluated EICO−MNP mixture and P being YSI, ρ, MW, C/H ratio, or DC. The global normalized error is defined through the following expression

$$\varepsilon_{global} = \sqrt{\varepsilon_{YSI}^2 + \varepsilon_\rho^2 + \varepsilon_{MW}^2 + \varepsilon_{C/H}^2 + \varepsilon_{DC}^2} \qquad (14)$$

By representing ε_{global} in terms of the binary mixture composition (Figure 11), the blend that minimizes the proposed global function can be obtained. This mixture, named SR3, corresponds to EICO-61.
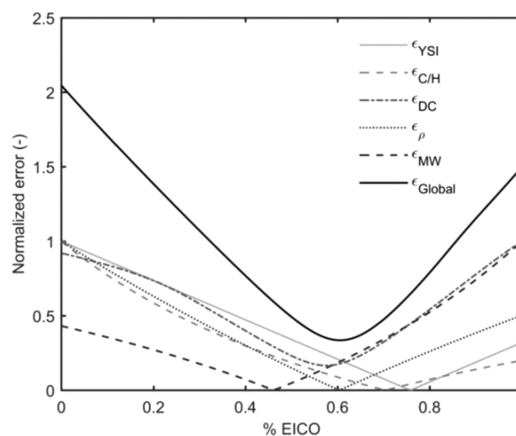

Figure 11. Graphical representation of the normalized global error (ε_{global}) along with the normalized errors of each design property for all of the studied EICO−MNP blends.

3.3. Experimental Evaluation of Surrogates. In previous sections, three different surrogates have been designed following different methodologies, with the aim of emulating the evaporative characteristics of the target heating oil (SR1: EICO-51), its sooting behavior (SR2: EICO-76), or a selection of physicochemical properties related with both (SR3: EICO-61). In this section, a sample of the heating oil will be experimentally tested at the DCF for all of the range of possible EICO−MNP mixtures to ascertain the degree of agreement shown between each surrogate and the target fuel. As an additional objective, by exploring the full range of EICO−MNP mixtures, the present work seeks to gain insight into the droplet evaporation and sooting behaviors of this binary mixture at conditions representative of real flames. Droplet combustion and evaporation results for the proposed

palette compounds are quite scarce, and therefore, the experimental data presented here for the full range of EICO−MNP mixtures can be of general interest, providing detailed evaporation data for pure and blended high-molecular-weight hydrocarbons.

Experimental tests were run at the DCF for both pure palette compounds (EICO and MNP), as well as for five different blends, namely, EICO-81, EICO-69, EICO-55, EICO-41, and EICO-20. The details regarding these experimental tests are presented in Section 2.2. The evaporative behavior will be characterized by means of the already presented droplet vaporization curves, whereas the propensity to soot will be studied through the developed aspirating soot probe.

3.3.1. Evaporation Behavior: DCF Curves. A comparison of the droplet evaporative behavior of the different proposed blends is displayed in Figure 12 along with the already

Figure 13. Characteristic times extracted for each EICO−MNP mixture, both experimentally at the DCF (exp.) and through the droplet vaporization model (calc.).
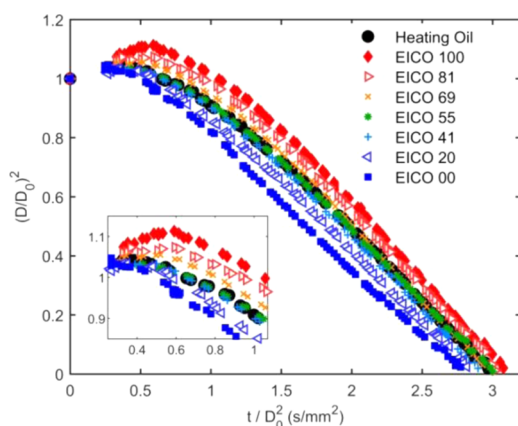
Figure 12. Experimental droplet vaporization curves obtained in the DCF for heating oil and all of the EICO−MNP mixtures.

presented droplet vaporization curve of the target fuel. Differences among blends are clear, with a slower initial heat-up period and a more pronounced thermal swelling as the mixture is enriched in EICO. Once the initial heating transient has finished, the squared droplet diameter decreases quite linearly with time, in accordance with the d^2 law. The quasi-steady slopes (i.e., the quasi-steady evaporation rates) are found to be slightly higher for EICO than for MNP, which in part compensates the already described longer heat-up period. At first sight, the mixtures which display a closer agreement with the target fuel vaporization curve are EICO-41 and EICO-55, both practically overlapping with the heating oil curve throughout all of the droplet lifespan. These two mixtures could be considered therefore to match the droplet vaporization behavior of the real fuel when tested at the high-temperature conditions described in Section 2.2.

The selected characteristic times can be extracted from the experimental curves displayed in Figure 12 for a more quantitative evaluation of the evaporative behavior of the different blends. Figure 13 displays the experimental times so obtained along with the theoretical predictions previously calculated by the droplet vaporization model for t_c, t_{60}, and t_{20} (Figure 7). When comparing the experimental and calculated values, it seems clear that the model adequately replicates the real behavior of the studied blends, in spite of some differences between predictions and experimental results. Significant deviations are only observed in t_c for EICO-rich mixtures,
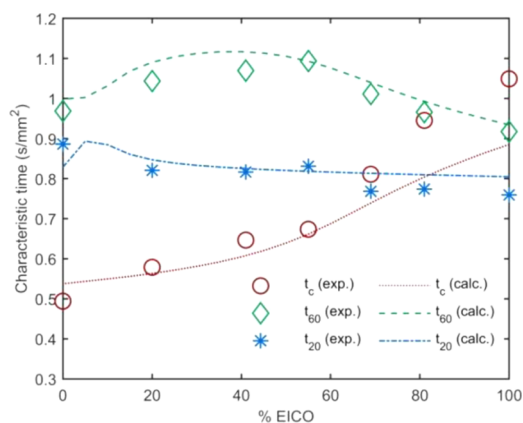
where the experimental heat-up period appears to last somewhat longer than predicted (probably because of the partial droplet freezing experimentally observed for eicosane). Nevertheless, this does not have any effect in this case since the optimum surrogates are found at eicosane concentrations <60%. The second parameter t_{60} experimentally confirms the domelike behavior predicted by the model, with a lesser degree of variation with composition than t_c. The already noted similar quasi-steady evaporation rates observed for both pure palette compounds causes the flatter behavior of t_{20} in Figure 13, with a small sensitivity of this design parameter to composition. It is noteworthy that the already described behaviors are highly dependent on the palette compounds' properties, and the weight of each of them in the final formulation could be therefore reversed with a different case study. For instance, in the case of palette compounds with similar initial heat-up transients and widely different quasi-steady vaporization rates, the characteristic time with a higher sensitivity toward composition would be expected to be t_{20} rather than t_c.

As the main objective of this experimental evaluation is to assess the degree of agreement between the three designed surrogates and the target fuel, the global error for evaporation (e_{ev}) is calculated for each blend experimentally tested at the DCF. These results are displayed in Figure 14 along with the relative errors obtained for each characteristic time. The optimal region is found to lie between EICO-41 and EICO-55, and therefore, any surrogate with a binary composition EICO−MNP located within this range could be considered to adequately emulate the droplet vaporization process of the target heating oil. SR1 (EICO-51) is precisely located in this region, and therefore, it may be regarded as a satisfactory surrogate if the objective is to reproduce the droplet vaporization behavior of the target fuel. SR2 (EICO-76), on the other hand, is located clearly outside of this optimal region, with significantly longer t_c ascribed to its EICO-rich composition. SR3 (EICO-61) displays an intermediate behavior. While it is also outside of the optimal composition region, it would display a closer evaporative behavior to the target fuel than SR2.

3.3.2. Soot Propensity: DCF Soot Probe. As stated above, the propensity to form soot of each fuel was experimentally tested by means of an aspirating soot probe (Figure 3). This probe retained the totality of the soot particles generated
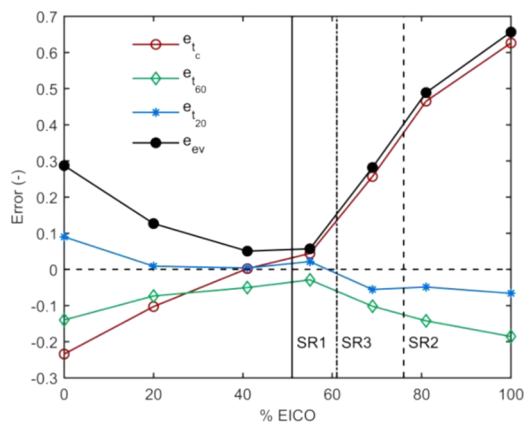
Figure 14. Characteristic time errors for each EICO−MNP blend along with the global error for evaporation (e_{ev}) experimentally obtained at the DCF. The three proposed surrogate mixtures are marked with vertical lines.

during the evaporation tests described in Section 3.3.1. The results are expressed in terms of the isolated droplet soot yield (IDSY, g_{soot}/g_{fuel}), which can be used to quantitatively characterize the soot yield for different fuels when subjected to the same experimental conditions. The evolution of the IDSY with binary composition is presented in Figure 15 for all
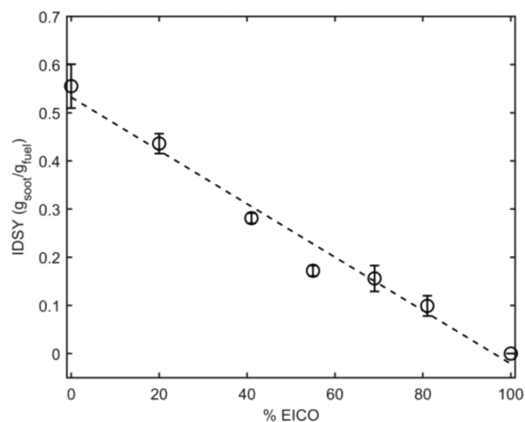
Figure 15. IDSY (g_{soot}/g_{fuel}) experimentally obtained for all of the studied EICO−MNP mixtures at the DCF.

of the studied EICO−MNP mixtures. The reported results are the average of at least three runs for each blend, except for pure eicosane, where the soot yield was below the detection limit attainable with this sampling method, and therefore, a soot index of zero was assigned.

It is noteworthy the quite linear behavior of the IDSY with binary composition in Figure 15. This linearity is not a trivial result, as the present configuration (a single liquid droplet evaporating under high temperature and reducing atmosphere) displays obvious differences with respect to the test conditions for YSI measurements, where the fuel sample is highly diluted (0.5% by mass) before entering a methane/air coflow flame.[21] The linearity found for the IDSY suggests the absence of significant interactions between the two surrogate components that could affect the amount of soot yielded by the isolated droplet's fuel vapors. The experimental conditions used at the DCF tests largely promote soot formation, explaining the high soot yields found for the fuels presented in Figure 15. It should

be noted that the soot collected is the result of the formation reactions around individual droplets, but subsequent oxidation is precluded by the lack of oxygen. This results in higher values than those usually found in real systems but has the advantage of making the result independent of the particular mixing and oxidation conditions to which soot particles can be subjected in different test stands. Therefore, the obtained IDSY values are thought to constitute a valid reference for the relative propensity to form soot of different fuels and blends, and will be used as a validation instrument for the designed surrogates.

The experimental IDSY data for the different blends are represented in Figure 16 against their respective predicted YSI values (see Section 3.2.2), along with the experimental point measured for the target heating oil.
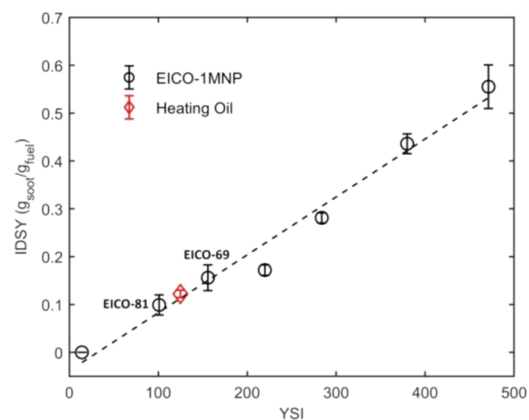

Figure 16. IDSY (g_{soot}/g_{fuel}) experimentally obtained for all of the studied EICO−MNP mixtures and the target fuel at the DCF in terms of their YSI predicted values.

As both the YSI and the proposed IDSY behave linearly with the binary mixture composition, the points displayed in Figure 16 form a straight line, and there is a clear (and linear) relationship between the predicted YSI values and the experimentally obtained soot yields. The fact that such a linear relationship can be drawn between the YSI and the soot experimentally collected at the single-droplet vaporization tests is a new finding and supports the feasibility of using this parameter to characterize the sooting propensity of a fuel under conditions significantly different from those used at the YSI experiments. The IDSY obtained for the target fuel (0.1220 ± 0.0077 g_{soot}/g_{fuel}) is located between those extracted for the mixtures EICO-81 (0.0990 ± 0.0211 g_{soot}/g_{fuel}) and EICO-69 (0.1560 ± 0.0268 g_{soot}/g_{fuel}). The blend which would yield the same amount of soot as heating oil could be estimated through lineal interpolation between these two mixtures. This optimal blend results to be EICO-76, exactly the same as SR2. The methodology used in the formulation of SR2, based on the YSI parameter (see Section 3.2.2), can be therefore considered to adequately predict the sooting behavior of both the target fuel and the different binary mixtures in the DCF, in spite of the already commented differences between the single-droplet approach and the configuration used for YSI measurements. SR1 (EICO-51), on the other hand, would yield a considerably higher amount of soot than the target fuel. The fact that SR1 adequately emulates the droplet vaporization behavior of heating oil, but not its sooting propensity (and vice versa for SR2) is a logical outcome of the simple surrogate palette chosen for this work,

as it contains only one adjustable parameter (e.g., the proportion of eicosane). The addition of more pure compounds to this palette would increase the degrees of freedom of the resulting mixture, allowing it to simultaneously match both target characteristics. As it happened with the evaporative validation, SR3 (EICO-61) displays an intermediate behavior between SR1 and SR2. The formulation methodology used with SR3 tried to match a set of physicochemical properties that are thought to be relevant for both behaviors, and therefore, this outcome agrees with the already stated impossibility of emulating both characteristics through the proposed binary palette.

4. SUMMARY AND CONCLUSIONS

This work proposes a novel approach for the design and evaluation of surrogates based on the single-droplet configuration. The obtained surrogates are intended to match the evaporative and sooting behaviors of a commercial heating oil, a fuel of interest due to its relevance and also because of the lack of studies addressing its behavior in the surrogate literature. The designed surrogate fuels are therefore thought to contribute in filling this gap. Heating oil displays a considerable physicochemical complexity, similar to that featured by other petroleum-derived fuels of higher global relevance such as diesel, gasoline, or kerosene, and therefore, the methodologies applied in the current work could be directly extrapolated for its application in those fuels. Additionally, the single-droplet experimental results obtained for both palette compounds (n-eicosane and 1-methylnaphtalene), as well as for several of their binary mixtures, are also thought to possess scientific value due to the scarcity of these data for pure and blended high-molecular-weight hydrocarbons.

A first surrogate (SR1) was formulated aiming to replicate the vaporization behavior of the target fuel. Its design involved a combination of single-droplet experimental tests and a multicomponent vaporization model. The obtained optimal blend (EICO-51) was afterward found to accurately match the experimental droplet evaporation curve of heating oil, supporting therefore the proposed formulation method. SR2 (EICO-76) was designed with the purpose of emulating the sooting characteristics of heating oil. The chosen design property was the well-known yield soot index (YSI), whereas a soot sampling probe was used at the single-droplet vaporization tests to validate its adequacy through the measurement of isolated droplet soot yield (IDSY, g_{soot}/g_{fuel}) for the various fuels and blends. In spite of the significant differences existing between both test experimental conditions, it was found that SR2 replicated remarkably well the IDSY of heating oil, achieving therefore the goal for which it was previously formulated based on the YSI. This result, in addition to the linearity found between the estimated YSI and the experimentally obtained IDSY supports the adequacy of the YSI as a sooting design parameter for experimental conditions and configuration considerably different from those used in its tests. A third surrogate (SR3) was formulated by matching a set of physicochemical properties relevant for both the evaporative and sooting characteristics. The chosen properties were C/H ratio, liquid density, molecular weight, YSI, and distillation curve. A multiproperty regression algorithm was applied to ascertain the binary mixture, which allowed for a better replication of all of the design parameters. The obtained blend (EICO-61) was subsequently found to display an

intermediate behavior between SR1 (which accurately matched the evaporative characteristic) and SR2 (with practically identical soot yield).

The simplicity of the binary palette used, in addition to the fact that the proposed surrogates were designed to match a single behavior (evaporation or sooting tendency), greatly facilitated the interpretation of the results and the evaluation of the proposed methodologies, which is the main objective of the current work. The obtained surrogates are somewhat restricted precisely by this simplicity, as binary mixtures offer only one degree of freedom and display a limited ability to replicate complex behaviors and to match multiple constraints. They have demonstrated, however, to closely emulate the target fuel characteristics for which they were formulated, validating thus the proposed approach. These methodologies can be used, either as stand-alone methods or in combination with others, to formulate more complex surrogates, which could simultaneously replicate a higher number of target behaviors of interest.

In summary, the methods described in this study have demonstrated to constitute valid and novel approaches to design and evaluate surrogates for complex liquid fuels based on the isolated single-droplet configuration. Future work in this regard could include the extension of the design behaviors, the use of a larger number of palette species to achieve a precise simultaneous replication of different complex characteristics, or the deployment of the aforementioned methods for other complex target fuels of interest such as diesel or Jet A. The general approach proposed here is perfectly valid also in those cases, although it is clear that obtaining accurate predictions becomes more difficult as the number of palette compounds increases. The advances in the evaporation models for multicomponent droplets can be incorporated in the same procedure framework, to facilitate the design of more complex surrogates, which can be duly refined by contrast with evaporation tests under realistic conditions.

■ ASSOCIATED CONTENT

ⓢ Supporting Information

The Supporting Information is available free of charge on the ACS Publications website at DOI: 10.1021/acs.energy-fuels.9b00737.

> Chemical composition by families of the target heating oil determined by GC−MS (PDF)

■ AUTHOR INFORMATION

Corresponding Author

*E-mail: ballester@unizar.es. Phone: +34 976 762 153. Fax: +34 976 761 882.

ORCID ⓘ

Álvaro Muelas: 0000-0003-1337-0310

Notes

The authors declare no competing financial interest.

also acknowledge the support of Luis Ojeda and Francisco Luño with the experimental tests.

■ REFERENCES

(1) Kim, D.; Violi, A. Hydrocarbons for the next generation of jet fuel surrogates. *Fuel* **2018**, *228*, 438−444.

(2) Farrell, J.; Cernansky, N.; Dryer, F.; Law, C.; Friend, D.; Hergart, C.; McDavid, R.; Patel, A.; Mueller, C. J.; Pitsch, H. *Development of an Experimental Database and Kinetic Models for Surrogate Diesel Fuels*; Report No. 0148-7191, SAE Technical Paper, 2007.

(3) Szymkowicz, P. G.; Benajes, J. Development of a Diesel Surrogate Fuel Library. *Fuel* **2018**, *222*, 21−34.

(4) Mueller, C. J.; Cannella, W. J.; Bruno, T. J.; Bunting, B.; Dettman, H. D.; Franz, J. A.; Huber, M. L.; Natarajan, M.; Pitz, W. J.; Ratcliff, M. A.; Wright, K. Methodology for formulating diesel surrogate fuels with accurate compositional, ignition-quality, and volatility characteristics. *Energy Fuels* **2012**, *26*, 3284−3303.

(5) Pitz, W. J.; Mueller, C. J. Recent progress in the development of diesel surrogate fuels. *Prog. Energy Combust. Sci.* **2011**, *37*, 330−350.

(6) Sarathy, S. M.; Farooq, A.; Kalghatgi, G. T. Recent progress in gasoline surrogate fuels. *Prog. Energy Combust. Sci.* **2018**, *65*, 67−108.

(7) Liu, Y. C.; Savas, A. J.; Avedisian, C. T. Spherically symmetric droplet combustion of three and four component miscible mixtures as surrogates for Jet-A. *Proc. Combust. Inst.* **2013**, *34*, 1569−1576.

(8) Liu, Y. C.; Avedisian, C. T. A comparison of the spherical flame characteristics of sub-millimeter droplets of binary mixtures of n-heptane/iso-octane and n-heptane/toluene with a commercial unleaded gasoline. *Combust. Flame* **2012**, *159*, 770−783.

(9) Liu, Y. C.; Savas, A. J.; Avedisian, C. T. Comparison of the burning characteristics of indolene and commercial grade gasoline droplets without convection. *Energy Fuels* **2012**, *26*, 5740−5749.

(10) Su, M.; Chen, C. Heating and evaporation of a new gasoline surrogate fuel: A discrete multicomponent modeling study. *Fuel* **2015**, *161*, 215−221.

(11) Elwardany, A.; Sazhin, S. S.; Farooq, A. Modelling of heating and evaporation of gasoline fuel droplets: a comparative analysis of approximations. *Fuel* **2013**, *111*, 643−647.

(12) Elwardany, A.; Sazhin, S.; Im, H. G. A new formulation of physical surrogates of FACE A gasoline fuel based on heating and evaporation characteristics. *Fuel* **2016**, *176*, 56−62.

(13) Kabil, I.; Sim, J.; Badra, J.; Eldrainy, Y.; Abdelghaffar, W.; Mubarak Ali, M. J.; Ahmed, A.; Sarathy, S.; Im, H.; Elwardany, A. A surrogate fuel formulation to characterize heating and evaporation of light naphtha droplets. *Combust. Sci. Technol.* **2018**, *190*, 1218−1231.

(14) Chen, X.; Khani, E.; Chen, C. A unified jet fuel surrogate for droplet evaporation and ignition. *Fuel* **2016**, *182*, 284−291.

(15) Dooley, S.; Won, S. H.; Heyne, J.; Farouk, T. I.; Ju, Y.; Dryer, F. L.; Kumar, K.; Hui, X.; Sung, C.-J.; Wang, H.; et al. The experimental evaluation of a methodology for surrogate fuel formulation to emulate gas phase combustion kinetic phenomena. *Combust. Flame* **2012**, *159*, 1444−1466.

(16) Bruno, T. J.; Smith, B. L. Evaluation of the physicochemical authenticity of aviation kerosene surrogate mixtures. Part 1: Analysis of volatility with the advanced distillation curve. *Energy Fuels* **2010**, *24*, 4266−4276.

(17) Wang, C.; Liu, X.; Law, C. Combustion and microexplosion of freely falling multicomponent droplets. *Combust. Flame* **1984**, *56*, 175−197.

(18) Law, C.; Faeth, G. M. Opportunities and challenges of combustion in microgravity. *Prog. Energy Combust. Sci.* **1994**, *20*, 65−113.

(19) Gill, R.; Olson, D. Estimation of soot thresholds for fuel mixtures. *Combust. Sci. Technol.* **1984**, *40*, 307−315.

(20) Yang, Y.; Boehman, A. L.; Santoro, R. J. A study of jet fuel sooting tendency using the threshold sooting index (TSI) model. *Combust. Flame* **2007**, *149*, 191−205.

(21) Das, D. D.; McEnally, C. S.; Kwan, T. A.; Zimmerman, J. B.; Cannella, W. J.; Mueller, C. J.; Pfefferle, L. D. Sooting tendencies of diesel fuels, jet fuels, and their surrogates in diffusion flames. *Fuel* **2017**, *197*, 445−458.

(22) Das, D. D.; John, P. C. S.; McEnally, C. S.; Kim, S.; Pfefferle, L. D. Measuring and predicting sooting tendencies of oxygenates, alkanes, alkenes, cycloalkanes, and aromatics on a unified scale. *Combust. Flame* **2018**, *190*, 349−364.

(23) Eurofuel. https://www.eurofuel.eu/ (accessed Sept 1, 2018).

(24) Bruno, T. J. Improvements in the measurement of distillation curves. 1. A composition-explicit approach. *Ind. Eng. Chem. Res.* **2006**, *45*, 4371−4380.

(25) *Standard Test Method for Distillation of Petroleum Products at Atmospheric Pressure*, ASTM Standard D 86-04b, ASTM International: West Conshohocken, PA, 2004.

(26) Muelas, Á.; Remacha, P.; Martínez, A.; Ballester, J. *Combustion Behavior of Jet A Droplets and its Blends With Butanol*, ASME Turbo Expo 2017: Turbomachinery Technical Conference and Exposition; American Society of Mechanical Engineers, 2017; p. V04AT04A073.

(27) Angeloni, M.; Remacha, P.; Martínez, A.; Ballester, J. Experimental investigation of the combustion of crude glycerol droplets. *Fuel* **2016**, *184*, 889−895.

(28) Muelas, Á.; Remacha, P.; Ballester, J. Droplet combustion and sooting characteristics of UCO biodiesel, heating oil and their mixtures under realistic conditions. *Combust. Flame* **2019**, *203*, 190−203.

(29) Li, T.; Zhu, D.; Akafuah, N.; Saito, K.; Law, C. Synthesis, droplet combustion, and sooting characteristics of biodiesel produced from waste vegetable oils. *Proc. Combust. Inst.* **2011**, *33*, 2039−2046.

(30) Perry, J. H. *Chemical Engineers' Handbook*; ACS Publications, 1950.

(31) Poling, B. E.; Prausnitz, J. M.; O'Connell, J. P. *The Properties of Gases and Liquids*; McGraw-Hill: New York, 2001.

(32) Huber, M. L.; Smith, B. L.; Ott, L. S.; Bruno, T. J. Surrogate mixture model for the thermophysical properties of synthetic aviation fuel S-8: Explicit application of the advanced distillation curve. *Energy Fuels* **2008**, *22*, 1104−1114.

(33) Abramzon, B.; Sirignano, W. Droplet vaporization model for spray combustion calculations. *Int. J. Heat Mass Transfer* **1989**, *32*, 1605−1618.

(34) Sazhin, S. S.; Elwardany, A.; Krutitskii, P.; Castanet, G.; Lemoine, F.; Sazhina, E.; Heikal, M. A simplified model for bi-component droplet heating and evaporation. *Int. J. Heat Mass Transfer* **2010**, *53*, 4495−4505.

(35) Skeel, R. D.; Berzins, M. A method for the spatial discretization of parabolic equations in one space variable. *SIAM J Sci. Stat. Comput.* **1990**, *11*, 1−32.

(36) Faeth, G.; Lazar, R. Fuel droplet burning rates in a combustion gas environment. *AIAA J.* **1971**, *9*, 2165−2171.

(37) Aldred, J.; Williams, A. The burning rates of drops of n-alkanes. *Combust. Flame* **1966**, *10*, 396−398.

(38) Faeth, G. Current status of droplet and liquid combustion. *Energy Combust. Sci.* **1979**, 149−182.

(39) Kim, D.; Martz, J.; Abdul-Nour, A.; Yu, X.; Jansons, M.; Violi, A. A six-component surrogate for emulating the physical and chemical characteristics of conventional and alternative jet fuels and their blends. *Combust. Flame* **2017**, *179*, 86−94.

Report Summary

1. Research objectives

In accordance with the previous description of the thematic unit, the main objective of the thesis is to develop methodologies for the description and characterization of the main evaporation and combustion behaviors of liquid fuels, both from the experimental and modeling points of view. To this effect, the following specific objectives were formulated:

- Development of experimental methods for studying the evaporation and combustion processes of isolated droplets under controlled and realistic conditions. For that purpose, a droplet combustion facility (DCF) was developed and thoroughly adjusted, including both optical and soot sampling methods.

- Experimental characterization of the combustion behaviors of a wide variety of liquids, both pure compounds and real fuels. The former will be used as the experimental input for the subsequent modeling exercises, whereas the latter will be focused on exploring the combustion characteristics of novel alternative fuels of relevance for stationary energy production, such as crude glycerol, bio-alcohols or pyrolysis oils. To this end, these novel fuels and their blends will be compared with the conventional fuel of reference in the corresponding application (e.g., heating oil or kerosene).

- Development and validation of droplet evaporation and combustion models, paying special attention to the marked multicomponent character of real fuels. The experiments performed at the DCF for pure fuels and their mixtures will be useful for validating the model under realistic in-flame environments.

- Joint use of model predictions and experimental results to explore advanced ways of characterizing the main combustion behaviors of liquids fuels of interest. For that purpose, the replacement of the complex real fuels by rather simple surrogate mixtures appears to be a useful approach which would significantly ease subsequent optimization strategies. This will be addressed through the introduction of the isolated droplet configuration to the surrogate design and validation processes.

2. Contributions of the doctoral candidate

The contributions of the doctoral candidate within the described project framework can be summarized in the following points:

- Further development of the droplet combustion facility (DCF), which was already operational at the time of the incorporation of the candidate (as it can be seen in (Angeloni *et al.* (2016))). After that point, the DCF capacities were further increased with the collaboration of the candidate: installation of new optical setups (cameras, lenses, filters, etc.), semi-automatization of the test data including the automatic size measurement of droplets and flames, development of a soot probe for global soot sampling, installation of new mass flow controllers, etc.

- Experimental characterization of a broad range of conditions at the DCF, aiming to find suitable test conditions and, at the same time, to obtain a detailed description of the gas coflow environment (i.e., determining burner stability, gas coflow temperature, composition and velocity for different conditions).

- Systematic droplet combustion tests at the DCF for a variety of liquid fuels of interest, both pure and real fuels. For the latter kind, the opportunities of study were previously detected through different literature reviews, including mixtures of relevance for the final application.

- Development and validation of droplet evaporation and combustion theoretical models. Starting from a review on the different models and submodels available in the literature, their implementation in the computing environment Matlab and their subsequent validation. For the case of the new analytical model developed in paper V for taking into account the vapors pyrolysis, the work of the doctoral candidate was framed in a research visit to the University of California San Diego.

- Undertaking studies aiming to characterize real fuels through the surrogate approach and, more specifically, through the introduction of the isolated droplet configuration to the surrogate design and validation processes. Review of the state of the art on physical surrogates for liquid fuels and joint use of droplet experiments and theoretical models for developing novel characterization methodologies.

- Collaboration in the writing and reviewing process of the different journal papers and conference communications listed in the Prologue.

3. Methodology

3.1 Droplet combustion facility

The single droplet experiments were conducted in the Droplet Combustion Facility (DCF), whose main characteristics are shown in Figure 3.1. A train of free-falling monosized droplets were created in a piezoelectric droplet generator, with initial diameters (d_0) of 150-180 μm. This is thought to be a compromise between experimental accuracy and closeness to real applications, as droplets in furnace sprays typically display mean diameters in the order of several tens of micrometers, with the tail of the spray distribution reaching the order of a hundred micrometers (e.g., see (Ballester and Dopazo (1994)) or (Ballester and Dopazo (1996))). The droplets were produced at a fixed d_0, with negligible changes over the course of the experiment. This steadiness in d_0 was critical for the validity of the results and therefore the droplet initial diameter was thoroughly checked in each experimental run yielding rms deviations below 0.5 μm. The droplet generation rate was set at 25 Hz, so that the free-falling droplets would not interfere with each other. Taking into account typical droplet and gas velocities (which shall be presented further on), it was checked that the interdroplet distance was always enough to prevent a given droplet from reaching any combustion product released by the preceding one.
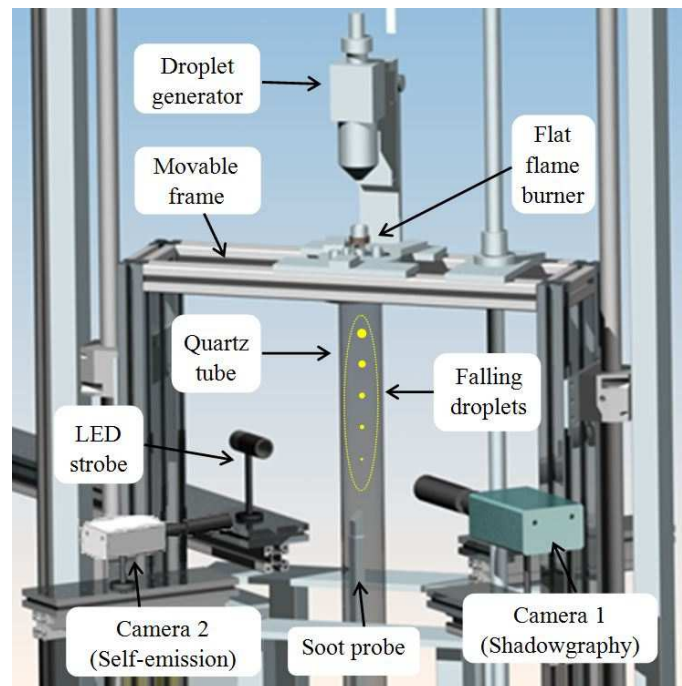

Figure 3.1. Schematic view of the droplet combustion facility (DCF).

This train of monosized droplets was injected by gravity in the combustion products of a flat-flame McKenna burner, which provided the hot gaseous coflow required for the droplet evaporation and combustion processes. Over the course of the thesis, the gas feed for this burner consisted in different mixtures of methane, hydrogen, air, N_2, O_2 and CO_2, depending on the desired coflow conditions (i.e., gas temperature, velocity and composition). The main aim here was to obtain a set of conditions which provided realistic combustion environments and, simultaneously, minimized the droplet-coflow relative velocities. Typically, the oxygen availabilities studied ranged from 0% (pure evaporation case) to 10% O_2, whereas the Reynolds numbers calculated from slip velocities were always < 1 (and < 0.2 during the quasi-steady evaporation stage). The droplet velocities were extracted from double-exposure pictures (as it will be detailed below) and the gas velocities were experimentally measured by means of the PIV technique using a Nd:YAG laser with Al_2O_3 particles as tracers. A summary of these PIV measurements and the resulting gas velocity profiles is presented in Addendum A3. As for the gas composition, it was monitored through an online paramagnetic analyzer (Testo 350-S). The most commonly used conditions at the DCF employed methane, air and O_2 as feed flows and therefore the flue gas composition consisted mainly in N_2, H_2O, CO_2 and, depending on the desired case, unburned O_2. The gas coflow temperatures were measured by means of a 50 μm thermocouple (type S), performing both radial and axial profiles of temperature. The axial profiles of temperature for the four most commonly used conditions are presented in Figure 3.2, where it can be observed that the droplets were tested in high temperature conditions infrequently studied in the droplet evaporation literature, as it will be elaborated further on. A detailed outline of these temperature measurements is provided in Addendum A3.
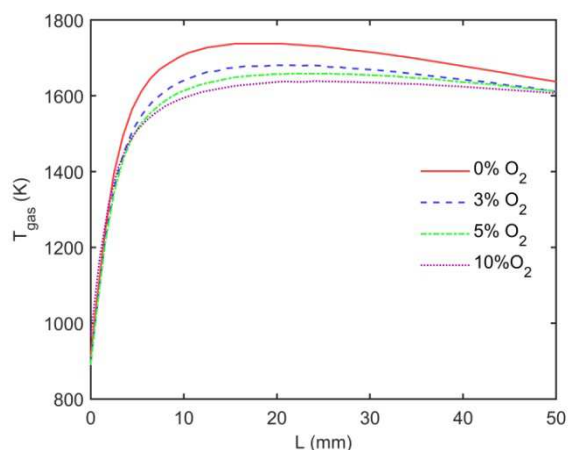

Figure 3.2. Axial temperature profiles measured for the four most commonly used gas coflow conditions (i.e., combustion of methane with different proportions of air and O_2, yielding 0, 3, 5 and 10% O_2 in the combustion products).

Once the free-falling droplets were injected into the hot gas coflow, different optical setups aimed to characterize their evaporation and, if oxygen was available, combustion process. A CCD camera (QImaging Retiga SRV, Camera 1 in Figure 3.1) was used in combination with a long distance microscope and a LED strobe to acquire sequential close-up shots of the droplets at different distances to the injection point. This was achieved through a movable frame which allowed for the axial displacement of the combustion chamber, modifying thereby the field of view of the fixed cameras (which typically ranged from the injection plane to the distance of droplet burnout). For a given position, Camera 1 worked with the multiple exposure technique, which was applied by synchronizing these elements with the droplet generation device by means of an Arduino board. The backlight LED strobe emitted very short (< 1 µs) light pulses every 500 µs and, thus, the adequate setting of the camera exposure time allowed for multiple shots of a given moving droplet in the same frame, as it can be observed in Figure 3.3a. In that image two sequential shots of the same droplet were obtained by using an exposure time of 1200 µs. Besides increasing the number of potential droplet size measurements per picture, this method enabled to determine the droplet velocity, as calculated from $v=e/\Delta t$ (being e the droplet displacement between shots and Δt=500 µs). Both the droplet diameter and velocity were automatically extracted from every image through a post processing code developed in-house in Matlab.
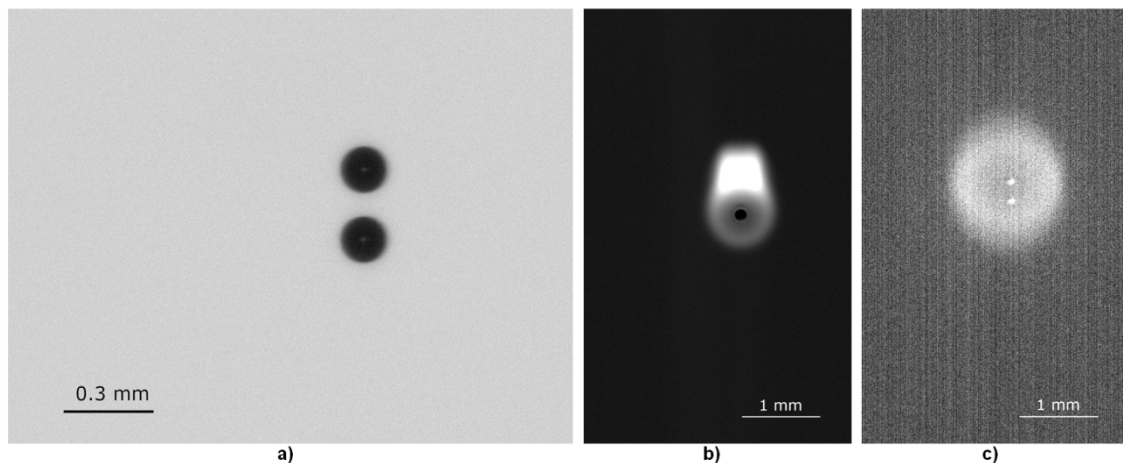

Figure 3.3. Pictures obtained at the DCF by means of: a) Camera 1 working with double exposure. The image displays twice an evaporating droplet of biodiesel; b) Camera 2 with the backlight on recording the sooty envelope flame of a heating oil droplet; c) Camera 2 without backlight recording the weak chemiluminescent blue flame surrounding a hexadecane droplet.

A second camera (Hamamatsu C11440-36U, Camera 2 in Figure 3.1) fitted with a telemicroscope was used to capture the diffusion flame which surrounded the droplet for all the combustion environments. In this case, the camera recorded the natural emission of both the

envelope flame and the incandescent soot particles generated in the region and, therefore, only a dim continuous backlight was provided in order to highlight the droplet shadow. This provided pictures similar to Figure 3.3b, where a heating oil droplet can be observed surrounded by a sooty flame. For the case of studying clean fuels without soot emission, the chemiluminescent blue flame was so faint that the dim backlight had to be switched off and the DCF had to be completely covered from exterior light in order to increase the weak signal-to-noise ratio (as it can be seen in Figure 3.3c for the case of a hexadecane droplet). Analogously to Camera 1, these pictures were post processed in Matlab to extract the flame sizes in an accurate and repeatable way.

A different kind of pictures were obtained through a third camera (Teledyne DALSA Genie Nano C4060) fitted with a DSLR lens. This color camera captured the macroscopic flame streak produced during the droplets' free fall along the combustion chamber. For sufficiently long exposure times, the individual droplets merged into a continuous trace which provided an integrated luminosity of a given number of consecutive droplets. This can be observed in Figure 3.4, where the flame traces of different fuels burning at the 10% O_2 condition are shown. Due to the characteristic luminosity stemming from soot particles, these images offer valuable information regarding the amount of soot produced for each fuel and condition and therefore they were also post processed in order to extract information in this regard.

Since the soot tendency is a relevant characteristic in liquid fuel combustion, this feature was also quantitatively studied at the DCF. To that end, two different soot sampling probes were developed. The first one, named Probe A, aimed to aspirate the small soot particles in the droplet's vicinity based on an aerodynamic separation process. The main components of the probe, its working principle and a picture of its operation are shown in Figures 3.5a, 3.5b and 3.5c respectively. As depicted in Figure 3.5.b, the broad differences between the inertia of the rather big droplets and the much smaller and lighter soot particles allowed for the lateral aspiration of the soot cloud without affecting the droplets trajectory when an appropriate intake flow was used. After being suctioned, the hot soot particles were quickly quenched by a cold N_2 flow and deposited on a quartz filter. The sampling of soot particles during a given test time provided a certain amount of soot which was subsequently dried in a furnace at 110 °C and weighed on an analytical scale (Sartorius CP225D; repeatability ±20 μg).
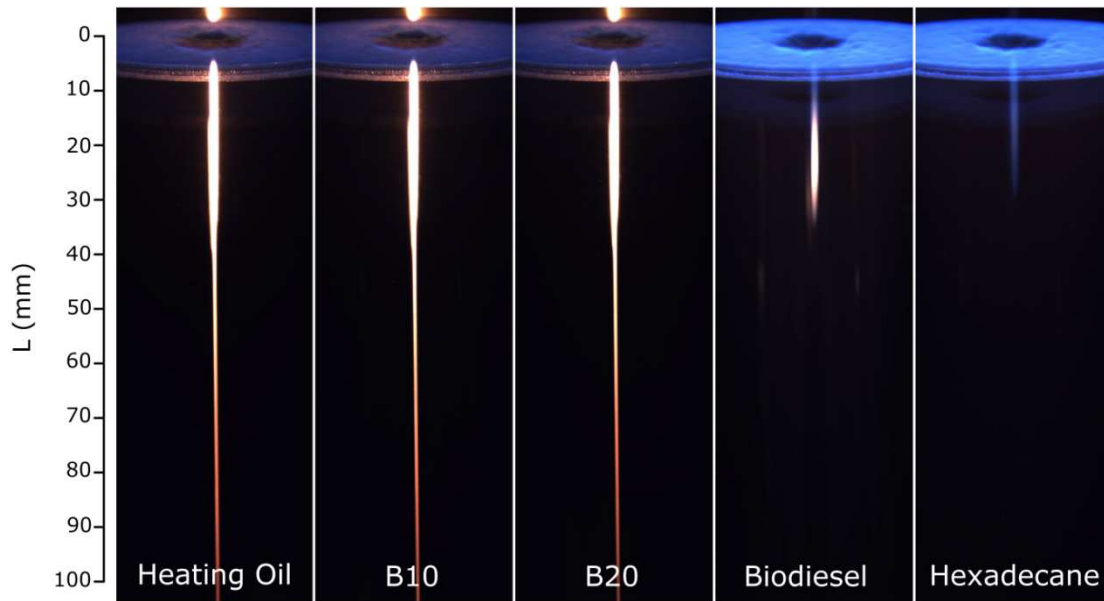
Figure 3.4. Flame traces captured for heating oil, biodiesel, two mixtures of both fuels with 10 and 20% biodiesel in volume and hexadecane. The pictures of heating oil and its blends were captured with an exposure time of 500 ms (integrating therefore the luminosity of 12.5 droplets), whereas for biodiesel and hexadecane 2 seconds had to be used (50 injected droplets). Figure extracted from Paper I.
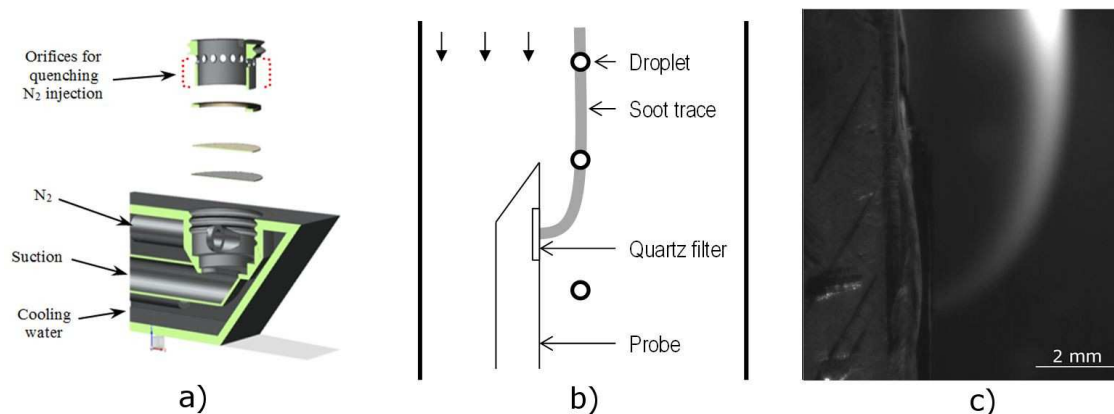

Figure 3.5. Probe A: a) Scheme with its main elements; b) Operation principle; c) Long exposure image of the incandescent soot cloud aspirated by the probe.

The sampling probe A provides complete information on the droplet's sooting behavior, since it can sample from different points along the droplet lifespan, generating thereby soot yield profiles. However, in some occasions the main interest can be focused on determining the global propensity to form soot of a given fuel under a specific set of conditions, rather than to study the soot production and oxidation dynamics along the droplet combustion process. For that purpose, the design of a simpler probe can provide some advantages, from both the

operational and the experimental accuracy viewpoints. Probe B (Figure 3.6) was developed during the framework of the thesis with the objective of quantifying the total amount of soot generated within the combustion chamber. In contrast to Probe A, which was able to study the soot production and depletion dynamics typical in oxidizing atmospheres, Probe B should only be used to characterize the global soot production under strictly reducing conditions (i.e., at the 0% O_2 case). Otherwise, the amount of soot reaching the sampling position would be a combination of soot production and oxidation processes and the interpretation of results would be significantly hindered due to the interlinked and uncontrolled variables.

However, if only a global soot indicator under reducing conditions is sought, Probe B displays some clear experimental advantages over Probe A, since the bigger filter (of the order of the combustion chamber diameter) allows for the collection of a far greater soot weight, significantly decreasing the experimental uncertainties in the weighing process. In addition to this, the fact that the cold metallic probe is located so far downstream from the droplets (Figure 3.6.b) ensures that the sampling process is completely non-intrusive, whereas the closeness of Probe A to the droplet stream was found to somewhat disturb the temperature field in the droplets' vicinity. For the case of Probe B, the soot agglomerates descended unoxidized and unaffected by the probe until the bottom of the combustion chamber, where they were collected on a quartz microfiber filter (Figure 3.6.c). Similarly to Probe A, these soot particles were dried in a furnace and weighed on an analytical scale, determining thereby an index for each fuel and condition in terms of the weight of collected soot per unit of injected fuel. In latter stages of the thesis, it was found that the hygroscopic behavior of the quartz filters was introducing significant uncertainties on the soot weight process through the absorption of room humidity. After that point, the weighing procedure was performed inside a controlled-humidity room with relative humidity levels of 10-15%.
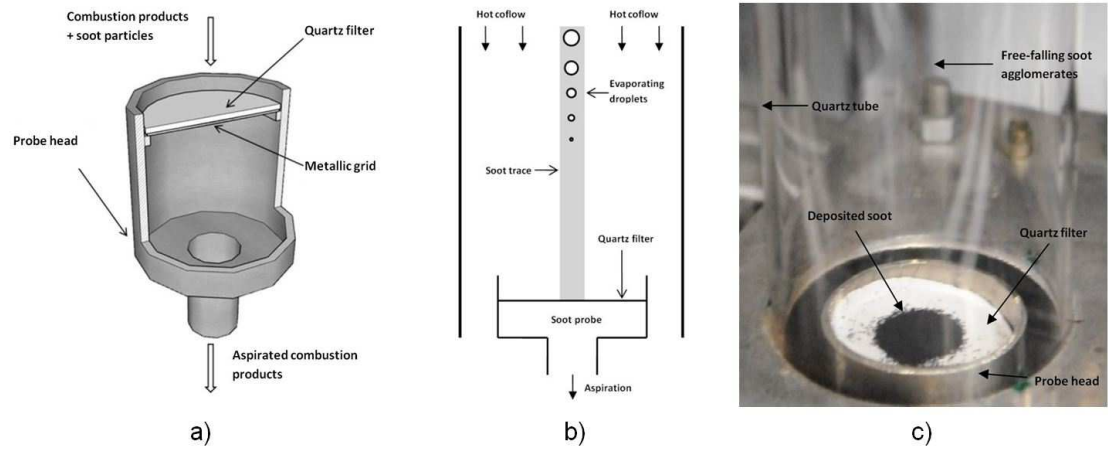
Figure 3.6. Probe B: a) Scheme of the probe head; b) Operation principle; c) Picture of the soot particles collected on the quartz filter at the bottom of the combustion chamber.

3.2 Droplet evaporation model

As already introduced, the second pillar of the thesis (together with the experimental tests) is based on the simulations provided by a theoretical droplet evaporation model. Although the experimental results obtained at the DCF encompasses both droplet evaporation and combustion results, from the simulation point of view most of the work developed in the current thesis was focused on evaporation conditions, that is, the simulation of a vaporizing droplet without combustion reactions in the gas phase. For that reason, the model presented here corresponds to a droplet evaporation model.

The problem considered here assumes an isolated, spherical monocomponent droplet of radius a vaporizing in an infinite stagnant atmosphere with temperature T_∞ and a mass fraction of the fuel $Y_{f,\infty}$ (typically $Y_{f,\infty}=0$). Assuming the absence of forced convection and buoyancy effects the resulting flow is completely one dimensional, and the profiles would appear as those sketched in Figure 3.7.
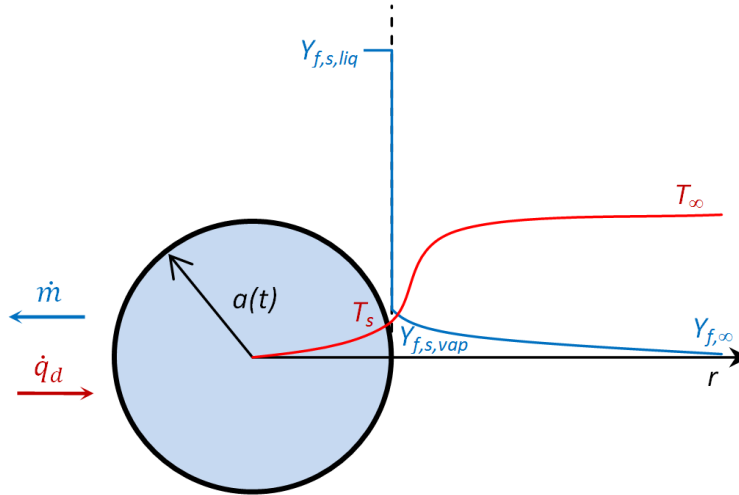

Figure 3.7. Scheme of the isolated droplet evaporation problem under spherico-symmetrical conditions.

The basic equations governing the gas phase of this process are the conservation of total mass, species and energy. Written in spherical coordinates:

$$\frac{d\rho}{dt} + \frac{1}{r^2}\frac{d}{dr}(r^2\rho\,v) = 0 \tag{3.1}$$

$$\rho\,\frac{dY_f}{dt} + \rho\,v\,\frac{dY_f}{dr} - \frac{1}{r^2}\frac{d}{dr}\left(r^2\rho\,D_f\,\frac{dY_f}{dr}\right) = 0 \tag{3.2}$$

$$\rho\,c_p\,\frac{dT}{dt} + \rho\,v\,c_p\,\frac{dT}{dr} - \frac{1}{r^2}\frac{d}{dr}\left(r^2\,k\,\frac{dT}{dr}\right) = 0 \tag{3.3}$$

Since this model will be mainly used for low pressure conditions, the small value of ρ / ρ_l (of the order of 10^{-3}) justifies the quasi-steady approximation in the analysis of the gas, as the response time of this gas phase is much shorter than that of the liquid (Liñán (1985)). As a result, the time-derivatives in Equations (3.1)-(3.3) can be neglected, significantly simplifying the problem. An additional assumption is the absence of radiative heating in Equation (3.3). This is due to the small droplets which are intended to be simulated by the model ($a_0 \approx 75$ μm), for which the effect of thermal radiation can be safely neglected (e.g., see (Long *et al.* (2015))).

Neglecting the time-derivative in Equation (3.1) implies that the evaporated mass flow rate ($\dot{m}$) is a constant, and does not depend on the radial position:

$$\dot{m} = 4 \, \pi \, r^2 \rho \, v = constant \tag{3.4}$$

This mass flow rate is actually the main unknown of the problem (as indicated in Figure 3.7), and therefore it is practical to rearrange Equations (3.2) and (3.3) in terms of $\dot{m}$:

$$\frac{\dot{m}}{4 \, \pi \, r^2} \frac{dY_f}{dr} - \frac{1}{r^2} \frac{d}{dr}\left(r^2 \rho \, D_f \frac{dY_f}{dr}\right) = 0 \tag{3.5}$$

$$\frac{\dot{m}}{4 \, \pi \, r^2} \, c_p \frac{dT}{dr} - \frac{1}{r^2} \frac{d}{dr}\left(r^2 \, k \, \frac{dT}{dr}\right) = 0 \tag{3.6}$$

Thus, the problem of the gas phase is reduced to solving these two differential equations constrained to the boundary conditions displayed in Figure 3.7:

$$T \, (r = a) = T_s \tag{3.7}$$

$$T \, (r \rightarrow \infty) = T_\infty \tag{3.8}$$

$$Y_f \, (r = a) = Y_{f,s} \tag{3.9}$$

$$Y_f \, (r \rightarrow \infty) = Y_{f,\infty} \tag{3.10}$$

For the droplet sizes used in this work, the liquid and gaseous phases can be safely considered to be in thermodynamic equilibrium at the interface, since non-equilibrium effects were found to only become significant for very small droplets ($a_0 < 25$ μm) (Miller *et al.* (1998)). Therefore, the temperature and fuel's vapor mass fraction at the surface can be related through the Clausius-Clapeyron equation:

$$Y_{f,s} = \frac{MW_f}{MW} \, e^{\left(\frac{L_v \, MW_f}{R_0 \, T_b}\right)\left(1 - \frac{T_b}{T_s}\right)} \tag{3.11}$$

Equations (3.5) and (3.6) can be integrated either numerically or, if the gas phase properties are considered to be spatially constant, analytically. This second approach is the one most

commonly followed in the literature, where different reference conditions are proposed in order to obtain a good agreement with experimental or detailed modeling results. Three of these reference state schemes were analyzed by Hubbard *et al.* (1975), where the *'1/3 rule'* proposed by Sparrow and Gregg (1958) was found to provide the most appropriate reference state for evaluating the gas properties. This method consists in evaluating gas properties at the following reference conditions:

$$T_{ref} = T_s + \frac{1}{3}(T_\infty - T_s) \tag{3.12}$$

$$Y_{f,ref} = Y_{f,s} + \frac{1}{3}(Y_{f,\infty} - Y_{f,s}) \tag{3.13}$$

Using constant gas-phase properties allows for the analytical integration of Equations (3.5) and (3.6). With the boundary conditions stated in Equations (3.7)-(3.10), this integration yields:

$$\dot{m} = 4\,\pi\,a\,\rho\,D_f\,ln\left(1 + \frac{Y_{f,s} - Y_{f,\infty}}{1 - Y_{f,s}}\right) \tag{3.14}$$

$$\dot{m} = 4\,\pi\,a\,\frac{k}{c_p}\,ln\left(1 + \frac{c_p\,(T_\infty - T_s)}{L_v + \dot{q}_d/\dot{m}}\right) \tag{3.15}$$

Recovering thus the droplet evaporation equations of the classic theory (e.g., see (Turns (1996), Williams (1985))). These analytical equations allow for the calculation of the two main unknowns of the problem, that is, $\dot{m}$ (the vaporization flow rate) and $\dot{q}_d$ (the sensible heat transferred to the liquid phase). The deviations obtained when using the constant property simplification and the *'1/3 rule'* reference state were verified in the framework of the thesis by comparison with a detailed numerical integration of Equations (3.5) and (3.6) taking into account variable gas phase properties. The negligible differences found between both cases justifies implementing the constant property simplification for the gas phase.

To close the problem, the liquid phase needs also to be analyzed. For the case of a monocomponent fuel, the only differential equation to solve for the liquid consists in the heat diffusion equation:

$$\rho_l c_l \frac{dT_l}{dt} = \frac{1}{r^2}\frac{d}{dr}\left(k_l\,r^2\,\frac{dT_l}{dr}\right) \tag{3.16}$$

With the following boundary conditions:

$$\frac{dT_l}{dr} = \frac{\dot{q}_d}{4\pi a^2 k_l}, \quad (r = a) \tag{3.17}$$

$$\frac{dT_l}{dr} = 0, \quad (r = 0) \tag{3.18}$$

If the study is extended for multicomponent fuels, the mass diffusion equation also needs to be considered to account for the migration of the different constituents within the liquid phase. Based on the work by (Sazhin *et al.* (2014), Sazhin *et al.* (2010), Sirignano (2010)), the following equations can be used to predict the mass fractions distributions of the liquid species within a spherically symmetric droplet:

$$\frac{dY_{li}}{dt} = D_l \left(\frac{d^2 Y_{li}}{dr^2} + \frac{2}{r} \frac{dY_{li}}{dr} \right) \tag{3.19}$$

$$\frac{|\dot{m}|}{4\pi \rho_l a^2} (\varepsilon_i - Y_{lis}) = -D_l \frac{dY_{li}}{dr}, \quad (r = a) \tag{3.20}$$

$$\frac{dY_{li}}{dr} = 0, \quad (r = 0) \tag{3.21}$$

Y_{lis} is the mass fraction of the component *i* at the surface in the liquid, whereas $\varepsilon_i = \frac{Y_{vis}}{\sum_i Y_{vis}}$, being Y_{vis} the mass fraction of the component *i* at the surface in the gas. The extension of the model to solve multicomponent cases does not affect the previously described gas phase equations since, following the approach proposed in (Sazhin *et al.* (2014), Sazhin *et al.* (2010), Sirignano (2010)), the fuel vapor is assumed to behave as a monocomponent gas (similarly to treat a mixture of N_2, O_2, Ar and CO_2 as air). This simplification implies that all fuel vapor components diffuse equally, being their relative composition spatially homogeneous.

The model analysis has relied so far on the assumption of a perfectly spherico-symmetrical evaporation process. As introduced before, this implies the absence of both natural and forced convection effects. Due to the small size of the droplets typically used at the DCF experiments, the assumption of negligible buoyancy effects in the evaporation is entirely justified (as assessed in an order-of-magnitude analysis in Appendix A of the Supplementary Materials of Paper I). As for the potential influence of forced convection on the DCF experimental results, even the small slip velocities typically found between the free-falling droplets and the gas coflow can introduce some noticeable disturbances to the 1-D situation, and therefore the model

has been adapted to take into account forced convection effects. Based on (Abramzon and Sirignano (1989)), for the gas-phase analysis, Equations (3.14) and (3.15) are modified to:

$$\dot{m} = 2\,\pi\,a\,\rho\,D_f\,Sh^*\,ln\left(1 + \frac{Y_{f,s} - Y_{f,\infty}}{1 - Y_{f,s}}\right) \tag{3.22}$$

$$\dot{m} = 2\,\pi\,a\,\frac{k}{c_p}\,Nu^*\,ln\left(1 + \frac{c_p\,(T_\infty - T_s)}{L_v + \dot{q}_d/\dot{m}}\right) \tag{3.23}$$

Being *Sh** and *Nu** the modified Sherwood and Nusselt numbers calculated as:

$$Sh^* = 2 + \frac{Sh - 2}{F_m} \tag{3.24}$$

$$Nu^* = 2 + \frac{Nu - 2}{F_t} \tag{3.25}$$

Sh and *Nu* in Equations (3.24) and (3.25) are calculated from the correlations proposed by Clift *et al.* (1978) for a sphere immersed in a fluid, whereas F_m and F_t are obtained from the correlations presented by Abramzon and Sirignano (1989), aiming to take into account the change of the film thickness due to the Stefan flow created by the evaporation process. It is worth to note that, for the case of zero slip velocity (*Re*=0), the resulting *Sh* and *Nu* numbers would equal 2 and therefore the analytical solution given by Equations (3.14) and (3.15) for the perfectly 1-D case would be recovered from Equations (3.22) and (3.23).

As for the liquid phase, the introduction of a slip velocity between the droplet and the gas ambience would result in the creation of internal convection transport in the liquid. For the case of high Péclet numbers ($Pe_l = \frac{2\,v_s\,r}{\alpha_l}$), this convective transport inside the droplet is stronger than thermal diffusion, appearing vortex structures which break the 1-D symmetry also in the liquid phase analysis. The use of the 'effective conductivity' model proposed in (Abramzon and Sirignano (1989)) is a well-known approach to overcome this complication by assuming that the heat is transferred within the droplet only by thermal conduction with an effective liquid thermal conductivity ($k_{l,eff}$) which accounts for the transport enhancement due to internal circulation. This model has proven to correctly predict the temperature at the surface as well as the evaporation rates, although it obviously cannot predict in a correct fashion the real temperature distribution inside the droplet. According to Abramzon and Sirignano (1989), convection effects in the liquid phase are introduced in the model by replacing k_l by $k_{l,eff}$ in Equations (3.16) and (3.17), being:

$$k_{l,eff} = k_l\,\chi_T \tag{3.26}$$

$$\chi_T = 1.86 + 0.86 \, tanh\left(2.245 \log_{10}\left(\frac{Pe_l}{30}\right)\right) \tag{3.27}$$

An analogous approach was proven in (Sirignano (2010)) to be valid for taking into account the effect of internal convection for the mass diffusion process. This is called the 'effective diffusivity' model, and is based on the substitution of D_l by $D_{l,eff}$ in Equations (3.19) and (3.20), being:

$$D_{l,eff} = D_l \, \chi_M \tag{3.28}$$

$$\chi_M = 1.86 + 0.86 \, tanh\left(2.245 \log_{10}\left(\frac{Re_l Sc_l}{30}\right)\right) \tag{3.29}$$

With the inclusion of forced convection effects, the model would be closed both for the gas and the liquid phases. This model was implemented in Matlab, along with a property database which allowed for the estimation of the different gas and liquid properties required by the model both for pure fuels and mixtures. All the properties were temperature-dependent, and followed the mixture rules summarized in Addendum A4.

The previously presented equations were numerically solved, assuming a constant droplet size during the very short time step (Δt), used for the integration. Starting from the initial conditions, the fuel's vapor mass fraction at the surface $Y_{f,s}$ could be determined through Equation (3.11), which in turn allowed for the calculation of the evaporated mass flow rate $\dot{m}$ (kg/s) by means of Equation (3.22). Knowing $\dot{m}$ enabled to obtain from Equation (2.23) the sensible heat gained or lost by the droplet $\dot{q}_d$ (W), which was introduced in Equation (3.17) as the boundary condition at the surface for the differential heat diffusion equation. Similarly, the knowledge of $\dot{m}$ and the fuel's mass fraction distribution in the liquid and vapor phases permitted to calculate the boundary condition stated by Equation (3.20) for the mass diffusion equation. Both differential equations were numerically solved by using a 1-D PDE solver integrated in Matlab and based on (Skeel and Berzins (1990)). For that purpose, a meshing of the droplet radius in 50 nodes with separations inversely proportional to $1/r^2$ was applied. The obtained changes in temperature and composition distributions within the liquid droplet during the evaluated time step Δt provided the initial conditions for the next iteration, whereas the droplet mass was diminished by subtracting the product $\dot{m}\Delta t$.

This model implementation was found to provide accurate results for monocomponent liquids, given that sufficiently small time steps were applied. However, for the case of liquid mixtures numerical errors frequently appeared in the mass diffusion equation irrespective of the time step used. This was especially true when the simulations considered high gas temperature conditions such as those found at the DCF experiments. For these cases, the direct application of Equations

(3.19)-(3.21) consistently presented numerical issues caused by the assumption of a constant droplet size during the evaluated time step. This is thought to be caused by the very low values of the liquid mass diffusion coefficients, causing that the migration speed of species become comparable to the receding velocity of the droplet surface. To avoid this problem, a coordinate transformation proposed in (Sirignano (2010)) was applied, transforming the PDE from an equation with a moving boundary to a fixed boundary problem with dimensionless variables. The new variables were calculated as follows:

$$\xi = r/a \tag{3.30}$$

$$\tau = \frac{\alpha_l t}{a_0^2} \tag{3.31}$$

$$\hat{a}(\tau) = a/a_0 \tag{3.32}$$

$$\beta = \frac{1}{2}\frac{d(\hat{a}^2)}{d\tau} \tag{3.33}$$

The mass diffusion equation based on these dimensionless variables becomes:

$$\frac{\alpha_l}{D_l}\left(\hat{a}^2\frac{dY_{li}}{d\tau} - \beta\,\xi\,\frac{dY_{li}}{d\xi}\right) = \frac{1}{\xi^2}\frac{d}{d\xi}\left(\xi^2\frac{dY_{li}}{d\xi}\right) \tag{3.34}$$

With the following boundary conditions:

$$\frac{\partial Y_{li}}{\partial \xi} = \frac{\rho\,D}{\rho_l\,D_l}\ln\left(1 + \frac{Y_{f,s} - Y_{f,\infty}}{1 - Y_{f,s}}\right)(Y_{lis} - \varepsilon_i)\,, \quad (\xi = 1) \tag{3.35}$$

$$\frac{\partial Y_{li}}{\partial \xi} = 0\,, \quad (\xi = 0) \tag{3.36}$$

The use of Equations (3.34)-(3.36) instead of (3.19)-(3.21) allowed to solve the mass diffusion equation without the aforementioned numerical issues. The fact that this transformation of the PDE to a fixed boundary problem was not required for the case of the heat equation is due to the much higher thermal diffusion coefficient in comparison to the liquid mass diffusion coefficient. Actually, the liquid Lewis number ($Le_l = \alpha_l/D_l$) for common liquid mixtures can usually located in the order of 100 (e.g., see (Rapp (2016))).

4. Results and discussion

This chapter summarizes the main results obtained over the course of the thesis. The presentation is divided in two sections, corresponding to the two approaches followed in the study: experimental droplet combustion tests and modeling exercises. A third and last section addresses the use of the isolated droplet configuration for the development of surrogates, a study which required the combined use of both experiments and theoretical models.

4.1 Experimental characterization of droplet evaporation and combustion

The experimental results obtained at the DCF are presented here and have been divided in two sub-sections. The first one deals with the testing of pure compounds of well-known properties, whereas the second one summarizes the results obtained for real fuels of relevance for heat and stationary energy production. This distinction is based on the different purpose of the results as well as on the different kind of behaviors that can be observed in each group, since real fuels can display distinct features due to their chemical complexity.

For any given fuel, the droplet evolution with the axial distance from the injection plane (L) was monitored by means of Camera 1 (Figure 3.1). Double-exposure shots provided detailed curves of both droplet diameter (d) and velocity (v) as a function of L, such as those displayed in Figure 4.1 for the case of the evaporation of n-butanol droplets. It is worth mentioning that the number of experimental points in Figure 4.1.a is the double than that of Figure 4.1.b, since each picture of Camera 1 allows for two droplet measurements but only one droplet velocity estimation (see Figure 3.3.a).
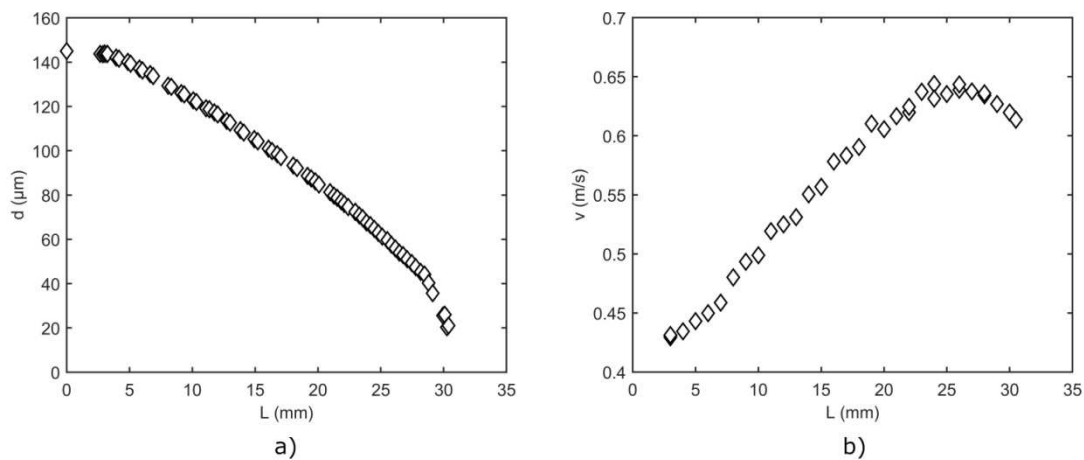

Figure 4.1. Axial profiles of droplet diameter (a) and velocity (b) obtained at the DCF for the evaporation of 150 μm droplets of pure n-butanol.

Even if the curves displayed in Figure 4.1 are of relevance for the description of the droplet evaporation process, it is preferred to work with the residence time as the independent variable since, unlike the axial distance L, it is not affected by the droplet velocity. A combination of both curves in Figure 4.1 allowed to create the final droplet size evolution curve shown in Figure 4.2.a which, following common practice in the field, is expressed in terms of squared droplet diameter versus residence time (t). This is due to the well known d^2-law (Spalding (1950)) which stems from the analytical description of the problem as stated Section 3.2: for any liquid monocomponent droplet subjected to a constant temperature ambience, and assuming that all the heat input to the droplet is employed in evaporating, the droplet diameter squared is found to linearly decrease with time. This linearity can be indeed experimentally observed in Figure 4.2.a, where the droplet evaporation curve for butanol at the 0% O_2 condition is shown. As it can be noticed, both axes in this plot have been normalized by the initial droplet diameter squared (d_0^2).
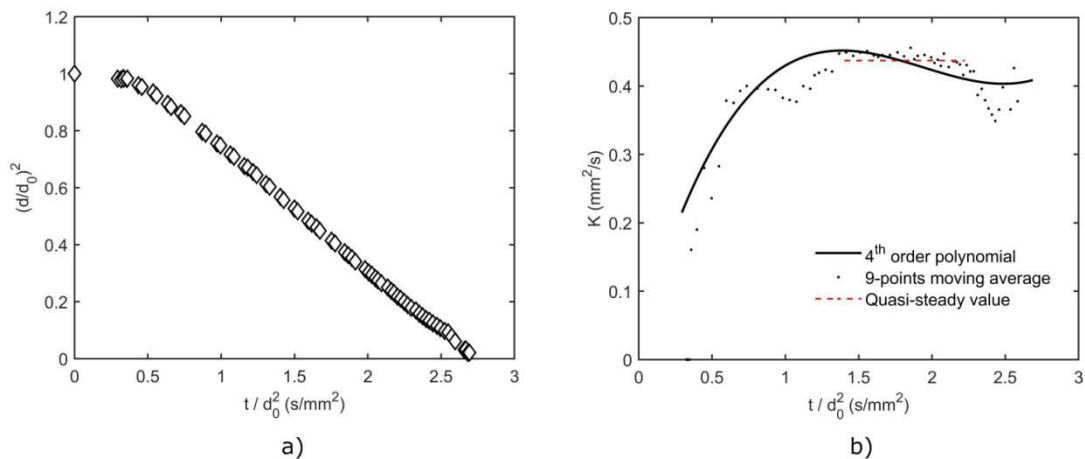

Figure 4.2. Normalized droplet size evolution with time for the evaporation of 150 μm droplets of n-butanol (a), and the subsequent estimation of evaporation rates through different methods (b).

Analyzing in greater detail the slope of the d^2-t plot or, as it is usually named, the evaporation rate ($K=-\mathrm{d}(d^2)/\mathrm{d}t$) reveals that K does not show a fixed value throughout all the droplet lifespan, but displays a transient behavior. Typically, the evaporation rate is close to zero at the injection point, quickly growing as the droplet heats-up to its quasi-steady state, where it reaches the constant value predicted by the d^2-law. For that reason, the results presented in this Section include different manners of expressing the evaporation or burning (if oxygen is present) rate. If only an average and global value corresponding to the quasi-steady state is sought, the points in Figure 4.2.a between $(d/d_0)^2$=0.6 and 0.2 were fitted to a straight line, being the global K value estimated from the line's slope. These boundaries were chosen because they are thought to

exclude both the initial heat-up phase and the final part of the curve, where the very small droplet sizes lead to higher experimental uncertainties. On the contrary, if the temporal evolution of K is sought, the d^2-t curve in Figure 4.2.a can be adjusted to a nth grade polynomial, whose derivative yielded the burning rate evolution with time. The polynomial grade n was always chosen as the minimum one which allowed to accurately capture the droplet size evolution, as the derivation of higher order polynomials can introduce numerical artifacts, as it is discussed in the Appendix A of (Liu *et al.* (2012)). These two ways of extracting the evaporation rate are compared in Figure 4.2.b, where it can be observed that the quasi-steady value predicted by the first method (red dotted line) provides quite close values to the local K values calculated by the second method (black solid line) for the quasi-steady region. Additionally, a 9-points moving average of K was added to Figure 4.2.b in order to confirm that, despite the higher uncertainty and scatter obtained when differentiating the experimental d^2-t data, all the methods appear to concur reasonably well.

The evaporation behaviors described in Figure 4.2 are only a part of the experimental characterization performed for liquid fuels in this Section. However, since this aspect is common for all of them, an introductory description seems appropriate at this point. Further analysis on other behaviors such as flame size measurements, soot shell appearance, occurrence of microexplosions or soot sampling will be presented at the place of first appearance of such phenomena.

4.1.1 Pure compounds

The experiments on pure compounds were primarily intended for the validation of the droplet evaporation model detailed in Section 3.2. The results presented here are organized in accordance to the different chemical families tested: alcohols, linear alkanes and aromatics.

4.1.1.1 Alcohols

The three alcohols tested at the DCF were ethanol, 1-butanol and glycerol. Their evaporation results are presented in Figure 4.3 for the three oxygen conditions explored (0, 3 and 10%). The temperature profiles measured for each of these oxygen conditions were displayed in Figure 3.2.
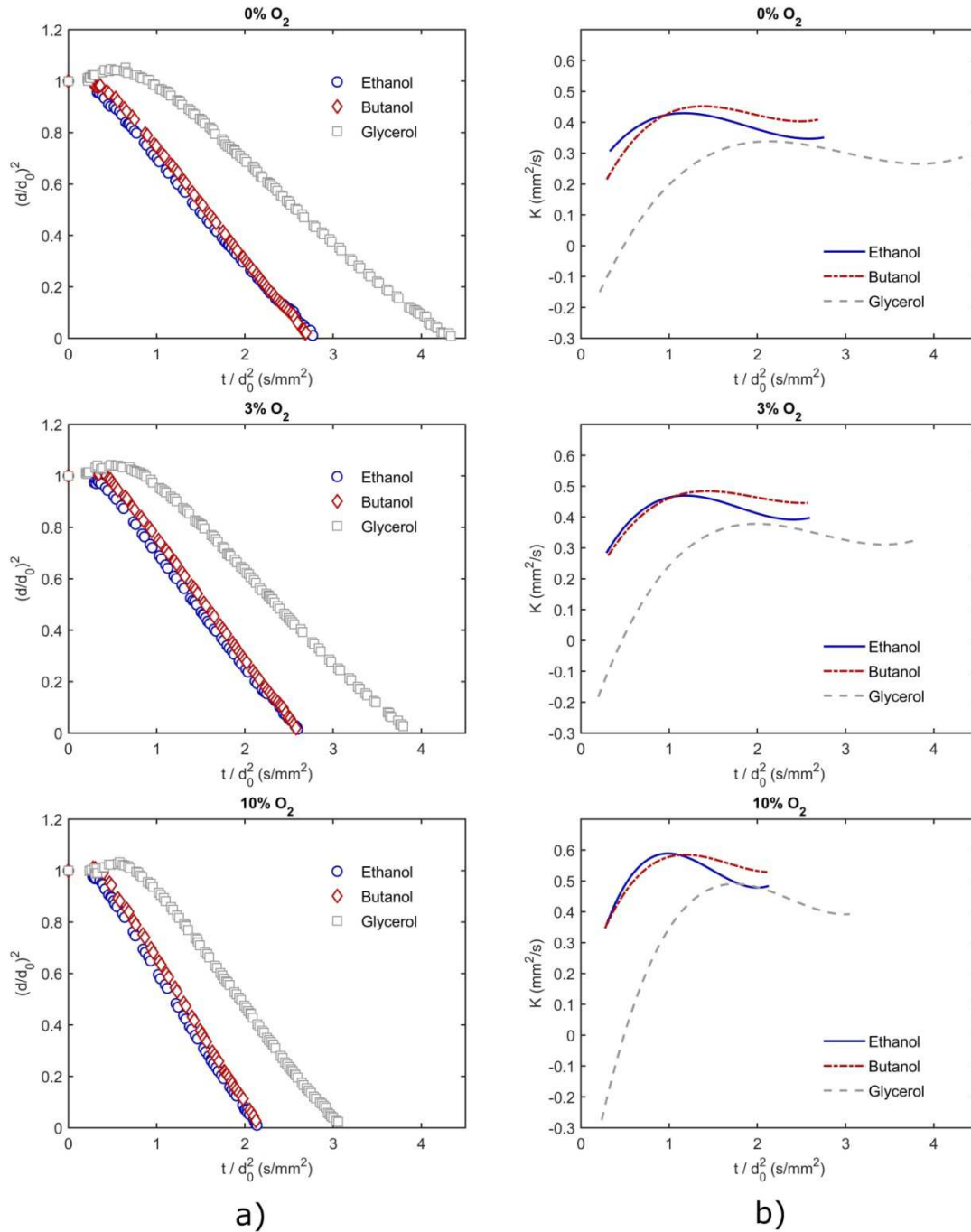
Figure 4.3. Normalized droplet size (a) and burning rate (b) evolution for the three pure alcohols at different oxygen conditions. The experimental points in (a) were fitted to 4th order polynomials in order to obtain the time-derivative plotted in (b).

As it can be observed in Figure 4.3, glycerol shows a quite distinct behavior compared to ethanol and butanol, with a considerably longer heat-up initial transient and lower quasi-steady burning rates. The first feature is primarily ascribed to the high boiling point of glycerol: 287 °C vs. 78°C for ethanol or 117°C for 1-butanol (NIST (2020)). The negligible vapor pressure of

glycerol at low temperatures causes that, during the first heat-up instants, the droplet increases its volume due to a decrease in the liquid density (Nayagam *et al.* (2018)). This thermal expansion can be also observed by the initial negative values of K, although the progressive increase of the vaporized mass as the droplet rises its temperature quickly overcomes this initial swelling. The lower burning rate of glycerol, on the other hand, is a consequence of a combination of different properties affecting this characteristic, such as the liquid density, the latent heat of vaporization or the vapor conductivity (see Equations (3.14) and (3.15)).

In Figure 4.3 it is also noteworthy that, for any given fuel, an increase of the oxygen availability in the coflow leads to a clear enhancement of the burning rate. Since evaporation is driven by the heat input to the liquid, the formation of a diffusion flame around the droplet when oxygen is available causes a distinct increase in the temperature gradient in the liquid vicinity. A composition of the gas richer in oxygen increases the flame temperature and also approximates the flame front to the droplet surface, boosting thus the burning rate and decreasing the total conversion time, as it can be verified in Figure 4.3. For a clearer comparison among fuels and conditions, the quasi-steady burning rates estimated for each case is presented in Table 4.1.

Table 4.1. Quasi-steady burning rates (mm^2/s) extracted for the three alcohols by fitting all the experimental points between $(d/d_0)^2$=0.6 and 0.2 to a straight line.

Fuel	0% O_2	3% O_2	10% O_2
Ethanol	0.4003	0.4467	0.5516
Butanol	0.4371	0.4787	0.5769
Glycerol	0.3124	0.3527	0.4692

Regarding the visual aspect of the burning alcohol droplets, different imaging methods were used to characterize this aspect. As already detailed, Camera 1 (Figure 3.1) was in charge of capturing the close-up pictures aimed to extract the evaporation behavior summarized in Figure 4.3 and Table 4.1. Since all alcohols showed a smooth evaporation until total conversion, this kind of images are not thought to provide further information, and therefore are not included here. The macroscopic traces of the free-falling droplets were captured with a DSLR camera (Nikon D5000). As expected, these pictures displayed no luminosity at all for the evaporation case, whereas a subtle blue trail appeared for the 3 and 10% O_2 conditions due to the chemiluminescent flame emission. These flame streaks are displayed in Figure 4.4 for the three alcohols at the 10% O_2 atmosphere. Interestingly, all of them show an orangish spot marking the point of droplet depletion. This spot was determined to arise from sodium emission, as corroborated through the use of a spectrometer (Ocean Optics HR2000) which revealed a

marked peak at 589 nm (D-lines of sodium). Even if high quality alcohols were used for this study (laboratory grade, purity > 99%), the presence of very small amounts of sodium in these polar compounds could create such emission without causing any significant impact on the droplet evaporation and combustion processes.
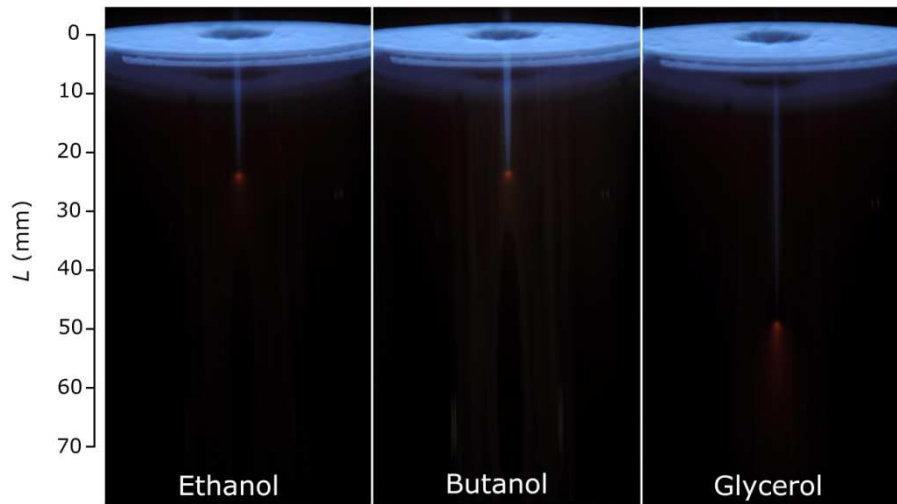

Figure 4.4. Long exposure pictures recorded for the three alcohols at the 10% O_2 condition. All the camera setups are coincident for the three pictures, with an exposure time of 2 seconds (50 injected droplets).

Further insight into the droplet diffusion flames can be gained from the pictures obtained from the monochrome Camera 2 (Figure 3.1), which used shorter exposure times and a much narrower field of view. The evolution of these flames for butanol is presented in Figure 4.5, where quite spherical envelope flames can be observed. This sphericity supports the previously discussed closeness of the evaporation and combustion process to a 1-D configuration, despite the fact that the DCF tests were performed under normal gravity. However, pictures in Figure 4.5 also display low signal-to-noise ratio caused by the weak intensity of the chemiluminescent emission and the high magnification required by the telemicroscope.
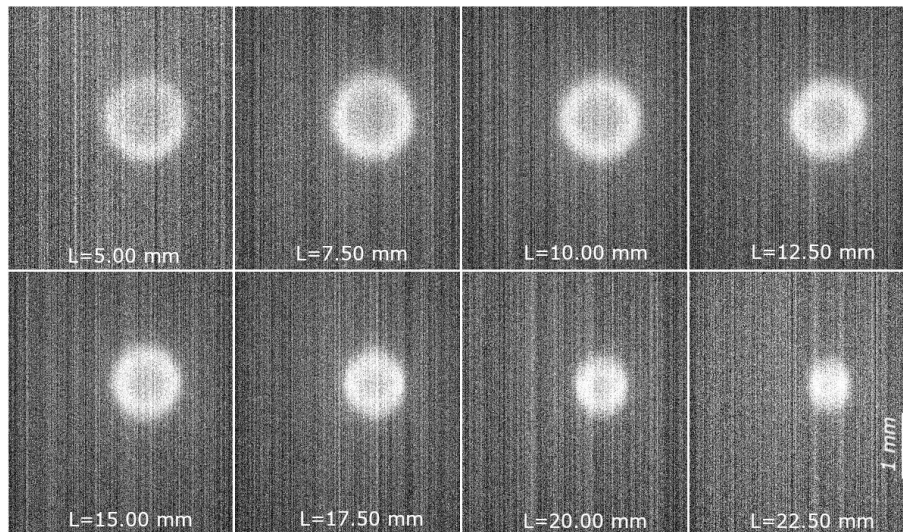
Figure 4.5. Individual envelope flames of butanol at the 10% O_2 condition. All the images are binned in order to increase their signal-to-noise ratio.

Finally, the individual envelope flames recorded with Camera 2 were measured in order to compare the flame sizes of the different alcohols. However, due to the close behaviors between the examined alcohols and the low quality of the flame images, the uncertainties in those measurements are believed to be too high to draw any conclusion in this aspect. Flame size measurements will be provided further on for other fuels with more defined flame shapes.

4.1.1.2 Alkanes

Four different linear alkanes were also tested at the DCF, namely n-heptane, n-dodecane, n-hexadecane and n-eicosane. This wide range of paraffins, from C_7 to C_{20}, is expected to cover interesting compounds which are usually studied in combustion science because of their presence in conventional liquid fuels. Most tests were performed under the usual coflow conditions already described for alcohols in the previous sub-section (and whose temperature profiles were displayed in Figure 3.2). A complementary study aimed to characterize the differences found for a given alkane when varying coflow variables such as the gas composition (conventional combustion vs. oxy-combustion) or its temperature (by modifying the kind of fuel or the composition of the oxidizer fed to the McKenna burner). For the sake of conciseness and clarity, these tests are not included here, although some of them will be used in Section 4.2.

The droplet evaporation results extracted for the linear alkanes under the four oxygen conditions explored (0, 3, 5 and 10%) are summarized in Figure 4.6. It is worth to note that the heavier paraffin (n-eicosane) was only tested for the pure evaporation case, whereas a mixture of

heptane and hexadecane (70-30%, by volume) has also been added to the comparison, since it introduces some first interesting results regarding the evaporation of a multicomponent fuel.

As it can be observed in Figure 4.6, the different pure alkanes display significant differences in the initial heat-up period but fairly similar quasi-steady burning rates. These results are consistent with the physicochemical properties of the compounds tested, as they are close among them with the notable exception of the boiling point, which increases from 98 °C for heptane to 343 °C for eicosane (NIST (2020)). This similarity in the quasi-steady K among fuels can be noted in Figure 4.6.a because the droplet size curves run practically parallel, as well as from the fact that all alkanes show quite close values of K during the final stages of droplet lifetime in Figure 4.6.b. Analogously to the results listed in Table 4.1 for the alcohols, the quasi-steady burning rates estimated for each pure alkane is presented in Table 4.2 in order to provide a clearer comparison among fuels and conditions. When comparing alkanes and alcohols, the former compounds consistently show higher burning rates.

The only mixture displayed in Figure 4.6.a shows a clearly distinct behavior, with two evaporation stages separated by a transition plateau. This behavior has also been observed in other experimental studies addressing binary mixtures with significantly different boiling points such as (Wang *et al.* (1984)), and it is explained by the transition from a preferential vaporization of the more volatile compound to a steady state where the surface is enriched in the heavier species while the composition of the droplet core remains frozen at the initial value. The slow mass diffusion mechanism is not capable of supplying heptane to the surface at the required rate, and therefore this region is progressively enriched in hexadecane to a point where the droplet temperature becomes dominated by the boiling point of this compound (Wang *et al.* (1984)). The drop in evaporated mass due to this enrichment in hexadecane at the surface implies a second heat-up transient, creating the plateau shown in Figure 4.6.a. Up to this transition plateau, both the droplet size curves and the burning rates obtained for the C_7-C_{16} mixture are quite similar to those of pure heptane, confirming the preferential vaporization of this compound during the first stage. Finally, it is worth to note that the relatively complex shapes of the experimental curves in Figure 4.6.a for the C_7-C_{16} blend made necessary to use 6th order polynomials to adequately fit them, introducing the aforementioned numerical artifacts which can be observed in Figure 4.6.b, especially at both extreme ends of the K - t/d_0^2 curves.
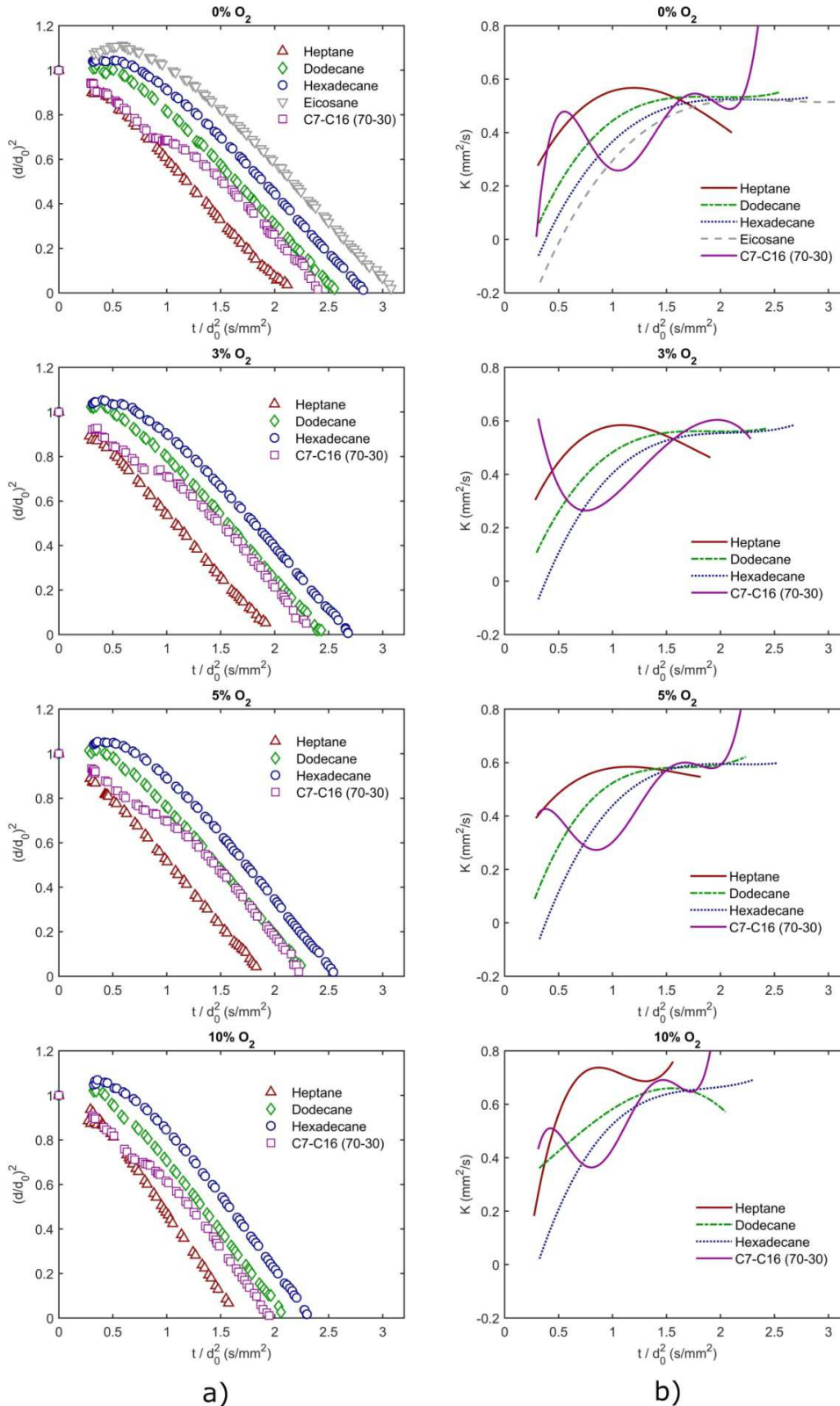
Figure 4.6. Normalized droplet size (a) and burning rate (b) evolution for the examined paraffins at the different oxygen conditions. The experimental points of all pure alkanes in (a) were fitted to 4th order polynomials in order to obtain the time-derivative plotted in (b), whereas a 6th order polynomial was required for the heptane-hexadecane mixture.

Table 4.2. Quasi-steady burning rates (mm^2/s) extracted for the pure alkanes by fitting all the experimental points between $(d/d_0)^2$=0.6 and 0.2 to a straight line.

Fuel	0% O_2	3% O_2	5% O_2	10% O_2
Heptane	0.5453	0.5687	0.5798	0.7105
Dodecane	0.5349	0.5686	0.5878	0.6530
Hexadecane	0.5317	0.5633	0.6000	0.6611
Eicosane	0.5355	-	-	-

Regarding the flame aspect, the burning of alkane droplets under an oxygen-rich atmosphere provided very similar pictures to those presented in the previous sub-section for alcohols. That is, the long exposure pictures of the macroscopic trace at the 10% O_2 condition showed weak chemiluminescent blue traces (such as those in Figure 4.4) and the short exposure images of the individual flames displayed spherical envelope flames very similar to those illustrated in Figure 4.5. This latter set of pictures could be post-processed because of their slightly higher signal-to-noise ratio, and the flame size evolution could be quantitatively extracted. These results are presented in Figure 4.7 for all the alkanes which were tested at the 10% O_2 atmosphere. As it is common practice in the field, flame sizes are presented normalized by the droplet diameter, yielding the flame standoff ratio (FSR = d_f / d).
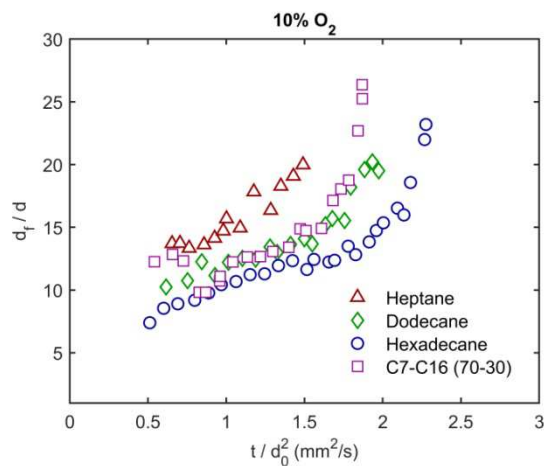

Figure 4.7. Flame standoff ratio evolution of the different alkanes tested at the 10% O_2 condition.

In spite of the uncertainties associated with flame measurements, the experimental data in Figure 4.7 point to larger flame sizes for the lighter alkanes and also to a sustained increase in the FSR of all fuels during their burning. This latter behavior is due to the fuel vapor

accumulation effect (Law *et al.* (1980)), particularly relevant for low ambient oxidizer concentrations such as those used here. The heptane-hexadecane mixture shows an interesting behavior, with initial flame sizes very similar to those measured for neat heptane until a sharp decrease in the flame diameter takes place. This sudden flame contraction occurs at the same residence time where the plateau appeared in Figure 4.6.a for the 10% O_2 case ($\approx$0.75 s/mm^2), and thus it is ascribed to the aforementioned second heat-up transient, where the heat input to the droplet was used to increase its temperature rather than in vaporizing. After this transition phase, the FSR shown in Figure 4.7 display an intermediate behavior between heptane and hexadecane, as expected from the fact that in this region the evaporated products are a mixture of both.

As previously stated, the flame images of these alkane compounds were qualitatively similar to those presented for alcohols in Figures 4.4 and 4.5. However, the pure vaporization case (0% O_2 coflow) showed significant differences, since a bright yellowish emission appeared in the long-exposure traces (while for alcohols no luminosity was found). This yellowish emission appears in Figure 4.8 for all the pure paraffins in oxygen-free conditions, and it is ascribed to the formation of soot particles. The high temperature and reducing conditions of the 0% O_2 atmosphere promoted gas-phase pyrolyzation reactions which broke the vaporized hydrocarbon molecules, yielding soot aggregates as final product. These solid carbonaceous particles glowed with a black-body emission when hot (as confirmed through the spectrometer measurements), and descended unoxidized towards the exit of the combustion chamber, where they showed their characteristic black color at colder temperatures. When comparing among fuels in Figure 4.8, it is clear that the heavier alkanes displayed a greater soot formation tendency, with a monotonic rise in sooty luminosity as the carbon chain increased. It is worth to note that, under this condition, the total droplet evaporation time varied between 24 mm (heptane) and 37 mm (eicosane), reaching thus the sooty traces longer axial distances than the droplets themselves.
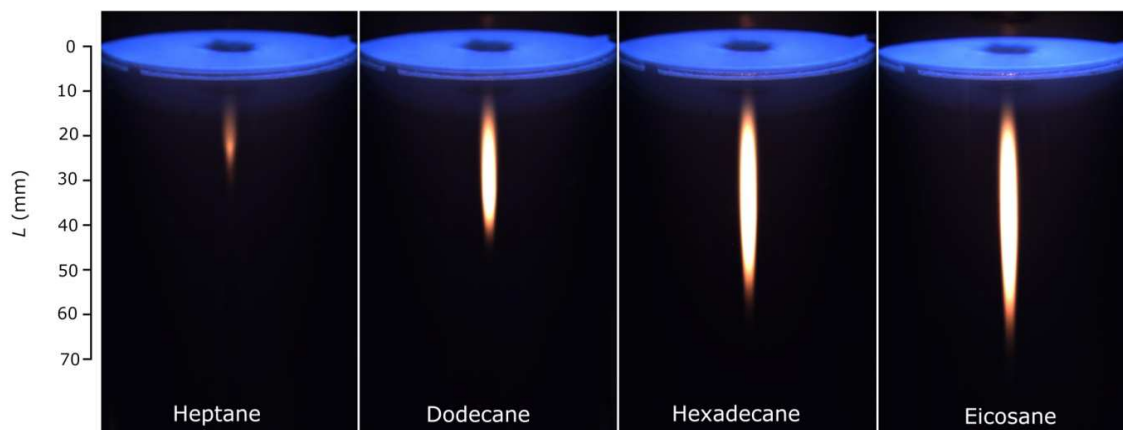
Figure 4.8. Long exposure pictures recorded for the four pure alkanes at the 0% O_2 condition. All the camera setups are coincident, with an exposure time of 1 second (25 injected droplets).

4.1.1.3 Methylnaphthalene and its mixtures

The last chemical family explored in this Section is that of aromatic hydrocarbons, namely through the study of 1-methylnaphthalene. It is well known that aromatic hydrocarbons are responsible for an important part of the soot produced in the combustion of conventional liquid fuels because of their strong soot generation tendencies (e.g., see (Das *et al.* (2018))). Taking into account the main objectives of this work, 1-methylnaphthalene was selected as a good representative of the aromatic family because of its physicochemical properties, highly sooty behavior (Das *et al.* (2018)), and its recognition in the combustion literature as a compound of interest for the study of conventional liquid fuels (e.g., see (Farrell *et al.* (2007), Mueller *et al.* (2016))).

For that purpose, five mixtures of methylnaphthalene (MNP) and eicosane were tested within the frame of a broader study (published in Paper VI). As determining the soot propensity of the different blends was among the main objectives of the study, it was studied in pure evaporation tests (0% O_2 atmosphere), in order to increase the soot yield and facilitate the soot sampling process. The droplet evaporation results for these mixtures are presented in Figure 4.9.
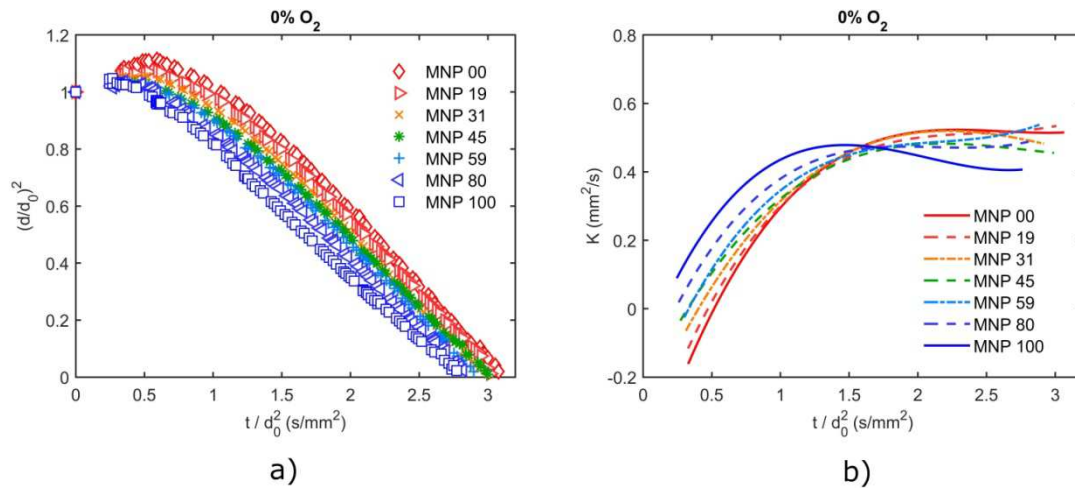
Figure 4.9. Normalized droplet size (a) and burning rate (b) evolution for methylnaphthalene and its mixtures with eicosane at the pure vaporization condition. The experimental curves in (a) were fitted to 4th order polynomials in order to obtain the time derivatives plotted in (b).

As it can be observed in Figure 4.9, the binary mixtures display a monotonic behavior with composition. As the percentage of MNP increases, the initial droplet heat-up transient accelerates, starting the vigorous droplet evaporation earlier. However, the quasi-steady evaporation rate decreases, being that of pure methylnaphthalene (0.4531 mm^2/s) noticeably lower than that of eicosane (0.5355 mm^2/s, Table 4.2). The same multicomponent evaporation mechanism described in Section 4.1.12 for the heptane-hexadecane blend is expected to be valid here, although in this case the evaporation curves show a quite different behavior, without a transition plateau for any of the mixtures displayed in Figure 4.9.a. This is ascribed to the closer boiling points of methylnaphthalene and eicosane when compared to heptane-hexadecane. This closeness in boiling points causes that when the droplet surface is being depleted in the most volatile compound, the interface temperature is still high enough to promote a significant evaporation of the heavier compound, being the second heat-up period much more progressive and distributed over time.

Regarding the propensity to form soot of these mixtures, their flame traces displayed very strong luminosities, significantly brighter than those illustrated for alkanes in Figure 4.8. In order to quantify the amount of soot yielded by each blend, Probe B (Figure 3.6) was used to collect all the soot particles generated by each fuel during a given time. The subsequent weighing procedure allowed to calculate the Isolated Droplet Soot Yield (IDSY, in grams of soot per gram of injected fuel). This information is presented in Figure 4.10 for all the studied mixtures, where a quite linear relation was found between the IDSY and the MNP percentage. This compound was responsible for practically all the soot generated from the mixtures, as pure

eicosane yielded negligible values of IDSY, whereas neat methylnaphthalene produced an IDSY of 0.56 (meaning that, under the specific set of conditions applied, 56% of the injected MNP mass was converted to soot particles).
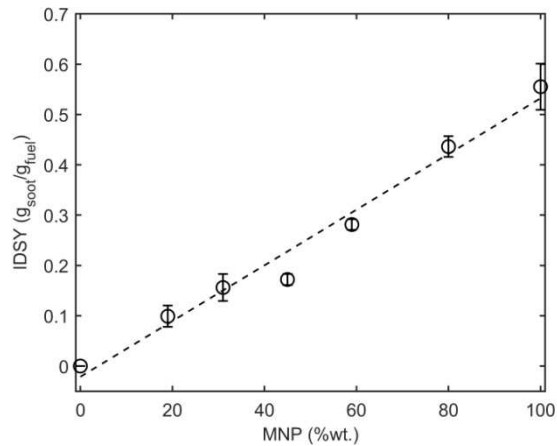

Figure 4.10. Isolated Droplet Soot Yield measured with Probe B for all the eicosane-methylnaphthalene mixtures. The uncertainty bars indicate ± SD (Standard Deviation) of the experimental measurements.

4.1.2 Real fuels

This Section aims to summarize the experimental characterizations performed on real fuels of interest for heat and energy generation. Besides heating oil, which was chosen as a reference conventional fuel, several alternative fuels were selected for study: Used Cooking Oil (UCO) biodiesel, different pyrolysis oils obtained from waste materials as well as crude glycerol and its mixtures with two kinds of acetals. Therefore, this Section is subdivided in the corresponding three sub-sections, each of them addressing the characterization of a different novel fuel. Since these results were published papers I, II, III and IV, only a brief summary of the main results will be provided here, being the interested reader redirected to the corresponding paper for further details.

4.1.2.1 UCO biodiesel, heating oil and their mixtures

Due to the already discussed relevancy of the mixtures biodiesel - heating oil, a study to experimentally characterize the isolated droplet combustion of these fuels and two of their mixtures was devised. As the blends commercially supplied for domestic use in boilers typically contain up to 20% by volume of biodiesel, the two mixtures tested in this study were B10 and

B20 (10 and 20% vol. of biodiesel respectively). This work was the first to be published in the framework of the thesis (Paper I), and therefore a detailed description and discussion of the experimental conditions was also included.

The droplet evaporation curves displayed in Figure 4.11 show distinct behaviors between heating oil and biodiesel, with a longer heat-up period and a more marked volumetric expansion for the latter. This is consistent with the higher boiling point of the main components of biodiesel (methyl esters) in comparison with the lighter fractions of heating oil. Hexadecane was also included in Figure 4.11 as a reference compound, showing a quite similar heat-up transient to that of heating oil. Once the droplet overcame this initial transient, its evaporation proceeded at a different rate for each fuel. This can be better seen in Figure 4.11.b, where the quasi-steady evaporation rate (K_{qs}) for biodiesel and hexadecane are found to be quite similar, being that of heating oil noticeably lower. This higher evaporation rate for biodiesel compensates the slower initial heat-up transient, being the droplet burnout times of heating oil and biodiesel akin, whereas hexadecane droplets display the quickest conversion. The two studied mixtures, B10 and B20, showed practically indistinguishable vaporization behaviors from those described for heating oil, although the K_{qs} of B20 for the combustion cases was slightly higher than that of heating oil and B10.
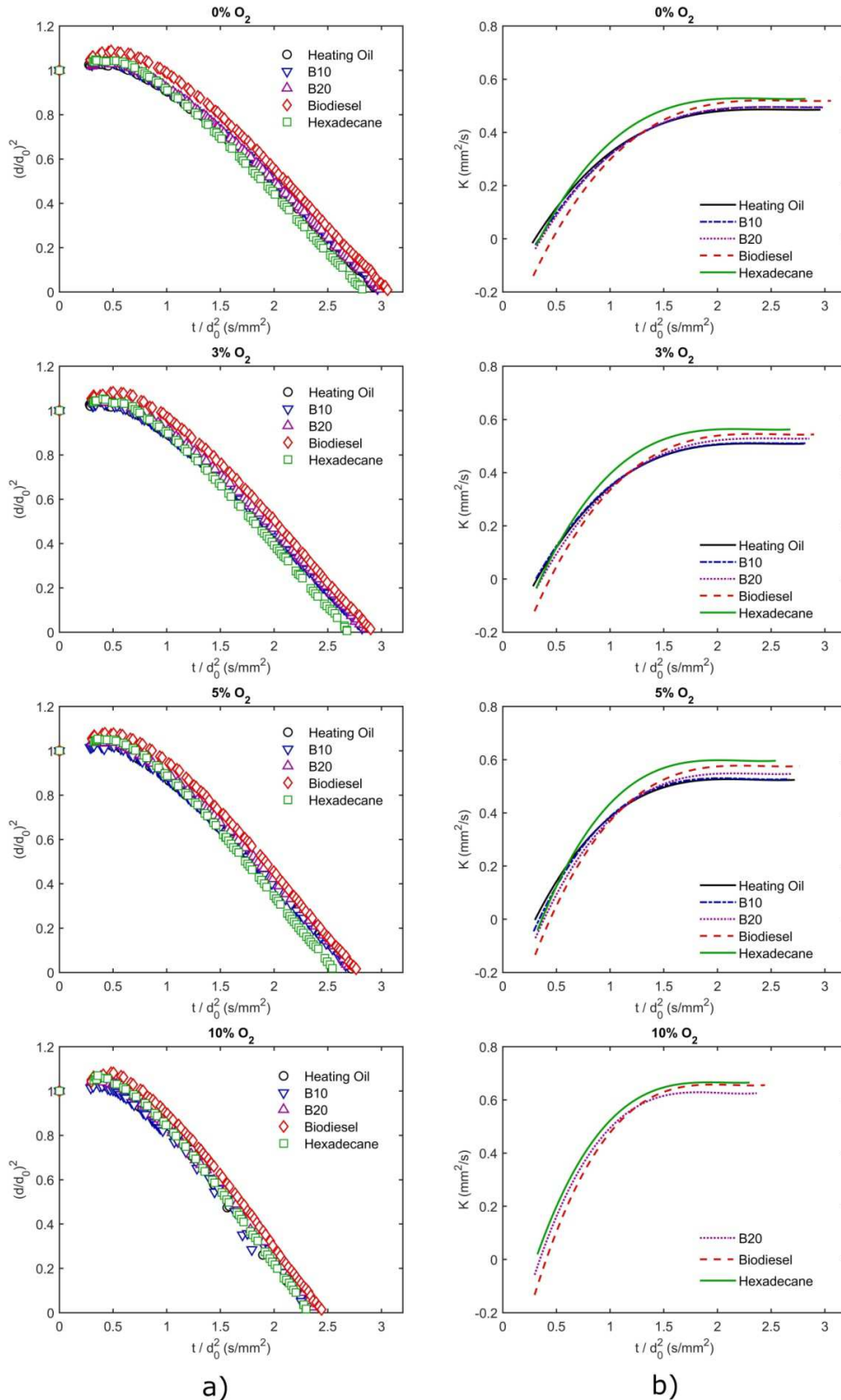
Figure 4.11. Normalized droplet size (a) and burning rate (b) evolution for the examined fuels at the different oxygen conditions. All the experimental curves in (a) were fitted to 4th order polynomials in order to obtain the time-derivatives plotted in (b).

Despite the differences in experimental conditions, the behaviors described in Figure 4.11 qualitatively concur with those presented in previous works on biodiesel and hexadecane droplet evaporation (Hashimoto *et al.* (2015)) and combustion (Li *et al.* (2011), Pan *et al.* (2009)), with comparable relative behaviors between fuels. Previous studies on biodiesel combustion often highlight the potential formation of polymeric residues for biodiesels rich in unsaturated fatty acid methyl esters. The UCO biodiesel studied in this work was highly unsaturated (70.63%, see Table C1 in the Supplementary materials of Paper I). However, none of the tests performed for biodiesel showed any hint of such polymeric residues, reported in other works as an abrupt decay in K just before the droplet burnout point. The very short droplet conversion times in this study (in the order of 60 ms) are thought to be the responsible for this since, as it is proposed in (Hashimoto *et al.* (2015)), the polymerization reactions compete with the evaporation process. The fast liquid evaporation significantly reduced or even inhibited polymerization, to a point where the identification of any solid residue was beyond the detection limit of Camera 1 (≈ 10 μm).

As it has been previously discussed, an increase in the O_2 availability in the gaseous coflow for any given fuel significantly accelerates the droplet conversion process, since the onset of an envelope flame increases thermal gradients in the droplet vicinity. This fact can be clearly observed in Figure 4.11, where droplet lifetimes were shorter for any given fuel as the oxygen composition in the coflow increased from 0 to 10%. Besides this enhancement in K, the apparition of a flame surrounding the droplet also induced the confinement of soot particles between the droplet surface and the flame front (as it will be detailed further on), hindering for some fuels and conditions the correct visualization and measurement of the droplet size. This is the reason why in Figure 4.11.a several points are missing for heating oil and its mixtures at the 10% O_2 atmosphere, since this condition promoted the strictest confinement of soot particles between the droplet surface and the envelope flame. For heating oil and B10 the scarcity of droplet size points in Figure 4.11.a did not allow to accurately extract the droplet evaporation rates in Figure 4.11.b.

It is well known that the nascent soot particles are originated in the fuel-side of the envelope flame (Randolph and Law (1986)), where the high temperatures and reducing conditions promote their formation. Under a perfectly 1-D configuration, without any external convection (either natural or forced), these soot particles are pushed towards the droplet surface by thermophoresis. These carbonaceous particles progressively agglomerate and grow in size, reaching an equilibrium location resulting from the balance of forces between the outward drag forces arisen from the Stefan flow and the inwardly-directed thermophoretic forces (Randolph and Law (1986)). This feature has been observed in many experimental studies on droplet

combustion under microgravity conditions (e.g., see (Liu *et al.* (2013a), Pan *et al.* (2009), Xu and Avedisian (2015))), where soot particles accumulate in thin layers around the droplet, creating the so-called soot shells. However, the occurrence of this feature for unsupported droplets burning under normal gravity is very rare, as the delicate equilibrium of forces required for the soot shell to appear can be easily eliminated by buoyancy or by forced convection. Due to the already discussed experimental conditions used in this work (d_0=150 μm, Re<0.2 during quasi-steady evaporation stage) the droplet combustion process is expected to be close to the sphericosymmetric case. A first proof of this was the quite spherical envelope flames presented in Figure 4.5 for the example of butanol droplets. A second indication of this closeness to the 1-D configuration is the onset in this work of well-defined soot shells for the sooty fuels (i.e., heating oil and its mixtures). These shells are presented in Figure 4.12 for all fuels at the 10% O_2 condition.
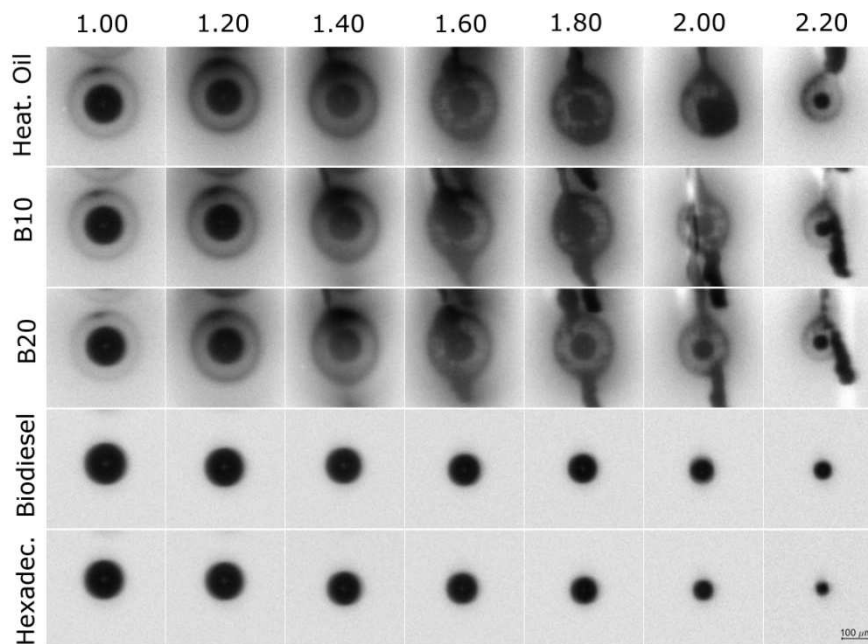

Figure 4.12. Droplet and soot shell evolution for all fuels at the 10% O_2 condition. Pictures are organized in terms of their normalized time after injection, t / d_0^2 (s/mm^2).

As displayed in Figure 4.12, only the fuels with a higher sooting propensity formed soot shells, without any distinguishable shell forming around biodiesel or hexadecane droplets. However, some previous studies using microgravity conditions (e.g., see (Pan *et al.* (2009))), showed this phenomenon for both fuels. This difference is ascribed to two different causes. The first one is the fact that, even if the set of conditions used in this work minimized forced and natural convection effects, they were still present, and their occurrence could drift away a substantial

34

amount of soot particles. For fuels with a strong propensity to form soot like heating oil and its mixtures, this leakage of soot particles does not prevent the onset of distinguishable soot shells around the droplet, although for cleaner fuels like biodiesel or hexadecane it could inhibit its formation. The second cause is the relevant differences between the experimental conditions used in this work and in (Pan *et al.* (2009)), namely the distinct values of d_0 used in each study. For the specific case of biodiesel, Pan *et al.* (2009) found clear soot shells for droplets with d_0=528 μm, and none for smaller ones (d_0=445 μm). The shorter residence time for soot precursors was found to be responsible for this difference. As this work uses much smaller droplet sizes (d_0=150 μm), no soot shells would be expected to occur, and therefore the results of both works appear to be consistent. The fact that hexadecane droplets at the 10% O_2 condition did not show any hint of soot at all (with a completely blue envelope flame, as it will be detailed further on) also seems to support this hypothesis.

The flame information also provided some interesting results regarding not only the specific behavior of each fuel but also for describing features arisen from the specific set of conditions chosen for the experimental tests. The macroscopic flame traces captured for each fuel at the 10% O_2 atmosphere were displayed in Figure 3.4 as an example of this kind of long-exposure photographs. Wide differences could be observed between heating oil (with a strong sooty emission), biodiesel (with the first millimeters displaying a blue trace followed by sooty luminosity) and hexadecane (showing a dim blue emission throughout all the droplet lifetime). The short-exposure individual flames obtained from Camera 2 can provide more insight into these distinct behaviors. To this effect, the envelope flames captured by this camera are displayed in Figure 4.13 for this same coflow condition (10% O_2) for two given droplet residence times.
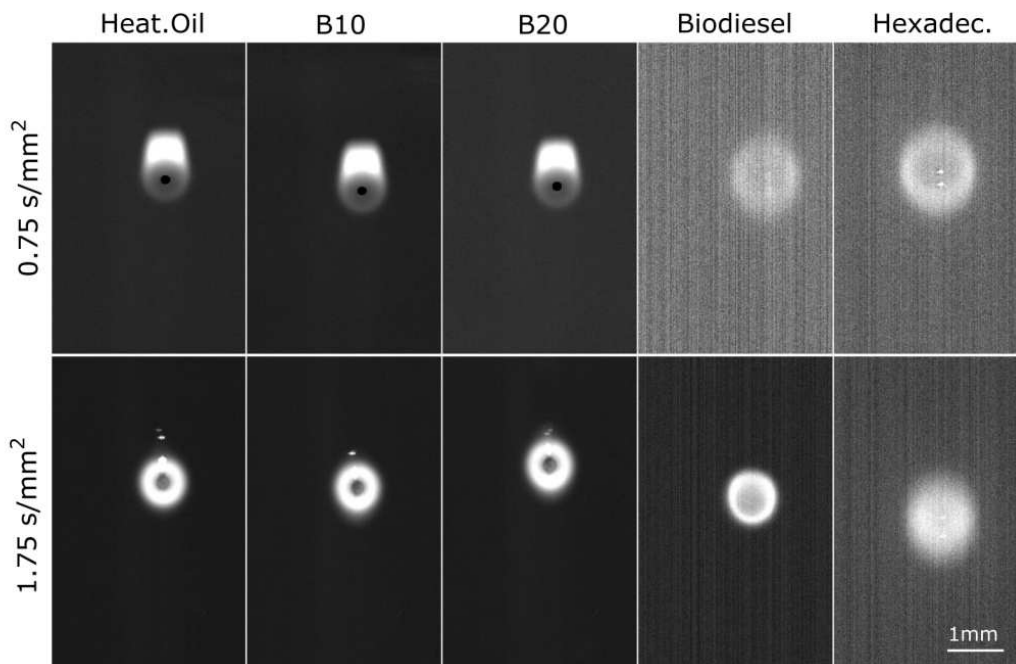
Figure 4.13. Comparison of the envelope flames recorded at two fixed residence times for different fuels at the 10% O_2 condition.

As displayed in Figure 4.13, heating oil and its mixtures showed practically identical envelope flames among them for both residence times. The strong sooty emission allowed for the backlight to be turned on for these cases, and therefore the droplet was visible at the center of the envelope flame. This is especially true for the pictures at 0.75 s/mm^2, whereas for images at 1.75 s/mm^2 the sooty emission outshined this backlight, and the droplet and soot shell were less clearly visible. The flame pictures of these fuels add some insight into the soot leakage mentioned when discussing the soot shells in Figure 4.12 since, as it can be observed in Figure 4.13, even for the case with a higher O_2 availability, there is indeed a drift of soot particles outside of the envelope flame, particularly for the earlier residence time. The hexadecane case is analogous to that illustrated in Figure 4.5 for butanol, with quite spherical and dim blue flames stemming from chemiluminescence emission. Due to the very weak signal of this kind of flame, the backlight had to be turned off and the image was binned in order to increase its signal-to-noise ratio. Biodiesel flames present an interesting behavior, since they transitioned from the bluish color associated with chemiluminescent emission to the orangish hue ascribed to the black-body emission from soot particles (as it was observed in Figure 3.4). The transition from the former to the latter kind of flame can be noted in the monochrome pictures of Figure 4.13 as a significant increase in the image quality, as the black-body emission of soot is significantly more intense than chemiluminescent emission.

Analogously to the results presented in Figure 4.7 for alkanes, in this work the flame size evolution with time was also characterized by measuring the envelope flames displayed in Figure 4.13. However, and contrary to the alkane case, in this occasion two different kinds of flames images can be distinguished: for sooty fuels (such as heating oil or its mixtures) the flame information in the pictures is determined by the strong thermal radiation emitted from soot particles, whereas for cleaner fuels like hexadecane the flame position is obtained from the chemiluminescent emission. The case of biodiesel is more interesting, since it shows both kinds of flame pictures, as illustrated in Figure 4.13. The results of these measurements are presented in Figure 4.14.
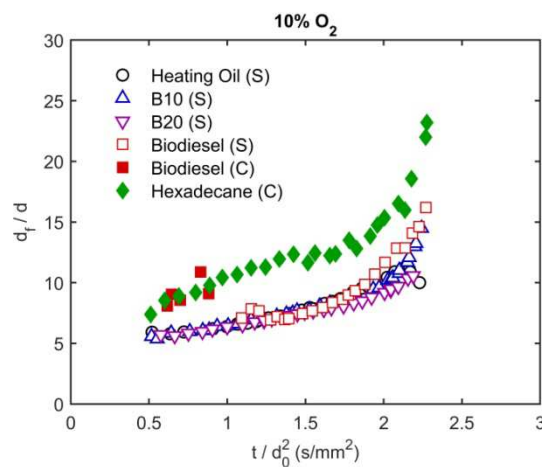

Figure 4.14. Flame standoff ratio evolution of all the fuels tested at the 10% O_2 atmosphere. Measurements based on the blue chemiluminescent front are marked with (C), whereas measurements referred to the outer boundary of the sooty luminous zone are labeled with (S).

Figure 4.14 displays clear differences between the data extracted from both kinds of flames, with distinctly wider flame sizes for measurements based on the chemiluminescent boundary. The case of biodiesel is quite clear, since the transition from a bluish flame to a sooty one involved a sudden reduction in the flame size measured. It is worth to note that, in the literature, the most common and accepted approach to experimentally determine the flame front location is to associate it with the chemiluminescence emission from electronically excited OH[*] radicals (peaking around 308 nm) or with CH[*] radicals (431 nm). The location of these radicals has been found to occur near the maximum temperature point and thus, their emission is a good indicator of the flame front position (Marchese *et al.* (1996)). When it comes to characterizing envelope flames in droplet combustion studies, the weak intensity of such narrow-band emissions, the required optical magnifications and the short exposure times led to several authors, such as Alam *et al.* (2015) or Farouk *et al.* (2013), to estimate the flame size from the outer boundary of

the blue luminous zone, that is, the combined chemiluminescent radiation stemming from all radicals emitting within the blue band (primarily CH^*, but also others like CO_2^* or C_2^* (Kathrotia (2011))). This approach has been also followed in the current work for non-sooty fuels like alcohols, alkanes or the first stage of biodiesel in Figure 4.14. For sooty fuels, however, the strong black-body emission from incandescent solid particles can be orders of magnitude stronger than that generated by the electronic transition of the aforementioned radicals, completely outshining the latter. This was the case for all the series marked in Figure 4.14 with a (S) label. For those cases, the measured flame diameters were based on soot emission, and therefore they are not directly related to the actual flame front. As soot particles are formed on the fuel side of the diffusion flame, it would be expected that these flame sizes would be somewhat smaller than those based on the bluish chemiluminescent emission, as it was confirmed in Figure 4.14 for biodiesel. Therefore, these measurements should be taken with caution, although they are thought to be valid for the purpose of comparing among fuels, given that flame location was obtained following the same criterion for all of them. This approach was followed is several droplet combustion experimental studies such as (Li *et al.* (2011), Pan *et al.* (2009)), and has been also used over the course of the thesis for the case of sooty fuels.

The final results of this study on heating oil, biodiesel and their mixtures are precisely related to their propensity to form soot particles. The data obtained from the different images (i.e., soot shells in Figure 4.12, long-exposure traces in Figure 3.4 and envelope flames in Figure 4.13) qualitatively point to a much higher soot production for the combustion of heating oil and its mixtures when compared to pure biodiesel. In order to quantify these differences, the soot probe A displayed in Figure 3.5 was applied for these fuel under the 3 and 10% O_2 conditions. The amount of soot yielded by biodiesel was below the detection limit of the method, and therefore the tests were focused on heating oil, B10 and B20. It is worthy to note that these three fuels obtained practically identical results for all the behaviors explored so far in this work, and thus it seems interesting to determine if their tendency to form soot could be the sole relevant difference among them. To that end, the spatially-resolved soot sampling procedure described in Section 3.1 was applied, obtaining the results summarized in Figure 4.15.
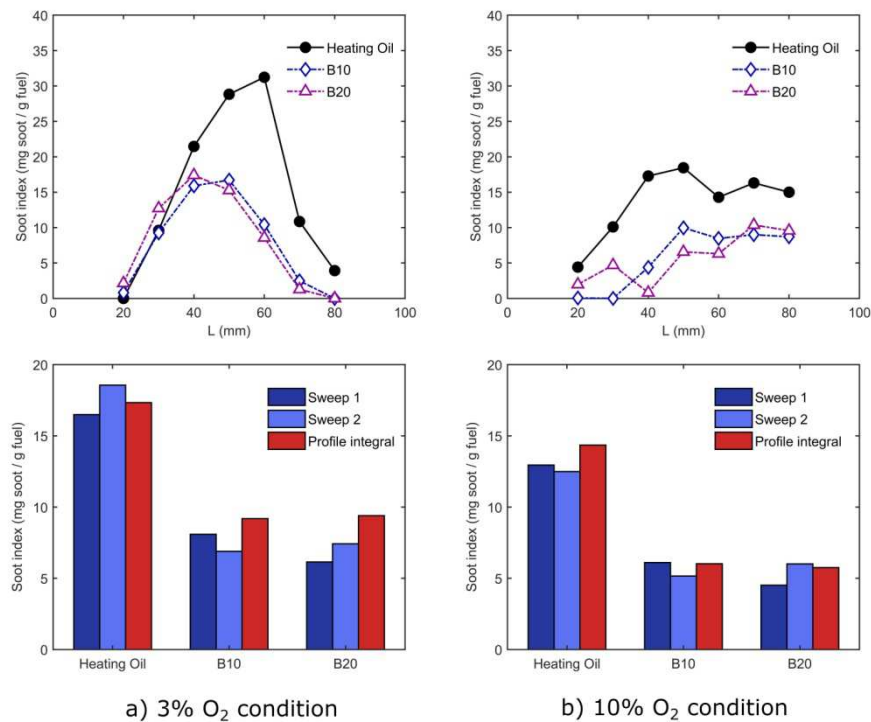
Figure 4.15. Soot results obtained with Probe A for the 3% and the 10% O_2 conditions. Droplets in these tests were 180 μm in d_0 to increase soot yield. For each oxygen condition, axial profiles are presented at the top, whereas the integrated values are displayed below.

The axial profiles of soot sampled along the flame traces are shown in the upper half of Figure 4.15, where clearly higher soot yields can be observed for heating oil, whereas B10 and B20 display similar behaviors. Contrary to the results provided by Probe B (obtained at the 0% O_2 condition), the fact that these tests were performed under combustion atmospheres (3 and 10% O_2) complicates the analysis of the results, since the soot sampled at a given position is the outcome of both formation and oxidation processes. The distinct behavior when comparing the axial profiles obtained at both conditions in Figure 4.15 is primarily ascribed to the larger soot agglomerates formed for the 10% O_2 case, since soot particles were more confined within the envelope flame for this rich oxygen condition (as illustrated in Figure 4.12). Whereas the small-sized particles produced under the 3% O_2 atmosphere quickly oxidized after the droplet burnout length (which, for these 180 μm droplets occurred around $L \approx 70$ mm), the much lower specific surface area of the large agglomerates produced under the 10% O_2 case significantly decreased their consumption rate, with a significant soot amount remaining after this point.

Since the main aim of this study was to characterize the relative sooting tendency of these fuels when tested under the same conditions, a single parameter representative of all the soot

39

collected over the whole trace was sought. To that end, sweep measurements were performed by continuously displacing the aspirating probe between the two flame trace limits (L=20-80 mm). This provided an integrated value, to be compared with the numerical integration of the aforementioned axial profiles. These results are displayed in the lower half of Figure 4.15, where the reduction of soot due to biodiesel addition can be clearly observed for both oxygen conditions. However, and consistently with the soot profiles, differences between B10 and B20 are not clear, with similar soot indices for both mixtures. On a final note, although the repeatability of these results is considered to be adequate (as determined from comparing the two sweep tests and the profile integral in Figure 4.15), it is also considerably lower than that obtained with Probe B (e.g., see uncertainty bars in Figure 4.10). Thus, the soot reductions found for B10 and B20 in comparison to neat heating oil should take this experimental uncertainty into account.

4.1.2.2 Crude glycerol and its blends with acetals

As it has been justified in the Introduction, the energetic valorization of crude glycerol (CG), a major by-product of biodiesel production, implies remarkable technical challenges due to the CG compositional and physicochemical properties, which significantly hinder its use in conventional combustion equipment. Some basic, low-cost post-treatments such as desalting or the blending of CG with other fuels have been proposed as potential approaches to tackle this issue. Given its relevance, the development and testing of such strategies is an interesting field of study where the droplet combustion configuration could contribute. In this context, a study was developed at LIFTEC in order to characterize the combustion behaviors of a CG sample and a desalted crude glycerol (DG), both neat and blended with a mixture of acetals (GF*) yielded as a by-product of the FAGE production process (Lapuerta *et al.* (2019)). These tests were performed at two different scales: isolated droplet combustion experiments and semi-industrial furnace tests. The study was published in Paper IV, and the main results obtained in the droplet combustion configuration (which were performed within this framework of the thesis) are summarized in this Section.

The droplet combustion tests were divided in two phases, focusing the first one in characterizing the base fuels (CG, DG, GF*), and exploring the second one the aforementioned mixtures with acetals (CG-GF* and DG-GF*). As for the base fuels, some relevant differences between CG, DG and GF* could be already observed by means of the macroscopic flame traces. These long-exposure pictures are displayed in Figure 4.16 for the three base fuels at the 10% O_2

atmosphere. Additionally, pure glycerol (PG) was also included to the study as a reference compound with a well-known behavior and properties.
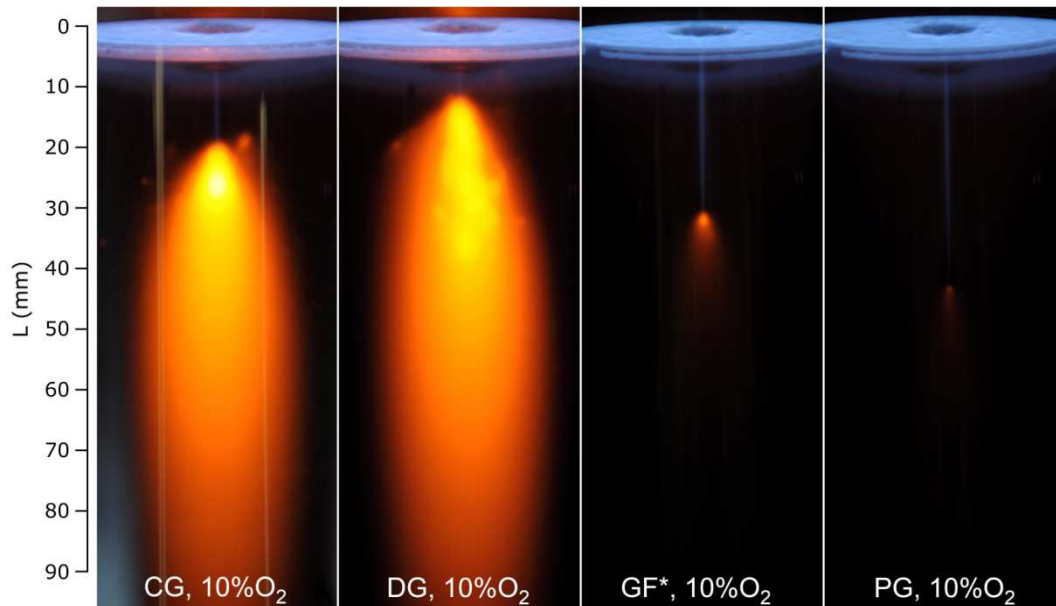

Figure 4.16. Long exposure pictures recorded for the 10% O_2 for all the base fuels. The exposure time for all pictures was set to 2 seconds (50 injected droplets).

In Figure 4.16, all fuels show dim blue streaks arisen from chemiluminescent emission, without any hint of soot black-body radiation. For the case of GF* and PG, this blue trace spans for the whole droplet lifespan, being the droplet consumption length clearly marked by an orangish spot. As it was documented for pure glycerol in Section 4.1.1.1, this spot is ascribed to sodium emission, as a spectrometer (Ocean Optics HR2000) revealed a marked peak at 589 nm corresponding to the D-lines of sodium. Given the fact that these spots were produced at the droplet consumption point, the amount of sodium content in these fuels is expected to be marginal, and its impact on the combustion process negligible. A quite different situation is found for CG and DG, where the subtle blue streak is suddenly interrupted by a much wider and more intense orangish umbrella, whose origin was also determined to stem from sodium emission. These two fuels contain relevant amounts of sodium (3.86 g/kg for CG and 3.80 g/kg for DG), namely as dissolved cations of alkali salts, with potassium being the major metallic compound (25.67 g/kg for CG, 6.00 g/kg for DG). As it will be discussed further on, these salts are thought to be responsible for the sudden breakup of the droplets due to the formation of internal vapor bubbles which overcome the capacity of the liquid surface tension to hold the droplet together. This microexplosion phenomenon dispersed the liquid across the combustion chamber through secondary atomization, as it can be observed for CG and DG in Figure 4.16. The sodium contained in these fuels acts as tracer due to its orangish emission when exposed to

high temperatures, and corroborates the fact that the liquid droplet was dispersed in a wide area around the microexplosion occurrence point. The long-exposure pictures in Figure 4.16 can provide some first insights into this bursting behavior, which appears to display clear differences between CG and DG. The latter shows a much earlier microexplosion onset, with a more distributed and asymmetrical sodium release that points to low-intensity droplet fragmentations. Crude glycerol, on the other hand, displays a latter occurrence of microexplosion events, although in this case the sodium emission is more centered around a clearly more intense area, where the majority of the 50 droplets recorded in Figure 4.16 burst into small fragments.

In order to study in more detail this bursting phenomenon, Figure 4.17 illustrates some representative microexplosions recorded with Camera 1 for both CG and DG. As detailed in Section 3.1, this camera used the multiple exposure technique to record several sequential shots of the same free-falling droplet with a time delay of 500 μm between them.
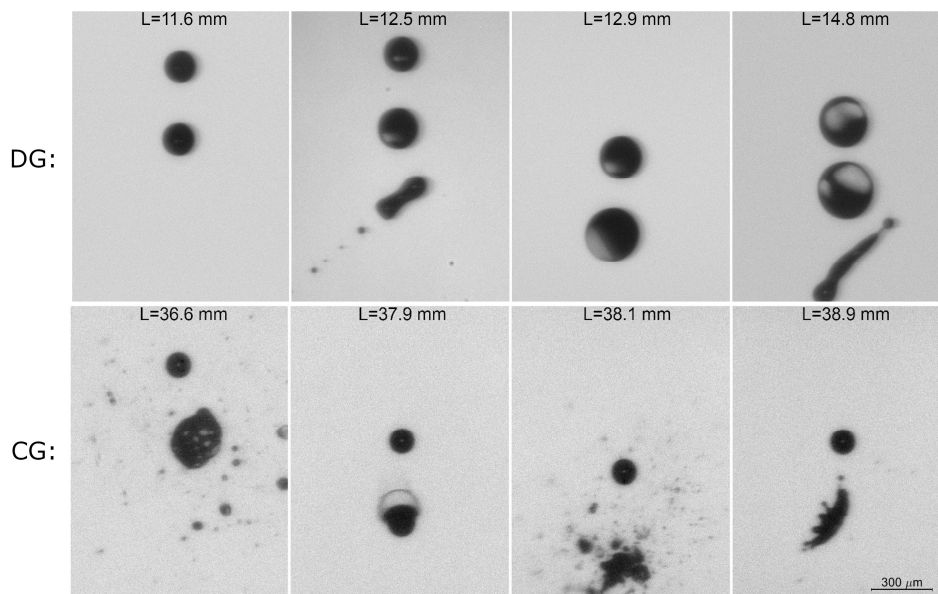

Figure 4.17. Droplet swelling and microexplosion sequences for DG (upper row) and CG (lower row) at different lengths after injection (*L*) and at the 0% O_2 condition.

As it can be observed in Figure 4.17, the microexplosion events recorded for DG and CG display clear differences. Whereas CG droplets showed abrupt microexplosions (characteristic time < 500 μs) which completely shattered the droplet into fragments, DG droplets underwent a clearly different phenomenon, with a significant droplet swelling followed by a weak microexplosion or a puffing event. The characteristic time of this droplet swelling was estimated to be in the order of a few milliseconds, and the droplet could double its size prior to the vapor release. The low intensity of these bursting events for DG caused that most of the

droplets could regain their spherical shape, resuming their evaporation process until eventually reaching a second microexplosion, this one akin to that described for CG and, thus, being finally shattered into fragments. This behavior is consistent with the long-exposure photographs in Figure 4.16, where the orangish luminosity related to sodium release was found to occur significantly earlier and in a more distributed manner for DG than for CG. Microexplosions are reported to be beneficial for fuel conversion in boilers or furnaces, since a secondary atomization would not only substantially shorten the droplet burnout time, but would also improve the fuel-air mixing within the combustion chamber, reducing thus pollutant emissions (Shaddix and Hardesty (1999)).

The scarce droplet combustion studies available in the literature for crude glycerol also report the occurrence of microexplosion events, although with some differences regarding the bursting typology. A previous work at the DCF for a different crude glycerol sample (Angeloni *et al.* (2016)) yielded microexplosions akin to those described in Figure 4.17 for CG, whereas Setyawan *et al.* (2016) found swelling and puffing events of rather low intensity which could not induce a complete breakup of the CG droplet. These differences are thought to mainly stem from the dissimilar experimental conditions, since Setyawan *et al.* (2016) relied on the suspended droplet technique with bigger droplet sizes and lower ambience temperatures.

Previous fundamental works such as (Lasheras *et al.* (1979, 1980a, 1980b), Wang *et al.* (1984)) addressed the experimental study of these microexplosion phenomena for different mixtures and emulsions of alkanes, alcohols and water. To that end, they employed the unsuspended droplet technique, avoiding therefore the influence of the solid filament (which can act as a heterogeneous vapor nucleation site). In these works, the shattering of both mixtures and emulsions of pure compounds were found to occur after a significant swelling of the droplet size, with a characteristic time in the order of a few milliseconds. The remarkable similarities with the DG microexplosions depicted in Figure 4.17 would lead to attribute to this fuel the same mechanism proposed in (Lasheras *et al.* (1979, 1980a, 1980b), Wang *et al.* (1984)), that is, the homogeneous nucleation of the more volatile liquid fractions within the droplet. Crude glycerol, on the other hand, displayed a clearly different shattering typology, which is found to concur with the microexplosions detailed in (Angeloni *et al.* (2016)), where this feature was attributed to the decomposition of alkali salts rather than to the evaporation of the lighter liquid compounds. Even if further research is clearly required in order to better understand this phenomenon, the fact that CG modified its original abrupt microexplosion typology for the slower swelling and puffing breakups precisely after the desalination process appears to confirm that alkali salts play indeed a relevant role in the droplet microexplosion mechanism.

After this brief analysis of the microexplosion events, the droplet images from Camera 1 were processed to quantify the evaporation rate for each base fuel. The obtained results are presented in Figure 4.18 for the three coflow conditions used in this work (0, 3 and 10% O_2). The droplet evaporation curves in Figure 4.18.a display very similar vaporization behaviors between CG and PG, at least during the first half of the droplet lifespan. This is consistent with the fact that the CG sample used in this work contains 81.4% of glycerol. The presence of some water and non-glycerol organic matter in CG would justify the slightly higher evaporation rates of this fuel in comparison with PG during this initial region (see insets in Figure 4.18.a). After the droplet completed the heat-up transient, CG significantly reduced its vaporization rate, departing its curves from those of PG for all the oxygen conditions studied. This behavior is thought to the related to the subsequent microexplosion onset which, as previously discussed, showed a violent and fast shattering of the droplet into many fragments, similar to the bursts described in (Angeloni *et al.* (2016)). The fact that the droplet lifespan scales with d^2 points to a complete conversion of the liquid fuels shortly after the occurrence of this secondary atomization process.

Desalted Glycerol, on the other hand, displayed remarkable droplet swelling already at the initial heat-up transient, quickly doubling the droplet size prior to the onset of the weak microexplosions and puffing events illustrated in Figure 4.17. As already mentioned, most droplets recovered their spherical shape after releasing the internal vapor content, their evaporation proceeding smoothly until the occurrence of a second microexplosion, this one quite violent and similar to those described for CG. The high data dispersion found for DG after the swelling is due to the variable intensity of the puffing and weak microexplosions which, for most cases, achieved to propel away some liquid mass from the parent droplet. Thus, the measurements displayed in Figure 4.18 for this fuel should only be regarded as a sample of the range of sizes observed after this event.

As for the acetal mixture (GF*), a completely different vaporization behavior was observed, without any hint of microexplosion or swelling phenomena. The heat-up transient was completed significantly earlier than for the glycerols, revealing GF* as a high-volatile fuel able to start its vaporization within the first instants after injection. In the quasi-steady evaporation phase, GF* also displayed burning rates remarkably higher than those of glycerol and, therefore, this fuel would show significantly better evaporation characteristics than CG or DG. However, it is worth to note that GF* evaporated smoothly until a complete droplet depletion, without the occurrence of any microexplosion. Thus, the total conversion times of GF* and both glycerols-based by-products are expected to be close due to the secondary atomization displayed by the latter fuels.
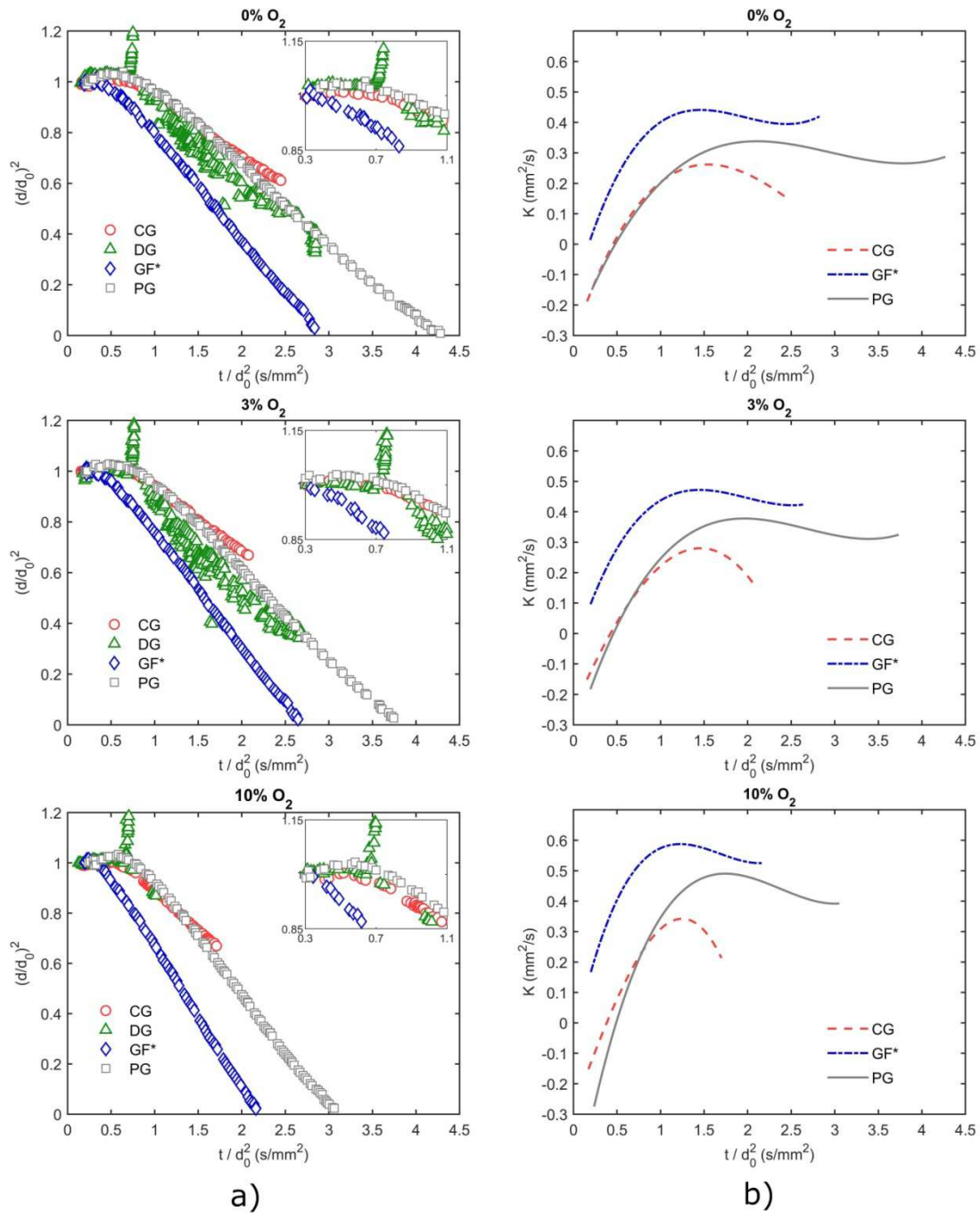
Figure 4.18. Normalized droplet size (a) and burning rate (b) evolution for the three fuels at the different oxygen conditions. All the experimental curves in (a) were fitted to 4th order polynomials in order to obtain the time-derivatives plotted in (b).

One of the main objectives of this part of the study was to experimentally determine the combustion behaviors of the mixtures of crude glycerol (both as received and desalted) with acetals. As it has been previously justified, this approach could contribute to overcome the

significant challenges posed by the bad combustion properties of crude glycerol. To address this, three blends of each kind of glycerol waste (CG and DG) with GF* were prepared, with 7, 15 and 30% GF* by volume. The droplet evaporation curves obtained at the DCF for these 6 mixtures are presented in Figure 4.19 for the 3% O_2 condition.
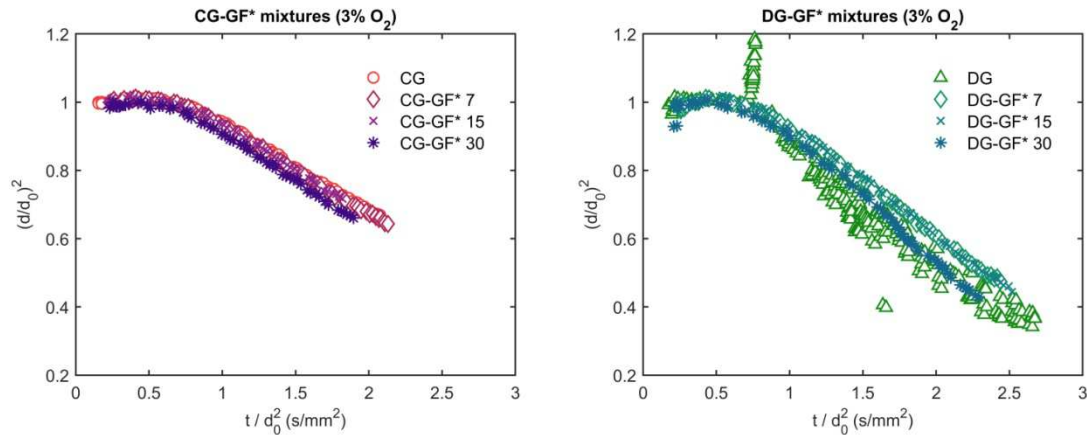

Figure 4.19. Normalized droplet size evolution for the glycerol-acetal mixtures at the 3% O_2 condition. Left: Crude Glycerol; Right: Desalted Glycerol.

The GF* addition to CG did not alter significantly this fuel's droplet vaporization behaviors, as CG-GF* mixtures displayed close burning rates than those extracted for CG (Figure 4.19). The microexplosion typology and the macroscopic flame traces were also akin to these of reported for CG in Figures 4.17 and 4.16 respectively. However, a slight but yet noticeable enhancement of the droplet vaporization process was noted for the blends with a higher composition in GF*. On the other hand, GF* addition to DG did modify the combustion features reported for this glycerol, since it suppressed the initial swelling and puffing stages. Since these events are thought to be caused by the homogeneous nucleation of the most volatile compounds of DG, the compositional changes induced by the addition of acetals might shift the mixture composition range out of the superheat limits, which were found in (Lasheras *et al.* (1980a, 1980b)) to depend on both the homogeneous superheat limit of the blend and the boiling point of the heavier compounds within the mixture. In spite of the suppression of the swelling and puffing events, the DG-GF* blends did microexplode around $(d/d_0)^2 \approx 0.45$, with violent disintegrations similar to those described for CG-GF* in $(d/d_0)^2 \approx 0.66$. This kind of microexplosions have been ascribed to salt content, and therefore the fact that DG contains a lower composition in alkali salts seems consistent with this delay in the onset of the droplet shattering. Similarly to the CG-GF* mixtures, the addition of acetals to DG noticeably accelerated its evaporation process, especially for the DG-GF*30 blend. Subsequent tests in a semi-industrial furnace showed that GF* addition widened the range of stable conditions in the burner, substantially improving

flame stability and reducing CO emissions. For simplicity and, since these tests were performed in collaboration with other researchers and not strictly within the framework of the thesis, they are not included here. Nevertheless, it is important to note, as a relevant conclusion, that the behaviors noted at the two different scales appear to be perfectly consistent, as discussed in Paper IV.

4.1.2.3 Pyrolysis Oils from Waste Tires, Polystyrene and Biomass

The pressing environmental concerns associated with the disposal of waste tires have motivated an intense research on different technologies to overcome this challenge. Among them, the pyrolysis of waste tires to obtain new products with added value is gaining relevance, as detailed in the Introduction. The liquid fraction obtained, or Tire Pyrolysis Liquid (TPL) is mainly intended for heat and power generation in furnaces and boilers. Given the large amounts of tires disposed every year and the high calorific value of TPL, its potential for fossil fuel substitution is significant. A study on single droplet combustion characteristics of a TPL was published in Paper II, where it was compared with heating oil, a reference fuel for domestic and industrial use. Additionally, a mixture of relevance for heating applications named TPL5 (with 5% TPL addition) was also characterized. The main results obtained in this study are summarized below.

Regarding the evaporation behavior, meaningful differences were found between heating oil and TPL, as it can be noticed in Figure 4.20 for the case of the 3% O_2 atmosphere. TPL displayed an earlier onset of evaporation, with higher burning rates during the initial heat-up phase, which could be ascribed to the lower boiling point of the lightest fractions of this fuel in comparison with those of heating oil. However, as the droplet transitioned towards its quasi-steady vaporization region, the burning rate of heating oil clearly surpassed that of TPL, which would show longer droplet conversion times were its curve not interrupted around $(d/d_0)^2 \approx 0.40$ by the onset of microexplosions. As for the TPL5 mixture, its evaporation characteristics were found to be essentially the same as those observed for neat heating oil, confirming therefore that TPL addition did not drive any relevant change. Similar behaviors were noticed for the rest of coflow conditions (0 and 5% O_2) explored in Paper II.

The high propensity to generate soot of both heating oil and TPL favored the formation of quite spherical soot shells around the droplets, as displayed in Figure 4.21. The earlier onset of these shells for TPL, in addition to their thicker appearance point to a higher soot yield for this fuel. This was also qualitatively corroborated by the higher intensity of soot emission for TPL, both in the macroscopic traces and in the envelope flames pictures. The TPL5 blend, however,

displayed close soot-generation characteristics to heating oil. It is worth to note that this work did not include the combustion case at the 10% O_2 atmosphere because of the thick soot shells arising for TPL, which completely hindered the droplet visualization. As already discussed, with higher oxygen availability, soot particles are confined within the flame front and the droplet surface, providing thicker and more spherical soot shells. This can be visually confirmed when comparing the soot shells of heating oil at the 5% O_2 condition (Figure 4.21) and 10% (Figure 4.12).
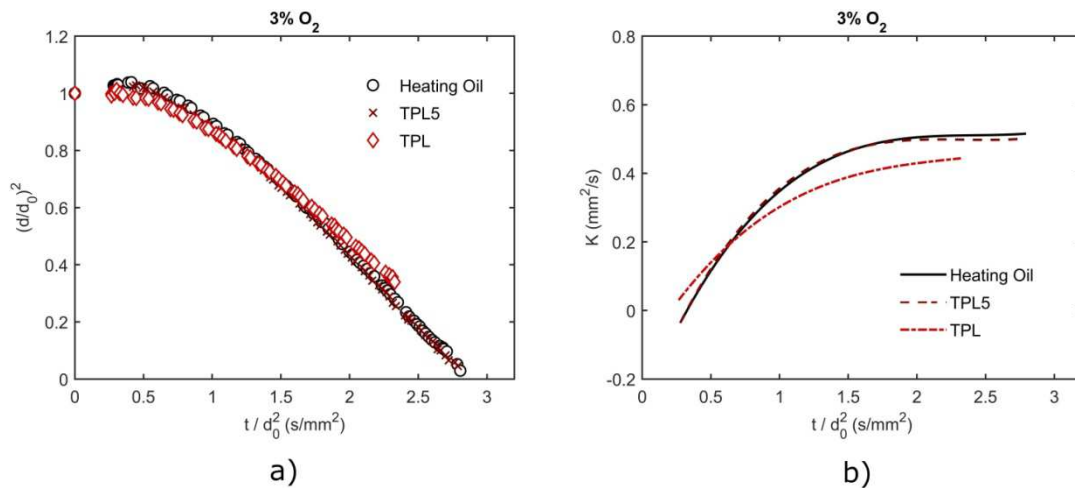

Figure 4.20. Normalized droplet size (a) and burning rate (b) evolution for the examined fuels at the 3% O_2 condition. The experimental curves in (a) were fitted to 4th order polynomials to obtain the time-derivatives plotted in (b).
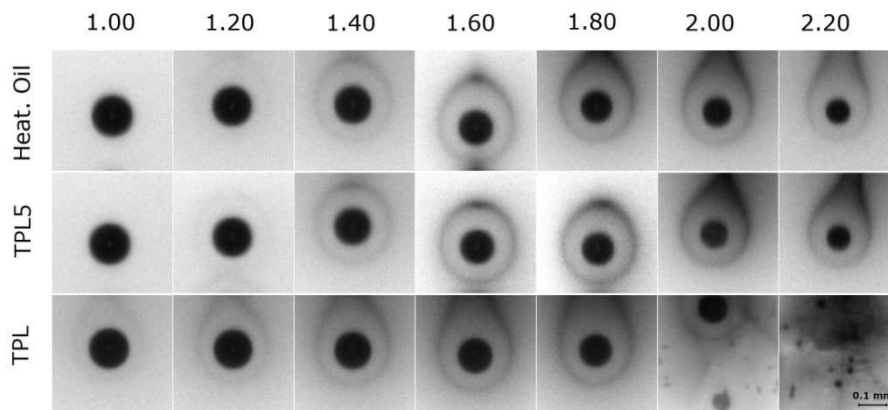

Figure 4.21. Droplet and soot shell evolution at the 5% O_2 condition. Pictures are organized in terms of their normalized time after injection, t / d_0^2 (s/mm^2).

In summary, the droplet combustion characteristics of TPL were found in Paper II to be quite appropriate when compared to the reference heating oil, with an earlier vaporization onset, a somewhat lower quasi-steady burning rate compensated by the occurrence of secondary

atomizations, similar envelope flame sizes and absence of any relevantly-sized solid residue such as coke or cenospheres. The only drawback found was its high propensity to form soot which, however, was only based on qualitative optical observations, as no measurements were performed with aspirating soot probes.

The aforementioned behaviors for TPL significantly differ from those reported in previous works on pyrolysis oils obtained from lignocellulosic biomass. These bio-oils have been considerably more explored in the droplet combustion literature (e.g., see (Shaddix and Hardesty (1999), Shaddix and Tennison (1998))), with results pointing to a much slower conversion than that reported in this work for TPL and, for some cases, with cenosphere formation. As it was detailed in the Introduction, the joint pyrolysis of biomass and a polymeric residue (such as waste tires) has been found to yield stable and high-quality oils, being the co-pyrolysis process a state-of-the-art technology which is thought to produce bio-oils with significantly improved properties. A collaboration with the *Grupo de Investigaciones Ambientales* from ICB-CSIC allowed for a work assessing the impact of two process variables on the final droplet combustion characteristics of the obtained bio-oils. Namely, the polymer type fed to the pyrolysis reactor (polystyrene or waste tires) and the nature of the low-cost, Calcium-based catalyst used (Carmeuse limestone, calcined dolomite or an inert material such as sand) were studied. This work led to Paper III, where all the details of this study can be found. A summary of the main results obtained is presented below.

In order to assess the impact of the aforementioned two process variables, four different bio-oils were produced in a pyrolysis pilot plant (100 kW$_{th}$). All of them were obtained by pyrolyzing a 80% (wt.) of grape seeds (GS) along with 20% of polymer, either polystyrene (PS) or waste tires (WT). The effect of the polymer type was therefore ascertained by comparing the two fuels named GS-WT and GS-PS, both produced under exactly the same experimental conditions and using the same catalyst (Carmeuse). As for exploring the effect of the low-cost catalyst, three GS-WT oils were produced with the different catalysts, yielding GS-WT Carmeuse, GS-WT Dolomite and GS-WT Sand. A detailed analysis of their physicochemical properties was performed at ICB-CSIC, where a significant improvement was noted when using a catalyst (lower viscosity, density and oxygen content), especially when the catalyst was the Carmeuse limestone. Regarding the change of polymer source, the shift from WT to PS provided a considerably less viscous oil, which also contained more aromatic compounds.

The subsequent droplet combustion tests revealed quire similar behaviors for the GS-WT bio-oils as those previously reported in this same Section for TPL. This outcome was not initially expected, since waste tires accounted for only 20% in mass of the total feedstock used for the

bio-oils explored in this work. The droplet evaporation behaviors for the four bio-oils are compared in Figure 4.22 along with those of heating oil which, given the intended use of these liquids, was also included as a reference conventional fuel.
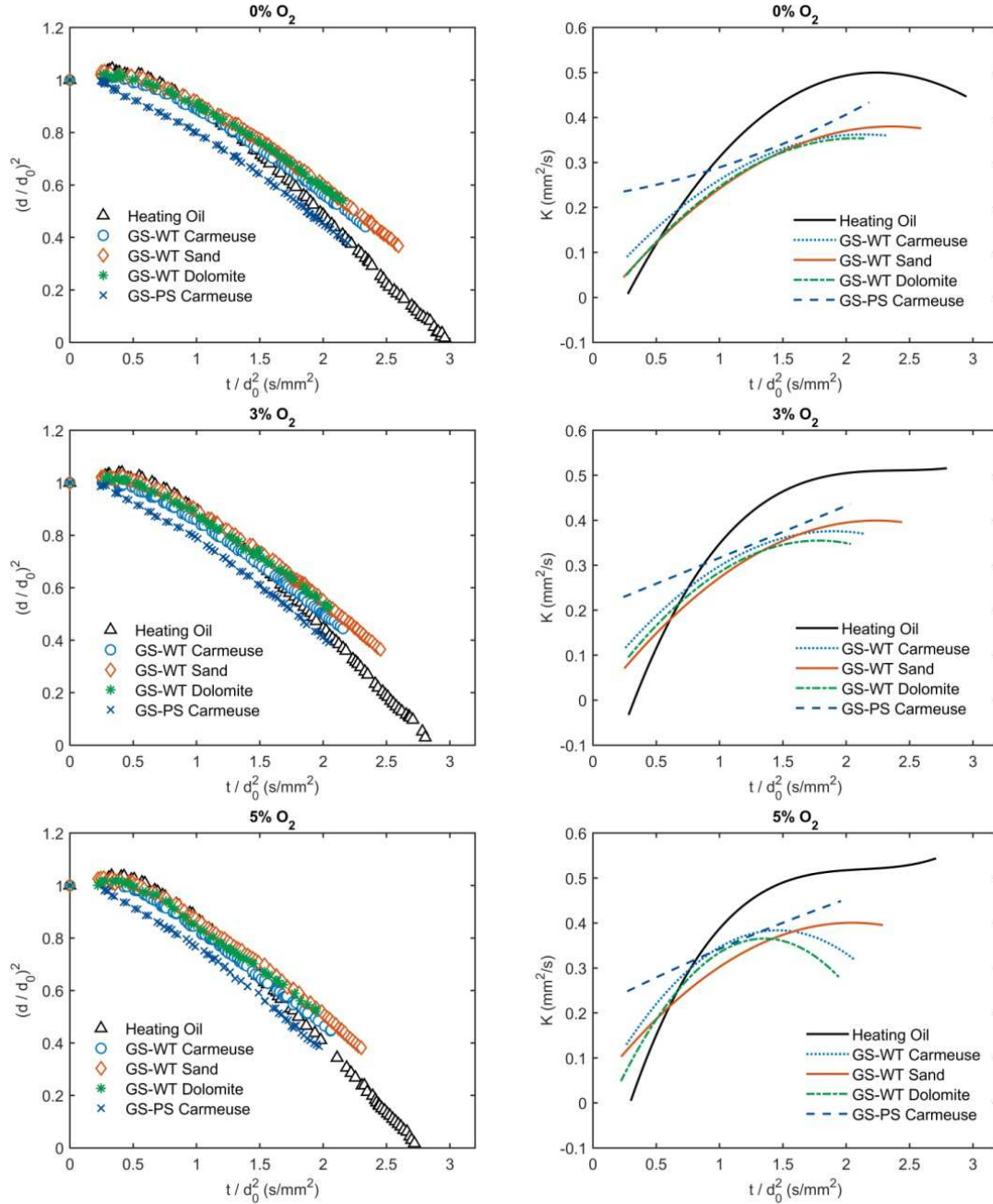

Figure 4.22. Normalized droplet size (left) and burning rate (right) evolution curves for all the fuels at the three studied oxygen conditions. The experimental curves in (a) were fitted to 3rd and 4th order polynomials to obtain the time derivatives plotted in (b).

As it can be observed in Figure 4.22, all fuels displayed a steady evaporation which reduced the droplet size until a total droplet depletion (for heating oil) or a sudden interruption in the curve,

which marks the appearance of droplet microexplosions for all the studied bio-oils. As it will be detailed below, these microexplosions completely shattered the parent droplet into small fragments and, therefore, a complete conversion of the bio-liquids is expected to occur shortly after the onset of their secondary atomization. Among the four bio-oils, GS-PS Carmeuse displayed the most differential behavior, with a substantial faster evaporation during the initial stage that would point to a richer composition in low boiling point compounds. Despite this fact, the increase in K was slower than for GS-WS oils, being the burning rates quite similar in the final stages prior to the microexplosion. When comparing between the three GS-WS liquids, small differences could be noticed among them, suggesting a more limited effect of the catalyst type in the process than the polymer feedstock. Even so, the liquid yielded when Carmeuse was used as a catalyst showed a noticeable faster conversion, followed by GS-WT Dolomite and GS-WT Sand.

The microexplosion onset noticeably varied between fuels, with GS-WT Dolomite showing the occurrence of this phenomenon for bigger droplets than the rest of bio-liquids for the three atmospheres explored in Figure 4.22. On the contrary, GS-WT Sand displayed microexplosions for the smallest droplet sizes which, in addition to its lower burning rates, resulted in the slowest total conversion for this oil. Regarding the microexplosion typology, all fuels displayed similar characteristics than those reported for TPL in paper II, with quick and violent bursting events which shattered the droplet into small fragments. A collection of representative microexplosion pictures recorded for each bio-oil are presented in Figure 4.23, where it can be noticed that the breakdown of the parent droplet was always achieved, although with different degrees of success. GS-PS Carmeuse consistently showed the most efficient and violent microexplosions, since the original droplet was for most times dispersed into a fine spray, without any relevantly-sized child droplet. GS-WT oils, on the other hand, displayed on average less violent bursting events, and in some cases the child droplets sizes could be even measured.

Similarly to TPL, the explored bio-oils displayed a high propensity to form soot. This conclusion was initially based on the different imaging methods used in this work, as bio-oils presented thick soot shells surrounding the droplet and bright flames with the characteristic luminosity stemming from thermal emission of soot particles. To confirm and quantify this relevant behavior, Probe B (Figure 3.6) was used to sample the total amount of soot particles yielded at the 0% O_2 condition. As a result, the IDSY (Isolated Droplet Soot Yield) was calculated for each oil, in terms of grams of weighed soot per gram of injected fuel. These tests were repeated at least three times for each fuel, and the mean IDSY calculated for each fuel is displayed in Figure 4.24.
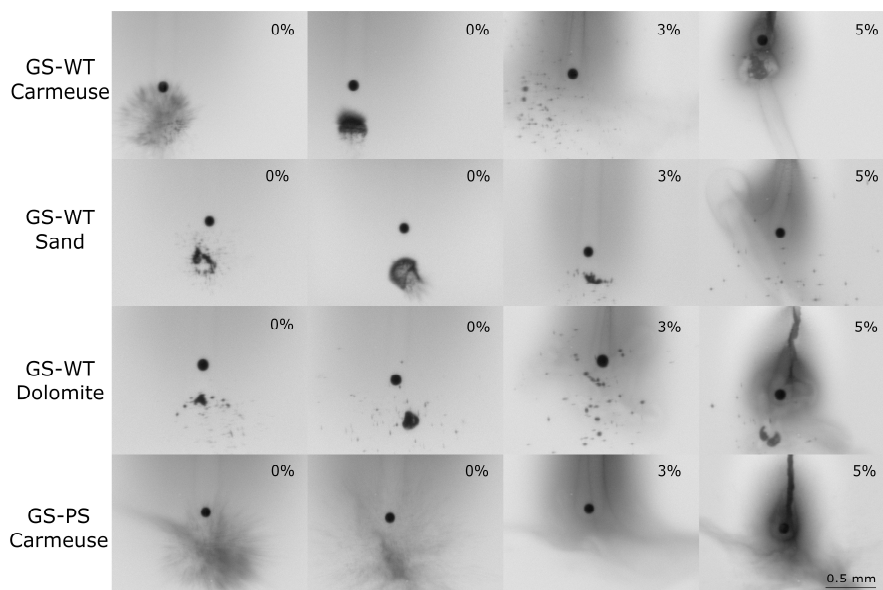
Figure 4.23. Double-exposure pictures of individual droplets microexploding for the bio-oils evaporating and burning under all oxygen conditions (O_2 level indicated for each image).
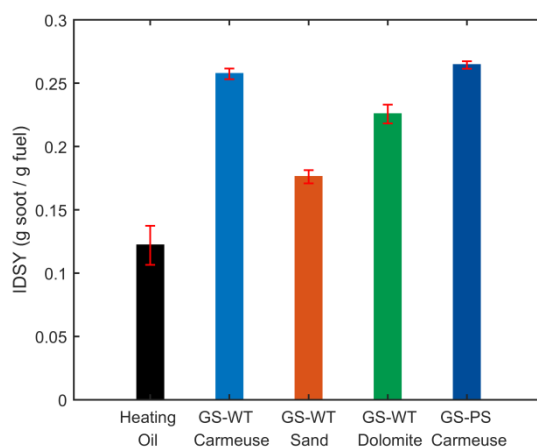

Figure 4.24. Isolated droplet soot yield (IDSY) obtained for each fuel through the aspirating soot probe tests. The uncertainty bars indicate $\pm$ 2 SD (Standard Deviation) of repeated measurements.

According to Figure 4.24, all the bio-liquids yielded considerably higher amounts of soot than heating oil, confirming their aforementioned sooty behavior. Among them, the two liquids produced with the Carmeuse catalyst displayed the highest soot yields, followed by GS-WT Dolomite and GS-WT Sand. This is ascribed to the higher aromatic content of the oils when using Carmeuse limestone as a catalyst, mainly due to aromatization and hydrodeoxygenation reactions in the pyrolysis reactor. Even if this high aromaticity leads to a significant soot

generation, the two liquids obtained with Carmeuse (and especially GS-PS Carmeuse) displayed the best global combustion behaviors from all the explored bio-oils, reinforcing the previously reported improvements in physicochemical properties. Finally, it is worth to note that a SEM analysis of the collected solid samples corroborated the absence of cenospheres or carbonaceous particles arisen from liquid-phase reactions, as virtually all the solids sampled corresponded to soot agglomerates.

4.2 Droplet evaporation modeling in high temperature conditions

This section summarizes the main results obtained over the course of the thesis in the droplet evaporation modeling field. To that end, the content has been distributed into three subsections. The first one deals with the validation of the monocomponent evaporation model through experiments on pure compounds at the DCF. In light of the deviations found for the alkane evaporation case, a novel analytical model taking into account the pyrolysis of the fuel's vapors was developed in Paper V, being a summary of this model presented in the second subsection. The third and last part covers some results obtained with the multicomponent droplet evaporation model for different liquid mixtures.

4.2.1 Validation of the monocomponent evaporation model

The experimental results on pure fuels presented in Section 4.1.1 were used to validate the droplet evaporation model described in Section 3.2. This initial validation was focused on the simplest case, that is, a monocomponent liquid evaporating under an inert atmosphere. The experimental conditions of the DCF tests were characterized (as detailed in Addendum A3), and applied as boundary conditions. Because of its relevance in the process, two different coflow temperature conditions were sought for these validations. The first one, named here as 'high T_∞', corresponds to the experimental condition applied along the thesis framework as the nominal 0% O_2 atmosphere (as detailed in Section 3.2). The second one aimed to provide complementary results, with also a 0% O_2 but with lower temperatures. Both temperature profiles were measured with a bare, fine-wire thermocouple and are compared in Figure 4.25.
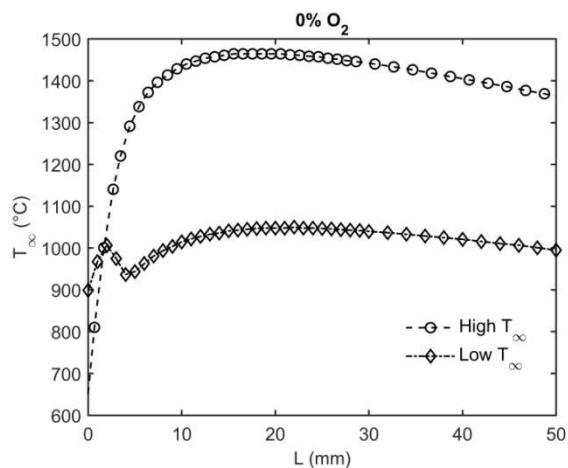

Figure 4.25. Axial profiles of temperature measured for the two coflow conditions used in this section.

As for the compounds used in this validation, two different chemical families were tested: n-alkanes and alcohols. The model theoretical predictions are compared with the experimental curves for different fuels within these families in Figure 4.26. All the experiments were performed with the high T_∞ coflow condition but for the case of hexadecane, which was tested at both temperatures.
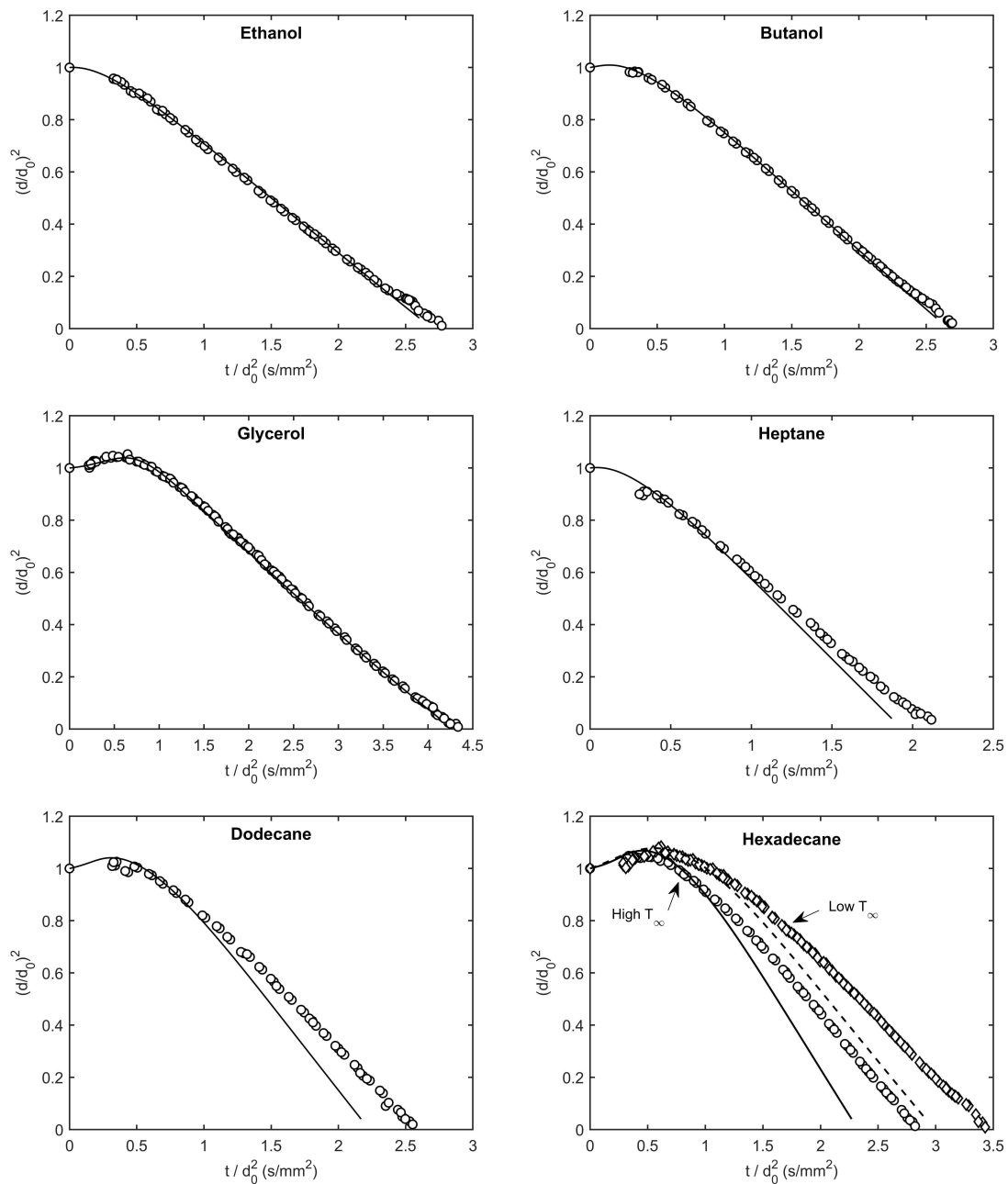

Figure 4.26. Experimental and theoretical droplet vaporization curves for all the pure compounds used for the model validation. Unless otherwise specified, the coflow temperature corresponded to the high T_∞ condition.

As it can be observed in Figure 4.26, the model is able to accurately predict the experimental evaporation curve of the three alcohol compounds, whereas it displays significant deviations for the alkanes. For these compounds, the theoretical model tends to overpredict the evaporation rate, clearly yielding a faster conversion than that observed in the experiments. To quantify these deviations, the quasi-steady evaporation rates of the different curves in Figure 4.26 are extracted and presented in Table 4.3.

Table 4.3. Experimental and predicted quasi-steady vaporization rates (mm^2/s) for all the cases shown in Figure 4.26, extracted by fitting the evaporation curve between $(d/d_0)^2$=0.6 and 0.2 to a straight line.

Fuel	Experimental	Model	Error (%)
Ethanol	0.4003	0.4195	4.80
Butanol	0.4371	0.4546	4.02
Glycerol	0.3124	0.3022	-3.28
Heptane	0.5453	0.6149	12.76
Dodecane	0.5349	0.6557	22.58
Hexadecane (high T_∞)	0.5317	0.7084	33.23
Hexadecane (low T_∞)	0.4623	0.5409	17.01

According to Table 4.3, the theoretical overprediction tends to increase with the alkane molecular mass, as the largest deviation is found for hexadecane, followed by dodecane and heptane. Similarly, a higher coflow temperature appears to increase the deviation between model and experiment, since the relative error for hexadecane was practically halved when employing the low T_∞ coflow.

A potential cause for these deviations was initially thought to stem from the assumption of constant gas-phase properties by following the *'1/3 rule'* proposed by Sparrow and Gregg (1958). As discussed in the model description in Section 3.2, the results obtained with this constant-property simplification were compared with numerical integrations of Equations (3.5) and (3.6) accounting for the variation of the gas-phase properties with temperature and composition. The negligible differences found completely justified the adequacy of the constant gas-phase property simplification.

So, the different degree of agreement obtained for both fuel groups could be related to some distinct behaviors observed in the tests: whereas alcohols evaporating at the 0% O_2 condition did not display any kind of luminosity, alkanes showed a bright orangish emission, which was
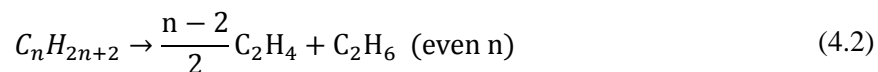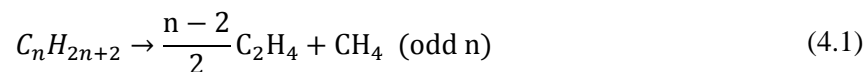
ascribed to the black-body radiation from incandescent soot particles. This can be visually confirmed in Figure 4.8, where the traces of different pure alkanes evaporating at the 0% O_2 coflow were presented. The formation of soot under such conditions points to the occurrence of endothermic fuel decomposition reactions in the gas phase. These pyrolysis reactions create the precursors needed to build-up the final soot particles and, since they are endothermic, they can lower the gas temperature around the droplet, reducing thus the experimental vaporization rates. This possibility was already discussed in (Faeth and Lazar (1971)), where also significant discrepancies were found between droplet combustion experiments and a theoretical evaporation model, especially for heavy alkanes. It was proposed that, since heavier hydrocarbons decompose more readily, it might be possible that this effect has a greater influence on this kind of fuels. This is also clearly the case in Figure 4.26, as the discrepancies model-experiment increase with the paraffin molecular mass. The traces displayed in Figure 4.8 also seem to confirm a higher soot yield for heavier alkanes. Consequently, the cause for the aforementioned discrepancies was finally ascribed to the gas-phase fuel decomposition in the droplet vicinity, a phenomenon that is not modeled by the theoretical model but occurs in the experiments for the set of conditions used in the DCF.

4.2.2 Development of a model for droplet evaporation with pyrolysis

The finding that gas-phase pyrolysis reactions reduced the evaporation rates of alkanes at the DCF experiments served as a motivation to develop a model which took into account this effect during the droplet evaporation process. It is well known that soot production is detrimental for most combustion applications, and that it primarily occurs in regions with high temperatures and reducing conditions. However, its interaction with the droplet vaporization process is poorly understood although, as it can be observed in Figure 4.26, it might be relevant. In spray combustion applications, an important fraction of the injected liquid fuel evolves in a group-combustion regime (Sánchez *et al.* (2015)), where a diffusion flame separates an inner region (rich in liquid and gaseous fuel, but practically oxygen-free) from an outer region which provides the oxygen required for combustion. Within this group-combustion region, the droplets vaporize under high temperature and reducing conditions, and therefore soot formation could affect the expected droplet evaporation behaviors. Given the relevance of the problem, a new analytical model was developed in collaboration with the University of California San Diego. This model is described in detail in Paper V, providing a novel theoretical description which takes into account these effects in the isolated droplet evaporation process.

4.2.2.1 Model for droplet vaporization with fuel-vapor pyrolysis

Under sufficiently high gas temperatures, the vaporized fuel molecules are considered to thermally decompose through endothermic pyrolysis reactions, lowering the gas temperature around the droplet. Even if these decomposition reactions involve complex kinetics (Savage (2000)), this work only considered a single irreversible reaction, as its main aim is to evaluate the global effects of these endothermic reactions on the droplet evaporation process. The main product of the gas-phase pyrolysis was assumed to be ethene (C_2H_4), so that the alkane molecules decomposed according to the following reactions:

$$C_nH_{2n+2} \rightarrow \frac{n-2}{2}C_2H_4 + CH_4 \text{ (odd n)} \tag{4.1}$$

$$C_nH_{2n+2} \rightarrow \frac{n-2}{2}C_2H_4 + C_2H_6 \text{ (even n)} \tag{4.2}$$

These reactions involve the following enthalpies of reaction for the alkanes examined in Figure 4.26: q=2.70 MJ/kg for heptane, 2.75 MJ/kg for dodecane and 2.90 MJ/kg for hexadecane. It is worth to note that these values are one order of magnitude lower than the corresponding heats of combustion, but one order of magnitude higher than the associated latent heats of evaporation.

Regarding the pyrolysis reaction rate ω (kg/m³/s), it was modeled through the following Arrhenius equation:

$$\omega = \rho \, B \, Y_f \, e^{-E_a/R_0 T} \tag{4.3}$$

Being B the pre-exponential factor and E_a the activation energy. For large values of E_a, the chemical reaction would display a strong dependence on the temperature, and ω would increase by many orders of magnitude as the temperature increases from T_s to T_∞. Under such assumption, the pyrolysis reaction would occur in a thin layer centered at $r=r_p$, with a temperature T_p intermediate between T_s and T_∞. This configuration is illustrated in Figure 4.27.
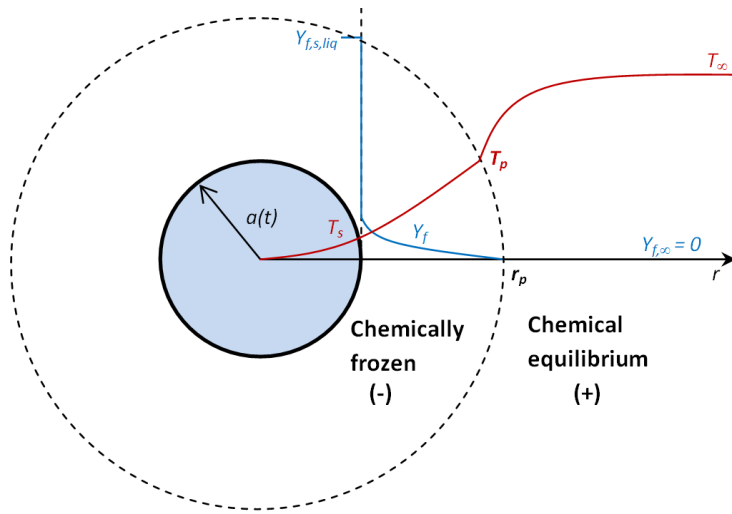

Figure 4.27. Scheme of the isolated droplet evaporation problem under spherico-symmetrical conditions with pyrolysis effects in the gas phase.

As depicted in Figure 4.27, the problem can be divided into two regions: an inner zone ($a \le r < r_p$) where the flow is chemically frozen because the temperature is too low to produce the fuel thermal decomposition and an outer region ($r > r_p$) where all the fuel has been consumed and, therefore, the flow is in chemical equilibrium. This arises from the comparison of the characteristic times associated with mass diffusion (a^2/D_f) and fuel-consumption processes $\left(B \, e^{-E_a/R_0 T} \right)^{-1}$ in each of these regions:

$$B \, e^{-E_a/R_0 T_s} \ll D_f/a^2 \ll B \, e^{-E_a/R_0 T_\infty} \tag{4.3}$$

The thickness of the reaction layer $\varepsilon \sim r\text{-}r_p$ can be determined through the reciprocal of the dimensionless activation energy:

$$\varepsilon = \left(\frac{E_a}{R_0 T}\right)^{-1} \ll 1 \qquad (4.4)$$

The problem of an evaporating droplet with pyrolysis can be addressed by adding the mass and heat sinks caused by the decomposition reaction to the right-hand side of Equations (3.5) and (3.6):

$$\frac{\dot{m}}{4\pi r^2}\frac{dY_f}{dr} - \frac{1}{r^2}\frac{d}{dr}\left(r^2 \rho \, D_f \frac{dY_f}{dr}\right) = -\omega = -\rho \, B \, Y_f \, e^{-E_a/R_0 T} \qquad (4.5)$$

$$\frac{\dot{m}}{4\pi r^2} c_p \frac{dT}{dr} - \frac{1}{r^2}\frac{d}{dr}\left(r^2 \, k \, \frac{dT}{dr}\right) = -\omega \, q = -\rho \, B \, Y_f \, q \, e^{-E_a/R_0 T} \qquad (4.6)$$

For convenience, the following dimensionless variables are defined:

$$\lambda = \frac{\dot{m} \, c_p}{4\pi k a} \qquad (4.7)$$

$$\tilde{r} = r/a \qquad (4.8)$$

$$Le = \frac{k}{\rho \, c_p \, D_f} \qquad (4.9)$$

Being λ and $\tilde{r}$ the dimensionless vaporization rate and radial coordinate, respectively. *Le* corresponds to the Lewis number. Using these variables, Equations (4.5) and (4.6) take the form:

$$\frac{\lambda}{\tilde{r}^2}\frac{dY_f}{d\tilde{r}} - \frac{1}{Le}\frac{1}{\tilde{r}^2}\frac{d}{d\tilde{r}}\left(\tilde{r}^2 \frac{dY_f}{d\tilde{r}}\right) = -\frac{B}{k/(\rho \, c_p \, a^2)} \, Y \, e^{-E_a/R_0 \, T} \qquad (4.10)$$

$$\frac{\lambda}{\tilde{r}^2}\frac{d}{d\tilde{r}}\left(\frac{c_p \, T}{q}\right) - \frac{1}{\tilde{r}^2}\frac{d}{d\tilde{r}}\left(\tilde{r}^2 \frac{d}{d\tilde{r}}\left(\frac{c_p \, T}{q}\right)\right)$$

$$= -\frac{B}{k/(\rho \, c_p \, a^2)} \, Y \, e^{-E_a/R_0 \, T} \qquad (4.11)$$

With the boundary conditions:

$$T\,(\tilde{r} = 1) = T_s \qquad (4.12)$$

$$T\,(\tilde{r} \to \infty) = T_\infty \qquad (4.13)$$

$$Y_f\,(\tilde{r} = 1) = Y_{f,s} \qquad (4.14)$$

$$Y_f\,(\tilde{r} \to \infty) = 0 \qquad (4.15)$$

As in the inner region the flow is chemically frozen, the chemical term at the right-hand side of Equations (4.10) and (4.11) can be neglected. Thus, the integration of these equations between the droplet surface ($\tilde{r} = 1$) and the pyrolysis-zone position ($\tilde{r} = \tilde{r}_p$) yields, at leading order, the fuel mass fraction and temperature profiles within this chemically frozen region:

$$\frac{Y_f{}^-}{Y_{f,s}} = \frac{e^{-Le\,\lambda/\tilde{r}_p} - e^{-Le\,\lambda/\tilde{r}}}{e^{-Le\,\lambda/\tilde{r}_p} - e^{-Le\,\lambda}} \tag{4.16}$$

$$\frac{T^- - T_s}{T_p - T_s} = \frac{e^{-\lambda/\tilde{r}} - e^{-\lambda}}{e^{-\lambda/\tilde{r}_p} - e^{-\lambda}} \tag{4.17}$$

Analogously for the outer region, where the flow is in chemical equilibrium:

$$Y_f{}^+ = 0 \tag{4.18}$$

$$\frac{T_\infty - T^+}{T_\infty - T_p} = \frac{1 - e^{-\lambda/\tilde{r}}}{1 - e^{-\lambda/\tilde{r}_p}} \tag{4.19}$$

However, these profiles depend on unknown variables, such as the dimensionless vaporization rate λ, eigenvalue of the problem. An expression for this variable can be obtained by the following mass-conservation equation at the droplet surface:

$$\dot{m} = \dot{m}\, Y_{f,s} - 4\,\pi\,\frac{k}{c_p}\frac{1}{Le}\,a\,\frac{dY_f}{d\tilde{r}}\Big|_{\tilde{r}=1} \tag{4.20}$$

$$\lambda\,(1 - Y_{f,s}) = -\frac{1}{Le}\frac{dY_f}{d\tilde{r}}\Big|_{\tilde{r}=1} \tag{4.21}$$

The required derivative of Y_f with respect to $\tilde{r}$ at the droplet surface can be provided by Equation (4.16). Substituting in Equation (4.21) yields an expression for λ:

$$\lambda = \frac{\ln\left[1/(1 - Y_{f,s})\right]}{Le(1 - 1/\tilde{r}_p)} \tag{4.22}$$

Analogously, the energy conservation at the droplet surface provides an additional correlation, this one useful to determine the sensible heat $\dot{q}_d$:

$$\dot{q}_d + L_v\,\dot{m} = 4\,\pi\,a\,k\,\frac{dT}{d\tilde{r}}\Big|_{\tilde{r}=1} \tag{4.23}$$

$$\frac{\dot{q}_d}{4\,\pi\,a\,k} + \frac{L_v}{c_p}\lambda = \frac{dT}{d\tilde{r}}\Big|_{\tilde{r}=1} \tag{4.24}$$

$$\frac{\dot{q}_d}{4\,\pi\,a\,k\,L_v/c_p} = \lambda\left[\frac{c_p\,(T_p - T_s)/L_v}{e^{\lambda(1-1/\tilde{r}_p)} - 1} - 1\right] \tag{4.25}$$

Another useful correlation can be obtained from the temperature and fuel mass fraction profiles provided by Equations (4.16), (4.17) and (4.19):

$$\frac{T_p - T_s}{T_\infty - T_s} = \frac{e^{-\lambda/\tilde{r}_p} - e^{-\lambda}}{1 - e^{-\lambda}} \left[1 - \frac{q \left(e^{\lambda/\tilde{r}_p} - 1 \right)}{c_p \left(T_\infty - T_s \right)} \right] \tag{4.26}$$

An analysis on both sides of the reaction layer yields, at leading order:

$$\frac{dT^+}{d\tilde{r}}\bigg|_{\tilde{r}=\tilde{r}_p} = \frac{dT^-}{d\tilde{r}}\bigg|_{\tilde{r}=\tilde{r}_p} - \frac{q/c_p}{Le} \frac{dY_f^-}{d\tilde{r}}\bigg|_{\tilde{r}=\tilde{r}_p} \tag{4.27}$$

Thus, a fraction γ of the heat reaching the reaction layer from the hot outer region is employed to pyrolyze the fuel at $\tilde{r}_p$:

$$\gamma = -\frac{q/c_p}{Le} \frac{dY_f^-}{d\tilde{r}}\bigg|_{\tilde{r}=\tilde{r}_p} \bigg/ \frac{dT^+}{d\tilde{r}}\bigg|_{\tilde{r}=\tilde{r}_p} < 1 \tag{4.28}$$

$$\gamma = \frac{q \left(e^{\lambda/\tilde{r}_p} - 1 \right)}{c_p (T_\infty - T_p)} \tag{4.29}$$

The analysis of the reacting layer provides the rest of equations needed to close the problem. One of them is the definition of the Damköhler number:

$$\Delta = \frac{B}{D_f/a^2} \left(\frac{E_a}{R_0 T_p} \right)^{-2} \left(\frac{\lambda}{\tilde{r}_p^2} \right)^{-2} \left(\frac{q}{c_p T_p} \right)^{-2} e^{-\frac{E_a}{R_0 T_p}} \tag{4.30}$$

The problem in the inner reaction layer is that of a reaction-diffusion balance, where a correlation between Δ and γ is sought. This was achieved through the numerical integration of the boundary-value problem detailed in Paper V. The resulting correlation is shown in Figure 4.28 for all the range of γ, along with the asymptotic predictions for both limits ($\Delta = 0.315236\gamma^{-2}$ for $\gamma \ll 1$ and $\Delta = 1.1517(1 - \gamma^3)$ for $(1 - \gamma) \ll 1$).
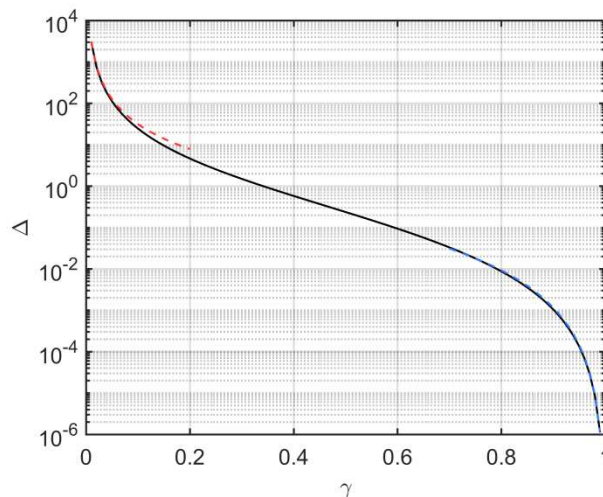
Figure 4.28. Variation of Δ with γ as obtained from the numerical integration (solid curve) and the asymptotic predictions (dashed curves).

With this correlation between Δ and γ the problem is closed, and the equations governing the gas-phase process of a vaporizing droplet with pyrolysis are established (the liquid-phase equations remain the same as those described in Section 3.2). Starting from the initial value of T_s, the fuel's vapor mass fraction at the surface ($Y_{f,s}$) can be determined through Equation (3.11). The system formed by Equations (4.22), (4.25), (4.26), (4.29), (4.30) and the correlation $\Delta(\gamma)$ provided by Figure 4.28 can be solved to calculate the values of λ, $\dot{q}_d$, $\tilde{r}_p$, T_p, γ, and Δ. The knowledge of the vaporization rate (λ) and the sensible heat gained or lost by the droplet ($\dot{q}_d$) allows the calculation of the initial conditions for the next iteration, yielding a new droplet mass and surface temperature, as detailed in Section 3.2.

However, it is worth to note that the pyrolysis kinetic parameters E_a and B are required to solve the aforementioned system, since they appear in Equation (4.30). However, these parameters are unknown, hindering the application of this model to the alkanes studied in the previous sub-section. The determination of E_a and B from droplet vaporization rates at different T_∞ would require very high accuracies (1% or better), due to their strong sensitivity to small changes in K. Unfortunately, given the experimental uncertainties associated with the isolated droplet experiments, this level of accuracy is thought to be unattainable.

4.2.2.2 Estimation of the pyrolysis temperature from experimental data

A useful approximation to the Arrhenius parameters E_a and B can be obtained by taking advantage of the strong temperature sensitivity of the chemical reaction (see Equation (4.30)).

For large values of the dimensionless activation energy $E_a/(R_0\, T_p) \gg 1$, the relative changes in T_p are limited to small values of order $\left[E_a/(R_0\, T_p)\right]^{-1} \ll 1$. Thus, the pyrolysis temperature T_p of a given fuel emerges as a constant kinetic parameter, independent from the droplet size or the ambient temperature and, therefore, it can be used to replace at leading order the Arrhenius parameters.

The value of T_p for the different alkanes can be readily extracted from the experimental droplet evaporation data presented in Figure 4.26. As it was described before, the droplet evaporation process of pure compounds was experimentally found to reach a quasi-steady state at the end of the initial heating period. During this quasi-steady state, the droplet heating rate $\dot{q}_d = 0$, and therefore T_s, Y_s, λ, $\tilde{r}_p$, T_p, γ and Δ reach constant values. Actually, the quasi-steady dimensional vaporization rate $K = -d(d^2)/dt$ was extracted from the experimental curves for all the pure compounds validated in Figure 4.26, with the results displayed in Table 4.3. Both vaporization rates can be related through the following expression:

$$\lambda = -\frac{\rho_l\, c_p}{2\, k}\frac{d(a^2)}{dt} = \frac{\rho_l\, c_p}{8\, k}\, K \tag{4.31}$$

Thus, the K values shown in Table 4.3 can be used as an experimental input to calculate the quasi-steady value of λ for each compound. Setting $\dot{q}_d = 0$ in Equation (4.25) and combining the results with Equation (4.26) yields:

$$\frac{T_p - T_s}{L_v/c_p} = \frac{(q + L_v)\big(e^\lambda - 1\big) - c_p(T_\infty - T_s)}{q + c_p(T_\infty - T_s) - L_v(e^\lambda - 1)} \tag{4.32}$$

$$\tilde{r}_p = \lambda\, ln^{-1}\left[1 + \frac{c_p(T_\infty - T_s) - L_v(e^\lambda - 1)}{q}\right] \tag{4.33}$$

The system formed by Equations (3.11), (4.22), (4.31), (4.32) and (4.33) can be solved by an iterative scheme in order to determine, for each fuel, the values of T_s, Y_s, λ, $\tilde{r}_p$ and T_p. The latter three parameters are displayed in Table 4.4 for the three alkanes at the high T_∞ condition. It can be noted that, as the chain length of the alkane molecule increases, the pyrolysis temperature T_p decreases, and therefore the reaction standoff ratio $\tilde{r}_p$ approaches to the droplet surface.

Table 4.4. Experimental quasi-steady vaporization rate (K_{exp}) extracted for each alkane at the high T_∞ condition along with the values obtained from the pyrolysis model when using this K_{exp} as an input through Equation (4.31).

Fuel	K_{exp} (mm^2/s)	λ	T_p	$\tilde{r}_p$
Heptane	0.5453	2.482	1080	7.342
Dodecane	0.5349	2.389	912	4.954
Hexadecane	0.5317	2.285	841	4.142

As it was shown in the temperature profiles presented in Figure 4.25, the high T_∞ condition reached coflow gas temperatures of ~1730 K. Since all the alkanes display T_p values below this temperature, all of them will undergo pyrolysis reactions at the location dictated by $\tilde{r}_p$, modifying their temperature profiles as shown in Figure 4.29 for heptane and hexadecane. The discontinuity in the temperature profiles is naturally sharper for the latter, since it displays a lower T_p value and the pyrolysis dip occurs closer to the droplet. It is worth to note that, for any fuel vaporizing under a $T_\infty < T_p$, the pure evaporation expressions described in Section 3.2 would be recovered, and therefore the temperature profiles calculated by the pyrolysis model would concur with those of the pure evaporation case.
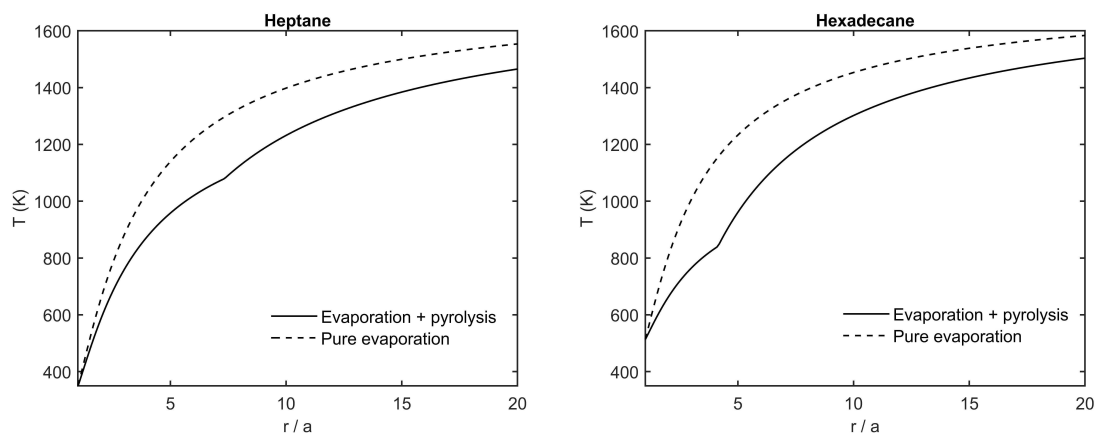

Figure 4.29. Radial profiles of gas temperature for heptane and hexadecane simulated for the high T_∞ condition.

An especially interesting variable is the pyrolysis temperature T_p, as it is assumed at leading order as a constant kinetic parameter, intrinsic for each fuel. For checking the accuracy of this assumption, a second experiment on hexadecane was performed at the DCF, this one under the so-called low T_∞ condition (Figure 4.25). The values of T_p and $\tilde{r}_p$ for hexadecane were recalculated using the new experimental vaporization rate, yielding $T_p = 969\ K$ and $\tilde{r}_p = 9.86$.

The difference of 128 K with the previous T_p value (841 K, Table 4.4) would point to a dimensionless activation energy in the order of $E_a/(R_0\,T_p)\sim 10$ for hexadecane.

4.2.2.3 The modified Spalding law

The pyrolysis temperatures presented in Table 4.4 could therefore be used to estimate the droplet evaporation process by considering T_p as a fixed kinetic parameter of the fuel. The quasi-state dimensionless vaporization rate can be calculated from:

$$\lambda = ln\left[1 + \frac{c_p(T_\infty - T_s)}{L_v} - \left(\frac{q}{L_v}\right)\left(\frac{c_p(T_\infty - T_f)}{q + L_v + c_p(T_f - T_s)}\right)\right] \tag{4.34}$$

Which can be rewritten as:

$$\lambda = ln\left[1 + \frac{c_p(T_a - T_s)}{L_v}\right] \tag{4.35}$$

Where the apparent temperature (T_a) is defined as:

$$T_a = \alpha\,T_p + (1 - \alpha)\,T_\infty \tag{4.36}$$

$$\alpha = \frac{q}{L_v + c_p(T_p - T_s) + q} \tag{4.37}$$

Equation (4.35) is analogous to the well-known classical Spalding solution for a vaporizing droplet (Spalding (1950), Godsave (1953)), with the only difference of the apparent temperature substituting T_∞. This apparent temperature is intermediate between T_p and T_∞, and is estimated through the weighting factor α (ratio of the heat employed to pyrolyze the fuel to the total heat required to vaporize the liquid fuel, heat it up to T_p and pyrolyize it). The α calculated from the results of Table 4.4 yield values of 0.48, 0.60 and 0.70 for heptane, dodecane and hexadecane, respectively. Again, a stronger effect of pyrolysis for the heavier alkanes can be ascertained from these values, since heavier alkanes display apparent temperatures closer to T_p than to T_∞ (Equation 4.36), resulting thus in a greater vaporization reduction (Equation 4.35).

It is worth to remember that these data were obtained from the high T_∞ coflow experiments. However, assuming the T_p=constant approximation, these values can provide an estimation of the droplet vaporization rate at different conditions. For instance, for the case of hexadecane at the low T_∞ condition, the model predicts a K=0.4196 mm²/s, which differs by 9.2% from the experimental value (0.4623 mm²/s, see Table 4.3). This departure is again consistent with the aforementioned errors of order $\left[E_a/(R_0\,T_p)\right]^{-1}$ introduced through the assumption of a constant

pyrolysis temperature. Future experimental tests at different ambient temperatures are planned for gaining further insight on both the evaluation of the pyrolysis temperature and the accuracy of the model developed in this work.

4.2.3 Multicomponent model results

The modeling exercises presented so far have been related to the monocomponent case, without attempting to cover the evaporation process of mixtures. However, as it was described in Section 3.2, this behavior was also included in the model, namely by following the so-called *'Effective Diffus*ivity' approach detailed in (Sirignano (2010)). The validation of this multicomponent characteristic by means of the DCF experiments displayed some difficulties due to the pyrolysis effects occurring for hydrocarbons evaporating at high gas temperatures, as the pyrolysis model described in Section 4.2.2 was developed for the case of pure liquids. Even if some simplifications to take into account these effects were employed for latter studies (as it will be detailed in the next Section), a validation of the multicomponent model under pure vaporization conditions was still thought to be necessary prior to its use. It is worth to note that only a brief validation with literature data is presented here, as a more extended evaluation of the multicomponent model through DCF experiments on alcohol mixtures (which do not display pyrolysis reactions) is planned as future work.

The simulation results published in (Gavhane *et al.* (2016)) for binary mixtures are thought to be useful as validation data for this purpose. This choice is based on the fact that this work provided with detailed information on droplet multicomponent behaviors which are extremely difficult to obtain experimentally (e.g., temporal evolution of the evaporation rate for each individual component or composition profiles within the liquid). The model presented in (Gavhane *et al.* (2016)) is also very similar to the one described in Section 3.2, as it stems from the analytical description of the 1-D evaporation of an isolated and quiescent droplet. Furthermore, it includes a case of study which is thought to be interesting for the validation process, with 50 μm droplets of heptane-dodecane blends vaporizing in air at relatively high temperature conditions (T_∞=750 K). It is worth to note that much of the droplet evaporation data in the literature (and especially the experimental data) addresses the evaporation process under rather low temperature atmospheres. This has a significant impact on the multicomponent behavior since, under such conditions, the droplet evaporation is close to a distillation scenario and composition gradients within the liquid are low or even non-existent. However, for high T_∞ conditions, the strong preferential vaporization of the more volatile species is thought to create significant compositional gradients near the surface (Makino and Law (1988)). As this is expected to be the case under typical combustion conditions, it seems desirable to validate the multicomponent model under such scenario.

The case of study addressed here considers pure n-heptane (C_7), n-dodecane (C_{12}), and three of their mixtures with a 75, 50 and 25% by mass of heptane (C_7-75, C_7-50 and C_7-25 respectively). The gas surrounding the 50 μm droplets consists in air at atmospheric pressure and 750 K.

Figure 4.30 displays the temporal evolution of the droplet mass for each of these liquids, both as published in (Gavhane *et al.* (2016)) (left), and as obtained in the current work (right).
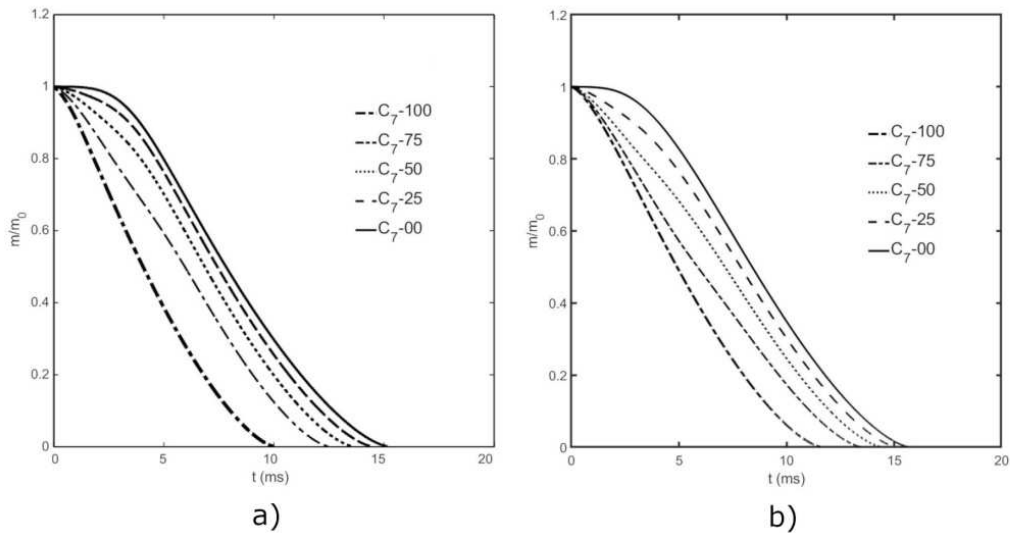

Figure 4.30. Temporal evolution of the normalized droplet mass for different heptane-dodecane mixtures at T_∞=750 K, as presented in (Gavhane *et al.* (2016)) (a), and calculated in this work (b).

As it can be observed in Figure 4.30, the droplet consumption times for the different fuels are very similar in both models, especially for dodecane and the three mixtures. Pure heptane, on the other hand, displays a slightly longer consumption time in the current model. Regarding the mass evolution for a given fuel, small differences can also be noted between both models, although in general the behaviors are found to be quite close. These dissimilarities are mainly ascribed to the differences in the estimated transport properties and, more specifically, in the liquid mass diffusion coefficient (D_l). The estimation of this parameter implies several assumptions, implying a relatively high uncertainty (see Addendum A4). From the results shown in Figure 4.30, it would appear that the D_l values estimated in the current model are somewhat higher than those used in (Gavhane *et al.* (2016)). This can be noted, for instance, in the mass evolution curve for C_7-75. Looking at the first instants after the droplet injection, this curve is found to run closer to pure heptane in Figure 4.30.b than in Figure 4.30.a. The higher D_l of the former simulation would enhance the transport of heptane from the droplet center towards the surface, securing a larger C_7 replacement rate. As in these first instants the evaporated mass corresponds primarily to heptane, a larger C_7 availability would imply a greater droplet mass loss, as depicted in Figure 4.30.b. In the same way, the C_7-25 mixture runs closer to pure dodecane in Figure 4.30.a when compared to Figure 4.30.b due to the larger heptane replacement rate of the latter.

To gain more insight into the differential vaporization of each compound, the mass evaporation rate of C_{12} has been plotted in Figure 4.31 for pure dodecane and its mixtures. Again, the general behavior of both models seems consistent and quite similar. However, it should be noted that the C_{12} evaporation rates calculated by the current model appear to be slightly shifted towards longer residence times, as resulted from the aforementioned larger mass diffusion coefficient for these simulations. It is worth to note that the numerical integration of the evaporation rate curves for each individual compound were found to recover the initial mass of each species at t=0, confirming therefore that the model complied with the mass balance.
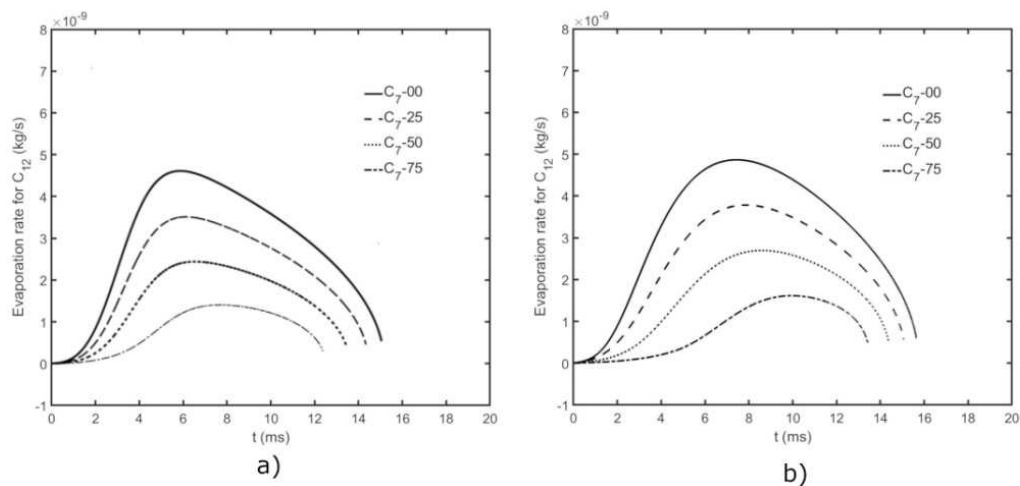

Figure 4.31. Temporal evolution of the mass evaporation rate for different heptane-dodecane mixtures at T_∞=750 K, as presented in (Gavhane *et al.* (2016)) (a), and calculated in this work (b).

Finally, the temporal evolution of the heptane mass fraction at the surface ($Y_{C7,s}$) was also thought to be an interesting parameter to analyze the multicomponent behavior of each model. These results are presented in Figure 4.32 for the C_7-75 mixture and, again, show quite similar characteristics among both models, although with subtle differences ascribed to the slightly higher D_l calculated in this work. Namely, the higher D_l in Figure 4.32.b would cause a more delayed decrease of the $Y_{C7,s}$, as the droplet center is replacing heptane at a faster rate. This also causes a sharper decrease in the C_7 fraction at the surface during the last period of the droplet lifespan, as the inner region of the droplet is more depleted in heptane. It is worth to note that, contrary to a pure distillation scenario, heptane remains available in the liquid throughout all the droplet evaporation process. In summary, the multicomponent model described in Section 3.2 was found to provide satisfactory results, in quite good agreement with those of Gavhane *et al.* (2016).
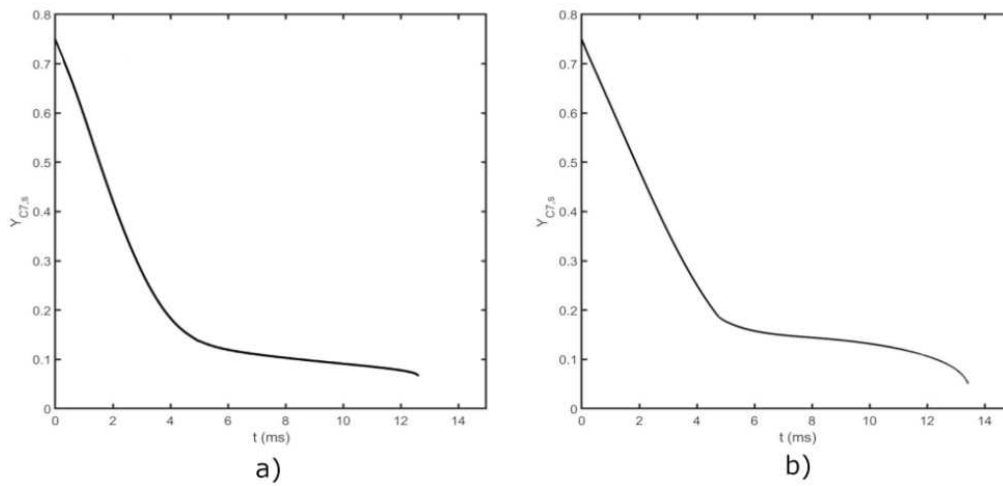
Figure 4.32. Temporal evolution of the heptane mass fraction at the surface ($Y_{C7,s}$) for the C_7-75 mixture evaporating at T_∞=750 K, as presented in (Gavhane *et al.* (2016)) (a), and calculated in this work (b).

4.3 Surrogate formulation and validation methodology

The third section of this chapter addresses the use of the single droplet configuration for the surrogate design and validation processes. As it has been discussed in the Introduction, the relative simplicity of this configuration, in addition to its resemblance to the final application of most liquid fuels (i.e., spray combustion), points to this layout as a most suitable benchmark to design and evaluate surrogates for liquid fuels. To this end, the joint use of the droplet evaporation experiments (Section 4.1) and modeling exercises (Section 4.2) is thought to provide powerful tools for developing novel methodologies in the surrogate field.

Within the framework of this thesis, a first step toward this end resulted in the work published in Paper VI, where both approaches were used to formulate and validate three surrogate mixtures aiming to emulate the evaporative and sooting behaviors of a Spanish heating oil. As this work intends to explore new methodologies for the formulation and evaluation processes, the surrogate palette was decided to consist of only two compounds: n-eicosane and 1-methylnaphtalene (MNP). Even if binary mixtures surely display a limited ability to match certain complex behaviors, their simplicity greatly eases result analysis, being this reason the main motivation for choosing this palette.

4.3.1 Surrogate formulation

Three different surrogates (SR1, 2 and 3) were defined, following different criteria, and evaluated.

As presented in the Introduction, a first surrogate (SR1) aiming to match the evaporative behavior of the target heating oil was formulated through the multicomponent droplet model. To this end, the vaporization curve of heating oil was experimentally obtained at the DCF, being afterwards parameterized in the three characteristic times illustrated in Figure 4.33. Therefore, if these characteristic times were the design properties chosen as representative of the vaporization behavior, the values t_c=0.645, t_{60}=1.126 and t_{20}=0.813 s/mm^2 were the property targets for SR1 to emulate.

The predictive tool required for estimating the evaporation behavior of the different eicosane-MNP mixtures consisted in the droplet multicomponent model described in Section 3.2. However, as detailed in Section 4.2, the pyrolysis of hydrocarbon vapors under the high-temperature conditions present at the DCF tests could induce significant discrepancies between the model predictions and the experiments, particularly for the heavier alkanes. The analytical model described in Section 4.2.2 was only designed for pure fuels, and therefore an alternative way had to be devised for ensuring a good agreement between the multicomponent droplet evaporation model and the DCF tests, as it is fundamental for a proper surrogate design process.

In this work, this was done by introducing an energy sink in the form of a constant endothermic heat of reaction in the heat transfer number (Equation 3.15). An empirical fitting of this heat of reaction was performed for both pure compound (eicosane and MNP), in order to calibrate the model for each particular fuel. This adjustment was also applied in the simulation of the mixtures, namely by weighting the heat of reaction of each pure compound with the relative mass flow rate vaporized from each species. The obtained simulation results are presented in Figure 4.34, both in terms of evaporation curves (a) and extracted characteristic times (b).
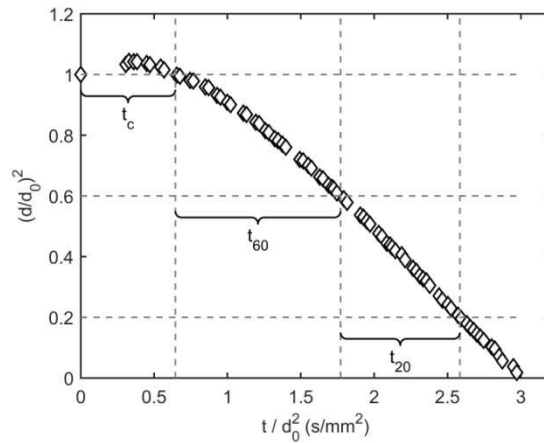

Figure 4.33. Evaporation curve obtained at the DCF (0% O_2 coflow) for heating oil along with the extracted characteristic times t_c, t_{60}, and t_{20} (0.645, 1.126, and 0.813 s/mm^2 respectively).
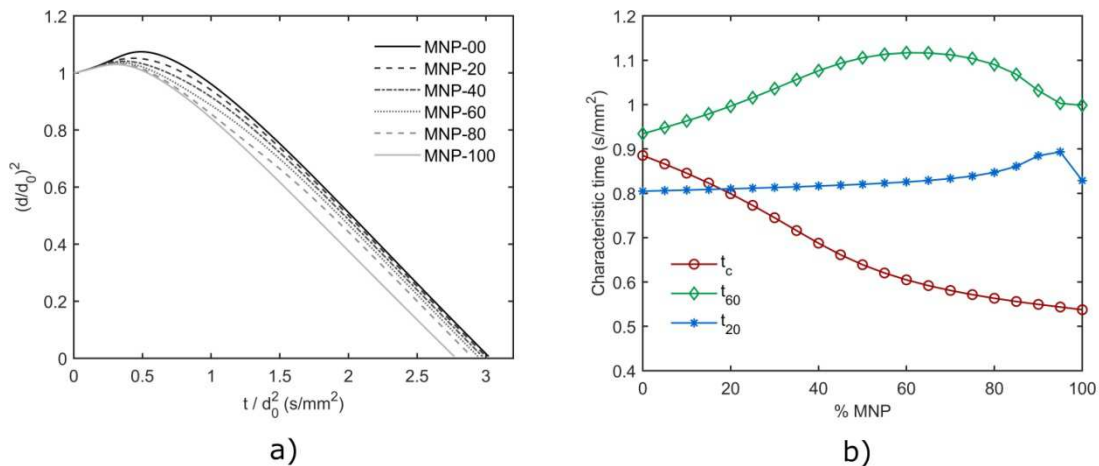

Figure 4.34. Evaporation curves predicted by the model for binary mixtures of MNP-eicosane (a), along with their corresponding characteristic times (b).

Finally, a comparison of the characteristic times predicted by the model in Figure 4.34 and the data experimentally obtained for the target heating oil (Figure 4.33) allowed for the selection of

the eicosane-MNP mixture which best reproduced the evaporation behavior, that is, of SR1. This was done by defining a global error for evaporation (e_{ev}), calculated as the quadratic mean of the three characteristic time individual errors (e_{tc}, e_{t60}, e_{t20}). The dependency of these errors on the binary mixture composition is shown in Figure 4.35, where it can be observed that the combined error e_{ev} displays a clear minimum for the MNP-49 mixture (i.e., 49% by mass of MNP and 51% of eicosane). This blend was therefore named SR1, and its adequacy to emulate the evaporative behavior of the target heating oil will be experimentally evaluated in the next section.
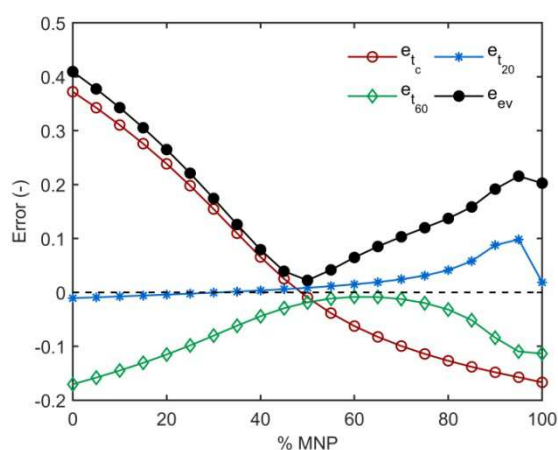

Figure 4.35. Relative errors calculated for each characteristic time along with the global error for evaporation (e_{ev}) for all the mixtures studied.

A second surrogate mixture, named SR2, was designed to match the sooting behavior of heating oil. In this case, the design property used to model this characteristic was the Yield Soot Index (YSI), a parameter based on the soot concentration measured in a doped flame. The literature offers a quite complete YSI database for both pure compounds (Das *et al.* (2018), Das *et al.* (2017)) and real fuels (Das *et al.* (2017)), and therefore this parameter allowed for the estimation of the sooting behaviors of both heating oil and the eicosane-MNP mixtures.

The YSI target value for heating oil was based on the data by (Das *et al.* (2017)), where the YSI of different jet and diesel fuels were explored, finding a good correlation between the YSI and the total aromatic content. A chemical analysis of the heating oil sample provided a 26.24% by volume of aromatics. Thus, after checking that the nature of the aromatic compounds present in heating oil is similar to those in jet and diesel fuels (i.e., similar single-ring/multiring aromatic ratio), the correlation presented in (Das *et al.* (2017)) was used to yield a YSI of 124.9 for the target heating oil. As for the binary mixtures, the YSI of pure eicosane and MNP was found in

(Das *et al.* (2017)) to be 14.1 and 471.2 respectively, whereas the following mixture rule could be applied to estimate the YSI of their mixtures:

$$YSI_{mix} = \sum_i Y_i \, YSI_i \qquad (4.38)$$

Being Y_i the mass fraction of compound i and YSI_i its YSI value as a pure fuel. Thus, the application of Equation (4.38) was enough to estimate the YSI of all the eicosane-MNP mixtures. The blend which minimized the error with the target value was found to be MNP-24. The ability of this mixture (named SR2) to emulate the soot production characteristic of heating oil will be evaluated through experiments at the DCF in the next section.

The last surrogate designed in this work, SR3, was created by matching a number of rather simple physicochemical properties which are indirectly related to the final behaviors (i.e., evaporation and sooting tendency). The design properties chosen to match both behaviors were: YSI, C/H ratio, molecular weight (MW), liquid density (ρ_l), and distillation curve (DC). The first two properties, YSI and C/H ratio, display a clear connection with the propensity to form soot, whereas the MW is closely linked to the diffusive properties of the fuel (Dooley *et al.* (2012)). The liquid density, on the other hand, displays a relevant impact on the droplet evaporation process (Liu *et al.* (2013b)), and the distillation curve has been widely used to describe the vaporization behavior of multicomponent fuels (e.g., see (Bruno and Huber (2010), Bruno and Smith (2010))). Even if some of these properties are not directly related to the final droplet evaporation and sooting behaviors, they are clearly relevant for these processes. Thus, by matching them, the resulting mixture SR3 could be expected to emulate the final behaviors of the target heating oil.

The liquid density, molecular weight, YSI and C/H ratio of heating oil were obtained by means of a physicochemical analysis of the fuel, whereas different mixture rules were used to estimate the value of these properties for the eicosane-MNP blends. The heating oil distillation curve, on the other hand, was experimentally extracted through a distillation setup based on the Advanced Distillation Curve (ADC) described in (Bruno (2006), Bruno and Huber (2010)). The prediction of this curve for the binary mixtures was obtained through a batch distillation model, which was developed and validated as detailed in Paper VI.

Similarly to the previous surrogates, the formulation of SR3 relied on finding the binary mixture that minimized the deviations between its predicted behaviors and those experimentally measured for the target heating oil. As several properties were used for the SR3 formulation, the relative error of each property was divided by its maximum deviation so that all the resulting normalized errors spanned from 0 to 1, and could therefore be compared in equal terms. The so

obtained normalized errors (ε) are plotted in Figure 4.36 for each design property, along with the global error (ε_{Global}), calculated as the quadratic mean of the individual ε. As it can be noticed, the minimum of ε_{Global} was located in MNP-39, and therefore this was determined to be the SR3 composition.
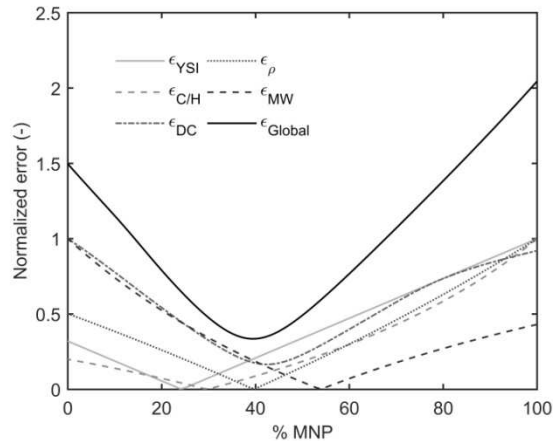

Figure 4.36. Normalized global errors estimated for each design property along with the global error (ε_{Global}) for all the binary mixtures.

4.3.2 Surrogate validation

At the end of the formulation phase, three different surrogate mixtures were proposed in order to emulate the evaporative behavior of heating oil (SR1: MNP-49), its sooting characteristic (SR2: MNP-24) or a set of physicochemical properties related with both (SR3: MNP-39). This section addresses the experimental evaluation of these mixtures by means of tests at the DCF, where both behaviors will be extracted and compared to those of the target heating oil. Since the palette chosen for this work only consists of two compounds, an additional objective of this section is to explore the full range of eicosane-MNP mixtures. This is thought to provide results of general interest, since it produces detailed data on the isolated droplet evaporation and sooting behaviors of pure and blended high-MW hydrocarbons under conditions representative of those occurring in real flames.

The vaporization curve of heating oil is compared with those of pure eicosane, MNP and five of their mixtures in Figure 4.37.a. In this plot, it is possible to observe that the MNP-45 blend accurately replicates the heating oil curve, whereas neat MNP and eicosane display clearly differentiated features. A more complete description of the multicomponent characteristics found for this set of binary mixtures was presented in Section 4.1.1.3. When it comes to evaluate the degree of agreement between the three surrogates and the target fuel, the extracted

characteristic times can provide some insight to quantify the deviations found for each case. This information is shown in Figure 4.37.b, where the global error for evaporation (e_{ev}) shows a clear minimum precisely around the SR1 surrogate composition. As SR1 was formulated in order to match the evaporative behavior of heating oil, this close agreement would support the efficacy of the proposed formulation method. On the other hand, SR2 is located clearly outside of this optimal region, primarily due to the longer t_c caused by the rich composition in eicosane. This deviation for SR2 could be expected beforehand, as SR2 was solely formulated to emulate the soot propensity of heating oil. Finally, SR3 displays an intermediate behavior between SR1 and SR2. Even if it is located outside the optimal composition region, its errors are significantly lower than those of SR2, and therefore it would show a closer evaporative behavior to the target fuel.
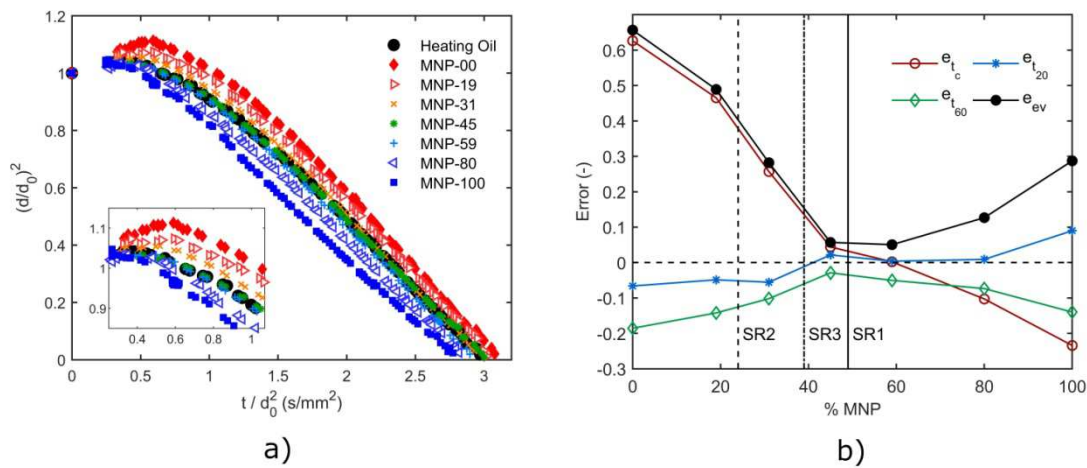

Figure 4.37. Experimental droplet vaporization curves for heating oil and the tested mixtures (a), along with the extracted characteristic time errors (b). In (b) the compositions of the three surrogates are marked with vertical lines.

The second behavior of interest (i.e., the propensity to form soot) was also experimentally tested for each fuel and mixture by means of the soot probe B illustrated in Figure 3.6. As detailed in Section 3.1, this probe retained the totality of the soot particles generated during the droplet evaporation tests, producing as a result the IDSY parameter (g_{soot}/g_{fuel}), used to quantify the soot yielded by different fuels when exposed to the same experimental conditions. As it was shown in Figure 4.10, the IDSY showed a quite linear behavior with the binary mixture mass fraction (Y_i), pointing to a lack of significant interactions between the two surrogate components that could affect the amount of soot produced by the isolated droplet's fuel vapors. As the YSI also depended linearly on Y_i (Equation 4.38), a quite good linear dependency can be also observed between the experimentally measured IDSY and the predicted YSI (Figure 4.38). The IDSY

obtained for the target heating oil (0.1220 ± 0.0077 g_{soot}/g_{fuel}) was located between that yielded for MNP-19 (0.0990 ± 0.0211 g_{soot}/g_{fuel}) and MNP-31 (0.1560 ± 0.0268 g_{soot}/g_{fuel}). Thus, the mixture that would produce the same amount of soot than heating oil could be estimated through a linear interpolation between these two blends. The resulting optimal mixture was MNP-24, exactly the same composition as the proposed SR2. These results support the formulation methodology used for this surrogate, based on the YSI, as a good alternative to design mixtures which can accurately emulate the sooting propensity behavior. The other two surrogates, SR3 (MNP-39) and especially SR1 (MNP-49), displayed significant higher sooting tendencies than heating oil, as demonstrated by their higher IDSY.
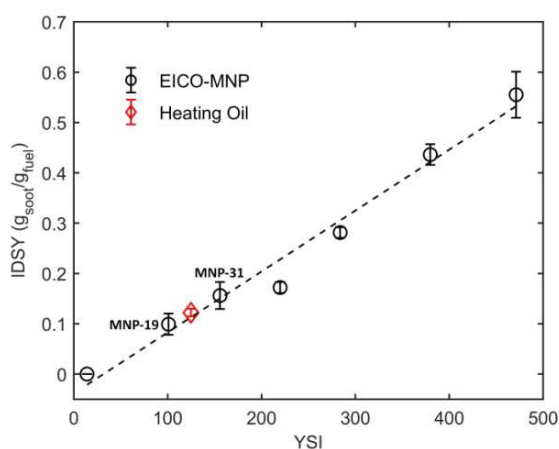

Figure 4.38. IDSY experimentally obtained for all the eicosane-MNP mixtures and for the target heating oil in terms of their YSI predicted values. The uncertainty bars indicate $\pm$ SD (Standard Deviation) of the experimental measurements.

The fact that SR1 and SR2 are able to respectively reproduce the heating oil evaporation and sooting behaviors in such an accurate manner is thought to support the aforementioned formulation methodologies tested in this work. On the other hand, the third surrogate mixture showed an intermediate behavior between SR1 (which matched the evaporative characteristic) and SR2 (which was able to reproduce the soot yield). The simplicity of the palette used, with only two compounds, significantly reduced the ability of the mixtures to simultaneously replicate different complex behaviors. However, this work is thought to serve as validation for the proposed methods, which have demonstrated to constitute valid and novel approaches to design and evaluate surrogates for complex liquid fuels based on the isolated single-droplet configuration. Thus, they could be used in future works, either as stand-alone methods or in combination with others, to formulate surrogates with a higher number of compounds, simultaneously replicating therefore a higher number of target behaviors.

5. Conclusions

5.1. Summary and concluding remarks

The isolated droplet configuration has been used to characterize the main combustion behaviors of a wide variety of liquids, both pure compounds and real fuels of interest for heat and energy generation. As revealed by a literature review, the results and behaviors extracted from droplet combustion tests can be significantly affected by the particular setup design and by the experimental conditions. Therefore, a careful selection and characterization of these conditions was required for ensuring their validity and interest. Namely, the tests were designed to simulate the conditions occurring in real applications, with unsupported and small droplets evolving within a hot gaseous coflow. In addition to these conditions being representative of those occurring in real flames, proximity with the one-dimensional combustion case was also sought, in order to yield a configuration which would allow for a more simplified result analysis while also easing modeling efforts. The consistent occurrence of quite spherical soot shells and chemiluminescent envelope flames proved that droplets indeed vaporized under conditions close to spherical symmetry, despite the fact that tests were performed at normal gravity.

As a result, the experiments on real fuels are thought to yield useful data on fuels and blends of interest for which these results are scarce in the literature. This experimental information might be either used for comparative purposes among fuels, as validation data for droplet evaporation and combustion models, or even as the fuel-specific input data required for the simulation of realistic spray flames.

Heating oil, used in these experiments as a reference baseline, was found to yield essentially the same behaviors as those noted for its two blends with biodiesel (B10 and B20) in all aspects but soot generation, where a remarkable decrease was obtained with biodiesel addition. These results are thought to support the use of such mixtures as drop-in replacements for heating oil. On the contrary, a Tire Pyrolysis Liquid (TPL) obtained from the thermal decomposition of waste tires displayed a slower conversion rate and a considerably higher propensity to form soot. Nonetheless, the consistent onset of microexplosion events which shattered the droplets in secondary atomizations allowed for a significant reduction in the droplet burnout times.

A subsequent work on different liquids obtained from the co-pyrolysis of biomass (grape seeds, GS) and two different polymers (waste tires and polystyrene, WT and PS respectively), yielded results remarkably akin to those noted for TPL, even if biomass accounted for a 80% of the original co-pyrolysis feedstock. This work assessed the impact of two relevant process

parameters of the pyrolysis liquid production on the droplet combustion behaviors. In particular, the kind of polymer source (WT or PS) and the nature of the catalyst used (Carmeuse limestone, calcined dolomite or none) were studied. The polymer source proved to have a bigger impact on the final combustion features, with a more volatile behavior and more efficient microexplosions for the GS-PS oil. The introduction of a catalyst in the oil production also led to a significant improvement in the bio-oil combustion characteristics, especially when using the Carmeuse catalyst. In light of these results, the aforementioned bio-oils could be considered as drop-in fuels (either neat or blended) for combustion applications where their sooty behavior and high sulfur content would not be an obstacle.

Finally, a crude glycerol obtained as a by-product of biodiesel production was tested both as received (CG) and desalted (DG). The results point to a remarkably slow conversion for these fuels, in agreement with their physicochemical properties and with the difficulties reported for their combustion in burners. Interestingly, two microexplosion typologies were found for these glycerols. The abrupt and violent secondary atomizations recorded for CG were ascribed to its high salt content, whereas the swelling and puffing events noted for DG were thought to arise from the homogeneous nucleation of the more volatile liquid fractions within the droplet. The blending of these glycerols with another industrial by-product of relevance (GF*) showed a noticeable acceleration of the evaporation process, especially for the case of DG. Subsequent tests in a semi-industrial furnace confirmed this improvement, as the range of stable conditions in the burner widened, with a better flame stability and a reduction of CO emissions for the glycerol-GF* mixtures.

A second pillar of the thesis consisted in the development and validation of a droplet evaporation model capable of accurately predict the behaviors observed in the experiments, including the multicomponent features of mixtures. To this effect, a variety of pure compounds from different chemical families were tested at the droplet combustion facility. The close agreement found between the model predictions and the experimental results for alcohols served as validation for this model, although significant deviations were noted for alkanes, with divergences increasing with the molecular weight of the compound tested. These deviations were ascribed to the thermal decomposition of the fuel vapors under the high-temperature and reducing conditions present at the experiments. The relevance of this phenomenon for real combustion applications motivated the development of a novel analytical model that introduced these gas-phase endothermic pyrolysis reactions to the problem of an isolated vaporizing droplet. This model was developed in collaboration with the University of California San Diego, and was based on activation-energy asymptotics. Through the combination of experimental data on droplet evaporation and the analytical model, some intrinsic kinetic parameters of these

pyrolysis reactions could be extracted. Namely, the pyrolysis temperature was identified as a useful replacement at leading order for the unknown Arrhenius parameters, and its value was estimated for different alkanes. Even if more experimental data is still required for validating the accuracy of the extracted kinetic parameters, this work is thought to be of clear relevance to the field, as it develops for the first time an analytical description which takes into account the impact of these reactions on the vaporizing characteristics of hydrocarbon liquid droplets.

To conclude, the combination of experiments and the evaporation model also allowed for the introduction of the isolated droplet configuration to the surrogate formulation and validation processes. A preliminary work on this topic was performed on heating oil, with binary mixtures of eicosane and methylnaphthalene attempting to match its vaporization and sooting behaviors. To that end, three surrogates were designed through different methods. SR1 was formulated with the aim of emulating the evaporation features of the target heating oil, making use of the multicomponent droplet evaporation model as predictive tool. On the other hand, SR2 was designed to match its sooting propensity, using the YSI as predictive instrument. The third surrogate was created through an approach widely used in the literature, entailing the simultaneous emulation of a number of physicochemical properties relevant for both behaviors (i.e., molecular weight, liquid density, YSI, C/H ratio and distillation curve). The subsequent validation by means of droplet evaporation tests revealed a very accurate emulation of the vaporization and sooting results of heating oil by SR1 and SR2 respectively. These results not only provided surrogate mixtures able to substitute the chemically complex heating oil in computational studies, but are also thought to support the efficacy of the aforementioned methods for developing novel surrogates based on the isolated droplet configuration.

5.2. Future work

From the experimental side, the strong dependence of some critical behaviors (microexplosions, pyrolysis reactions, radiative heating, etc.) on the experimental conditions used in the droplet evaporation and combustion tests is thought to require further investigation to fully understand the differences observed among works in the literature. To that effect, controlled comparisons varying key variables (gas temperature, droplet initial size, etc.) and even the kind of facility (drop tube vs. suspended droplet facility) could help to gain insight into these apparently conflicting results.

As already introduced, the further development of the droplet vaporization model with gas-phase pyrolysis also requires additional experiments, namely by testing alkanes at different levels of ambient temperature. This would allow for a more accurate estimation of the extracted

pyrolysis temperatures, as well as for a more complete validation of the model. Additionally, the extension of this model to address multicomponent cases would certainly be of great interest to the field, since the vast majority of real fuels consist in hydrocarbon mixtures.

Also in the modeling side, the development of droplet combustion models that include microexplosion phenomena would be required in order to fully understand this complex behavior featured in the experiments. A model which considers the potential homogeneous nucleation of vapors within the liquid phase could be a first step towards this goal, which would be helpful for the interpretation of experimental data. A clear example of this is the completely different modes of microexplosions experimentally observed for both kinds of crude glycerols. Additionally, and in connection with the previously discussed differences among droplet combustion setups, the modeling of a case where the liquid phase is in contact with a suspending filament (and therefore with heterogeneous nucleation sites) could also provide insight into the aforementioned different microexplosion behaviors reported in the literature.

The experimental and modeling tools developed along the thesis could also be applied to a wide variety of liquid fuels that pose difficulties for their combustion. Most of these difficult-to-burn fuels consist in low quality fuels such as the already explored crude glycerol, where their challenging combustion properties can hinder residue valorization and, depending on the fuel origin, production of renewable energy. A wide variety of these kind of fuels (heavy oil from refineries, process by-products, alternative biofuels, etc.) could benefit from detailed characterization methods such as those proposed in this work.

Finally, the further development of the surrogate design and validation methodologies is thought to be an interesting field of study where several improvements and novel developments could be undertaken. The more obvious one is the extension of the method used in Paper VI to a greater number of palette compounds in order to simultaneously match several complex behaviors. The surrogates developed through these isolated droplet configuration methodologies could also be compared with other surrogates of the literature, either in droplet combustion tests or even in a configuration closer to the final application (e.g., a spray flame). The clear relation found between the IDSY and the YSI also points to the potential modeling of the former index, which is thought to present a clear interest because of its proximity to the soot formation regime in real flames. The development and further validation of correlations between this index and other well-known soot indicators could also be complemented with the proposal of empirical mixture rules, which would allow to directly using the IDSY as a soot predictive tool in the surrogate formulation phase.

Addenda

A1: Impact factors and thematic units of the Journals

Journal	Editorial	Impact factor[*]	Thematic unit[*]
Combustion and Flame	Elsevier	4.57	Chemical Engineering
Fuel Processing Technology	Elsevier	4.98	Chemical Engineering
Experimental Thermal and Fluid Science	Elsevier	3.44	Physics, Fluids & Plasmas
Energy & Fuels	ACS	3.42	Chemical Engineering

* JCR (2019), extracted from Web of Science.

A2: Contribution of the doctoral candidate in each paper

Paper I. *Muelas, Á., Remacha, P., Ballester, J. (2019). Droplet Combustion and Sooting Characteristics of UCO Biodiesel, Heating Oil and their Mixtures under Realistic Conditions. Combustion and Flame, 203, 190-203. DOI:10.1016/j.combustflame.2019.02.014.*

The contribution of the candidate Á. Muelas in this first paper included an initial literature review aimed to determine the current state of the art of droplet combustion experiments, with a special focus on results obtained in previous works for heating oil and biodiesel. He also actively collaborated in designing the approach of the study and in conducting the experimental tests at the droplet combustion facility. After analyzing the results, the candidate was in charge of preparing the first draft and actively participated in elaborating the final version of the paper as well as in the preparation of the rebuttals for the journal referees.

Paper II. *Muelas, Á., Callén, M. S., Murillo, R., Ballester, J. (2019). Production and Droplet Combustion Characteristics of Waste Tire Pyrolysis Oil. Fuel Processing Technology, 196, 106149. DOI:10.1016/j.fuproc.2019.106149.*

This second paper was developed in collaboration with the *Grupo de Investigaciones Ambientales* from ICB-CSIC, which produced the TPL sample that was experimentally characterized at the DCF. The candidate undertook the droplet combustion tests, as well as a specific literature review to gain insight into previous droplet combustion experiments on different pyrolysis oils. He also took an active role in the results analysis, preparing a first draft of the paper, and elaborating with the other coauthors the final version of the paper, as well as the subsequent rebuttals.

Paper III. *Muelas, Á., Aranda, D., Callén, M. S., Murillo, R., Veses, A., Asrardel, M., Ballester, J. (2020). Properties and combustion characteristics of bio-oils from catalytic co-pyrolysis of grape seeds, polystyrene and waste tires. Energy & Fuels, 34(11), 14190-14203. DOI:10.1021/acs.energyfuels.0c02257.*

This paper was also developed in collaboration with the *Grupo de Investigaciones Ambientales* from ICB-CSIC. In this case, a broader study was devised in comparison with Paper II, as different bio-oil samples were characterized in order to ascertain the effect of modifying some

key parameters in the bio-oil production process. Thus, a closer collaboration between both research groups was required. The candidate took an active part in the different meetings where the approach of this study was designed. He also was in charge of conducting the droplet combustion tests, with the collaboration of D. Aranda and M. Asrardel. The results analysis and the elaboration of the paper was done as a joint work between both research groups, with ICB-CSIC focusing on the sections detailing the bio-oils production and physicochemical characterization and LIFTEC dealing with the droplet combustion results. The candidate undertook an active role in the elaboration of the latter kind of sections. This role included the preparation of a first draft, the collaboration in writing the final version and also the elaboration of the rebuttals for the journal referees (in coordination with ICB-CSIC and the other coauthors).

Paper IV. *Muelas, Á., Remacha, P., Pina, A., Barroso, J., Sobrino, Á., Aranda, D., Bayarri, N., Estévez, C., Ballester, J. (2020). Combustion of Crude Glycerol and its Blends with Acetals. Experimental Thermal and Fluid Science, 114, 110076. DOI:10.1016/j.expthermflusci.2020.110076.*

The development of this paper was framed in a research project with the company Inkemia IUCT Group. This project aimed to characterize the combustion behaviors of crude glycerol and its blends with other by-products of relevance, namely through two different scales: isolated droplet experiments and tests in a semi-industrial furnace. The candidate took an active part in the former kind of experiments, as well as in its results analysis and related literature review. He also collaborated in writing a communication to the 11th Mediterranean Combustion Symposium, which ultimately led to the publication of this fourth journal paper after a revision process. His contribution to the writing of the paper was focused in the sections addressing the droplet combustion tests, where he was in charge of preparing the first draft and actively participated in elaborating the final version, as well as in the preparation of the rebuttals.

Paper V. *Muelas, Á., Carpio J., Ballester, J., Sánchez A.L., Williams, F.A. (2020). Pyrolysis Effects during High-Temperature Vaporization of Alkane Droplets. Combustion and Flame, 217, 38-47. DOI:10.1016/j.combustflame.2020.03.033.*

The work that led to the publication of this paper was developed during a 3 months research visit of the candidate to the University of California San Diego (UCSD). As detailed in Section 4.2, significant deviations were consistently found between the predicted vaporization rates of

alkanes and those experimentally measured at the DCF, whereas accurate agreements were obtained for all the alcohols examined. During this period at UCSD, different hypothesis that could explain these results were tested under the supervision of Prof. Antonio Sánchez and, finally, the thermal decomposition of the hydrocarbon molecules was ascribed as responsible for these deviations. The theoretical development of the analytical model detailed in this paper was possible thanks to the expertise of Profs. Antonio Sánchez and Forman Williams. The candidate took part in the model development, collaborating with the model revision, testing and implementation. When it comes to the writing of the paper, the contribution of the candidate primarily focused on the experimental sections, collaborating also in the elaboration of the rebuttals.

Paper VI. *Muelas, Á., Aranda, D., Ballester, J. (2019). Alternative Method for the Formulation of Surrogate Liquid Fuels Based on Evaporative and Sooting Behaviors. Energy & Fuels, 33(6), 5719-5731. DOI:10.1021/acs.energyfuels.9b00737.*

The study that led to this publication was originally framed in the Bachelor Thesis of D. Aranda, where the Ph.D. candidate figured as co-supervisor. During an initial phase, the candidate undertook a thorough literature review on surrogates for liquid fuels, with a special focus on the works using the isolated droplet configuration for either the formulation or validation processes. He also took an active part (along with the other coauthors) in the design of the study approach, in performing the experimental tests at the DCF and in the results analysis that led to the elaboration of the Bachelor Thesis by D. Aranda. In a second phase, the candidate applied some changes to the methodology (e.g., replacement of a diffusion-limited multicomponent droplet evaporation model by an effective-diffusivity model, modification of some design parameters, etc.). This reformulation of the study also included additional droplet vaporization experiments, and led to the elaboration of the sixth journal paper.

A3: Experimental characterization of the DCF test conditions

This addendum summarizes the methods used for characterizing the experimental conditions of the gas phase at the DCF tests. As specified in Section 3.1, the gas composition was monitored through an online paramagnetic analyzer (Testo 350-S). The gas temperature and velocity measurements are detailed in the following sections.

A3.1. Gas temperature measurements

Gas temperature characterizations were performed by means of a bare, butt-welded, fine wire thermocouple of 50 μm in diameter (type S). This thermocouple was attached to a support wire of 500 μm which was inserted into a 3 mm ceramic rod, as displayed in Figure A3.1.a. This setup was hold by a 2-D positioner which allowed displacement in both radial directions (R_x and R_y, noted in Figure A3.1.a). The axial distance to the injection plane (L) was varied by displacing the movable frame illustrated in Figure 3.1. The hot junction (i.e., the welding) was positioned at the tip of the thermocouple (Figure A3.1.b), so that the measuring location was always well defined. Since the metallic wires could vary their length due to thermal expansion, pictures of the thermocouple were obtained through Camera 1 (Figure 3.1) in order to correct these potential displacements for each probe position. Figure A3.1.b is an example of such kind of picture.
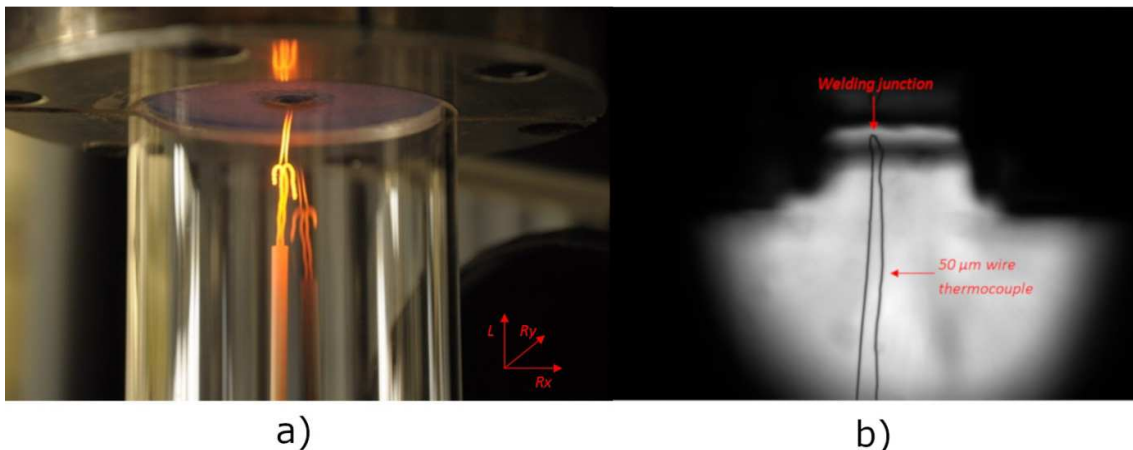

Figure A3.1. Thermocouple measuring inside the DCF combustion chamber (a). Picture (b) corresponds to a detailed view of the thermocouple tip obtained through Camera 1 (Figure 3.1).

As already discussed, different coflow atmospheres were used along the course of the thesis. The most common ones corresponded to the so-called 0, 3, 5 and 10% O_2 conditions, obtained through the combustion at the McKenna flat-flame burner of the gas flow rates summarized in Table A3.1. It is worth to note that a small flow of 0.5 Nl/h of N_2 was supplied through the injection orifice for all these conditions.

Table A3.1. Reactant flow rates fed to the McKenna burner to yield the most commonly used gas atmospheres at the DCF.

Gas condition	q_{CH4} (Nl/h)	q_{AIR} (Nl/h)	q_{O2} (Nl/h)
0% O_2	104	965	0
3% O_2	104	1103	0
5% O_2	104	1230	0
10% O_2	104	1288	55

The gas temperature profiles corresponding to these atmospheres were measured, both along axial and radial directions. It is worth to note that the data directly provided by the thermocouple corresponds to the temperature of the solid wire T_{sol} (and more specifically, the temperature at the welding), which could differ from the gas temperature (T_{gas}). Since the objective is to measure T_{gas}, some considerations had to be taken into account to correctly estimate it. As detailed in (Shaddix (1999)), the temperature of the gas can be estimated by considering the main heat transport mechanisms present in the thermocouple-gas configuration: conduction, convection and radiation. Thermal conduction along the wire could be minimized by using a sufficiently long and thin thermocouple wire. For the case depicted in Figure A3.1, the ratio of the thermocouple length to its diameter was around 300, so that the potential conduction of heat from the junction towards the cooler 500 μm support wires could be neglected (Shaddix (1999)). Thus, under a steady state condition, the heat balance of the system simplifies to:

$$Nu \frac{k}{d_{sol}}(T_{gas} - T_{sol}) - \varepsilon \sigma(T_{sol}^4 - T_w^4) = 0 \qquad (A3.1)$$

Being d_{sol} the diameter of the wire at the junction ($\approx$75 μm), ε the emissivity of the thermocouple material (assumed to be 0.2), and σ the Stefan-Boltzmann constant. The wall temperature (T_w) was assumed to be 600 K, and the thermal conductivity of the gas (k) was estimated as that of air. A critical issue when applying (A3.1) is the selection of the Nusselt number correlation. For the low Reynolds numbers present in our configuration, the correlation

proposed in (Andrews *et al.* (1972)) for a flow over a cylinder was used (valid for $0.02 < Re < 20$):

$$Nu = 0.34 + 0.65 \, Re^{0.45} \tag{A3.2}$$

The numerical solving of Equation (A3.1) provided the actual gas temperatures (T_{gas}) from the wire temperatures (T_{sol}) recorded by the thermocouple. Since thermal radiation is a heat loss mechanism for the solid wire, it is worth to note that the estimated gas temperatures were higher than the temperatures provided by the thermocouple. All the following results are presented in terms of the corrected gas temperature.

The axial temperature profiles recorded along the centerline for the coflow conditions of Table A3.1 are displayed in Figure A3.2, both for the region of greater interest for typical droplet combustion tests ($L \leq 50$ mm) and for the whole length of the combustion chamber ($L \leq 300$ mm). As it can be noticed, all conditions share an abrupt increase in the axial gas temperature during the first 10 mm, due to the transition from the cold injection orifice to the hot combustion products. The heat losses across the quartz tube justify the drop in T_{gas} found for increasing values of L, being the shorter gas residence times for the oxygen-rich conditions consistent with their lower temperature decrease rate.
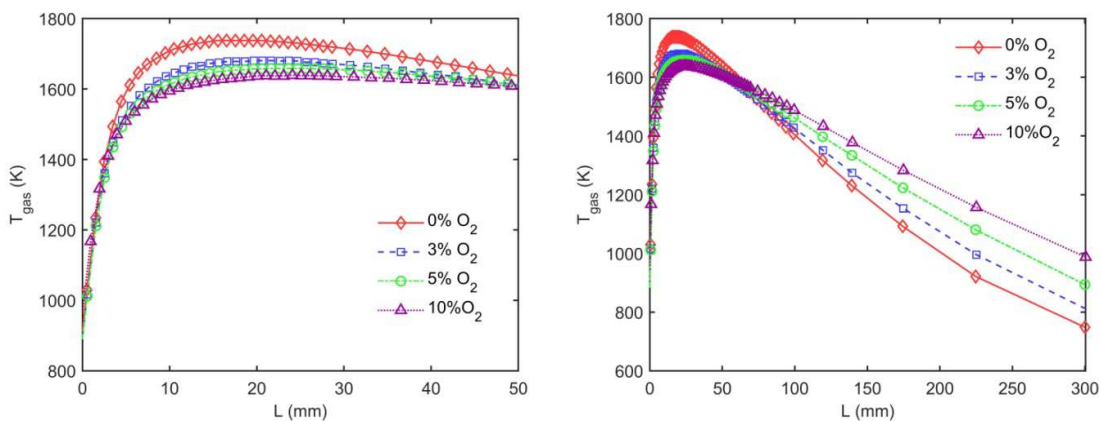

Figure A3.2. Axial temperature profiles recorded along the DCF centerline for the coflow conditions summarized in Table A3.1.

Besides axial measurements along the combustion chamber centerline, radial profiles of temperature were also obtained in order to characterize the homogeneity of the flow across the cross section. These results are presented in Figure A3.3 for the case of the 0% and 10% O_2 conditions. Both cases clearly show a cold region at the center (R_x=0 mm) ascribed to the effect of the injection orifice. Thermal gradients in this central region are progressively smoothed as

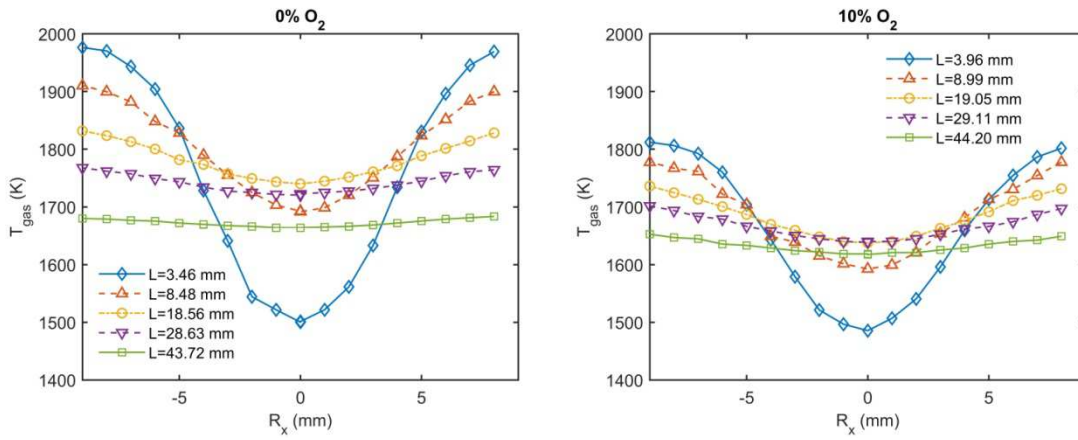the axial distance to the injection plane increased, becoming the radial profiles quite homogeneous for $L>25$ mm.

Figure A3.3. Radial temperature profiles recorded at different axial distances (L) and two coflow conditions (0 and 10% O_2).

A3.2. Gas velocity measurements

The determination of the gaseous coflow velocity was possible thanks to Dr. Antonio Lozano, who actively helped in this task, from the design and installation phase of the PIV (Particle Image Velocimetry) setup, to the data acquisition and processing part. This section aims to summarize the PIV measurements that were carried out at the DCF for two coflow conditions displayed in Table A3.1 (0 and 10% O_2).

The PIV equipment was kindly provided by Dr. Antonio Lozano, and consisted of:

- Double-pulsed Nd:YAG laser (PILS, Quanta Systems). Able to generate pulses of 6 ns with a nominal maximum energy of 250 mJ (532 nm).
- Digital Delay and Pulse Generator DG 535 (Stanford Research Systems), with 4 delay channels and 2 pulse channels.
- CCD Camera Hamamatsu Orca-ER C4742-95-12 fitted with telemicroscope Navitar 7000. This optical setup provided a field of view of approximately 20x27 mm^2.
- Interference bandpass filter Corion P-10-532-S-P523 with 10 nm FWHM.
- Alumina particles of 0.3 μm in nominal diameter. For its seeding, a small N_2 coflow of 2 Nl/h was used as carrier gas, and introduced in the combustion chamber through the droplet injection orifice.

The laser and pulse generator can be clearly observed in Figure A3.4.a, whereas a picture illustrating the optical setup used for the PIV measurements is shown in Figure A3.4.b.

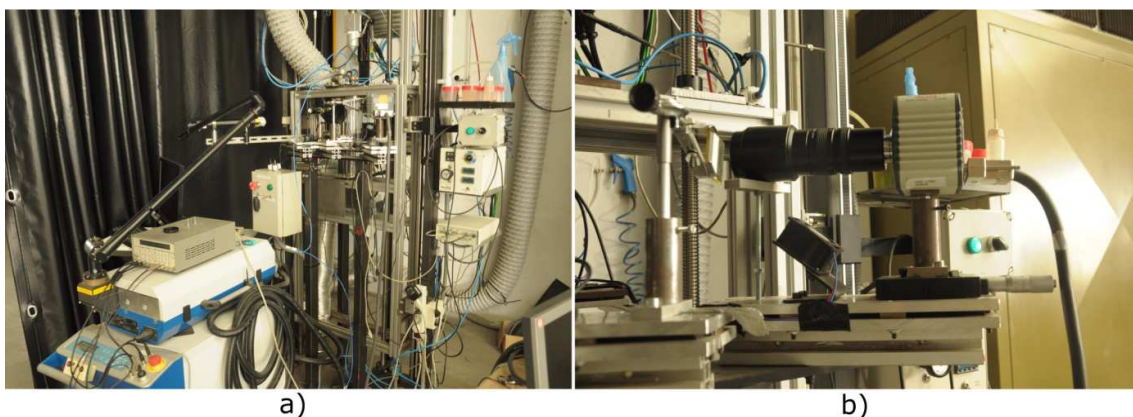Figure A3.4. Pictures showing the PIV setup installed next to the DCF (a), and a detailed view of the optical system (b).

The laser pulse was diverged into a vertical plane through a combination of spherical and cylindrical lenses, focalizing the plane at the combustion chamber centerline. The camera was located perpendicularly to this illumination plane, placing the interference bandpass filter

(centered at 532 nm) in front of the Navitar lens. Camera and laser were synchronized through the DG 535 delay and pulse generator. The system was programmed to obtain two sequential pictures, delayed between 500 and 876 µs depending on the flow velocity. Series of 100 pairs of images were obtained for each camera position (corresponding to, approximately, a window of 20 mm in height). Since the region of interest was determined to be L=0-100 mm, five camera positions were explored, yielding a total of 500 pairs of images for each coflow condition.

The processing of these images was carried out by Dr. Antonio Lozano through the program CCDPIV (Monash University), specifying a square window of 32 pixels with an overlapping of 50%. It is noteworthy that a background image (resulted from averaging 5 pictures) was subtracted for each position prior to the estimation of instantaneous velocities to minimize the influence of a reflection of the laser sheet in the combustion chamber wall. Figure A3.5 shows a vector map featuring the average velocity at each point for both coflow conditions. To reduce experimental noise, only the points which displayed more than 50 correlated pairs positively validated (over the total of 100) were included to Figure A3.5.
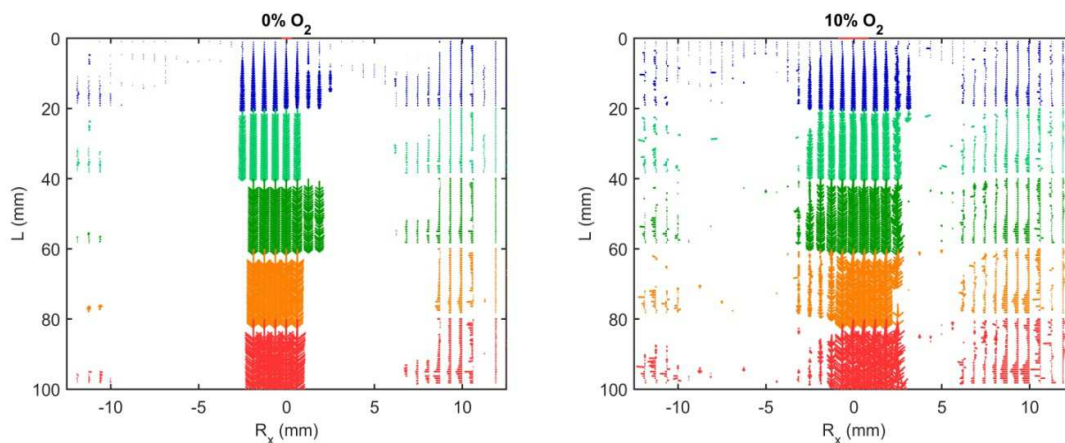

Figure A3.5. Vector map of gas velocities extracted for both coflow conditions (0 and 10% O_2). Each map is composed by the superposition of 5 camera positions, each one depicted by one color.

As displayed in Figure A3.5, the total field of view explored was to 27x100 mm^2, corresponding each color to a given camera position (27x20 mm^2). The only region of this field of view with enough correlated points was clearly a ≈3 mm-wide strip located around R_x=0. Since R_x=0 denotes the center of the injection orifice (where the alumina particles were introduced), these results were somehow to be expected, as the flow velocity appears to only display a downward axial component.

Thus, after their injection in the combustion chamber, the alumina particles were not dispersed but followed a straight path along the chamber centerline. This clearly marks the trajectory and

velocity of the gas flow which would surround the free-falling droplets, as in droplet combustion tests they are also introduced through this injection orifice. For any given distance to the injection plane (L), it was possible to estimate a representative velocity of this coflow through averaging the velocity values found in the 3 mm-wide strip centered around $R_x=0$. The resulting axial profiles of velocity are presented in Figure A3.6 for both oxygen conditions, being these profiles introduced as an experimental input to the simulations in Section 4.2 (namely, in order to calculate the Reynolds number between the droplet and the coflow). In Figure A3.6, it is worth to note that the gas flow was rapidly accelerated from very low velocities close to the injection plane to a maximum value of around 0.65 m/s (0% O_2) or 0.85 m/s (10% O_2). After that point, the flow velocity steadily dropped due to the gas temperature decrease already discussed in Figure A3.2.
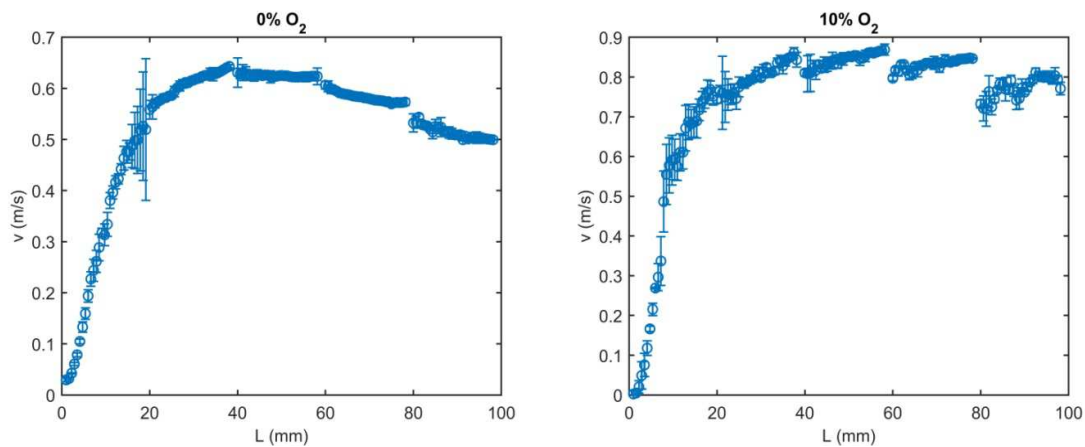

Figure A3.6. Axial profiles of velocity along the centerline for both coflow conditions (0 and 10% O_2). The velocity value for each L was obtained as the median calculated from all the points contained in the 3 mm-wide strip centered around $R_x=0$ in Figure A3.5. Each median value is accompanied by an uncertainty bar representing $\pm$ SD (Standard Deviation).

A4: Methods for the estimation of thermophysical and transport properties

The droplet evaporation model described in Section 3.2 required estimating a number of thermophysical and transport properties for both pure compounds and mixtures. This addendum details the methods and sources used for the calculation of each of those properties.

A4.1. Properties of liquids

A4.1.1. Density.

The liquid density (ρ_l) of pure compounds was extracted from (NIST (2020)) and (Perry and Green (2008)). As for the estimation of the ρ_l of mixtures, the following mixture rule was applied (Poling *et al.* (2001)):

$$\rho_{l,mix} = \frac{1}{\sum_{i=1}^{N} Y_i/\rho_{l,i}} \tag{A4.1}$$

Being Y_i the mass fraction of compound *i*.

A4.1.2. Specific heat

The specific heat of pure liquids (c_l) was extracted from (NIST (2020)) and (Perry and Green (2008)). The calculation of the c_l of mixtures was done through the following expression:

$$c_{l,mix} = \sum_{i=1}^{N} (Y_i \, c_{l,i}) \tag{A4.2}$$

A4.1.3. Latent heat of vaporization

The latent heat of vaporization of pure liquids (L_v) was extracted from (NIST (2020)) and (Perry and Green (2008)). The calculation of the L_v of mixtures was done through the following expression:

$$L_{v,mix} = \sum_{i=1}^{N} (\epsilon_i \, L_{v,i}) \tag{A4.3}$$

Being $\epsilon_i = Y_i/(\sum_{i=1}^{N} Y_i)$, the mass fraction of compound *i* over the total fuel in the vapor phase.

A4.1.4. Viscosity

The viscosity of pure liquids was obtained from (NIST (2020)) and (Perry and Green (2008)). The mixture rule of Grunberg and Nissan (Poling *et al.* (2001)), widely used in the literature, was used for estimating the viscosity of liquid mixtures. Since the blends tested in this work always corresponded to mixtures of chemically similar compounds, the interaction factor was neglected, resulting in the expression:

$$\mu_{l,mix} = e^{\sum_{i=1}^{N}(X_i \ln(\mu_{l,i}))} \tag{A4.4}$$

With X_i being the molar fraction of compound i.

A4.1.5. Thermal conductivity

The thermal conductivity of pure liquids (k_l) was extracted from (Perry and Green (2008)) and (Yaws (1995)). For binary mixtures, the Filippov equation recommended in (Perry and Green (2008)) was used:

$$k_{l,mix} = Y_1 k_{l,1} + Y_2 k_{l,2} - 0.72\, Y_1 Y_2 |k_{l,2} - k_{l,1}| \tag{A4.5}$$

On the other hand, for mixtures of more than two compounds, (Perry and Green (2008)) recommends using the Li method:

$$k_{l,mix} = \sum_{i=1}^{N} \sum_{j=1}^{N} \phi_i \, \phi_j \frac{2\, k_{l,i}\, k_{l,j}}{k_{l,i} + k_{l,j}} \tag{A4.6}$$

Where $\phi_i = \frac{X_i/\rho_{l,i}}{\sum_{j=1}^{N} X_j/\rho_{l,j}}$.

A4.1.6. Mass diffusion coefficient

The binary liquid diffusion coefficients at infinite dilution (D^0_{AB}) were estimated through the Wilke-Chang method (Poling *et al.* (2001)):

$$D^0_{AB} = \frac{7.4\,10^{-12}\sqrt{\varphi\, MW_B}\; T}{\mu_B\, V_A^{0.6}} \tag{A4.7}$$

Being φ the association factor, μ_B the viscosity of the solvent (B) and V_A the molecular volume of the solute (A). From the calculated values of D^0_{AB}, the Sanchez-Clifton formula was used to estimate the mass diffusion coefficient (D_l). As detailed in (Poling *et al.* (2001)):

$$D_l = \left(D_{BA}^0 \, X_A + D_{AB}^0 \, X_B\right)(1 - m + m \, \alpha) \tag{A4.8}$$

Being α a thermodynamic correction factor (dependent on the activity coefficient and the molar fraction), and m a parameter specific for the explored mixture. As it is common in the literature (e.g., see (Sazhin *et al.* (2010))), a thermodynamically ideal mixture ($\alpha = 1$) was assumed, and therefore the value of m was not required.

It is worth to note that the Sanchez-Clifton formula is only applicable to binary mixtures. The estimation of D_l for liquid blends with more species becomes much more cumbersome, with very complex and detailed methods requiring a wide range of chemical parameters of the mixture. As a compromise between accuracy and simplicity, the Wilke-Chang approximation proposed in (Sazhin *et al.* (2014)) was employed for such cases:

$$D_l = \frac{7.4 \; 10^{-15} \; \sqrt{MW_{mix}} \; T}{\mu_l \; V_{mix}^{0.6}} \tag{A4.9}$$

A4.2. Properties of gases

A4.2.1. Density.

As the model assumes ideal gas, the vapor density can be readily calculated through:

$$\rho_{mix} = \frac{P \; MW_{mix}}{R \; T} \tag{A4.10}$$

A4.2.2. Specific heat at constant pressure

The specific heat at constant pressure (c_p) of pure gases and vapors were extracted from (McBride (1993)) and (Perry and Green (2008)). The calculation of the c_p of mixtures was done through the following expression:

$$c_{p,mix} = \sum_{i=1}^{N} (Y_i \; c_{p,i}) \tag{A4.11}$$

A4.2.3. Viscosity

The dynamic viscosity (μ) of pure gases and vapors was obtained from (McBride (1993)) and (Perry and Green (2008)). As for estimating the viscosity of mixtures, the Wilke rule (Kee *et al.* (2005), Poling *et al.* (2001)) was applied:

$$\mu_{mix} = \sum_{i=1}^{N} \frac{X_i \, \mu_i}{\sum_{j=1}^{N} X_j \, \Phi_{ij}} \tag{A4.12}$$

Being:

$$\Phi_{ij} = \frac{1}{\sqrt{8}} \left(1 + \frac{MW_i}{MW_j}\right)^{-0.5} \left(1 + \left(\frac{\mu_i}{\mu_j}\right)^{0.5} \left(\frac{MW_j}{MW_i}\right)^{0.25}\right)^2 \tag{A4.13}$$

A4.2.4. Thermal conductivity

The thermal conductivity (k) of pure gases and vapors was estimated through the kinetic theory of gases, namely by following the method detailed in (Kee *et al.* (2005)). The different parameters involved in these calculations (Lennard-Jones potential well depth, Lennard-Jones collision diameter, dipole moment, rotational relaxation collision number, etc.) were obtained from different sources depending on availability: (University of California San Diego (2020)), (Poling *et al.* (2001)), and (Kee *et al.* (1999)). For some heavy molecules, these kind of transport parameters could not be obtained in the bibliography. In such cases, the empirical relations proposed in (Kee *et al.* (2005)) were employed to estimate them based on simpler and well-known physical properties (i.e., critical point and boiling temperature).

As for the estimation of the thermal conductivity of blends, the mixture average formula recommended in (Kee *et al.* (2005)) was used:

$$k_{mix} = \frac{1}{2} \left(\sum_{i=1}^{N} X_i \, k_i + \frac{1}{\sum_{i=1}^{N} X_i / \, k_i}\right) \tag{A4.14}$$

A4.2.5 Mass diffusion coefficient

The binary mass diffusion coefficients (D_{fi}) for any pair fuel-gas (e.g., fuel-N_2, fuel-CO_2, fuel-H_2O, etc.) were estimated through the kinetic theory of gases detailed in (Kee *et al.* (2005)). Analogously to the gas thermal conductivity, the parameters required for this calculation were obtained from different sources depending on availability: (University of California San Diego (2020)), (Poling *et al.* (2001)), and (Kee *et al.* (1999)). For the cases where no specific data could be found, the empirical relations proposed in (Kee *et al.* (2005)) were used to estimate them from simpler physical properties.

For the case of multicomponent gas mixtures, the combination of the different binary diffusion coefficients (D_{fi}) through the Wilke approximation recommended in (Fairbanks and Wilke (1950)) provided the final mass diffusion coefficient (D):

$$D = \frac{1 - X_f}{\sum_{i \neq f}^{N} X_i \big/ D_{fi}}$$

(A4.15)

References

Abnisa, F., and Daud, W. M. (2014). A review on co-pyrolysis of biomass: an optional technique to obtain a high-grade pyrolysis oil. *Energy Conversion and Management, 87*, 71-85.

Abramzon, B., and Sirignano, W. (1989). Droplet vaporization model for spray combustion calculations. *International Journal of Heat and Mass Transfer, 32*(9), 1605-1618.

Alam, F. E., Liu, Y., Avedisian, C., Dryer, F., and Farouk, T. (2015). n-Butanol droplet combustion: Numerical modeling and reduced gravity experiments. *Proceedings of the Combustion Institute, 35*(2), 1693-1700.

Alvarez, J., Amutio, M., Lopez, G., Santamaria, L., Bilbao, J., and Olazar, M. (2019). Improving bio-oil properties through the fast co-pyrolysis of lignocellulosic biomass and waste tyres. *Waste Management, 85*, 385-395.

Andrews, G., Bradley, D., and Hundy, G. (1972). Hot wire anemometer calibration for measurements of small gas velocities. *International Journal of Heat and Mass Transfer, 15*(10), 1765-1786.

Angeloni, M., Remacha, P., Martínez, A., and Ballester, J. (2016). Experimental investigation of the combustion of crude glycerol droplets. *Fuel, 184*, 889-895.

Avedisian, C. T. (2014). Developing Surrogates for Liquid Transportation Fuels: The Role of Spherically Symmetric Droplet Combustion. *Novel Combustion Concepts for Sustainable Energy Development* (pp. 379-402).

Aylón, E., Fernández-Colino, A., Murillo, R., Navarro, M., García, T., and Mastral, A. (2010). Valorisation of waste tyre by pyrolysis in a moving bed reactor. *Waste Management, 30*(7), 1220-1224.

Ballester, J., and Dopazo, C. (1994). Experimental study of the influence of atomization characteristics on the combustion of heavy oil. *Combustion Science and Technology, 103*(1-6), 235-263.

Ballester, J., and Dopazo, C. (1996). Drop size measurements in heavy oil sprays from pressure-swirl nozzles. *Atomization and Sprays, 6*(4), 377-408.

Ballester, J. M., Fueyo, N., and Dopazo, C. (1996). Combustion characteristics of heavy oil-water emulsions. *Fuel, 75*(6), 695-705.

Batey, J. E. (2003). *Combustion testing of a bio-diesel fuel oil blend in residential oil burning equipment.* National Oilheat Research Alliance Technology Symposium (p. 103).

Bohon, M. D., Metzger, B. A., Linak, W. P., King, C. J., and Roberts, W. L. (2011). Glycerol combustion and emissions. *Proceedings of the Combustion Institute, 33*(2), 2717-2724.

Brassard, P., Godbout, S., and Raghavan, V. (2017). Pyrolysis in auger reactors for biochar and bio-oil production: A review. *Biosystems Engineering, 161*, 80-92.

Bruno, T. J. (2006). Improvements in the measurement of distillation curves. 1. A composition-explicit approach. *Industrial & Engineering Chemistry Research, 45*(12), 4371-4380.

Bruno, T. J., and Huber, M. L. (2010). Evaluation of the physicochemical authenticity of aviation kerosene surrogate mixtures. Part 2: Analysis and prediction of thermophysical properties. *Energy & Fuels, 24*(8), 4277-4284.

Bruno, T. J., and Smith, B. L. (2010). Evaluation of the physicochemical authenticity of aviation kerosene surrogate mixtures. Part 1: Analysis of volatility with the advanced distillation curve. *Energy & Fuels, 24*(8), 4266-4276.

BTG-BTL. (2020). Empyro project webpage.   Retrieved August 2020, from https://www.btg-btl.com/en/company/projects/empyro

Clift, R., Grace, J. R., and Weber, M. E. (1978). *Bubbles, Drops, and Particles*: Academic Press, Inc.

Chauveau, C., Birouk, M., and Gökalp, I. (2011). An analysis of the d2-law departure during droplet evaporation in microgravity. *International Journal of Multiphase Flow, 37*(3), 252-259.

Chen, X., Khani, E., and Chen, C. (2016). A unified jet fuel surrogate for droplet evaporation and ignition. *Fuel, 182*, 284-291.

Council Directive EU 1999/31/EC of 26 April 1999 on the landfill of waste. *Official Journal of the European Communities, 182*, 1-19.

Das, D. D., John, P. C. S., McEnally, C. S., Kim, S., and Pfefferle, L. D. (2018). Measuring and predicting sooting tendencies of oxygenates, alkanes, alkenes, cycloalkanes, and aromatics on a unified scale. *Combustion and Flame, 190*, 349-364.

Das, D. D., McEnally, C. S., Kwan, T. A., Zimmerman, J. B., Cannella, W. J., Mueller, C. J., and Pfefferle, L. D. (2017). Sooting tendencies of diesel fuels, jet fuels, and their surrogates in diffusion flames. *Fuel, 197*, 445-458.

Dhyani, V., and Bhaskar, T. (2018). A comprehensive review on the pyrolysis of lignocellulosic biomass. *Renewable Energy, 129*, 695-716.

Dietrich, D. L., Nayagam, V., Hicks, M. C., Ferkul, P. V., Dryer, F. L., Farouk, T., . . . Liu, Y. C. (2014). Droplet combustion experiments aboard the international space station. *Microgravity Science and Technology, 26*(2), 65-76.

Dooley, S., Won, S. H., Heyne, J., Farouk, T. I., Ju, Y., Dryer, F. L., . . . Wang, H. (2012). The experimental evaluation of a methodology for surrogate fuel formulation to emulate gas phase combustion kinetic phenomena. *Combustion and Flame, 159*(4), 1444-1466.

Elwardany, A., Sazhin, S., and Im, H. G. (2016). A new formulation of physical surrogates of FACE A gasoline fuel based on heating and evaporation characteristics. *Fuel, 176*, 56-62.

Elwardany, A., Sazhin, S. S., and Farooq, A. (2013). Modelling of heating and evaporation of gasoline fuel droplets: a comparative analysis of approximations. *Fuel, 111*, 643-647.

Faeth, G., and Lazar, R. (1971). Fuel droplet burning rates in a combustion gas environment. *AIAA Journal, 9*(11), 2165-2171.

Fairbanks, D., and Wilke, C. (1950). Diffusion coefficients in multicomponent gas mixtures. *Industrial & Engineering Chemistry, 42*(3), 471-475.

Farouk, T., and Dryer, F. (2011). Microgravity droplet combustion: effect of tethering fiber on burning rate and flame structure. *Combustion Theory and Modelling, 15*(4), 487-515.

Farouk, T., Liu, Y., Savas, A., Avedisian, C., and Dryer, F. (2013). Sub-millimeter sized methyl butanoate droplet combustion: Microgravity experiments and detailed numerical modeling. *Proceedings of the Combustion Institute, 34*(1), 1609-1616.

Farrell, J., Cernansky, N., Dryer, F., Law, C. K., Friend, D., Hergart, C., . . . Pitsch, H. (2007). Development of an experimental database and kinetic models for surrogate diesel fuels. *SAE Technical Papers*, 2007-01-0201.

Flach, B., Lieberz, S., and Bolla, S. (2019). EU Biofuels Annual 2019; Global Agricultural Information Network (GAIN) Report Number: NL1902. *US Department of Agriculture (USDA) Foreign Agricultural Service: Washington, DC, USA*.

Garcia-Perez, M., Lappas, P., Hughes, P., Dell, L., Chaala, A., Kretschmer, D., and Roy, C. (2006). Evaporation and combustion characteristics of biomass vacuum pyrolysis oils. *IFRF Combustion Journal, 200601*, 1-27.

Gavhane, S., Pati, S., and Som, S. (2016). Evaporation of multicomponent liquid fuel droplets: Influences of component composition in droplet and vapor concentration in free stream ambience. *International Journal of Thermal Sciences, 105*, 83-95.

Ghorbani, A., Bazooyar, B., Shariati, A., Jokar, S. M., Ajami, H., and Naderi, A. (2011). A comparative study of combustion performance and emission of biodiesel blends and diesel in an experimental boiler. *Applied Energy, 88*(12), 4725-4732.

Godsave, G. (1949). Combustion of Droplets in a Fuel Spray. *Nature, 164*(4173), 708-709.

Godsave, G. (1953). *Studies of the combustion of drops in a fuel spray—the burning of single drops of fuel.* Symposium (International) on combustion, 4(1), 818-830.

Hashimoto, N., Nomura, H., Suzuki, M., Matsumoto, T., Nishida, H., and Ozawa, Y. (2015). Evaporation characteristics of a palm methyl ester droplet at high ambient temperatures. *Fuel, 143*, 202-210.

Hubbard, G., Denny, V., and Mills, A. (1975). Droplet evaporation: effects of transients and variable properties. *International Journal of Heat and Mass Transfer, 18*(9), 1003-1008.

IEA (2019). World Energy Statistics and Balances, International Energy Agency (IEA): OECD, Paris (France).

Kathrotia, T. (2011). Reaction kinetics modeling of OH*, CH*, and C2* chemiluminescence. Doctoral dissertation, Ruprecht-Karls-Universität Heidelberg.

Kee, R., Dixon-Lewis, G., Warnatz, J., Coltrin, M., Miller, J., and Moffat, H. (1999). Transport: a software package for the evaluation of gas-phase, multicomponent transport properties. *Chemkin Collection*, Release 3.6, Reaction Design, Inc., San Diego, CA.

Kee, R. J., Coltrin, M. E., and Glarborg, P. (2005). *Chemically reacting flow: theory and practice*: John Wiley & Sons.

Kermes, V., and Bělohradský, P. (2013). Biodiesel (EN 14213) heating oil substitution potential for petroleum based light heating oil in a 1 MW stationary combustion facility. *Biomass and Bioenergy, 49*, 10-21.

Kijewska, A., and Bluszcz, A. (2016). Analysis of greenhouse gas emissions in the European Union member states with the use of an agglomeration algorithm. *Journal of Sustainable Mining, 15*(4), 133-142.

Kim, D., and Violi, A. (2018). Hydrocarbons for the next generation of jet fuel surrogates. *Fuel, 228*, 438-444.

Lapuerta, M., González-García, I., Céspedes, I., Estévez, C., and Bayarri, N. (2019). Improvement of cold flow properties of a new biofuel derived from glycerol. *Fuel, 242*, 794-803.

Lasheras, J., Fernandez-Pello, A., and Dryer, F. (1979). Initial observations on the free droplet combustion characteristics of water-in-fuel emulsions. *Combustion Science and Technology, 21*(1-2), 1-14.

Lasheras, J., Fernandez-Pello, A., and Dryer, F. (1980a). Experimental observations on the disruptive combustion of free droplets of multicomponent fuels. *Combustion Science and Technology, 22*(5-6), 195-209.

Lasheras, J., Fernandez-Pello, A., and Dryer, F. (1980b). *On the disruptive burning of free droplets of alcohol/n-paraffin solutions and emulsions.* Symposium (International) on Combustion, 18(1), 293-305.

Law, C., Chung, S., and Srinivasan, N. (1980). Gas-phase quasi-steadiness and fuel vapor accumulation effects in droplet burning. *Combustion and Flame, 38*, 173-198.

Li, T., Zhu, D., Akafuah, N., Saito, K., and Law, C. (2011). Synthesis, droplet combustion, and sooting characteristics of biodiesel produced from waste vegetable oils. *Proceedings of the Combustion Institute, 33*(2), 2039-2046.

Liñán, A. (1985). Theory of droplet vaporization and combustion. *Modélisation des Phénomenes de Combustion, CEA-EDF INRIA, 59*, 73-103.

Liu, Y. C., and Avedisian, C. T. (2012). A comparison of the spherical flame characteristics of sub-millimeter droplets of binary mixtures of n-heptane/iso-octane and n-heptane/toluene with a commercial unleaded gasoline. *Combustion and Flame, 159*(2), 770-783.

Liu, Y. C., Savas, A. J., and Avedisian, C. T. (2012). Comparison of the burning characteristics of indolene and commercial grade gasoline droplets without convection. *Energy & Fuels, 26*(9), 5740-5749.

Liu, Y. C., Savas, A. J., and Avedisian, C. T. (2013a). The spherically symmetric droplet burning characteristics of Jet-A and biofuels derived from camelina and tallow. *Fuel, 108*, 824-832.

Liu, Y. C., Savas, A. J., and Avedisian, C. T. (2013b). Spherically symmetric droplet combustion of three and four component miscible mixtures as surrogates for Jet-A. *Proceedings of the Combustion Institute, 34*(1), 1569-1576.

Liu, Y. C., Xu, Y., Hicks, M. C., and Avedisian, C. T. (2016). Comprehensive study of initial diameter effects and other observations on convection-free droplet combustion in the standard atmosphere for n-heptane, n-octane, and n-decane. *Combustion and Flame, 171*, 27-41.

Long, W., Yi, P., Jia, M., Feng, L., and Cui, J. (2015). An enhanced multi-component vaporization model for high temperature and pressure conditions. *International Journal of Heat and Mass Transfer, 90*, 857-871.

Makino, A., and Law, C. K. (1988). On the controlling parameter in the gasification behavior of multicomponent droplets. *Combustion and Flame, 73*(3), 331-336.

Maqua, C., Castanet, G., and Lemoine, F. (2008). Bicomponent droplets evaporation: Temperature measurements and modelling. *Fuel, 87*(13-14), 2932-2942.

Marchese, A., Dryer, F., Nayagam, V., and Colantonio, R. (1996). *Hydroxyl radical chemiluminescence imaging and the structure of microgravity droplet flames.* Symposium (International) on Combustion, 26(1), 1219-1226.

Martínez, J. D., Puy, N., Murillo, R., García, T., Navarro, M. V., and Mastral, A. M. (2013). Waste tyre pyrolysis–A review. *Renewable and Sustainable Energy Reviews, 23*, 179-213.

McBride, B. J. (1993). *Coefficients for calculating thermodynamic and transport properties of individual species* (Vol. 4513): NASA Langley Research Center.

Mendez, C., Parthasarathy, R., and Gollahalli, S. (2012). *Performance and Emission Characteristics of a Small-Scale Gas Turbine Engine Fueled with Ethanol/Jet A Blends.* Paper presented at the 50th AIAA Aerospace Sciences Meeting, AIAA 2011-619.

Mendez, C., Parthasarathy, R., and Gollahalli, S. (2014). Performance and emission characteristics of butanol/Jet A blends in a gas turbine engine. *Applied Energy, 118*, 135-140.

Miller, R., Harstad, K., and Bellan, J. (1998). Evaluation of equilibrium and non-equilibrium evaporation models for many-droplet gas-liquid flow simulations. *International Journal of Multiphase Flow, 24*(6), 1025-1055.

Mueller, C. J., Cannella, W. J., Bays, J. T., Bruno, T. J., DeFabio, K., Dettman, H. D., . . . McConnell, S. S. (2016). Diesel surrogate fuels for engine testing and chemical-kinetic modeling: Compositions and properties. *Energy & Fuels, 30*(2), 1445-1461.

Naik, C. V., Puduppakkam, K. V., Modak, A., Meeks, E., Wang, Y. L., Feng, Q., and Tsotsis, T. T. (2011). Detailed chemical kinetic mechanism for surrogates of alternative jet fuels. *Combustion and Flame, 158*(3), 434-445.

Nayagam, V., Dietrich, D. L., and Williams, F. A. (2018). Unsteady droplet combustion with fuel thermal expansion. *Combustion and Flame, 195*, 216-219.

Ng, H. K., and Gan, S. (2010). Combustion performance and exhaust emissions from the non-pressurised combustion of palm oil biodiesel blends. *Applied Thermal Engineering, 30*(16), 2476-2484.

NIST. (2020). NIST Chemistry Webbook 2020, Retrieved September 2020 from http://webbook.nist.gov/.

Pan, K.-L., Li, J.-W., Chen, C.-P., and Wang, C.-H. (2009). On droplet combustion of biodiesel fuel mixed with diesel/alkanes in microgravity condition. *Combustion and Flame, 156*(10), 1926-1936.

Perry, R. H., and Green, D. W. (2008). *Perry's Chemical Engineers' Handbook (8th edition)*. New York: McGraw-Hill.

Pitz, W. J., and Mueller, C. J. (2011). Recent progress in the development of diesel surrogate fuels. *Progress in Energy and Combustion Science, 37*(3), 330-350.

Poling, B. E., Prausnitz, J. M., and O'Connell, J. P. (2001). *The properties of gases and liquids*. New York: McGraw-Hill.

Queirós, P., Costa, M., and Carvalho, R. (2013). Co-combustion of crude glycerin with natural gas and hydrogen. *Proceedings of the Combustion Institute, 34*(2), 2759-2767.

Quispe, C. A., Coronado, C. J., and Carvalho Jr, J. A. (2013). Glycerol: Production, consumption, prices, characterization and new trends in combustion. *Renewable and Sustainable Energy Reviews, 27*, 475-493.

Rahmes, T., Kinder, J., Crenfeldt, G., LeDuc, G., Abe, Y., McCall, M., . . . Lewis, C. (2009). *Sustainable bio-derived synthetic paraffinic kerosene (Bio-SPK) jet fuel flights and engine tests program results.* Paper presented at the 9th AIAA Aviation Technology, Integration, and Operations conference (ATIO), AIAA 2009-7002.

Randolph, A., and Law, C. (1986). Influence of physical mechanisms on soot formation and destruction in droplet burning. *Combustion and flame, 64*(3), 267-284.

Rapp, B. (2016). *Microfluidics: Modelling, Mechanics and Mathematics*. Elsevier.

Reutzsch, J., Kieffer-Roth, C., and Weigand, B. (2020). A consistent method for direct numerical simulation of droplet evaporation. *Journal of Computational Physics*, 109455.

Sanahuja-Parejo, O., Veses, A., López, J. M., Murillo, R., Callén, M. S., and García, T. (2019). Ca-based Catalysts for the Production of High-Quality Bio-Oils from the Catalytic Co-Pyrolysis of Grape Seeds and Waste Tyres. *Catalysts, 9*(12), 992.

Sánchez, A. L., Urzay, J., and Liñán, A. (2015). The role of separation of scales in the description of spray combustion. *Proceedings of the Combustion Institute, 35*(2), 1549-1577.

Savage, P. E. (2000). Mechanisms and kinetics models for hydrocarbon pyrolysis. *Journal of Analytical and Applied Pyrolysis, 54*(1-2), 109-126.

Sazhin, S., Al Qubeissi, M., Kolodnytska, R., Elwardany, A., Nasiri, R., and Heikal, M. (2014). Modelling of biodiesel fuel droplet heating and evaporation. *Fuel, 115*, 559-572.

Sazhin, S. S. (2006). Advanced models of fuel droplet heating and evaporation. *Progress in Energy and Combustion Science, 32*(2), 162-214.

Sazhin, S. S. (2017). Modelling of fuel droplet heating and evaporation: Recent results and unsolved problems. *Fuel, 196*, 69-101.

Sazhin, S. S., Elwardany, A., Krutitskii, P., Castanet, G., Lemoine, F., Sazhina, E., and Heikal, M. (2010). A simplified model for bi-component droplet heating and evaporation. *International Journal of Heat and Mass Transfer, 53*(21-22), 4495-4505.

Setyawan, H. Y., Zhu, M., Zhang, Z., and Zhang, D. (2016). Ignition and combustion characteristics of single droplets of a crude glycerol in comparison with pure glycerol, petroleum diesel, biodiesel and ethanol. *Energy, 113*, 153-159.

Shaddix, C. R. (1999). Correcting thermocouple measurements for radiation loss: a critical review. *Proceedings of the 33rd National Heat Transfer Conference*, HTD99-282.

Shaddix, C. R., and Hardesty, D. R. (1999). Combustion properties of biomass flash pyrolysis oils. Final Project Report (No. SAND99–8238), Sandia National Labs, Livermore, CA (US).

Shaddix, C. R., and Tennison, P. J. (1998). *Effects of char content and simple additives on biomass pyrolysis oil droplet combustion.* Symposium (International) on Combustion, 27(2), 1907-1914.

Sienkiewicz, M., Janik, H., Borzędowska-Labuda, K., and Kucińska-Lipka, J. (2017). Environmentally friendly polymer-rubber composites obtained from waste tyres: A review. *Journal of Cleaner Production, 147*, 560-571.

Sirignano, W. A. (2010). *Fluid dynamics and transport of droplets and sprays*: Cambridge University Press.

Skeel, R. D., and Berzins, M. (1990). A method for the spatial discretization of parabolic equations in one space variable. *SIAM journal on scientific and statistical computing, 11*(1), 1-32.

Spalding, D. B. (1950). Combustion of liquid fuels. *Nature, 165*(4187), 160-160.

Sparrow, E., and Gregg, J. (1958). The variable fluid property problem in free convection. *Transactions of the American Society of Mechanical Engineers, 80*, 879-886.

Steinmetz, S. A., Herrington, J. S., Winterrowd, C. K., Roberts, W. L., Wendt, J. O., and Linak, W. P. (2013). Crude glycerol combustion: Particulate, acrolein, and other volatile organic emissions. *Proceedings of the Combustion Institute, 34*(2), 2749-2757.

Su, M., and Chen, C. (2015). Heating and evaporation of a new gasoline surrogate fuel: a discrete multicomponent modeling study. *Fuel, 161*, 215-221.

Tashtoush, G., Al-Widyan, M. I., and Al-Shyoukh, A. O. (2003). Combustion performance and emissions of ethyl ester of a waste vegetable oil in a water-cooled furnace. *Applied Thermal Engineering, 23*(3), 285-293.

Thompson, J. C., and He, B. B. (2006). Characterization of crude glycerol from biodiesel production from multiple feedstocks. *Applied Engineering in Agriculture, 22*(2), 261-265.

Turns, S. R. (1996). *Introduction to combustion*. New York: McGraw-Hill.

University of California San Diego (2020). Chemical-Kinetic Mechanisms for Combustion Applications. Retrieved September 2020 from https://web.eng.ucsd.edu/mae/groups/combustion/mechanism.html

Uzoejinwa, B. B., He, X., Wang, S., Abomohra, A. E.-F., Hu, Y., and Wang, Q. (2018). Co-pyrolysis of biomass and waste plastics as a thermochemical conversion technology for high-grade biofuel production: Recent progress and future directions elsewhere worldwide. *Energy Conversion and Management, 163*, 468-492.

Wang, C., Liu, X., and Law, C. (1984). Combustion and microexplosion of freely falling multicomponent droplets. *Combustion and Flame, 56*(2), 175-197.

Williams, F. A. (1985). *Combustion theory*: CRC Press.

Woltjer, G., Daioglou, V., Elbersen, B., Ibañez, G. B., Smeets, E., González, D. S., and Barnó, J. G. (2017). *Study report on reporting requirements on biofuels and bioliquids stemming from the directive (EU) 2015/1513*: EU Commission.

Xu, Y., and Avedisian, C. T. (2015). Combustion of n-butanol, gasoline, and n-butanol/gasoline mixture droplets. *Energy & Fuels, 29*(5), 3467-3475.

Yang, S., and Wu, M. (2017). The droplet combustion and thermal characteristics of pinewood bio-oil from slow pyrolysis. *Energy, 141*, 2377-2386.

Yaws, C. L. (1995). *Handbook of Thermal Conductivity, Volume 2: Organic Compounds C5 to C7*: Elsevier.